

**A Precision Measurement of the e^+p/e^-p
Elastic Scattering Cross Section Ratio at the
OLYMPUS Experiment**

by

Brian Scott Henderson

B.S. in Physics, William Marsh Rice University (2010)

B.A. in Mathematics, William Marsh Rice University (2010)

Submitted to the Department of Physics
in partial fulfillment of the requirements for the degree of

Doctor of Philosophy

at the

MASSACHUSETTS INSTITUTE OF TECHNOLOGY

September 2016

© Massachusetts Institute of Technology 2016. All rights reserved.

Author

Department of Physics

August 15, 2016

Certified by

Richard Milner

Professor of Physics

Thesis Supervisor

Accepted by

Nergis Mavalvala

Curtis and Kathleen Marble Professor of Astrophysics

Associate Department Head of Physics

A Precision Measurement of the e^+p/e^-p Elastic Scattering Cross Section Ratio at the OLYMPUS Experiment

by

Brian Scott Henderson

Submitted to the Department of Physics
on August 15, 2016, in partial fulfillment of the
requirements for the degree of
Doctor of Philosophy

Abstract

Measurements of the ratio of the proton elastic form factors ($\mu_p G_E/G_M$) using Rosenbluth separation and those using polarization-based techniques show a strong discrepancy, which has persisted both in modern experimental results and in re-analyses of previous data. The most widely accepted hypothesis to explain this discrepancy is the treatment of the contributions from hard two-photon exchange (TPE) to elastic electron-proton scattering in the radiative corrections applied to the Rosenbluth separation measurements. Calculations of the hard TPE contribution are highly model dependent, but the effect may be measured experimentally with a precise determination of the ratio of the positron-proton and electron-proton elastic scattering cross sections.

The OLYMPUS experiment collected approximately 4 fb^{-1} of e^+p and e^-p scattering data at the DORIS storage ring at DESY in 2012, with the goal of measuring the elastic $\sigma_{e^+p}/\sigma_{e^-p}$ ratio over the kinematic range ($0.4 \leq \epsilon \leq 0.9$), ($0.6 \leq Q^2 \leq 2.2$) GeV^2/c^2 at a fixed lepton beam energy of 2.01 GeV. The detector for the OLYMPUS experiment consisted of refurbished elements of the Bates Large Acceptance Spectrometer Toroid (BLAST) surrounding an internal gaseous hydrogen target, with the addition of multiple systems for the monitoring of the luminosity collected by the experiment. A detailed simulation of the experiment was developed to account for both radiative corrections and various systematic effects.

This work presents preliminary results from the OLYMPUS data, demonstrating that the elastic $\sigma_{e^+p}/\sigma_{e^-p}$ ratio rises to several percent at $\epsilon \approx 0.4$ and indicating a significant contribution from TPE to $e^\pm p$ scattering. Additionally, the value of $\sigma_{e^+p}/\sigma_{e^-p}$ has been measured to unprecedented precision at $\epsilon = 0.98$, which provides a valuable normalization point for other experimental data.

Thesis Supervisor: Richard Milner
Title: Professor of Physics

Acknowledgments

Foremost, OLYMPUS was a decade-long project (from conception to the final analyses) involving a collaboration of 60+ people from 6 countries who made contributions to the various phases of the experiment that are far too numerous to list here. In particular, of course, I am extremely grateful to my advisor Professor Richard Milner. It has been a true privilege to learn from Richard's expertise over the past six years, both in terms of physics and in management of an experiment. Thank you also to my other committee members Professors Robert Redwine and Robert Jaffe, who both provided excellent guidance in the construction of this thesis.

The staff, technicians, and engineers of the MIT-Bates Research and Engineering Center were not only instrumental to the design and construction of OLYMPUS, but are also great people and were an absolute pleasure to work with from my first day at MIT. While I risk missing somebody by listing names, I learned much of what I know about putting together an experiment from Jim Kelsey, Chris Vidal, Peter Binns, Brian O'Rourke, and Joe Dodge, who all made several treks to Hamburg to lend their expertise to the construction of the experiment.

Numerous technicians and engineers at DESY worked on the construction of the experiment as well, and while I never worked with any of them closely, their important contributions must be acknowledged. Special recognition goes to the DESY accelerator team, led by Frank Brinker, who delivered consistent and well-maintained electron and positron beams to the experiment throughout our data-taking periods (and would greet the off-going OLYMPUS night shift crew with a hearty "moin moin" and handshake at 7 AM as they arrived for the day). I would also like to thank the managers of the MIT Engaging computing cluster, who provided a, quite frankly, miraculous resource for the analysis of this experiment. Although I have never met them in person, they were always quick to resolve any issues we had in using the cluster and patient in putting up with my excessive disk usage.

Looking further into the past, I would like to thank two teachers, in particular, from my junior high and high school years, Christine Moore and Terry Crane, who encouraged me to think seriously about physics and helped open the door to a much larger academic world.

Among members of the OLYMPUS collaboration, I would like to thank several in particular. First, thanks to Michael Kohl, Uwe Schneekloth, and Douglas Hasell for their roles in making OLYMPUS happen and keeping things on track (and especially to the latter for helping take care of us MIT students as we traveled back and forth from Hamburg and pushed through the analysis).

While not on the author list, Joanne Gregory was an immense help in all aspects of coordinating travel to and from Germany, finding places to stay while there, and generally navigating LNS and MIT. Her expertise in managing the hadronic physics group will most certainly be missed.

Several of the OLYMPUS post-docs were monumentally critical in making OLYMPUS happen: Jan Bernauer, Alexander Winnebeck, and Jürgen Diefenbach. Each of them performed apparent miracles in finding last-minute solutions to hardware and

software problems, and given another six years in grad school I don't think I could learn everything they would have had to teach me about experimental physics.

A true place of honor among my acknowledgments belongs to the other OLYMPUS graduate students: Axel Schmidt, Colton O'Connor, Rebecca Russell, and Lauren Ice. Each of them played a critical role in constructing the OLYMPUS results, taking on responsibilities above a grad student's pay-grade and finding creative, excellent solutions to many of the challenges we faced. In addition to their enormous contributions to the experiment, they were great friends who made the whole experience of living in Germany and the grind of building, operating, and conducting the analysis for the experiment much better.

My parents, Patricia and Scott, are certainly responsible for much of this accomplishment, as they have always been unwaveringly supportive of my education and my goals, and instilled in me a strong desire to learn and fight for answers. Thank you, Mom and Dad.

More than anybody else, my wife Hilary has helped me through grad school (even marrying me in the thick of it). Through the time spent apart in Hamburg, the frustration when the analysis was stalled, and the crush of work that accompanied the last several months of the project, she has always been loving and supportive, all while going through law school and the bar exam herself. Thank you, Hil.

Contents

1	Introduction	21
1.1	The Fundamentals of OLYMPUS: Motivation and Goals	22
1.2	Notes on the Organization and Content of this Work	26
2	The Proton, Form Factors, and Theoretical Motivation of the OLYM- PUS Experiment	29
2.1	Fundamentals and Formalism	30
2.1.1	Elastic Lepton-Proton Scattering	30
2.1.2	Elastic Form Factors	34
2.1.3	Physical Interpretation of the Elastic Form Factors	35
2.2	Determination of the Proton Elastic Form Factors	36
2.2.1	Rosenbluth Separation	36
2.2.2	Polarization-Based Techniques	37
2.3	Existing Data and the Proton Form Factor Discrepancy	39
2.4	Possible Causes of the Discrepancy and the Two-Photon Exchange Hypothesis	40
2.4.1	Theoretical Calculations of TPE and their Effect on the $\frac{\mu_p G_E}{G_M}$ Ratio	43
2.4.2	Experimental Signature of TPE	45
2.5	Experiments Measuring $\sigma_{e+p}/\sigma_{e-p}$ and Physics Goals of the OLYMPUS Experiment	46
3	The OLYMPUS Experiment	49

3.1	Conventions for the Description of the Experiment	50
3.2	The DORIS III e^+/e^- Storage Ring	51
3.2.1	OLYMPUS at DORIS	52
3.2.2	Beam Specifications	53
3.3	The OLYMPUS Internal Hydrogen Target	55
3.3.1	Scattering Chamber	56
3.3.2	Target Cell	58
3.3.3	Collimator	58
3.3.4	Wakefield Suppressors	59
3.3.5	Cryogenic System	61
3.3.6	Vacuum System	61
3.3.7	Hydrogen Gas Supply System	62
3.4	The OLYMPUS $e^\pm p$ Spectrometer	63
3.4.1	Toroidal Magnet	64
3.4.2	Time-of-Flight (ToF) Scintillator System	66
3.4.3	Drift Chamber Tracking System	68
3.5	12° Tracking Telescope Luminosity Monitors	71
3.5.1	Silicon Photomultiplier (SiPM) Scintillator Tiles	72
3.5.2	Lead Glass Calorimeters	74
3.5.3	Gas Electron Multiplier (GEM) Detectors	75
3.5.4	Multi-Wire Proportional Chambers (MWPCs)	78
3.6	Symmetric Møller/Bhabha Scattering Luminosity Monitor	80
3.7	Slow Control System	83
3.8	The OLYMPUS Trigger and Readout	83
3.8.1	Main Kinematic Trigger and Second-Level Drift Chamber Trigger	85
3.8.2	12° Telescope Trigger	86
3.8.3	SYMB Readout	87
3.8.4	Additional Triggers	88
3.8.5	Readout	88
3.9	Experiment Operation	89

4	Analysis Strategy, Detector Calibration, and Monte Carlo Simulation	91
4.1	Calibration of the Spectrometer Position and Magnetic Field	93
4.1.1	Detector Position Survey and Modeling	93
4.1.2	Beam Position	95
4.1.3	Magnetic Field Survey and Modeling	95
4.2	Event Reconstruction	100
4.2.1	Time-to-Distance (TTD) Conversion for the Drift Chambers	102
4.2.2	Track Reconstruction	105
4.3	The OLYMPUS Monte Carlo Simulation	108
4.3.1	Procedure	110
4.3.2	Event Generation	110
	The OLYMPUS Treatment of Radiative Corrections and Ra- diative Event Generator	112
4.3.3	Digitization of the Detector System	114
5	Determination of the Luminosity	117
5.1	Slow Control Luminosity and Target Gas Distribution Determination	119
5.1.1	Principle of the Measurement	120
5.1.2	Simulation of the Target Gas Distribution	121
	Relevant Details Regarding the Target System	121
	Physics of the Target System Gas	122
	Molecular Flow	124
	Conductance Modeling	124
	Simulation of Molecular Flow and Conduit Geometry	126
	Simulation Implementation and Results	129
5.1.3	Systematic Uncertainty and Discussion of the Slow Control Luminosity	131
5.2	Luminosity Determined Using the 12° System	133

5.2.1	Principle of the Measurement	134
	Constraints of a Single Arm Measurement	136
	Possible Contribution of TPE	136
5.2.2	Discussion of the Exclusion of the GEM Detectors	137
5.2.3	Hit Reconstruction	139
	GEM Detectors	140
	MWPC Detectors	143
5.2.4	Tracking in the 12° Telescope	146
5.2.5	System Performance	149
	Detector Efficiencies	150
	Hit Resolution	152
	Lepton Tracking Efficiency	155
	Lepton Tracking Resolutions	155
5.2.6	Method of Analysis	156
	Exclusive Event Selection Scheme	157
	Simulation of 12° Events	159
5.2.7	Comparison of Data and Simulation	160
5.2.8	Systematic Uncertainties	163
	ToF Trigger Efficiency	164
	SiPM Trigger Efficiency	167
	MWPC Plane Efficiency	168
	Magnetic Field	169
	Lepton Tracking Efficiency	172
	Proton Tracking Efficiency	174
	Beam Position and Slope	176
	Beam Energy	177
	Detector Position	180
	Fiducial Cuts	184
	Elastic Cuts	187
	Radiative Corrections	192

	Elastic Form Factors	192
	TPE at 12°	195
	Additional Discussion on Systematic Uncertainties	198
5.2.9	Results	199
5.3	Luminosity Determined Using the SYMB System	200
5.3.1	Discussion of the Untenability of the Original Coincident Event Analysis	205
5.3.2	The Multi-Interaction Event Luminosity Determination	208
	Principle of the Measurement	209
	Systematic Uncertainties	211
	Results	213
5.4	Discussion of the Luminosity Analyses	213
6	The e^+p/e^-p Cross Section Ratio Analysis	217
6.1	Spectrometer Performance and Modeling in Simulation	218
6.1.1	Drift Chambers	218
	Efficiency	218
	Time Resolution	222
6.1.2	Time-of-Flight System	223
6.1.3	Reconstruction	223
6.2	Method of the Analysis	225
6.2.1	Particle Identification and ToF Hit Association	226
6.2.2	Elastic $e^\pm p$ Pair Selection	231
6.2.3	Background Subtraction	233
6.2.4	Final Processing	237
6.3	Comparison of Data and Simulation	238
6.4	Systematic Uncertainties	241
6.4.1	Detector Acceptance and Efficiency	242
6.4.2	Elastic and Fiducial Cuts	244
6.4.3	Background Subtraction	246

6.4.4	Radiative Corrections	247
6.4.5	Form Factors	248
6.4.6	Discussion of Current Total Systematic Uncertainty Estimate	249
7	Results and Discussion	251
7.1	Note on the Choice of the Luminosity Normalization	252
7.2	$R_{2\gamma}$ Results as a Function of ϵ and Q^2	253
7.2.1	The $\sigma_{e+p}/\sigma_{e-p}$ Ratio at $\epsilon \approx 0.98$ ($\theta \approx 12^\circ$)	253
7.3	Comparison of Independent Analyses	256
7.4	Implications for Two-Photon Exchange and the Proton Form Factors	259
7.5	Outlook	261
A	The OLYMPUS 3D Event Display	263
B	Histograms of Data Events by the Quantities used for the Elastic Event Selection	265
	Bibliography	275

List of Figures

1-1	The G_E/G_M discrepancy	23
1-2	Existing data, model predictions, and projected OLYMPUS uncertainty on $\sigma_{e^+p}/\sigma_{e^-p}$	25
2-1	Feynman diagram of the first order $e^\pm p$ scattering process	32
2-2	Example application of Rosenbluth separation	38
2-3	Selection of Rosenbluth separation measurements of G_E	40
2-4	Selection of Rosenbluth separation measurements of G_M	41
2-5	QED diagrams of up to order α^2 that contribute to elastic $e^\pm p$ scattering	42
2-6	QED diagrams involving a soft external photon that contribute to elastic $e^\pm p$ scattering	43
2-7	Example of a theoretical model for the effect of TPE on Rosenbluth separation $\frac{\mu_p G_E}{G_M}$ measurements	44
2-8	Contribution of TPE diagrams to the total $e^\pm p$ matrix element	46
2-9	Kinematic reaches of the three TPE experiments	47
2-10	Results from VEPP-3 and CLAS with the OLYMPUS projections	48
3-1	Solid-model of the OLYMPUS detector	51
3-2	Overhead view of the DORIS III e^+/e^- storage ring	54
3-3	Typical beam current during OLYMPUS operation	56
3-4	Schematic of the OLYMPUS scattering chamber	57
3-5	Photograph of the OLYMPUS target cell	59
3-6	Components of the OLYMPUS target system within the scattering chamber	60

3-7	Diagram of the target system vacuum components	62
3-8	The OLYMPUS toroid prior to installation	65
3-9	Map of B_y in the tracking detector region	66
3-10	Arrangement of the right side ToF detectors	68
3-11	Schematic of an assembled OLYMPUS drift chamber	70
3-12	Lines of drift within the OLYMPUS drift chamber cells	71
3-13	Diagram of the forward detector systems	73
3-14	Photograph of the right-side 12° tracking telescope	74
3-15	Simulated lead glass trigger event	75
3-16	Electric field in the vicinity of a GEM foil	76
3-17	Exploded view showing the components of an OLYMPUS GEM detector	78
3-18	Micrograph of the GEM detector readout plane pattern	79
3-19	Schematic of the SYMB calorimeter system	82
3-20	Photographs of the SYMB calorimeter crystals and assembly	82
3-21	Map of allowed OLYMPUS trigger conditions	86
3-22	Approximate integrated luminosity collected by OLYMPUS during Run II	90
4-1	Grid box indexing scheme for the magnetic field interpolation	98
4-2	Event display of a reconstructed e^-p event	101
4-3	Simulated lines of electron drift in an OLYMPUS drift chamber cell	103
4-4	Calculated electric field strength for a simulated drift chamber cell	104
4-5	Example fitted TTD functions for two drift chamber cells	106
4-6	Toy example of the tracking pattern library function	107
5-1	Simulated path of a hydrogen gas molecule in the target system	128
5-2	Predicted target gas distributions from TargetSim	131
5-3	Comparison of target distribution simulation to data	132
5-4	Event display of a typical 12° telescope event	135
5-5	Time-varying efficiency of the GEM detectors	138
5-6	Example of a 1D GEM hit in the raw ADC data	141

5-7	Example GEM efficiency map using a previous hit-finding algorithm	142
5-8	Channel-to-channel noise in the GEM ADC counts	144
5-9	Hits found by the new GEM hit-finder for a single event	145
5-10	Local coordinate system for the MWPC planes	147
5-11	Distribution of track sagittas in the MWPC telescopes (simulated)	149
5-12	Efficiencies of the SiPM scintillator tiles for the 12° trigger	151
5-13	Efficiencies of the MWPC detectors	153
5-14	Average efficiencies of the GEM detectors	154
5-15	Distributions of Q^2 for 12° leptons in data and simulation	161
5-16	Distributions of vertex z for 12° leptons in data and simulation	161
5-17	Distributions of reconstructed momentum for 12° leptons in data and simulation	162
5-18	Distribution of single-arm missing energy for 12° leptons in data and simulation	162
5-19	Distributions of proton ToF hits for e^+p and e^-p 12° events	165
5-20	Effect of ToF efficiency uncertainty on the 12° luminosity ratio	166
5-21	Magnetic field model for B_y in the 12° region	171
5-22	Survey data/field model residuals for B_y in the 12° region	172
5-23	Effect of magnetic field uncertainty on the relative 12° luminosity	173
5-24	Effect of magnetic field uncertainty on the absolute 12° luminosity	174
5-25	Effect of beam x shifts on the 12° luminosity	177
5-26	Effect of beam y shifts on the 12° luminosity	178
5-27	Effect of E_{beam} uncertainty on the Rosenbluth cross section near 12°	179
5-28	Effect on angular acceptance of the 12° system for shifts toward/away from the target center	182
5-29	Effect on angular acceptance of the 12° system for shifts up/down	182
5-30	Normalized lepton θ distributions of accepted e^+p and e^-p events in the 12° luminosity system	183
5-31	Effect of shifts in the θ acceptance of the 12° telescopes	184
5-32	Distribution of y vertex positions for left-going 12° electrons	185

5-33	Effect of vertex y fiducial cut on the extracted 12° luminosity	186
5-34	Effect of coplanarity cut on the extracted 12° luminosity	188
5-35	Effect of vertex z correlation cut on the extracted 12° luminosity . . .	189
5-36	Effect of reconstructed beam energy from angles cut on the extracted 12° luminosity	191
5-37	Effect of lepton missing energy cut on the extracted 12° luminosity .	191
5-38	Effect of radiative corrections uncertainty on the 12° luminosity ratio	193
5-39	Effect of radiative corrections uncertainty on the absolute 12° luminosity	194
5-40	Normalized Q^2 distributions of accepted e^+p and e^-p events in the 12° luminosity system	195
5-41	Effect of form factor uncertainty on the relative 12° luminosity	196
5-42	Effect of form factor uncertainty on the absolute 12° luminosity . . .	197
5-43	Luminosity determined by the left 12° arm by run	201
5-44	Luminosity determined by the right 12° arm by run	202
5-45	Luminosity determined by the combined left and right 12° arm results by run	203
5-46	Tree-level differential cross sections for SYMB processes	207
5-47	Example of the SYMB left-master histogram in data	210
5-48	Luminosity determined by the multi-interaction event SYMB analysis by run	214
5-49	Ratio of the 12° and MIE luminosities run	216
6-1	Efficiency for all three wires to fire in the left innermost drift chamber cell layer	219
6-2	Set of correlated efficiency maps for the outermost cell layer in the left chamber	221
6-3	Difference between ToF hit ϕ and reconstructed track ϕ by bar	224
6-4	Meantime distribution by ToF bar for proton candidates in e^- beam data	228

6-5	Meantime distribution by ToF bar for electron candidates in e^- beam data	228
6-6	Meantime distribution by ToF bar for proton candidates in e^+ beam data	229
6-7	Meantime distribution by ToF bar for positron candidates in e^+ beam data	229
6-8	ToF meantime vs. meantime assuming proton mass for Bar 7 in e^+ beam data	230
6-9	Vertex z correlation of the background sample	234
6-10	Example of the background subtraction method for a single Q^2 bin .	236
6-11	Background fraction after initial event selection as a function of Q^2 for leptons going left	237
6-12	Background fraction after initial event selection as a function of Q^2 for leptons going right	238
6-13	Width of the $\Delta\phi$ distribution as a function of Q^2 for leptons going left	239
6-14	Width of the $\Delta\phi$ distribution as a function of Q^2 for leptons going right	240
6-15	Ratio of data yields over simulation yields by lepton species and detector side with the Kelly form factor model	241
6-16	Background-subtracted lepton-summed data yields over simulation for several form factor models	242
6-17	Ratio of lepton left/right background-subtracted yields in data and simulation	244
6-18	Ratio of the $R_{2\gamma}$ results for leptons going left and right in the detector	245
6-19	Estimate of the total systematic uncertainty due to event selection cuts	246
6-20	Ratio of the $R_{2\gamma}$ results for simulation using exponentiated and non-exponentiated radiative corrections	248
6-21	Ratio of the $R_{2\gamma}$ results for simulation using the Maximon/Tjon and Mo/Tsai radiative corrections prescriptions	249
6-22	Ratio of the $R_{2\gamma}$ results for simulation with the Kelly and Bernauer form factor models	250

7-1	Result for $R_{2\gamma}$ as a function of Q^2 (fine bins)	254
7-2	Result for $R_{2\gamma}$ as a function of Q^2 (wide bins)	255
7-3	Result for $R_{2\gamma}$ as a function of ϵ (fine bins)	256
7-4	Result for $R_{2\gamma}$ as a function of ϵ (wide bins)	257
7-5	Comparison of three $R_{2\gamma}$ analyses (fine bins)	259
7-6	Comparison of three $R_{2\gamma}$ analyses (wide bins)	260
A-1	User interface of the OLYMPUS 3D Event Display	264
B-1	Histogram of the Δt cut parameter for the e^-p initial pair selection	266
B-2	Histogram of the Δt cut parameter for the e^+p initial pair selection	266
B-3	Histogram of the Δz cut parameter for the e^-p initial pair selection	267
B-4	Histogram of the Δz cut parameter for the e^+p initial pair selection	267
B-5	Histogram of the elastic angle correlation cut parameter for the e^-p initial pair selection	268
B-6	Histogram of the elastic angle correlation cut parameter for the e^+p initial pair selection	268
B-7	Histogram of the $E_{\text{beam},p}$ cut parameter for the e^-p initial pair selection	269
B-8	Histogram of the $E_{\text{beam},p}$ cut parameter for the e^+p initial pair selection	269
B-9	Histogram of the $E_{\text{beam},\theta}$ cut parameter for the e^-p initial pair selection	270
B-10	Histogram of the $E_{\text{beam},\theta}$ cut parameter for the e^+p initial pair selection	270
B-11	Histogram of the $\Delta E'_\theta/E'^2$ cut parameter for the e^-p initial pair selection	271
B-12	Histogram of the $\Delta E'_\theta/E'^2$ cut parameter for the e^+p initial pair selection	271
B-13	Histogram of the p_z balance cut parameter for the e^-p initial pair selection	272
B-14	Histogram of the p_z balance cut parameter for the e^+p initial pair selection	272
B-15	Histogram of the $\Delta\phi$ cut parameter for the e^-p initial pair selection	273
B-16	Histogram of the $\Delta\phi$ cut parameter for the e^+p initial pair selection	273

List of Tables

3.1	DORIS beam parameters for OLYMPUS operation	55
3.2	Parameters of the SiPM tiles and their operation	74
4.1	Mapping of coefficients for the tricubic spline defined by Equation 4.8	99
5.1	Approximate tracking resolutions in the 12° telescopes	156
5.2	Systematic uncertainties of the 12° luminosity determination	164
5.3	Difference in the determination of $\sigma_{e+p}/\sigma_{e-p}$ in the 12° system between EAA and SA proton tracking	176
5.4	Effect of varying the upstream z fiducial cut for 12° events	187
5.5	Summary of the 12° luminosity results	204
5.6	Systematic uncertainties of the SYMB MIE luminosity determination	212
7.1	$R_{2\gamma}$ results in the finer binning (Figures 7-1 and 7-3)	258
7.2	$R_{2\gamma}$ results in the wider binning (Figures 7-2 and 7-4)	258

Chapter 1

Introduction

While protons and neutrons comprise nearly all of visible matter by mass, their inner workings remain relatively poorly understood. Since Rutherford reported the “anomalous” discovery that collisions between α particles (helium nuclei) and nitrogen nuclei could produce hydrogen nuclei (i.e., protons) [1] in 1919, understanding the role of the proton in nuclei and the nature of the proton itself has been one of the primary goals of particle physics. Shortly after his discovery, Rutherford proposed that the nuclei of atoms consist of protons and related neutral particles of very similar mass [2]. Chadwick discovered Rutherford’s neutral particles in 1932 [3, 4], and he found that they behaved suspiciously similarly to protons, despite their neutral charge, indicating that interesting physics hid within the nature of protons and neutrons. The first hint of the proton’s internal complexity came with Otto Stern’s 1933 discovery that the magnetic moment of the proton deviated by a factor of 2.79 from the value expected if it was a point-like particle [5, 6]. Experiments such as those of Hofstadter at Stanford began to probe the structure of the proton with elastic electron-proton scattering in the 1950s, demonstrating the proton’s finite size [7–9]. Concurrent with the experiments of Hofstadter, other experiments were discovering a previously unknown sector of particles related to the proton: a variety of hadronic states varying widely in mass, quantum numbers, lifetimes, and decay products. The quark model proposed by Gell-Mann and Zweig in 1964 [10, 11] gave order to the mess of hadrons, and the MIT-SLAC experiments in the 1960s and 1970s slowly uncovered the point-

like nature of the proton's, and other hadrons', constituents (i.e., quarks and gluons) [12, 13].

While quantum chromodynamics (QCD) comprises a complete quantum field theory of the strong interaction of quarks and gluons [14, 15], the non-perturbative nature of this theory at low energies poses significant difficulties in modeling the interactions that give rise to the bound states of QCD. Thus, experimental tests of QCD remain critical to furthering knowledge of the strong force. In particular, a complete understanding of the proton, the fundamental bound state of QCD, is crucial. Despite over a century of both theoretical and experimental study, basic questions remain about the proton, including whether it is truly stable [16, 17], how its constituents give rise to its total spin ($S = \frac{1}{2}$) [18, 19], and more seemingly simple topics such as the physical extent and distribution of charge within protons [20–22]. OLYMPUS is chiefly concerned with a recent puzzle in the latter category.

1.1 The Fundamentals of OLYMPUS: Motivation and Goals

The OLYMPUS experiment concerns fundamental properties that were examined by the earliest studies of the proton's finite size and structure, i.e., measurement of the form factors G_E and G_M for the elastic scattering of electrons from protons that encode how the structure of the proton affects the electromagnetic interaction between the two particles. The form factors are typically represented as functions of the square of the four-momentum transfer that occurs in the e^-p interaction Q^2 , so as to make them Lorentz invariant representations of the proton's structure. Measurements of the form factors began in the 1950s with the work of Hofstadter at Stanford [7–9] and continued using the method originally formulated by Rosenbluth [23] (Section 2.2.1) into the 1990s, pushing the measurements to higher values of Q^2 [24–27]. In the 1990s, the development of polarized electron beams and targets provided a new method to study the elastic form factors, offering a means of measuring the ratio $\frac{\mu_p G_E}{G_M}$

as a function of Q^2 rather than a method of measuring them individually [28–33]. When comparing the behavior of $\frac{\mu_p G_E}{G_M}$ as found by the previous data (shown in blue in Figure 1-1) to the new data based on methods employing polarization (the red data in 1-1), a significant disparity between the results yielded by each method was discovered. All data prior to the polarization-based measurements was consistent with a value of $\frac{\mu_p G_E}{G_M}$ that stays relatively constant and near unity as a function of Q^2 while the polarization data favors a clear downward sloping trend that is completely inconsistent with the previous results. Theorists reanalyzed the data of the older experiments using modern methods [34] and new experiments using the method of Rosenbluth were conducted [35, 36], but the discrepancy persisted.

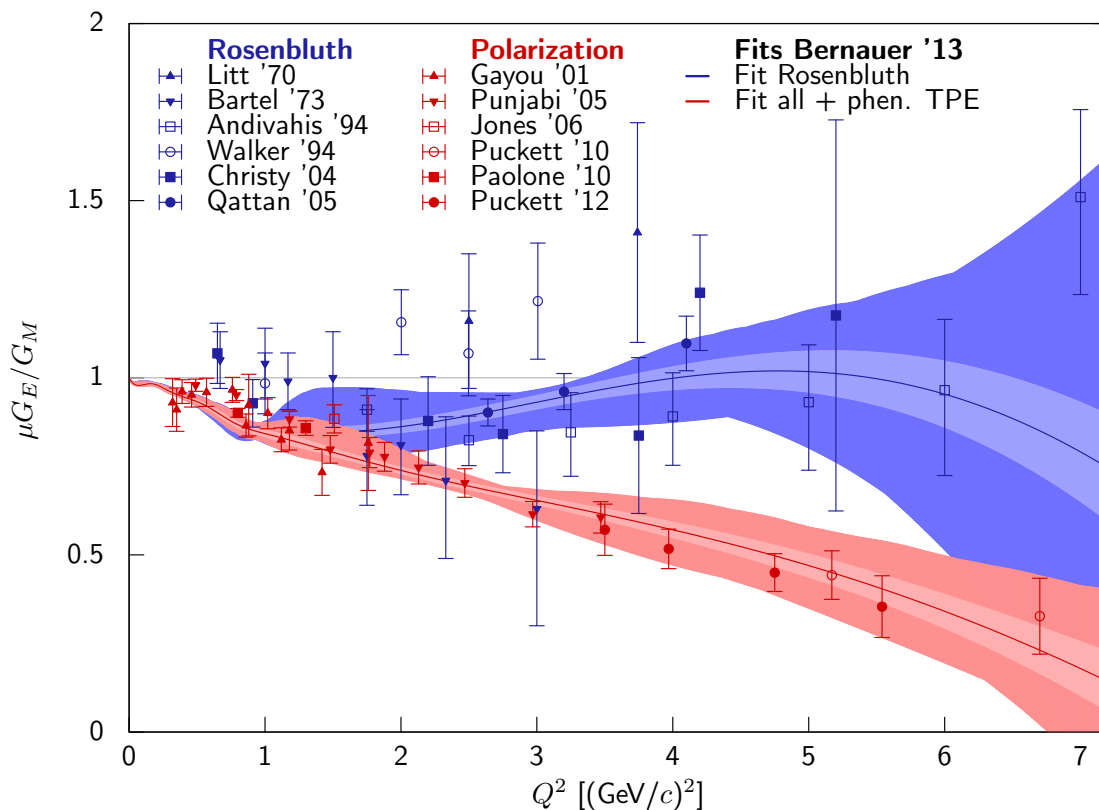


Figure 1-1: Selection of experimental results on the ratio $\frac{\mu_p G_E}{G_M}$ along with phenomenological fits to the data, illustrating the discrepancy between experiments using Rosenbluth separation and polarization-based methods. (Rosenbluth separation data: [24–27, 35, 36], polarization data: [28–33], phenomenological fits: [37]) (Figure reproduced from Reference [38]).

The most widely-accepted hypothesis to explain this discrepancy is that the Rosen-

bluth method of extracting the form factors from e^-p scattering data does not properly account for an effect that was previously assumed to be negligible: the contribution to the scattering cross section from two photons being exchanged between the particles. Typically, calculations assume a single photon carrying the full momentum transfer. Due to the complexity of the proton's state between the exchange of the two photons, this contribution is not analytically calculable from theory and predictions from various models vary significantly [39–45]. Experiments to test this hypothesis were necessary.

As will be discussed in Section 2.4.2, a measurement of the ratio of the cross section for positron-proton scattering to that of electron-proton scattering provides an experimental signature of two-photon exchange in the lepton-proton interaction. To test the hypothesis, and provide a means of discriminating between different theoretical and phenomenological predictions for the significance of the two-photon exchange contributions, measurements must have very small uncertainties ($\lesssim 1\%$). The OLYMPUS experiment was designed to achieve this goal. The approach taken by OLYMPUS to make this measurement is summarized by the following equation:

$$R_{2\gamma}(\epsilon, Q^2) = \frac{\sigma_{e^+p}(\epsilon, Q^2)}{\sigma_{e^-p}(\epsilon, Q^2)} = \frac{N_{e^+p,\text{data}}(\epsilon, Q^2)}{N_{e^-p,\text{data}}(\epsilon, Q^2)} \cdot \frac{N_{e^-p,\text{MC}}(\epsilon, Q^2, \mathcal{L}_{e^-})}{N_{e^+p,\text{MC}}(\epsilon, Q^2, \mathcal{L}_{e^+})}. \quad (1.1)$$

OLYMPUS compared an experimental measurement of the rates of elastic $e^\pm p$ scattering ($N_{e^\pm p,\text{data}}(\epsilon, Q^2)$) with a detailed simulation of the expected rates in the absence of two-photon exchange ($N_{e^\pm p,\text{MC}}(\epsilon, Q^2, \mathcal{L}_{e^p m})$). In addition to collecting a high-statistics sample of both e^-p and e^+p events to control statistical uncertainties, it was also critical to precisely measure the relative luminosity collected for each of the lepton species ($\mathcal{L}_{e^+}/\mathcal{L}_{e^-}$), and to create a model of the experiment in simulation that accurately reflected the reality of the experiment to control the systematic uncertainties of the measurement. This thesis provides a comprehensive discussion of the OLYMPUS experiment and analysis to produce a measurement of $R_{2\gamma}$ with $\lesssim 1\%$ total uncertainty in the kinematic range of ($0.4 \leq \epsilon \leq 0.9$), ($0.6 \leq Q^2 \leq 2.2$) GeV^2/c^2 . Projections for the precision of the experiment, the world's existing data

prior to 2015 on $\sigma_{e^+p}/\sigma_{e^-p}$, and various theoretical and phenomenological predictions for the results of OLYMPUS are shown in Figure 1-2.

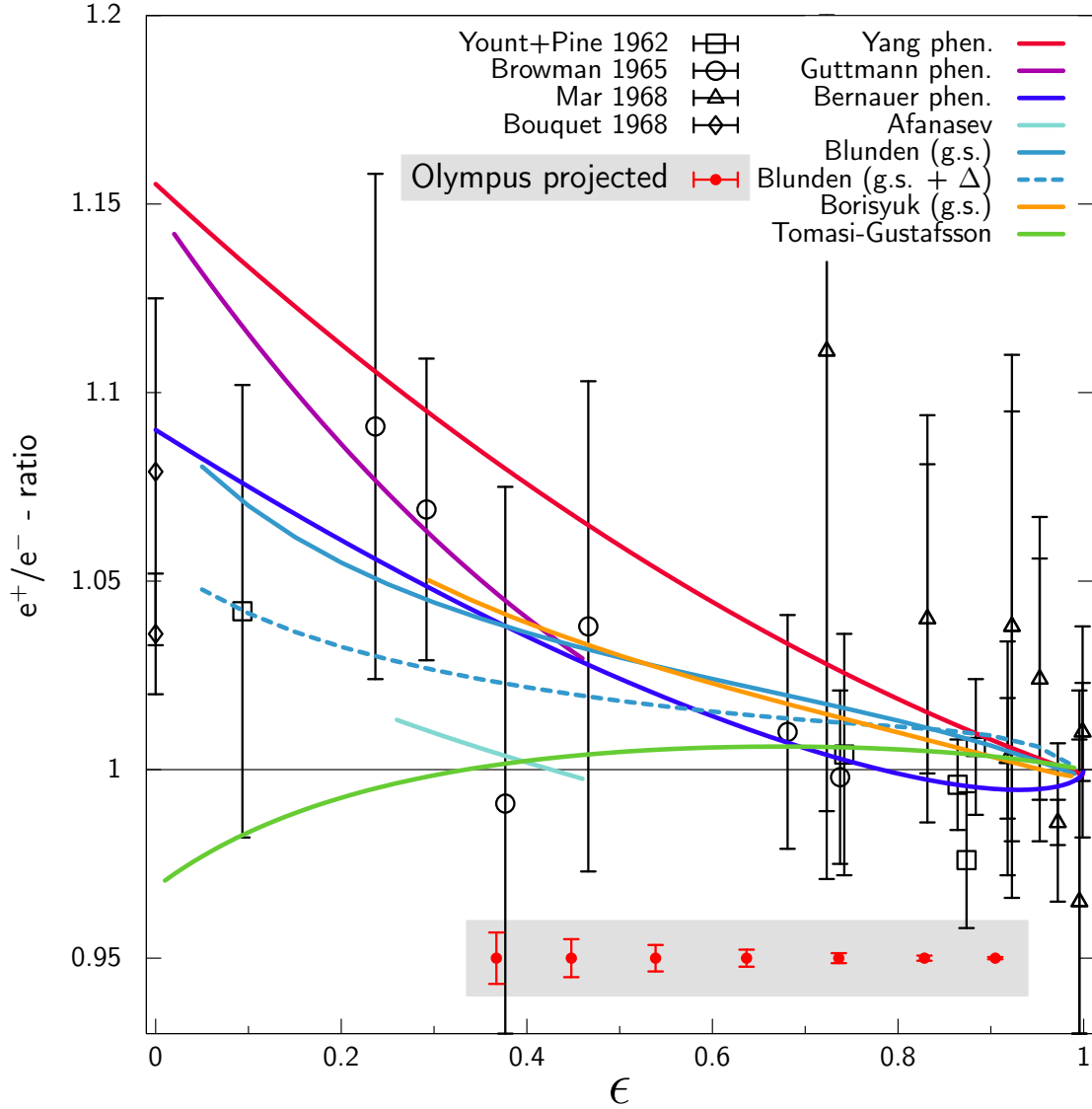


Figure 1-2: The ratio of e^+p to e^-p scattering at a lepton beam energy of 2.01 GeV as a function of the kinematic variable ϵ (see Equation 2.8) as predicted by phenomenological models [37, 46, 47], theoretical calculations of possible two-photon exchange contributions [39–45], and projected uncertainties of the measurement OLYMPUS will provide. The existing world data on $\sigma_{e^+p}/\sigma_{e^-p}$ prior to ~ 2015 is shown [48–51], although these experiments were all at different beam energies. (Figure reproduced from Reference [38].)

1.2 Notes on the Organization and Content of this Work

The intent of this work is to provide discussion of the essential parts of all elements of the OLYMPUS experiment and complete details on the primary elements which the author contributed to the experiment. Topics in the latter category include various elements of the detector construction and calibration (in particular, the hydrogen target system (Section 3.3)), the survey of the magnetic field and implementation of the results as a field map for tracking and simulation (Section 4.1.3), the slow control luminosity analysis (Section 5.1), all aspects of the 12° luminosity analysis from calibration to the event selection analysis (Section 5.2), and a complete independent analysis of the main OLYMPUS $\sigma_{e+p}/\sigma_{e-p}$ result (Chapter 6). Appendix A presents a 3D event display framework created by the author for the visualization of both data and simulated events for OLYMPUS using ROOT libraries [52] that is easily adaptable for other experiments. The other theses written on OLYMPUS provide detailed descriptions of a number of topics including radiative corrections (References [53] and [54]), track reconstruction (References [53] and [54]), the symmetric Møller-Bhabha luminosity analyses (Reference [55] and [53]), the analysis and simulation of the time-of-flight detector system (Reference [54]), implementation of the surveyed detector geometry in the simulation detector model [55], and independent $\sigma_{e+p}/\sigma_{e-p}$ analyses in each.

Rather than reproduce discussion on basic topics of particle physics that are well covered in other works, this thesis assumes basic knowledge of essential particle and nuclear physics concepts, both in the description of physics processes and the detection of particles, and thus only includes introductions to essential advanced topics that are critical to the motivation and execution of the OLYMPUS experiment. Excellent references for any unfamiliar terms and concepts include References [15] and [56] for essential concepts of particle physics, Reference [57] for particle detection related topics, and Reference [58] for the basics of particle physics theory.

As a guide to the contents of this work, the following summarizes the main topics

and goals of each chapter:

- Chapter 2 provides an introduction to the fundamentals of proton form factors and their experimental determination and a more detailed discussion regarding the proton form factor puzzle, the two-photon exchange hypothesis, and the goals of OLYMPUS.
- Chapter 3 describes the essential elements of the design and operation of the OLYMPUS experiment, including conventions for description of the experiment, the beam, the hydrogen target, and the detector systems.
- Chapter 4 outlines the OLYMPUS analysis strategy, in particular the work done to ensure that the OLYMPUS simulation robustly represented the experimental conditions to allow comparison of data and Monte Carlo for the final analyses.
- Chapter 5 details the measurement of the relative luminosity of electron and positron data collected in the three independent systems designed for the measurement, with particular attention to the slow control and 12° luminosities. For the 12° luminosity, all relevant details of the analysis are presented including calibration, hit reconstruction, track reconstruction, simulation implementation, event selection, and a detailed systematic uncertainty analysis. For the slow control luminosity, a novel Monte Carlo code is presented that simulates the density of gas undergoing molecular flow within a geometry.
- Chapter 6 describes the independent analysis of the main cross section result conducted by the author, including aspects of the detector performance and simulation, the analysis methods used, and an estimate of systematic uncertainties.
- Chapter 7 presents the results of the analysis from the previous chapter and discusses it in the context of the other analyses, existing data on $\sigma_{e^+p}/\sigma_{e^-p}$, and the implications for the form factor discrepancy and future work.

Chapter 2

The Proton, Form Factors, and Theoretical Motivation of the OLYMPUS Experiment

Fundamentally, OLYMPUS seeks to address the question of how charge and magnetization are distributed within the proton. While a complete and consistent theoretical model of the strong force interactions that give rise to the proton and other hadronic states exists in the form of quantum chromodynamics (QCD)¹, calculations of the complex bound state of three valence quarks, quark-antiquark pairs, and gluons that comprise the proton have proven extremely difficult due to the non-perturbative nature of QCD at low energies ($\lesssim \Lambda_{\text{QCD}} \approx 200 \text{ MeV}$). While there has been some recent success in calculating properties of the proton and other light bound hadronic states using lattice QCD [59–61], full descriptions of the distributions and interactions of particles within bound states of QCD remain elusive. Since the proton is the only fundamental, stable bound state of QCD, experimental examination of the proton to determine its nature is critical to furthering knowledge of the strong force.

Since Rose first suggested in 1948 that the charge distributions within protons and nuclei could be examined by scattering leptons from protons [62], a variety of

¹See Chapter 9 of Reference [15] for a review of the fundamentals of QCD or Reference [14] for a more detailed discussion.

experiments have studied the proton in this way over a large range of energies. Before proceeding with a description of the OLYMPUS experiment and the analysis of the experiment's data, it is useful to briefly review the theoretical formalisms regarding the structure of the proton, methods of probing this structure, and the discrepancy in proton structure measurements that OLYMPUS probed by searching for two-photon exchange (TPE) in $e^\pm p$ scattering. Complete reviews of proton form factors may be found in References [21] and [63], while References [64] and [65] specifically review the physics and experimental landscape of TPE.

2.1 Fundamentals and Formalism

Since the observation that the proton magnetic moment deviated significantly from the value expected for a point-like spin- $\frac{1}{2}$ by Otto Stern in 1933 [5, 6], the nature of the proton's finite structure and the physics that gives rise to it has formed a deep and rich field of study in nuclear and particle physics. While atomic physics-based experiments measuring the Lamb shift in hydrogen provide precise measurements of the proton's charge radius [66–69], lepton-proton scattering has provided the key means of more comprehensively examining the structure of the proton. In particular, elastic lepton-proton scattering provides insight into the distribution of charge and magnetization within the proton, providing information about the size of the proton and the interactions that govern its structure.

2.1.1 Elastic Lepton-Proton Scattering

First, it is useful to establish conventions for the description of elastic scattering events. For a given $e^\pm p$ event in which a lepton elastically scatters from a proton via the exchange of one or more photons (i.e., via the electromagnetic interaction), the kinematics are completely described by the initial and final four-momenta of the lepton (defined to be k and k' respectively), those of the proton (p and p' respectively), and the electron and proton masses (m and M respectively) as labeled in Figure 2-1.

The four-momentum transfer from the electron to the proton is then:

$$q = p' - p = k - k'. \quad (2.1)$$

For the kinematics relevant to OLYMPUS, where a beam of leptons strikes protons at rest, and using natural units in which $c = 1$:

$$k = \left(E_{\text{beam}}, 0, 0, \sqrt{E_{\text{beam}}^2 - m^2} \right), \quad (2.2)$$

$$p = (M, 0, 0, 0), \quad (2.3)$$

where E_{beam} is the beam energy (2.01 GeV for OLYMPUS) and the initial direction of the lepton is along z . The angle θ is used to represent the polar angle relative to the beam axis (z as described) of the post-scatter three-momentum of the lepton. Throughout this work, the *lab reference frame* or *lab frame* will refer to these convention in which the proton is at rest initially. For more information on the description of event kinematics as they pertain to the conventions used for OLYMPUS, see Section 3.1.

While the variables in the previous paragraph describe the kinematics of the interaction, it is often more convenient to use Lorentz invariant variables that allow direct comparison between experiments conducted at different beam energies. Of particular utility are the square of the four-momentum transfer, $q^2 = q \cdot q$, and variable ϵ that is related to the scattering angle of the electron θ in the lab frame. For elastic scattering, note that $q^2 < 0$ and so it is convenient to define:

$$Q^2 = -q^2 > 0. \quad (2.4)$$

The variable ϵ may be formally defined most easily by first defining two intermediate

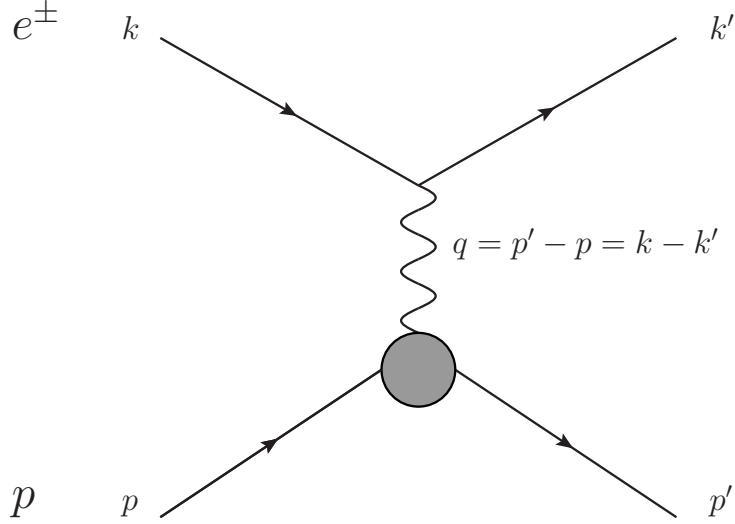


Figure 2-1: Feynman diagram representing the first order contribution to the process of elastic $e^\pm p$ scattering, i.e., the Born or single photon exchange approximation [70]. As in the text, k and k' represent the incoming and outgoing four-momenta of the lepton and p and p' those of the proton. The four-momenta transferred to the proton is q . The circle at the proton vertex represents the complex interaction of the proton with the exchanged photon, which is a function of its internal structure and interactions.

variables ²:

$$\tau = \frac{Q^2}{4M^2}, \quad (2.5)$$

$$\nu = \frac{k \cdot p}{M^2} - \tau. \quad (2.6)$$

Then,

$$\epsilon = \frac{\nu^2 - \tau(1 + \tau)}{\nu^2 + \tau(1 + \tau)}. \quad (2.7)$$

While this appears to be a cumbersome variable, it has a straightforward interpretation in terms of the lab frame scattering angle of the lepton θ :

$$\epsilon = \left[1 + 2(1 + \tau) \tan^2 \left(\frac{\theta}{2} \right) \right]^{-1}. \quad (2.8)$$

Thus, ϵ varies from one for very forward scattering in the lab frame ($\theta = 0^\circ$) to zero

²The variable ϵ has a physical interpretation as the relative flux of longitudinally polarized virtual photons. The derivation of this interpretation is well beyond the scope of this work, but is detailed in Section 2.4 of Reference [71].

for very backward scattering ($\theta = 180^\circ$). To interpret Q^2 in the lab frame, it is useful to neglect the electron mass ($m \ll M, E_{\text{beam}}$), which results in:

$$Q^2 = 4E_{\text{beam}}E' \sin^2\left(\frac{\theta}{2}\right), \quad (2.9)$$

where E' is the outgoing lepton energy in the lab frame.

Having established conventions for the description of elastic lepton-proton scattering, the question of the cross section for the process and the insight it offers regarding the structure of the proton may be addressed. Since the weak interaction is suppressed by the masses of the W^\pm and Z bosons ($M_{W^\pm, Z} \sim \mathcal{O}(100 \text{ GeV})$), it is negligible relative to the electromagnetic interaction (in terms of its contribution to the overall interaction cross section). Additionally, since each photon-fermion interaction vertex in a quantum electrodynamics (QED) Feynman diagram carries a factor of $\sqrt{\alpha} \approx \sqrt{\frac{1}{137}}$ to the contribution of that diagram to the matrix element for a given interaction (and thus a factor of α to the cross section), often the approximation is made that only lowest-order allowed diagram (that with the fewest number of vertices) is used to compute the matrix element for an interaction. In the case of elastic $e^\pm p$ scattering, the lowest-order approximation is single photon exchange with no additional initial or final state radiation, as shown in Figure 2-1. This is known as the Born approximation [70].

To construct the most general cross section for lepton-proton elastic scattering, first consider the case of a light lepton (spin- $\frac{1}{2}$) scattering from a much more massive, spinless target (e.g., a spin-0 nuclei or “spinless proton”). The only first-order QED diagram that contributes to the process is a diagram akin to that shown in Figure 2-1. Such a process is known as Mott scattering [72, 73], and the cross section is straightforward to compute from the rules of QED [56, 58]:

$$\sigma_{\text{Mott}} = \frac{\alpha^2 E' \cos^2\left(\frac{\theta}{2}\right)}{4E^3 \sin^4\left(\frac{\theta}{2}\right)}. \quad (2.10)$$

The problem of lepton-proton scattering then effectively reduces to properly adjusting

the treatment of the proton to account for both its structure and spin.

2.1.2 Elastic Form Factors

To account for the effect of the proton's structure and spin, first consider the general invariant matrix element for the Feynman diagram in Figure 2-1 (using the notation and conventions of Reference [64]):

$$\mathcal{M}_\gamma = -\frac{e^2}{q^2} j_{\gamma\mu} J_\gamma^\mu, \quad (2.11)$$

where e is the electron charge. The current $j_{\gamma\mu}$ is that of the lepton, and is thus the standard current of a Dirac fermion:

$$j_{\gamma\mu} = \bar{u}_e(k') \gamma_\mu u_e(k), \quad (2.12)$$

where u_e represents the lepton's Dirac spinor. The proton's current, J_γ^μ , is more complicated. As first shown by Foldy in 1952 [74], the most general current for a spin- $\frac{1}{2}$ particle in QED that satisfies current conservation and Lorentz invariance may be written as:

$$J_\gamma^\mu = \bar{u}_p(p') \left(\gamma^\mu F_1(Q^2) + \frac{i\sigma^{\mu\nu} q_\nu}{2M} F_2(Q^2) \right) u_p(p), \quad (2.13)$$

where u_p is the proton spinor and $F_1(Q^2)$ and $F_2(Q^2)$ are respectively Dirac and Pauli form factors for elastic scattering from the proton. In the Born approximation, these are functions of Q^2 alone (making them Lorentz invariant) and they encode the internal behavior of the proton to all orders in QCD.

When discussing the structure of the proton it is most useful to recast the form factors as the following linear combinations of the Dirac and Pauli form factors F_1 and F_2 :

$$G_E(Q^2) = F_1(Q^2) - \tau F_2(Q^2), \quad (2.14)$$

$$G_M(Q^2) = F_1(Q^2) + F_2(Q^2), \quad (2.15)$$

which are respectively the electric and magnetic elastic form factors, and were defined by Hand, Miller, and Wilson [75]. These form factors are normalized such that $G_E(0) = 1$ and $G_M(0) = \mu_p = 2.793$, i.e., the static values of the proton’s charge and magnetic moment in the units of $e = c = \hbar = 1$. Parameterizing the form factors in this way leads to a simpler form for the final computed differential cross section in the Born approximation, known as the Rosenbluth formula [23]³:

$$\left(\frac{d\sigma}{d\Omega}\right)_{\text{Born}} = \frac{\sigma_{\text{Mott}}}{\epsilon(1 + \tau)} [\epsilon G_E^2(Q^2) + \tau G_M^2(Q^2)]. \quad (2.16)$$

2.1.3 Physical Interpretation of the Elastic Form Factors

In addition to simplifying the form of the Rosenbluth formula for the $e^\pm p$ elastic cross section, the electromagnetic form factors G_E and G_M additionally offer some insight into more intuitive properties of the proton’s structure, namely the distribution of charge and magnetization within the proton. As first noted by Sachs in 1962 [76], in a reference frame in which both the lepton and proton exchange three-momentum but no energy (and thus the lepton rebounds in the opposite direction from its initial trajectory with the same energy)⁴ the form factors G_E and G_M are the Fourier transforms of the charge and magnetization distributions of the proton. Note, however, that the velocity of this frame relative to the lab frame varies as a function of Q^2 and that the transformation of spatial distributions between these frames is generally very complex. While model-dependent methods of conducting such transformation have been established [77], it is generally quite difficult and caution should be exercised when interpreting the direct physical meaning of G_E and G_M .

³When first computed by Rosenbluth in 1950, the formula did not take the form shown in Equation 2.16, but the modern representation of the formula is presented here.

⁴This reference frame is known as the Breit frame or “brick wall” frame.

2.2 Determination of the Proton Elastic Form Factors

While a number of theoretical models exist for computing the proton elastic form factors (see Section 4 of Reference [21] for an overview), none have been successful in providing a complete and predictive description of the proton's elastic electromagnetic interactions due to complexity of the underlying interactions. Thus, the determination of the values of G_E and G_M has been an active experimental question since they were first formulated. The first measurements of quantities related to the form factors were conducted by Hofstadter and McAllister at Stanford in the mid-1950s, who measured a single form-factor-like quantity (effectively a single factor modifying the Mott cross section, i.e., the combination of the effects of two form factors) [7–9]. As theory progressed, it was realized that experiments were needed that separated the effects of the two form factors. The technique of Rosenbluth separation was developed allowing the independent extraction of G_E^2 and G_M^2 . Measurements using this technique began in the late 1960s [24, 25, 75, 78–83] and continued through the turn of the century [26, 27, 35, 36, 84]. In the 1990s, the advent of polarized beams and targets provided a new method of measuring the ratio G_E/G_M , used in experiments conducted at MIT-Bates and Jefferson Lab [28–32, 85–91]. The two techniques are briefly summarized here, while the results from each method are discussed in Section 2.3.

2.2.1 Rosenbluth Separation

The Rosenbluth separation technique takes advantage of the form of the Rosenbluth formula (Equation 2.16) for the $e^\pm p$ elastic cross section and the dependence of the form factors on Q^2 alone. While the exact techniques used by various experiments differ slightly, Rosenbluth separation effectively amounts to rewriting Equation 2.16

in the form:

$$\left(\frac{d\sigma}{d\Omega}\right)_{\text{reduced}} = \frac{\epsilon(1+\tau)}{\tau\sigma_{\text{Mott}}} \left(\frac{d\sigma}{d\Omega}\right)_{\text{exp}} = G_M^2(Q^2) + \frac{\epsilon}{\tau} G_E^2(Q^2), \quad (2.17)$$

where $\left(\frac{d\sigma}{d\Omega}\right)_{\text{exp}}$ is the experimentally measured value of the elastic $e^\pm p$ cross section as a function of ϵ and τ . Since $\tau = \frac{Q^2}{4M^2}$ and $\epsilon = [1 + 2(1 + \tau) \tan^2(\frac{\theta}{2})]^{-1}$, measuring the cross section at fixed Q^2 over a variety of scattering angles θ and plotting the values of the reduced cross section defined by Equation 2.17 as a function of ϵ results in a linear function. Fitting this function yields $\frac{1}{\tau} G_E^2(Q^2) = \frac{4M}{Q^2} G_E^2(Q^2)$ as the slope and $G_M^2(Q^2)$ as the intercept. By conducting these measurements for a variety of Q^2 values, the form factors may be mapped out. In most experiments the values of Q^2 and ϵ are selected by adjusting narrow acceptance single- and double-arm spectrometers and collecting data in a number of spectrometer configurations [57, 92]. An example of the application of this technique from Reference [26] is shown in Figure 2-2. Rosenbluth separation is the only technique currently available that allows independent measurement of the individual form factors.

2.2.2 Polarization-Based Techniques

The Rosenbluth formula (Equation 2.16) and Rosenbluth separation assume unpolarized lepton beams and proton targets. As first observed by Akhiezer and Rekalov, the Rosenbluth separation technique suffers from the dominance of the $\frac{\tau}{\epsilon} G_M^2$ term at high Q^2 (subjecting the extraction of G_E to large uncertainty) [93]. They, and others, proposed methods involving experiments with longitudinally polarized electron beams on unpolarized proton targets and measuring the polarization of the recoil proton (i.e., the *polarization transfer* from the lepton to the proton) [94, 95]. Additionally, techniques were proposed using unpolarized beams on polarized targets [96].

Considering the case of a polarized beam on an unpolarized target to illustrate the method, the cross section for elastic $\vec{e}p \rightarrow e\vec{p}$ scattering in the Born approximation may be calculated from the rules of QED in a similar fashion to the spin-averaged unpolarized case [94, 95]. The differential cross sections for the outgoing proton spin

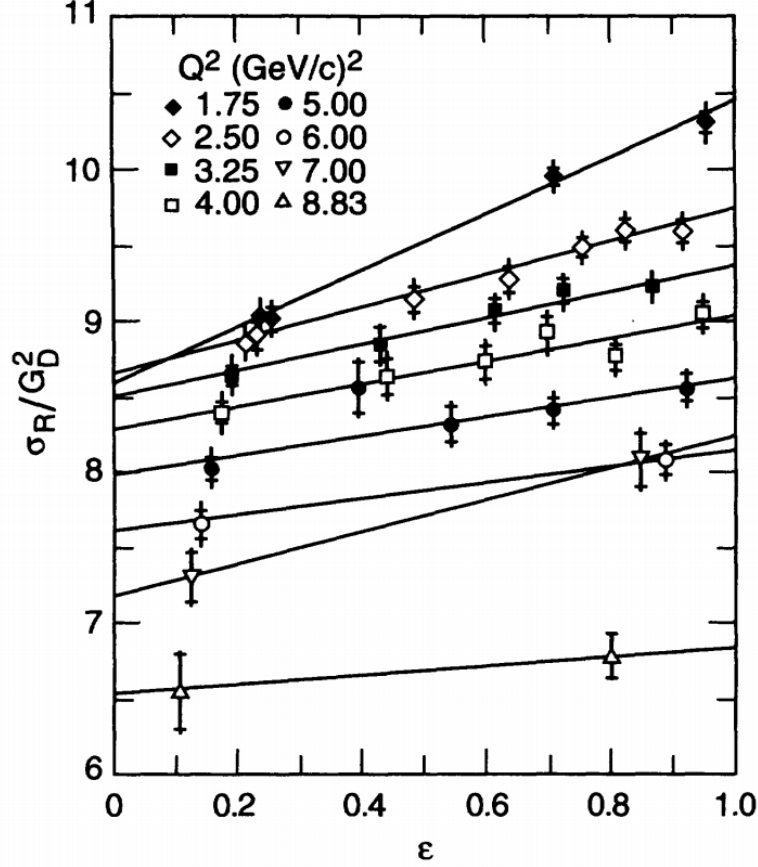


Figure 2-2: Application of the Rosenbluth separation technique at eight values of Q^2 . (Figure reproduced from Reference [26].)

to be aligned longitudinally or transversally are respectively:

$$\frac{d\sigma^{(L)}}{d\Omega} = h\sigma_{Mott} \frac{E + E'}{M} \sqrt{\frac{\tau}{1 + \tau}} \tan^2\left(\frac{\theta}{2}\right) G_M^2, \quad (2.18)$$

$$\frac{d\sigma^{(T)}}{d\Omega} = 2h\sigma_{Mott} \sqrt{\frac{\tau}{1 + \tau}} \tan\left(\frac{\theta}{2}\right) G_E G_M, \quad (2.19)$$

where h is the electron helicity. The average longitudinal and transverse polarizations P_L and P_T of the outgoing protons are then proportional to their respective outgoing spin cross sections. Taking the ratio of the expressions for the cross sections (and thus polarizations), the unknown electron helicity cancels to yield:

$$\frac{G_E}{G_M} = -\frac{E_{\text{beam}} + E'}{2M} \tan\left(\frac{\theta}{2}\right) \frac{P_T}{P_L}. \quad (2.20)$$

This technique provides a robust measurement of the $\frac{\mu_p G_E}{G_M}$ ratio, helped by cancellation of various systematic uncertainties caused by the simultaneous measurement of the two polarizations using the same setup, and when paired with Rosenbluth measurements of G_M provides the most sensitive method of extracting G_E at high Q^2 . A review of the methods used to extract $\frac{\mu_p G_E}{G_M}$ from polarized target experiments may be found in Section 3.2 of Reference [21].

2.3 Existing Data and the Proton Form Factor Discrepancy

As noted previously, numerous experiments have measured the proton elastic form factors (or the ratio $\frac{\mu_p G_E}{G_M}$ in the case of the polarization-based measurements) over a range of $0.05 \text{ GeV}^2 \lesssim Q^2 \lesssim 10 \text{ GeV}^2$. A selection of Rosenbluth separation data for G_E and G_M is shown in Figures 2-3 and 2-4 respectively, reproduced from Reference [21]. The form factors are typically displayed, as in the figures, normalized to the dipole form factor:

$$G_D = \frac{1}{\left(1 + \frac{Q^2}{0.71 \text{ GeV}^2}\right)^2}, \quad (2.21)$$

which corresponds (in the Breit frame) to an exponentially falling charge or magnetization distribution. As can be seen in the figures, the dipole model roughly describes the form factor data obtained via Rosenbluth scattering below a few GeV^2 , especially G_E , but that the data deviate from the dipole model at higher Q^2 . As shown in Figure 1-1, the ratio $\frac{\mu_p G_E}{G_M}$ measured using Rosenbluth scattering is ~ 1 and reasonably flat.

Data from polarization-based measurements, however, provide a starkly different measurement of $\frac{\mu_p G_E}{G_M}$. As Figure 1-1 shows, the data from such experiments cluster around a line that decreases as a function of Q^2 with a slope of approximately -0.14 GeV^{-2} . At $Q^2 \gtrsim 5 \text{ GeV}^2$, global fits to Rosenbluth separation data and polarization-based data show more than a factor of two difference in $\frac{\mu_p G_E}{G_M}$. This is known as the proton form factor ratio discrepancy, and has been an active field of research for both

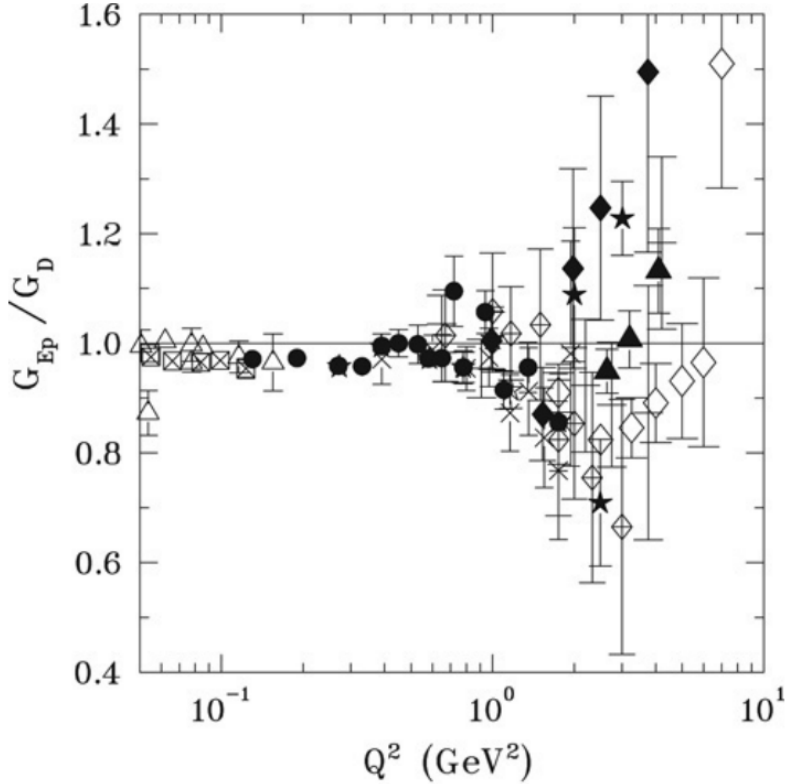


Figure 2-3: Selection of experimental measurements of $G_E(Q^2)$ using Rosenbluth separation, normalized to the dipole form factor G_D (Equation 2.21) and proton magnetic moment μ_p . (Original data: [24–27, 35, 36, 75, 80–83, 97]) (Figure reproduced from Reference [21]).

theorists and experimentalists.

2.4 Possible Causes of the Discrepancy and the Two-Photon Exchange Hypothesis

Given the significant discrepancy between the different methods of measuring the proton form factor ratio (and the consistency of measurements of the same type) discovered in the 1990s, efforts were made both to verify the discrepancy with modern measurement and to explore possible causes of the discrepancy. Rosenbluth separation experiments conducted in 2004-2005 (References [35] and [36]) and reanalysis of the existing data (References [34] and [22]) confirmed the discrepancy at values of Q^2

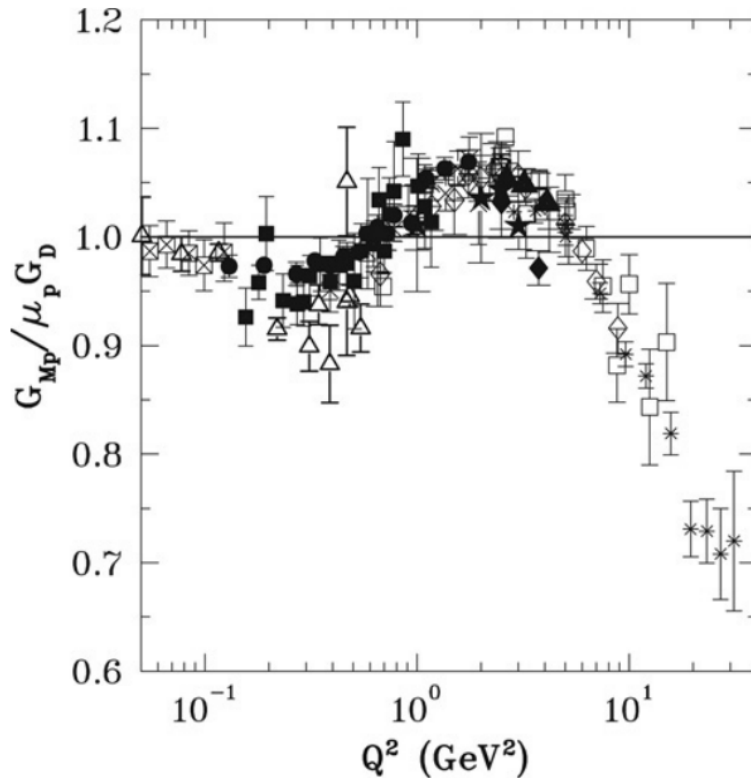


Figure 2-4: Selection of experimental measurements of $G_M(Q^2)$ using Rosenbluth separation, normalized to the dipole form factor G_D (Equation 2.21). (Original data: [24–27, 35, 36, 75, 78–84]) (Figure reproduced from Reference [21]).

up to $\sim 8 \text{ GeV}^2$, further increasing the call for explanations of the discrepancy from the standpoint of theory and of understanding the physics implicit in the analysis methods used for each technique. In particular, the *radiative corrections* applied for each measurement were examined carefully.

In general, the term radiative corrections encompasses any shift applied to a raw measured cross section, form factor, etc. to account for the effect of making the Born approximation. In practice, for $e^\pm p$ scattering, this amounts to considering changes to the cross section that occur due to contributions from higher-order Feynman QED diagrams that are experimentally indistinguishable from elastic scattering by single photon exchange, like those shown in Figures 2-5 and 2-6. Note that the event types shown in Figure 2-6 may be indistinguishable in an experiment from an event with no externally emitted photon, due to the photon having very small energy such that the

deviation from elastic kinematics is smaller than the resolution of the detector. Past experiments (prior to 2000) accounted for the effects of diagrams up to order α^2 using the prescription of Mo and Tsai [98,99]. This prescription, however, did not account for the structure of the nucleon and made a number of other approximations. The method for applying radiative corrections to elastic $e^\pm p$ data was improved upon by Maximon and Tjon [100], who included the effect of the proton form factors in their calculations and avoided several of the approximations made by Mo and Tsai, which altered the size of the radiative correction (itself typically a correction of $\mathcal{O}(10\%)$ to measured cross sections) by several percent, an effect not large enough to explain the discrepancy [34]. Radiative corrections are also critical to the OLYMPUS result and the approach used for OLYMPUS is described in Section 4.3.2. A detailed discussion of the OLYMPUS radiative corrections may be found in References [53] and [54].

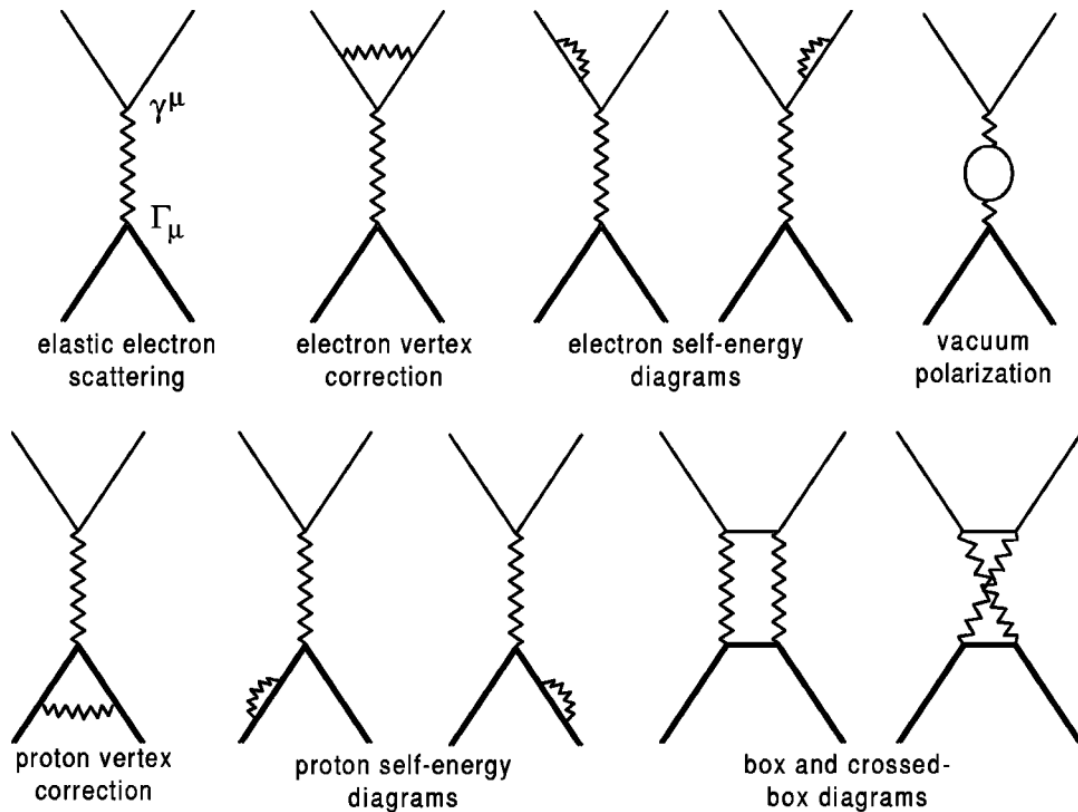


Figure 2-5: QED diagrams up to order α^2 that contribute to elastic $e^\pm p$ scattering. (Figure reproduced from Reference [100].)

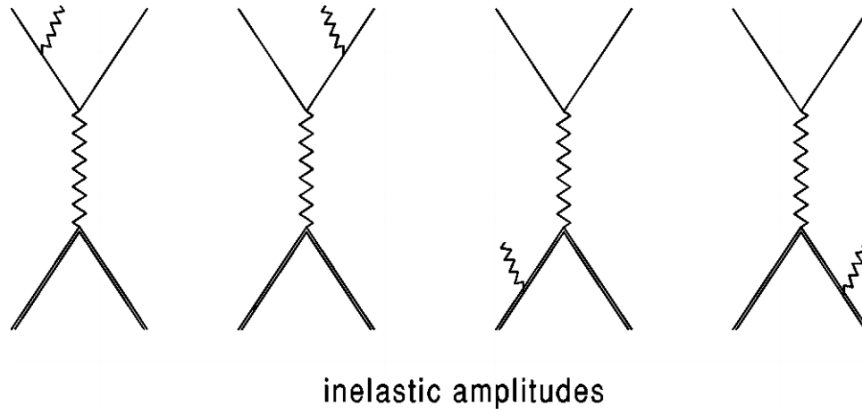


Figure 2-6: QED diagrams involving a soft external photon that contribute to elastic $e^\pm p$ scattering. (Figure reproduced from Reference [100].)

In these radiative corrections calculations, however, effects due to the two-photon exchange (TPE) diagrams in which both photons carry comparable energy (hard two photon exchange) were not considered (the diagrams marked “box” and “crossed-box” in Figure 2-5). In particular, it is difficult to account for the behavior of the proton between the proton-photon vertices, since in that leg of the diagram the proton may be off shell or possibly even in an excited state such as a Δ^+ . While early models of two-photon exchange suggested that the contribution of TPE was considerably smaller than 1% of the cross section, the validity of these models was limited to values of Q^2 below $\sim 1 \text{ GeV}^2$ where the probability of hard TPE is smaller [101–107].

2.4.1 Theoretical Calculations of TPE and their Effect on the $\frac{\mu_p G_E}{G_M}$ Ratio

Given that radiative corrections due to the TPE diagrams were the least understood among the corrections of order up to α^2 , renewed efforts were made to better model this effect and examine the effect of such models’ predictions on the form factor ratio [39–45, 108, 109]. Descriptions of the details of these models are beyond the scope of this work, but an overview may be found in References [64] and [65]. As an example, the effect of the model developed in Reference [42] on $\frac{\mu_p G_E}{G_M}$ is shown in Figure 2-7, and as can be seen such predictions tend to explain at least some of the discrepancy

between the Rosenbluth separation and polarization-based measurements.

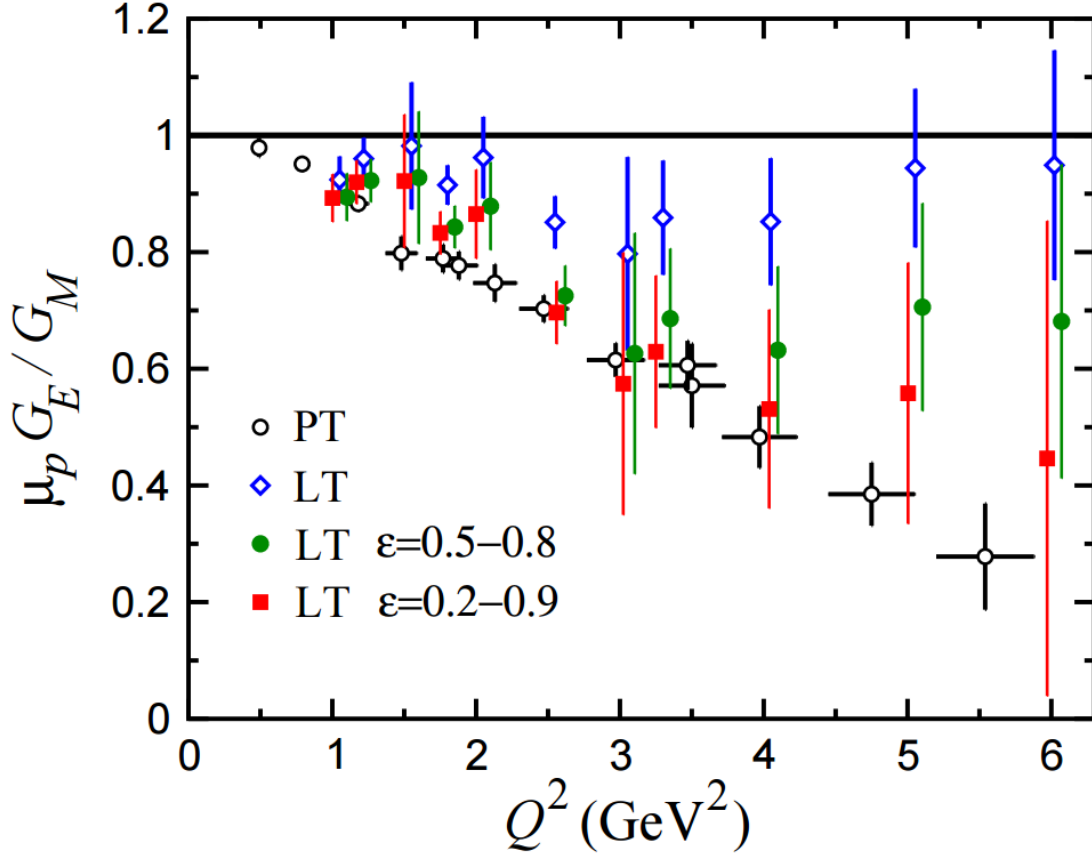


Figure 2-7: Example of a theoretical model for the effect of TPE on Rosenbluth separation $\frac{\mu_p G_E}{G_M}$ measurements, showing the shift of the Rosenbluth separation points (“LT”) towards the polarization transfer points (“PT”) for two separate assumptions regarding the amount of TPE that occurs (filled markers). Note that the TPE model accounts for a significant fraction of the form factor discrepancy. (Figure reproduced from Reference [42].)

Since QCD does not provide an unambiguous, calculable method for modeling the proton, such predictions vary significantly; models range from accounting for none of the discrepancy to nearly all of it, as can be seen in wide spread of model predictions for $\sigma_{e^+p}/\sigma_{e^-p}$ due to TPE in Figure 1-2. Thus, there exists a strong demand for experimental measurements of the contributions of TPE to $e^\pm p$ scattering.

2.4.2 Experimental Signature of TPE

Given the hypothesis of TPE and an established need for experimental measurement of its contribution to $e^\pm p$ elastic scattering, it was quickly realized that a comparison of $e^- p$ and $e^+ p$ elastic scattering cross sections provides direct experimental access to the size of the TPE matrix elements $\mathcal{M}_{\gamma\gamma}$ corresponding to the box and crossed-box diagrams of Figure 2-5. This can be approximately understood by considering the toy example of the calculation of the total squared matrix element in Figure 2-8. Terms of the total matrix element \mathcal{M} that represent an interference of the one-photon and two-photon diagrams are proportional $(\pm\alpha)^3$ where the \pm is determined by the charge of the lepton. Thus, the matrix element is shifted downward for electron scattering by these terms and upward for positron scattering, creating an asymmetry that could be measured experimentally. Using \mathcal{M}_γ to represent the single photon exchange matrix element (with positive sign, i.e, for $e^+ p$ scattering) and $\mathcal{M}_{\gamma\gamma}$ for the TPE elements, the ratio expressed in terms of an experimental measurement in Equation 1.1 may be expressed in terms of the matrix elements as:

$$R_{2\gamma}(\epsilon, Q^2) = \frac{\sigma_{e^+}}{\sigma_{e^-}} \sim 1 + 4\alpha \frac{\mathcal{M}_{\gamma\gamma}}{\mathcal{M}_\gamma}. \quad (2.22)$$

Thus, an experiment which can measure this cross section ratio at the relevant kinematics provides direct access to the value of the TPE contribution to the cross section, which would put valuable constraints on theoretical models and offer insight into what fraction of the form factor ratio discrepancy can be explained by TPE. An important note is that in addition to the Born/TPE interference contribution differing in sign between $e^- p$ and $e^+ p$ scattering, interference between the Born diagram and the externally radiated photon (bremsstrahlung) diagrams (Figure 2-6) and thus careful correction for these effects is required in the analysis of any $\sigma_{e^+ p}/\sigma_{e^- p}$ experiment attempting to extract the TPE contribution.

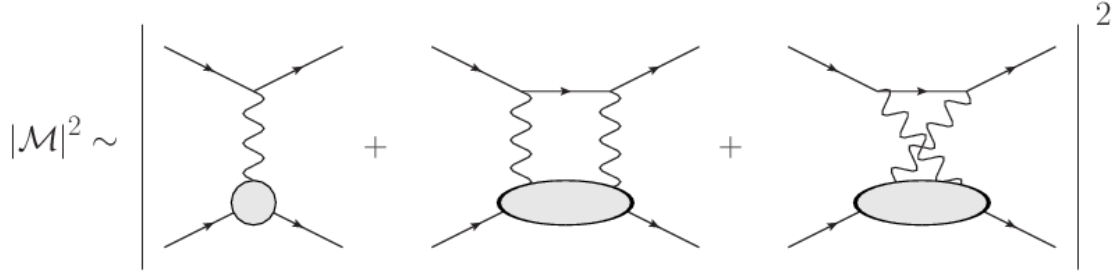


Figure 2-8: A simplified visual representation of the contribution of the TPE Feynman diagrams to the total matrix element for $e^\pm p$ scattering. Interference terms between the one-photon exchange diagram and two-photon exchange diagrams contribute terms proportional to $(\pm\alpha)^3$ due to the lepton vertices, changing sign for e^+p and e^-p scattering.

2.5 Experiments Measuring $\sigma_{e^+p}/\sigma_{e^-p}$ and Physics Goals of the OLYMPUS Experiment

Given the spread in theoretical models for TPE and their effect on the value of $\sigma_{e^+p}/\sigma_{e^-p}$ (Figure 1-2), experiments measuring $\sigma_{e^+p}/\sigma_{e^-p}$ at the accuracy of 1% or better at values of $Q^2 \gtrsim \mathcal{O}(1 \text{ GeV}^2)$ are required to differentiate the models, with preference towards higher Q^2 where the form factor discrepancy is largest. Existing data on this quantity from the 1960s (shown in Figure 1-2) is much more imprecise than this goal, especially at higher values of Q^2 [48–51, 110–112]. Thus, three modern experiments have sought to measure $\sigma_{e^+p}/\sigma_{e^-p}$ via complimentary experimental setups:

1. OLYMPUS at DESY, Hamburg, Germany [38],
2. CLAS at Jefferson Lab, Newport News, Virginia [113, 114], and
3. VEPP-3 at Novosibirsk, Russia [115].

The relative kinematic reaches of these experiments are shown in Figure 2-9. Details on these experiments may be found in the cited references, but it is worthwhile to note the fundamentally different approaches of the experiments. The VEPP-3 experiment operated at lower energies than OLYMPUS with a non-magnetic spectrometer (to avoid differences in e^-p and e^+p acceptance), while the CLAS experiment utilized a

magnetic spectrometer with a simultaneous e^+/e^- beam produced by pair production from photons.

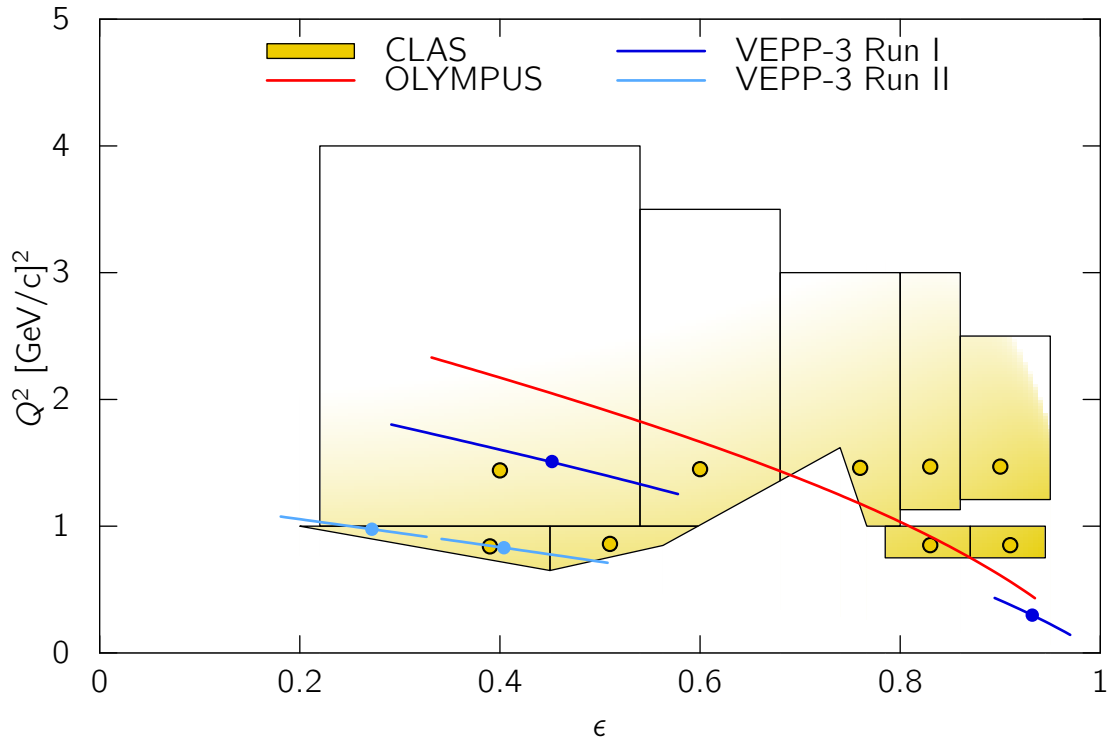


Figure 2-9: Kinematic reaches of the three TPE experiments. Note that since the CLAS experiment did not have fixed beam energy, the elastic events are spread across the (ϵ, Q^2) bins shown, dominated by the higher cross section in the bottom right of the bins. (Figure reproduced from Reference [53].)

Results from the latter two experiments preceded OLYMPUS results, and are shown in Figure 2-10. As can be seen in the figure, these results are limited in statistics (requiring broad binning) and, while suggestive of an upward trend in $\sigma_{e^+p}/\sigma_{e^-p}$ with decreasing ϵ , do not provide a definitive trend for the TPE contribution. Given that OLYMPUS collected much higher statistics than either CLAS or VEPP-3 and reaches higher in Q^2 , OLYMPUS is expected to provide a considerably more definitive ratio result. It is the goal of OLYMPUS to measure $\sigma_{e^+p}/\sigma_{e^-p}$ to a total (statistical+systematic) uncertainty of better than 1% across the full kinematic range of the experiment, as shown by the red projected bins of Figure 2-10. The remainder of this work discusses the OLYMPUS analysis and results in detail.

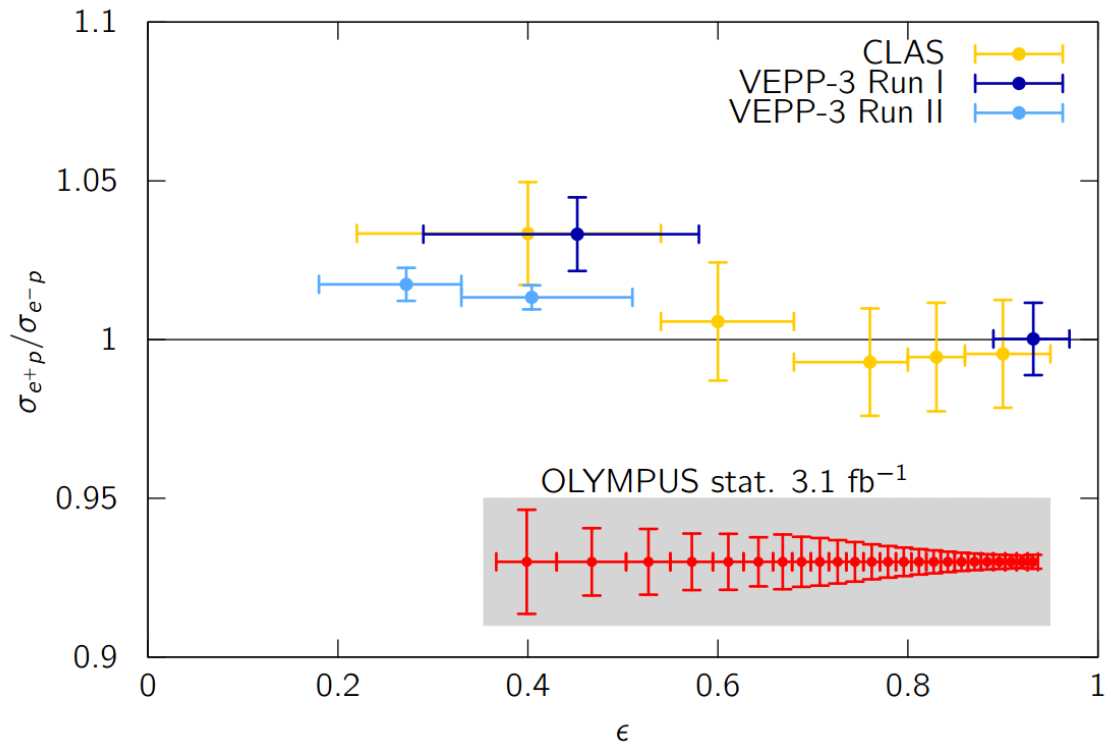


Figure 2-10: Results on $\sigma_{e+p}/\sigma_{e-p}$ from CLAS [113] and VEPP-3 [115], along with projected uncertainties for OLYMPUS (limiting any bin to at most 1% statistical uncertainty). Note the different experiments cover different Q^2 ranges for the shown ϵ range, and so are not directly comparable on this plot, but that the data are chosen so as to provide a rough comparison. (Figure reproduced from Reference [53].)

Chapter 3

The OLYMPUS Experiment

To construct an experimental setup suitable for the physics goals of OLYMPUS, a large acceptance spectrometer was assembled, capable of exclusively reconstructing $e^\pm p$ elastic scattering events while precisely measuring the recorded luminosity for each lepton species. To achieve this, the spectrometer consisted of the principal elements of the Bates Large Acceptance Spectrometer Toroid (BLAST) [116, 117] combined with several newly constructed luminosity monitors, operated at the DORIS III electron/positron storage ring at the Deutsches Elektronen-Synchrotron (DESY) in Hamburg, Germany [118, 119]. This spectrometer surrounded a gaseous hydrogen target, internal to the DORIS beamline. During the experiment, the target was exposed to electron and positron beams from DORIS, with the beam species changed approximately daily. Great care was taken to ensure that running conditions for the two different leptons species were as identical as possible to avoid unwanted systematic differences between the two modes.

Data for the experiment were taken in two periods: January 20, 2012–February 27, 2012 (Run I) and October 24, 2012–January 2, 2013 (Run II). Approximately 4.5 fb^{-1} of integrated luminosity was acquired, including various calibration runs that are not included in the sample of data used to construct the $\sigma_{e^+p}/\sigma_{e^-p}$ result. The vast majority of these data were collected in the second run, after several improvements to the trigger, target system, and other detector elements were made between runs.

This chapter describes the important details of the experimental setup used to

measure the elastic $\sigma_{e^+}/\sigma_{e^-}$ ratio, including both the detectors used for the reconstruction of $e^\pm p$ events over a large range of kinematics and the luminosity monitors. Also discussed are the essential elements of the data acquisition system (DAQ) and the operation of the experiment, especially as they pertain to the analysis of the detector data. Much of this chapter summarizes the complete published descriptions of the experiment in References [38] and [120]. Additional references that discuss certain elements of the system in greater detail are cited in the relevant sections.

3.1 Conventions for the Description of the Experiment

Throughout this work, the “OLYMPUS global” coordinate system will be used to describe the positions, orientations, and trajectories of various elements of the experiment, in addition to various “local” coordinate systems defined for specific detectors. Figure 3-1 shows the coordinate axes of the global system relative to the detector setup. The origin of this system is defined to be the center of the target cell for the purpose of defining positions throughout the detector. The beam traversed the experimental setup approximately along the $+z$ -axis through the origin, up to measured beam offsets on the order of a millimeter and angles relative to the axis on the order of 0.5 mm. Thus, “upstream” refers to the $-z$ direction and “downstream” to the $+z$ -direction, corresponding to the movement of beam particles. In describing the layout of the experiment, the positive x -direction is referred to as “beam left” and the negative x -direction as “beam right”, or more succinctly, the left and right sides of the detector. Unless otherwise noted, references to coordinate axis in the text and figures refer to this system.

Additionally, standard spherical coordinate angles (the polar angle θ and azimuthal angle ϕ) are used when convenient, especially when describing the kinematics of particle trajectories as described in Section 2.1.1. Note that θ and ϕ for a tracked or simulated particle refer to the angles relative to a coordinate system aligned with

the global system but centered on the scattering vertex for the event in question.

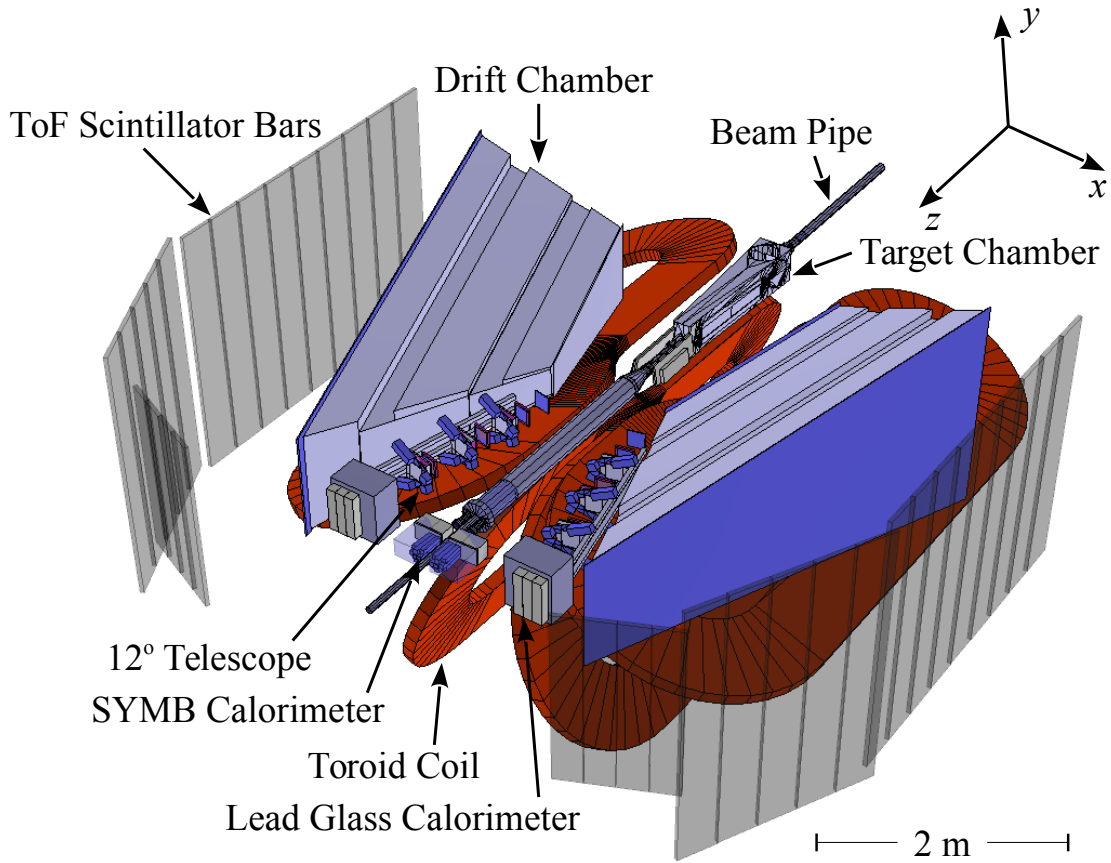


Figure 3-1: Solid model of the OLYMPUS detector, with essential components, an approximate scale, and the orientation of the global coordinate system labeled. The origin of the global coordinate system is at the center of the target chamber. The top four (+y) toroid coils have been removed to make other detector systems visible. Various components that are replicated on each side of the detector are not labeled to avoid redundancy.

3.2 The DORIS III e^+/e^- Storage Ring

A stable storage ring source of GeV scale positron and electron beams was critical to the OLYMPUS experiment goals. While several accelerators were initially assessed as candidates for the location of the experiment [121], the Doppel-Ring-Speicher ¹

¹Doppel-Ring-Speicher translates to “double-ring storage” in English.

(DORIS) III storage ring at the Deutsches Elektronen-Synchrotron, Hamburg, Germany² was selected as the facility most capable of delivering both the desired beam conditions for the experiment and the laboratory support structure for the construction, commissioning, and execution of the experiment [118, 119].

Historically DORIS operated as an electron-positron collider, operating at the energy of 3.5 GeV per beam between 1974 and 1978, and at 5.0 GeV per beam starting in 1978. Over the course of the 1980s, the ring was converted to be a synchrotron light source and became a full time light source in 1993. A key physics discovery, the mixing of the neutral B -mesons, was made at DORIS in 1987 by the ARGUS experiment [122]. OLYMPUS, which began installation at the former site of the ARGUS experiment in 2010, took data in 2012 and witnessed the last beams from the facility as the last experiment to run there on January 2, 2013. Following OLYMPUS, the accelerator was dismantled [123].

3.2.1 OLYMPUS at DORIS

Since OLYMPUS was the last experiment to run at DORIS, it was possible to make a number of modifications to the accelerator to provide for the needs of the experiment. Additionally, because the accelerator was operated as a synchrotron light source between the two OLYMPUS data runs, several constraints were placed on the design of the experiment. In particular, the target system was installed as a permanent part of the beamline, and as such the system was required to handle a variety of conditions. The experiment was placed in the large straight section of the ring, as seen in Figure 3-2. Several changes were made to the ring and experiment design to facilitate both the goals of OLYMPUS and synchrotron light production:

- a large effort was made to reconfigure the operation of the beam for OLYMPUS running (2.01 GeV, with the beam in ten bunches),
- several RF acceleration cavities were relocated away from the detector site,

²From this point forward the accelerator will be referred to as “DORIS”

- extra quadrupole magnets were installed on each side of the detector in the beamline to reduce the beam width in the interaction region and then return it to its original size for the synchrotron light creation elements of the ring, and
- the OLYMPUS target was continuously cooled to allow the operation of the ring in the harsher conditions of synchrotron light production (4.5 GeV beam in five bunches, at 150 mA currents).

The implementation of the target system to meet these requirements is discussed in Section 3.3 and in greater detail in Reference [124]. Several changes also were required to facilitate the frequent switching between the lepton species of the beam that OLYMPUS required:

- the high voltage pulse power supplies for the pre-accelerator beam extraction line and DORIS injector kicker magnets were heavily refurbished,
- the septa magnets in the pre-accelerator and injection line were modified to operate in both polarities, and
- remote control switches were constructed and installed for the magnet power supplies throughout the accelerator system.

The beam position in the interaction region was continuously measured by monitors installed on either side of the target chamber. Additionally, a dipole reference magnet was installed downstream of the experiment in series with the ring's bending dipoles to continuously measure the beam current. This data, along with a number of relevant parameters, was recorded by the accelerator archive systems and was made available to the OLYMPUS archiving systems.

3.2.2 Beam Specifications

During OLYMPUS operation, the beam was operated at ~ 2.01 GeV and distributed in ten bunches. The beam species was switched approximately daily, but in general a concerted effort was made to keep the running conditions identical for both

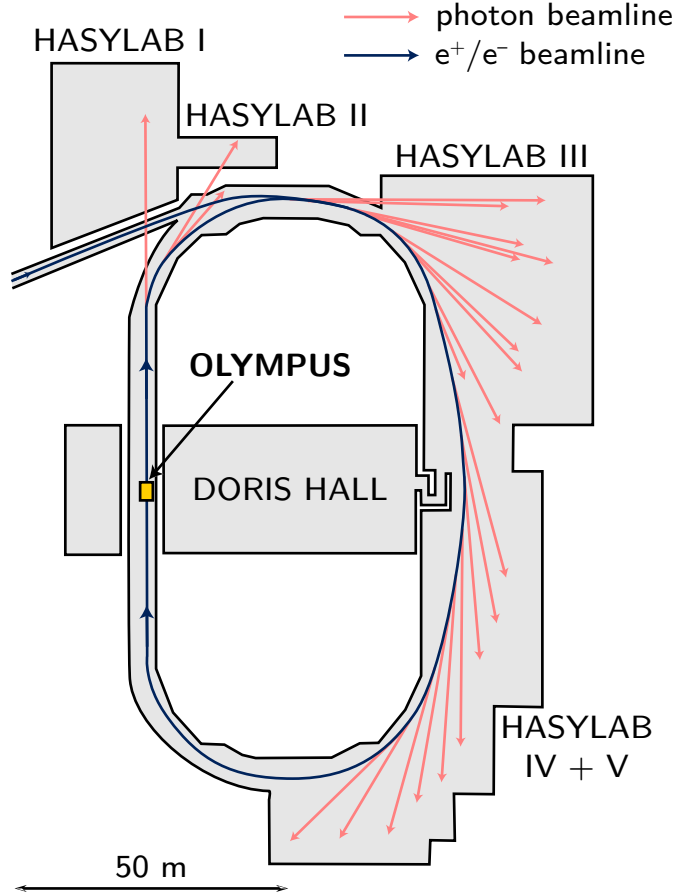


Figure 3-2: Overhead view of the DORIS III e^+/e^- storage ring, showing the direction of beam circulation and the locations of the OLYMPUS spectrometer in the straight segment of the ring and the synchrotron light experiment stations around the ring (which were not active during OLYMPUS data taking). The total length of the beamline was approximately 300 m [124].

species. Due to the fact that the beam injected into DORIS was at full energy during OLYMPUS running, OLYMPUS ran in “top-up” mode throughout the fall run. In this mode, leptons were added to the beam after the current dropped by only a few percent rather than waiting until a significant fraction of the beam had decayed to refill. This allowed OLYMPUS to collect data at a much more constant beam current, which helped to both increase the collected luminosity and maintain stable data-taking conditions. Top-up mode was periodically interrupted during electron running, since approximately every 30 minutes the pre-accelerator system at DESY was switched to positrons to fill the PETRA ring. During these times, the current

dropped below the top-up level while waiting for the system to permit a refill. Typical beam current levels during Run II over the course of a 14 hour period are presented in Figure 3-3, showing the stability of the current in top-up mode, the periodic PETRA fill period, and the typical 20 minute daily pause to switch the beam species. The beam parameters for operation of the experiment are summarized in Table 3.1.

Parameter	Value
Species	e^+ or e^- (alternated \sim daily)
Energy	2.01 GeV
Current	60–65 mA (top-up mode)
Bunches	10
Bunch spacing	96 ns (100 ns every fifth bunch)
Lifetime with gas in target	40–55 minutes
Bunch length	19.5 mm (\sim 0.1 ns)

Table 3.1: A summary of the typical parameters of the DORIS beam during OLYMPUS data-taking.

3.3 The OLYMPUS Internal Hydrogen Target

Lepton-proton scattering events were generated by placing a windowless, internal gaseous hydrogen target in the DORIS beamline, which simultaneously provided a high target density of protons while minimizing adverse effects on the beam due to the presence of the target (increased emittance, uneven bunch charges, etc.). The target system consisted of several key components, including the hydrogen gas cell, a beam collimator, a cryogenic cooling system, an aluminum scattering chamber enclosing the cell, wakefield suppression elements to prevent heating due to the large charge-per-bunch of the DORIS beams, and a multi-stage vacuum system to remove hydrogen from the beamline to prevent spoiling the ring vacuum. The primary goals of the target system were to present an effective thickness of $\sim 3 \cdot 10^{15}$ H atoms/cm² to the beam in view of the detectors while handling the intense heating conditions of the bunched DORIS beam.

A detailed discussion of these components may be found in [124], while an es-

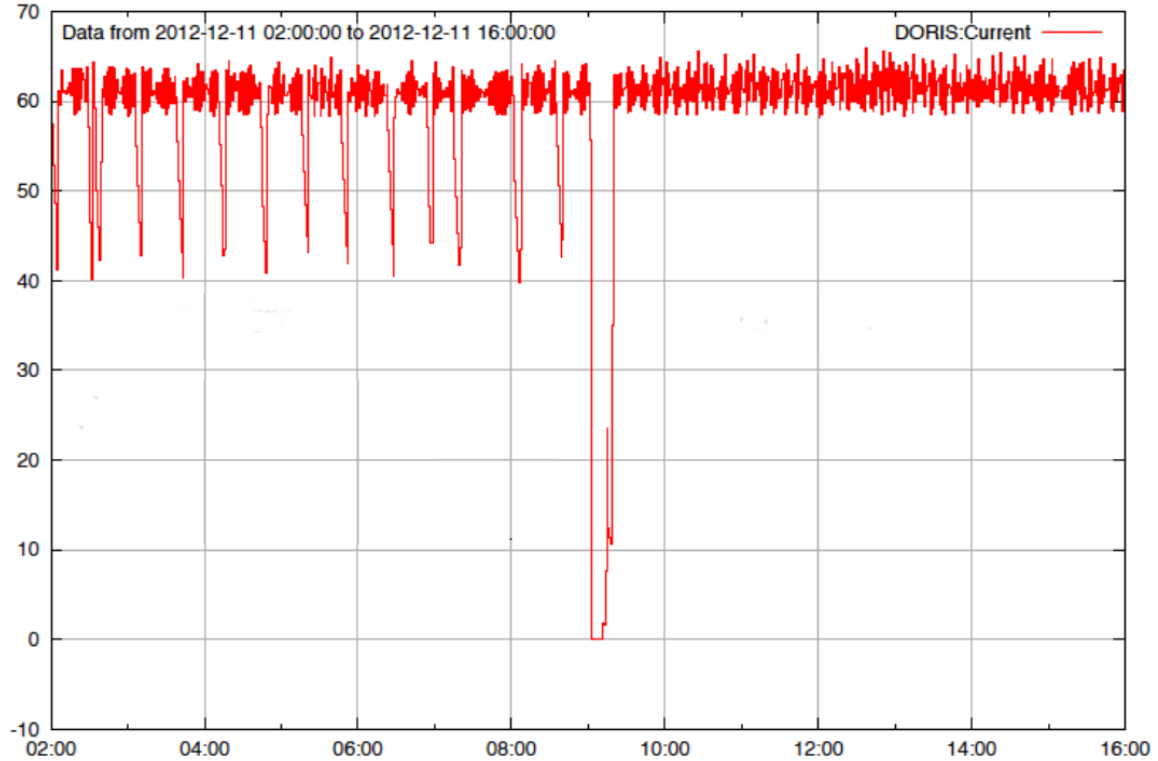


Figure 3-3: The beam current in mA as a function of time for a typical 14-hour period of OLYMPUS running, showing the 20 minute pause in operation to switch the beam species at 9:00. To the left of the pause, electron running is shown with the regular larger drops in current caused by the refills of the PETRA ring. To the right, positron running is shown, which did not have the top-up interruptions since PETRA also used positrons. Outside these interruptions, a stable beam current of around 62 mA was maintained [125].

sential overview is provided in this section. A discussion of the physics of the gas contained within the system and its effect on the experiment’s kinematic acceptance and luminosity is found in Section 5.1.

3.3.1 Scattering Chamber

The main elements of the target system were contained within a scattering chamber, manufactured from a single solid block of aluminum to provide high vacuum integrity. This chamber was 1200 mm long and 254 mm high. The chamber tapered from a width of 245 mm at its upstream end to 114.3 mm at its downstream end, resulting in a trapezoidal prism shape for the chamber. This design increased the visibility of the

target cell within the chamber to the forward detector elements while still providing room for the installation of the collimator and access ports at the upstream end. The chamber interfaced directly with the beamline (and the beamline vacuum) at each end. The chamber was designed at the MIT-Bates Linear Accelerator Center, taking advantage of experience gained designing similar targets for BLAST and other experiments [126]. Figure 3-4 shows the key elements of the chamber design.

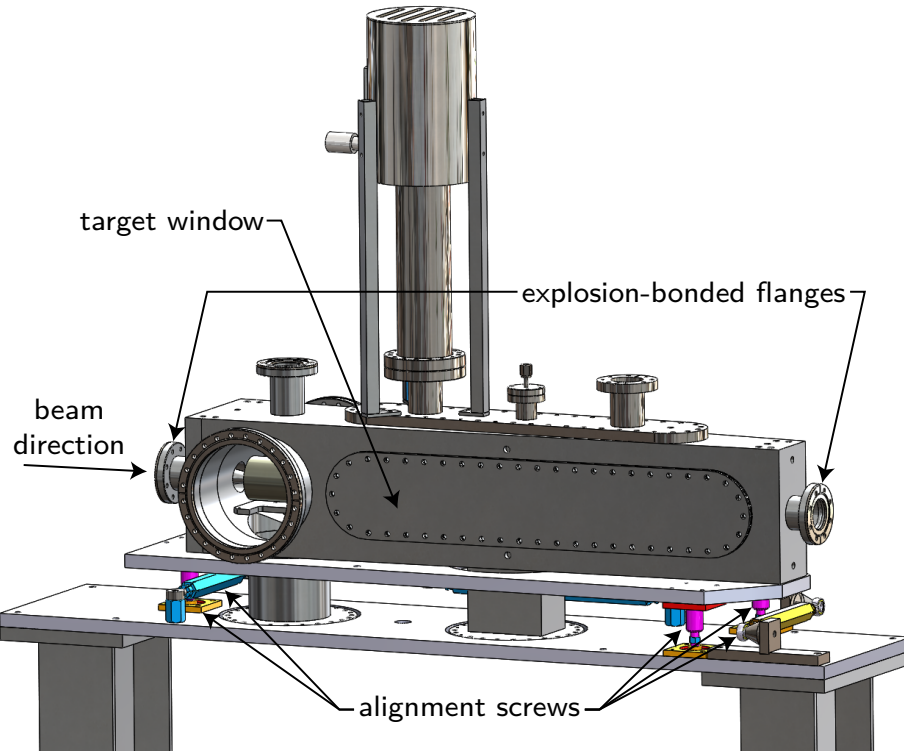


Figure 3-4: Schematic of the OLYMPUS scattering chamber, showing the principal elements of the design as viewed from beam right [124].

The chamber included several ports to allow access to the inside of the chamber, both for installation and/or repair work and to provide windows for scattered particles to escape the target. The ports were sealed either with Atlas³ explosion-bonded bimetallic flanges or O-rings (in the case of the window ports). The target windows consisted of 0.25 mm thick 1100 aluminum foil, and subtended a polar angle range of 8° to 100° relative to the center of the target to provide a complete view of the cell to the detector systems (with the exception of the 12° system which could not view the

³Atlas Technologies, Port Townsend, WA, USA

most downstream portion). The chamber was mounted on an aluminum table, which supported its weight above the vacuum system and provided screws for the alignment of the chamber to match the beamline.

3.3.2 Target Cell

The target cell, used to contain a considerable concentration of hydrogen in the vicinity of the beam before it escaped to the vacuum system, was a 600 mm long elliptical aluminum tube through which the beam passed directly. The elliptical cross section (27 mm wide by 9 mm high) was chosen to mimic the envelope of the DORIS beam to mitigate any unwanted interactions of the beam with solid material in the target system. The target cells used in the experiment were manufactured by molding two sheets of 75 μm thick Goodfellow⁴ aluminum foil and mounting them in an aluminum support frame. The cells were constructed at Ferrara University/INFN, where similar cells were constructed for the HERMES experiment [127]. A photograph of an OLYMPUS target cell mounted in the scattering chamber (with the windows and other internal target system components removed) is shown in Figure 3-5, and its connections to the other internal components is shown in Figure 3-6. More details on the manufacturing process for these cells are described in Reference [124].

3.3.3 Collimator

Also among the internal components of the target system shown in Figure 3-6 is a collimator placed on the upstream side of the target cell to block beam halo from entering the OLYMPUS interaction region. The collimator was manufactured from a solid tungsten cylinder, with an outer diameter of 82.55 mm and length of 139.7 mm. The bore of the collimator was elliptical in cross section, 25 mm by 7 mm at its upstream face and flaring to the 27 mm by 9 mm size of the target cell and intermediate wakefield suppressor at its downstream end. The size of the collimator and its bore were chosen based on the results of Monte Carlo simulation of beam halo

⁴Goodfellow Corporation, Coraopolis, PA, USA



Figure 3-5: The OLYMPUS target cell, mounted within the aluminum scattering chamber (with the windows and wakefield suppressors removed) [124].

particles and synchrotron radiation impinging on the collimator, and considering the resulting predicted heat loads and forward scattering of unwanted particles into the interaction region. During the 4.5 GeV synchrotron light production operation of DORIS, the collimator was exposed to ~ 25 W of heating, which was well within the dissipation capabilities of the cooling system. During OLYMPUS operation, the heat load was considerably less (~ 1 W).

3.3.4 Wakefield Suppressors

The final internal components of the system shown in Figure 3-6 were the wakefield suppression elements, which served to provide a continuous and smooth electrical conductance connection between the beamline interfaces at each end of the target chamber and among the internal target chamber components. This was required due to the bunched nature of the DORIS beam, which caused strong electromagnetic wakefields that could induce considerable heating of the system if not provided a highly conductive means of conveyance in the system. Three wakefield suppressors

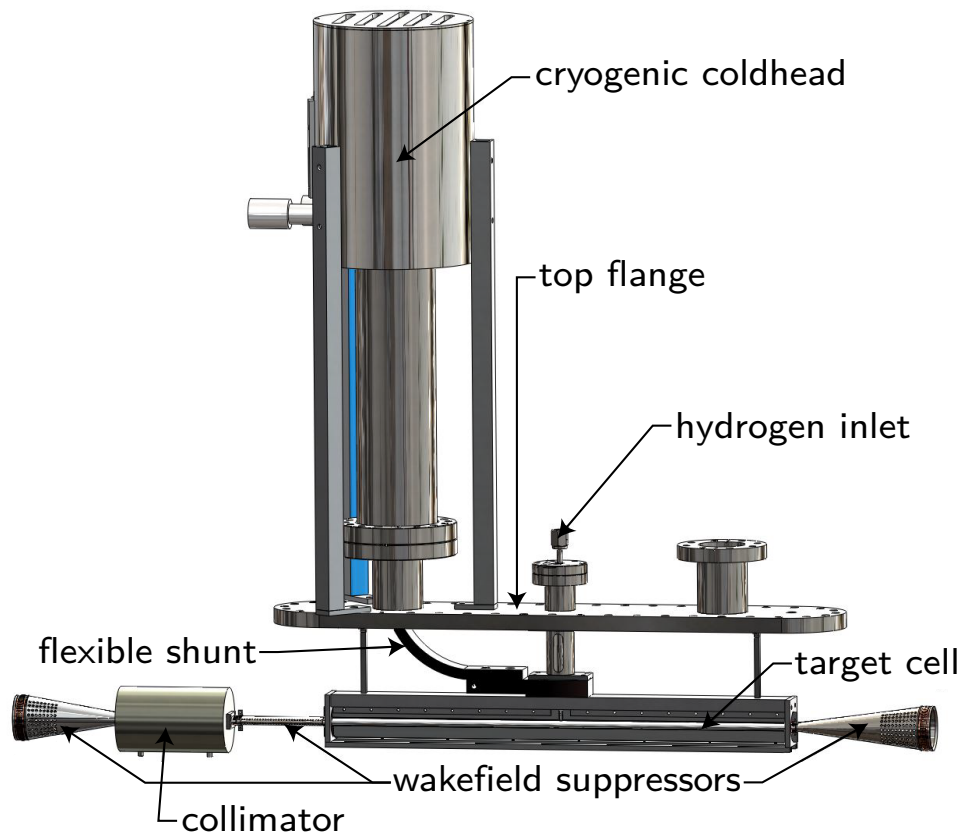


Figure 3-6: Schematic of the components of the hydrogen target system contained within the scattering chamber, including the gas inlet, target cell, connection to the cryogenic system, collimator, and wakefield suppressors. For reference, the origin of the OLYMPUS coordinate system is the center of the target cell directly beneath the inlet, and the beam passed from left-to-right (positive OLYMPUS z), approximately through the center of the wakefield suppressors, collimator, and target cell as shown in the figure. The conal wakefield suppressors at each end connect smoothly to the beamline [124].

were present in the system: an elliptical tube element between the cell and the collimator, and two conal elements which flared from elliptical profiles at their interfaces with the target system to circular profiles at their interfaces with the beamline. The elements were coated with a thin layer of silver to increase their conductivities and their connections to other system elements included beryllium-copper spring cones to ensure good electrical contact. Holes were drilled through the wakefield suppressors to allow the escape of beam gas, but these holes were placed as far as possible from the beam to mitigate their impact on the conductivity of the system.

3.3.5 Cryogenic System

To mitigate the heating caused by the beam and to increase the target density by cooling the H₂ gas within the system, the target system was actively cooled to temperatures below 75 K whenever beam was in the DORIS ring. This was achieved using a CryoMech⁵ AL230 coldhead and CP950 compressor system. The interface of the coldhead with the components of the target system can be seen in both Figures 3-4 and 3-6. The cooling system connected to the target cell assembly via a solid copper shunt coated with indium at the interface with the cell assembly. The aluminum scattering chamber (exposed to the beam hall atmosphere) was at the temperature of the beam hall air and was thus thermally insulated from the cooled elements. The system was capable of dissipating 36 W at 25 K, sufficient to handle the heating caused by both synchrotron light production and OLYMPUS beam conditions. This was verified by the installation of seven Pt100 thermocouple temperature sensors along the length of the target that were used to monitor the system temperature whenever beam was in the ring.

3.3.6 Vacuum System

Due to the fact that hydrogen gas was flowed directly into the beamline, it was necessary to include a powerful vacuum system to remove the gas from the beamline as it escaped the target cell assembly to avoid spoiling the vacuum necessary for the beam. The system included six turbomolecular pumps (split between Osaka⁶ TG 1100M and Edwards⁷ STP 1003C models). Since the system was required to remove hydrogen from the ring at low pressures, four non-evaporable getters (NEGs) were installed with four of the turbomolecular pumps. Due to the fact that turbomolecular pumps operate using magnetically levitated rotors, the pumps were required to be placed outside of the OLYMPUS magnetic field (either along the beamline from the interaction region or in a pit below the experiment). The placement of the pumps is

⁵CryoMech, Inc., Syracuse, NY, USA

⁶Osaka Vacuum, Ltd., Osaka, Japan

⁷Edwards, Crawley, United Kingdom

shown in Figure 3-7. The pumps placed below the experiment were connected to the system with large-diameter piping to insure a high conductance connection. As can be seen in the figure, the pumps were arranged in three stages, each of which reduced the pressure by approximately an order of magnitude. This reduced the $\sim 10^{-6}$ Torr pressure inside the chamber to the 10^{-9} Torr pressure of the ring.

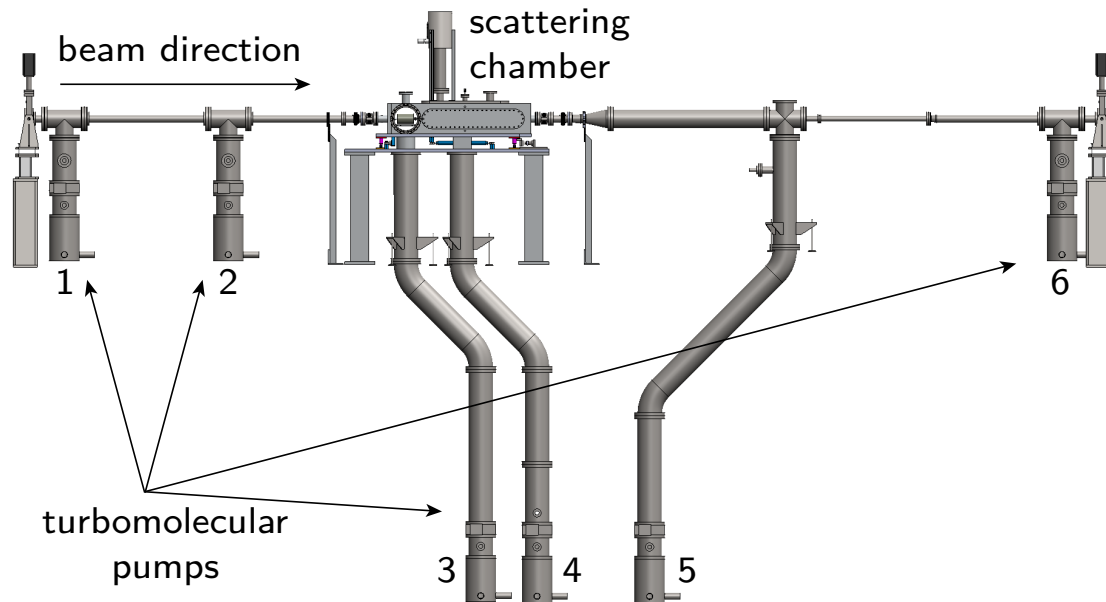


Figure 3-7: Diagram of the vacuum components of the OLYMPUS target system, showing the six turbomolecular pumps and their high conductance connections to the target chamber and beamline. The non-evaporable getters were placed at the locations of turbomolecular pumps 1, 2, 5, and 7 to assist with the removal of hydrogen at low pressures. [124].

3.3.7 Hydrogen Gas Supply System

The source of protons for $e^\pm p$ scattering in the system (and of electrons for the luminosity monitoring processes) was molecular hydrogen gas flowed into the middle of the target cell. The binding energies of hydrogen atoms and molecules are negligible compared to the GeV scale beam energy, and thus the target effectively served as a free proton target. The H_2 gas used for the target was supplied by a Parker⁸ hydrogen gas generator, which produced ultra-pure (<200 ppb impurity) hydrogen via the

⁸Parker-Hannifin Corporation, Haverill, MA, USA

electrolytic dissociation of deionized water. Within the generator, the dissociation occurred in palladium tubes, which were opaque to all atoms and molecules in the system except H^+ ions. The generator produced a pressure of 20 psi on the supply line to the target. This rate of gas production exceeded the target's actual supply needs by orders of magnitude, but was done to maintain positive pressure relative to the atmosphere outside the line.

The actual gas flow into the target was controlled by a system of remotely-controlled mass flow controllers (MFCs) and pneumatic solenoid valves modeled on the system used for the BLAST target [126], and operated using the slow control system described in Section 3.7. Two buffer vessels of known volume were used to calibrate the MFCs. The MFCs could provide reliably calibrated flow rates between 0.1 and 1.0 standard cubic centimeters per minute (sccm), and the range used during the experiment running was approximately 0.4-0.8 sccm.

3.4 The OLYMPUS $e^\pm p$ Spectrometer

The OLYMPUS spectrometer used for the reconstruction of elastic $e^\pm p$ events was predominantly constructed from various components of the BLAST experiment [117]. The detector consisted of gas drift chambers to the left and right of the beam for particle trajectory reconstruction, scintillator panels beyond the drift chambers to provide timing and trigger information, and a toroidal magnetic field to provide particle bending for momentum reconstruction and background suppression. The total acceptance of the main detector package for $e^\pm p$ events ranged over approximately ($25^\circ \leq \theta \leq 80^\circ$) and $(-15^\circ \leq \phi \leq 15^\circ) \cup (165^\circ \leq \phi \leq 185^\circ)$ in the particle scattering angles, corresponding to the instrumentation of the left and right sides of the detector. This corresponds to ranges in the kinematic parameters of approximately ($0.4 \leq \epsilon \leq 0.9$) and ($0.6 \leq Q^2 \leq 2.2$) GeV^2/c^2 . The essential details of these components are described in this section (and in more detail in References [38, 120, 128]).

3.4.1 Toroidal Magnet

Momentum reconstruction for particles detected in the OLYMPUS detector was made possible by the generation of a toroidal magnetic field around the target. Additionally, the field produced by the toroid bent low-energy particles (produced by Møller and Bhabha scattering in the target and other sources of background tracks) away from the detector systems to reduce the number of unwanted hits in the detectors. Eight water-cooled copper coils carrying a nominal current of 5000 A arranged symmetrically around the beamline produced this field. The lower four of these coils are shown in Figure 3-1, while Figure 3-8 shows the complete coil configuration prior to installation of the magnet in the DORIS beamline. The coils pinched towards the beamline in their downstream sections, but opened away from each other in the upstream sections to accommodate the target. The peak field strength was approximately 0.3 T in the regions of the tracking detectors.

The coils were originally part of the BLAST experiment, and the design of the magnet is described in detail in Reference [129]. A toroidal field was originally chosen for the BLAST experiment to minimize the magnetic field near the beam, which was critical to the polarized target experiments conducted at BLAST [19, 117]. While zeroing the field along the beamline was not critical to OLYMPUS, the coils were aligned when installed to minimize the field in this region to avoid perturbing the beam.

During data-taking, the toroid was set to produce a field that bent positively charged particles towards positive θ trajectories as they moved through the detector system. The strength of the field in the y direction in the $y = 0$ plane bisecting the detector systems is shown in Figure 3-9. While the original conception of the OLYMPUS experiment included regularly switching the toroid polarity to reduce the systematic uncertainties associated with the relative acceptance of positron and electron events, this was in practice infeasible. In the opposite polarity, low energy electrons originating from the target were bent into the detectors which caused an intractable background that obscured desired events. While efforts were made to mit-

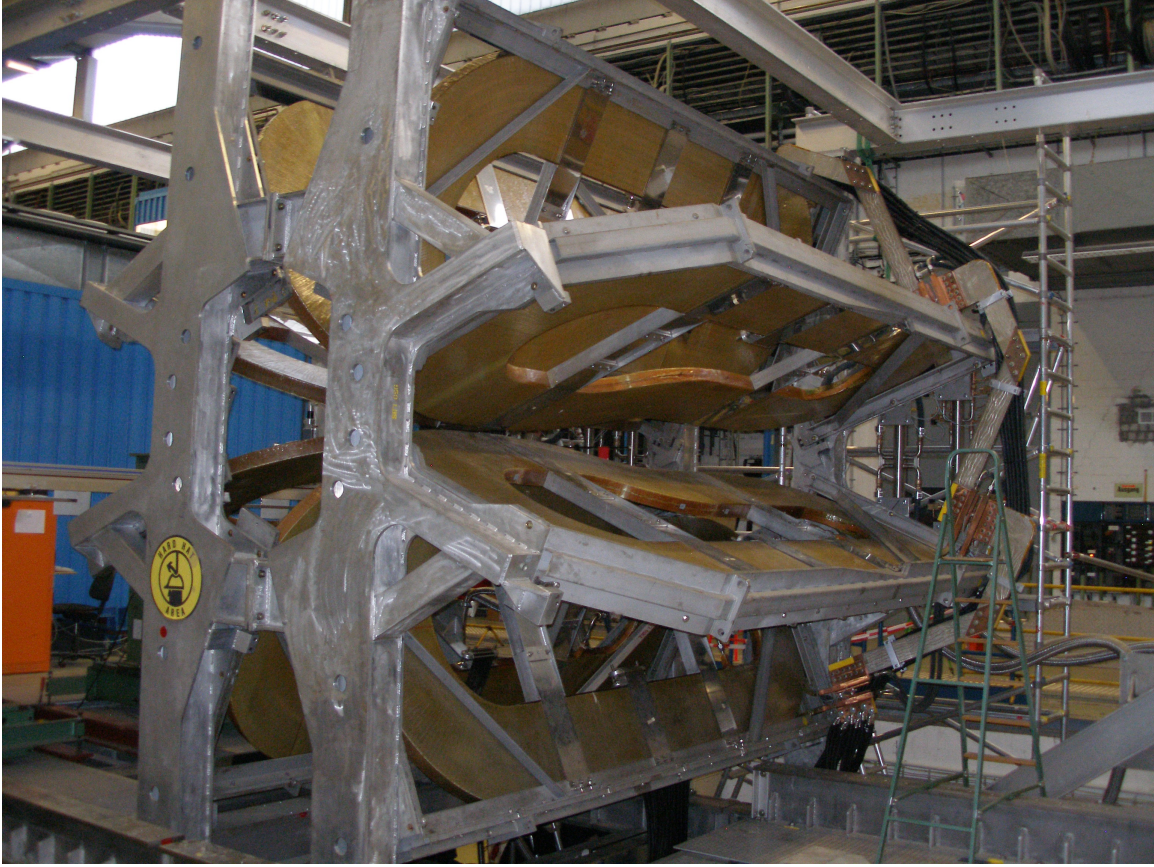


Figure 3-8: Photograph of the OLYMPUS toroid prior to installation in the DORIS beamline, showing the symmetric arrangement of the eight coils [38].

igate this effect to permit running with the second polarity (including increasing the field strength and physically shielding the detectors with material to stop low energy particles), these changes were not sufficient to create a good environment for elastic event reconstruction. While some data were taken with the opposite polarity for testing purposes, this dataset only represents approximately 13% of all data collected, since it was limited to low luminosity running in which the noise rate was sufficiently low to permit event reconstruction.

To ensure that the magnetic field was well understood for the purposes of track reconstruction and event simulation, a large effort was undertaken after the conclusion of data-taking to survey the field throughout the detector volumes. This effort is described in Section 4.1.3 and Reference [128].

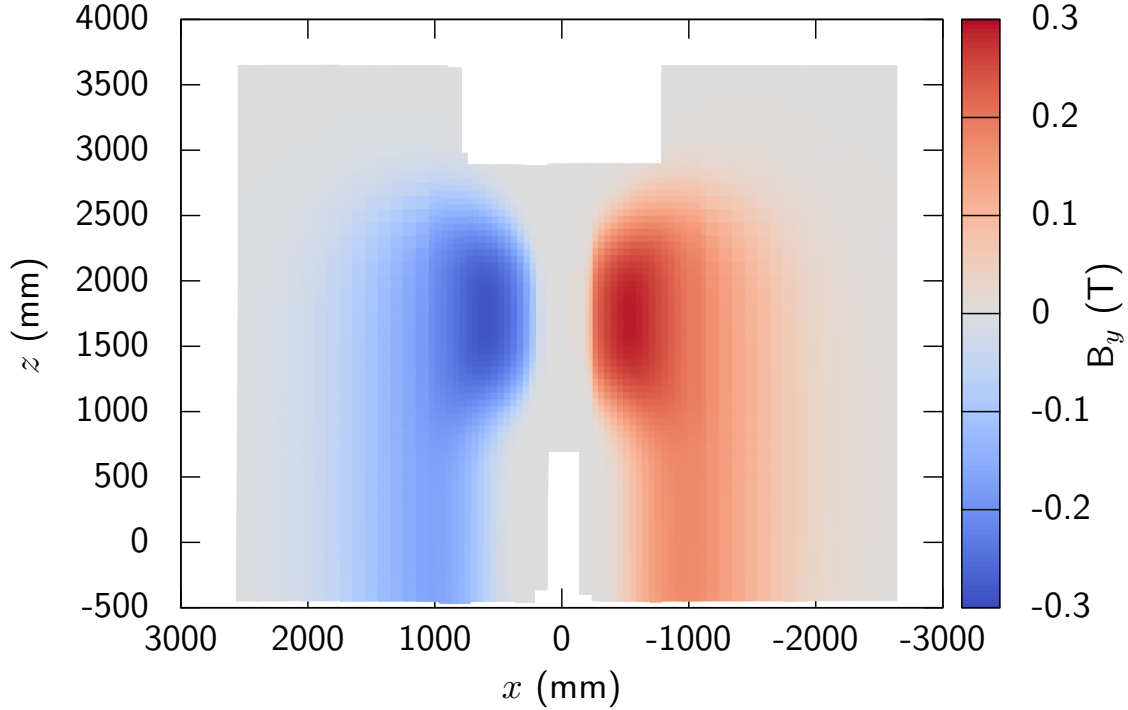


Figure 3-9: Map of the strength of the B_y component of the OLYMPUS magnetic field in the global $y = 0$ plane as measured in the field survey (Section 4.1.3). The regions of strongest field occurred within the drift chamber tracking volumes, while the field was much smaller in the vicinity of the target along the z -axis [38].

3.4.2 Time-of-Flight (ToF) Scintillator System

The time-of-flight (ToF) scintillator system, also inherited from the BLAST experiment [117], consisted of 36 scintillator bars (18 per side) arranged in walls on each side of the detector, as shown in Figure 3-1. These bars played the critical role of providing timing signals for the trigger and the readout of the main detector elements, as described in Section 3.8. The bars were arranged in panels of four, five, and nine bars on each side with the panels arranged to point the normal vector of the panel plane approximately towards the target. The forward panel bars measured $119.4 \text{ cm} \times 17.8 \text{ cm} \times 2.54 \text{ cm}$, while the bars in the rear two panels were larger: $180.0 \text{ cm} \times 26.2 \text{ cm} \times 2.54 \text{ cm}$. This arrangement guaranteed that the acceptance of the ToF bars for tracks originating from the target completely included that of the drift chambers and 12° luminosity telescopes.

Each bar consisted of a solid block of Bicron⁹ BC-408 scintillator, a plastic scintillator designed for applications requiring fast response times (0.9 ns) over large areas such as in the OLYMPUS experiment [130]. While new BC-408 exhibits attenuation lengths on the order of two meters, due to the age of the scintillator bars and their exposure to radiation throughout the BLAST and OLYMPUS experiments, the scintillators' attenuation in the bars during OLYMPUS running was significantly worse. While efforts were made to replace the most damaged bars, a large analysis effort was made to properly account for the state of the scintillator, which is described in detail in Reference [54].

Each bar was instrumented with two 3-inch diameter Electron Tubes¹⁰ 9822B02 photomultiplier tubes, connected to the top and bottom of each bar via Lucite¹¹ light guides. The light guides were arranged to orient their connected PMTs approximately perpendicularly to the toroidal magnetic field to minimize the effect of the field on the PMT gain, as shown in Figure 3-10. The PMTs were also wrapped in mu-metal shielding to further reduce any such effects. Signals from the detectors were passed to dedicated ADC and TDC channels for each PMT, processed using constant fraction discriminators for the downstream 16 bars on each side and leading-edge discriminators for the upstream 2 bars on each side. This distinction was due to the fact that the upstream bars were not included in the original design, and were added only after it was realized that a larger margin of safety was desired to cover the full acceptance of the 12° telescopes.

The signals from the PMTs were rapidly digitized for processing by the trigger. When triggered, these signals produced a common-start signal for the ToF TDCs and a common-stop signal for the drift chamber TDCs. The total ADC counts were recorded as a measure of the energy deposition in the ToF bars, and the ToF TDC information for each bar could be used to estimate both the vertical position at which the bar was hit and the flight time of the particle from the vertex to the bar. This analysis is described in Section 4.2.

⁹Bicron, Solon, OH, USA

¹⁰Electron Tubes, Ltd., Ruislip, Middlesex, United Kingdom

¹¹Lucite International, Southampton, Hampshire, United Kingdom

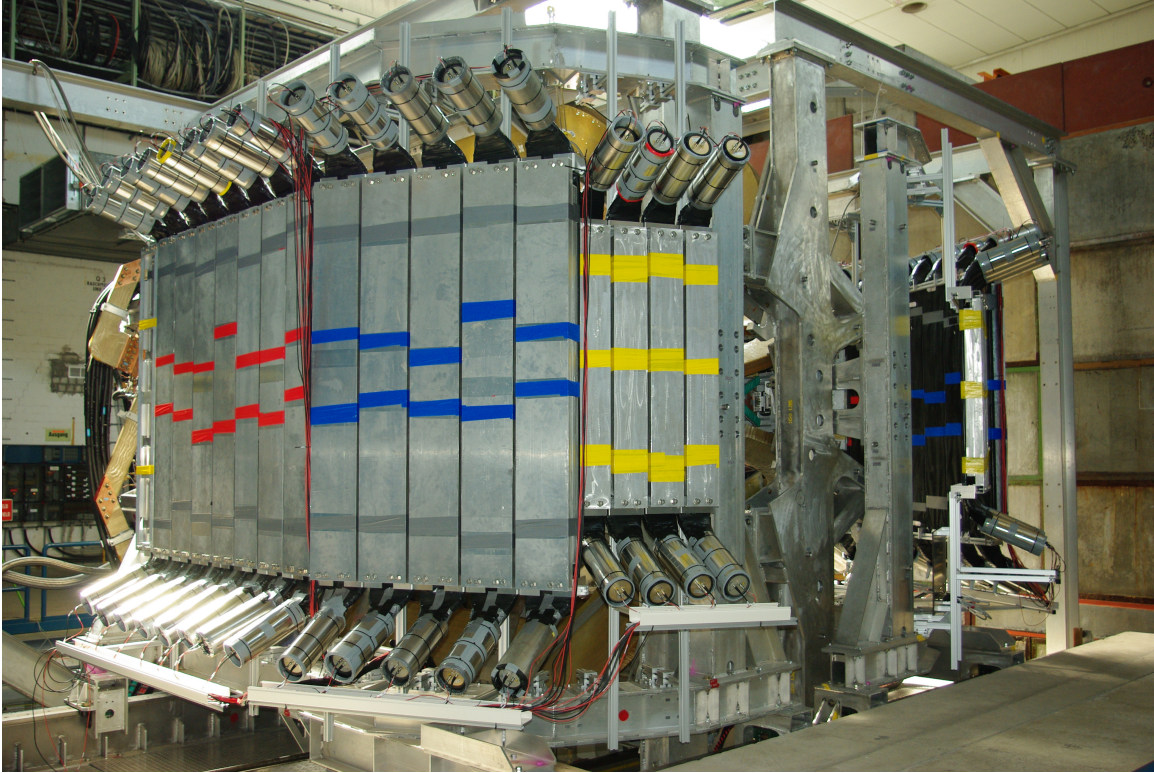


Figure 3-10: Photograph of the right side of the ToF detector system prior to installation of the detector package within the DORIS beamline, showing the orientation of the PMTs perpendicular to the direction of the toroidal magnetic field [38].

3.4.3 Drift Chamber Tracking System

The main detectors that provided hit position information for reconstruction of $e^\pm p$ events were two large drift chambers mounted between the toroid coils on the left and right sides of the detectors. Functioning as a typical drift chamber, charged particles passing through the gas contained within these chambers induced ionization, and the electric field created by the wires held at potential throughout the chamber caused the resulting electrons to drift towards dedicated detection wires. Better position resolution was achieved by recording the signal time using TDCs, with a common-stop signal provided by the fast signal of the time-of-flight system. Since drift speeds of the electrons in the gas were on the order of 5-6 cm/ μ s, the arrival of the drifting electrons across the centimeter-scale cells occurred well after the ToF signal. This extended drift time was converted to a distance from the wire at which the particle passed (Section 4.2.1), which provided positional information for track reconstruction.

Once again, these detectors were inherited from the BLAST experiment [117], but underwent a complete refurbishment for OLYMPUS. The refurbishment included a complete rewiring of the chambers as well as new voltage distribution electronics and connections for all wires. Each chamber consisted of three trapezoidal frustum-shaped aluminum frames joined to create a single gas volume, a schematic of which is shown in Figure 3-11. Thin plastic windows closed off the gas volume on the inner and outer faces of the connected frame assemblies. Each of the three frames contained two layers of wire “cells”. A cell was formed by an array of wires that were arranged to form a rectangular box region used to create an electric drift region, as shown in Figure 3-12. The wires were held at stepped voltages from ground at the boundary between two cells to 2800 V at the center of a cell. In the center of the cell, an additional column of wires contained three sense wires held at 3900 V to attract drifting electrons to generate the detector’s signals. To help resolve the ambiguity of a single time recorded on a sense wire, the three sense wires were offset from the center plane of the cell by ± 0.5 mm to create a small difference in drift times from each side of the cell. Each cell was 78 mm by 40 mm, and extended from the top inner face of the frame to the bottom inner face. The two layers of cells in each frame extended parallel to each other, 20 mm apart, arranged such that wires in layer were at $\pm 5^\circ$ from vertical to create a stereo angle for 2D position reconstruction. A total of 318 cells were present in the two drift chambers, containing 954 sense wires and approximately 10,000 total wires.

The chambers were filled with an Ar:CO₂:C₂H₆O gas mixture at a ratio of approximately 87.4:9.7:2.9. The argon and carbon dioxide were mixed at a 9:1 ratio by a dedicated mixing system, while the ethanol was introduced by bubbling the mixed gas through liquid ethanol at 5 °C. Unfortunately, this method of introducing ethanol to the system resulted in fluctuation in the concentration of ethanol during data-taking, which altered the drift properties of the gas. This required careful calibration of the drift chamber time-to-distance calibration, as described in Section 4.2.1¹². The gas

¹²The introduction of ethanol to the drift chamber gas was part of an attempt to reduce the number of noise hits in the drift chambers, particularly in the inner layers. This, however, was not a sound decision from the standpoint of achieving that goal. While it did confer the benefit of

pressure in the chambers was maintained at about 1 inch of water above local atmosphere to create positive pressure within the chambers, corresponding to a flow rate of approximately 5 L/min.

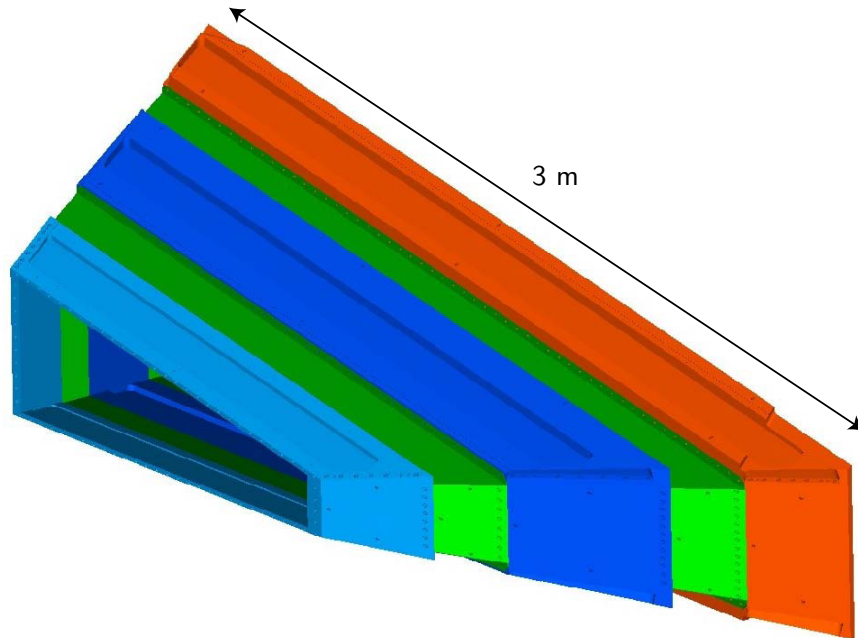


Figure 3-11: An isometric schematic of one of the drift chambers, illustrating how the three frames were assembled to create a single gas volume [38].

Pulse signals from arriving drift electrons on sense wires were first decoupled from the high voltage on the voltage distribution electronics, and then discriminated and amplified on dedicated front-end electronics attached directly to distribution boards on the chambers. The discriminated signals were passed to LeCroy¹³ 1877 multi-hit TDC modules. Conversion of recorded drift times to distances from the wires and the method of reconstructing those distances into trajectories are discussed in Section 4.2.

slowing the drift speed of electrons in the gas (thus increasing the resolution somewhat), ethanol is typically introduced to drift chambers so as to reduce the amount of carbon “whisker” build-up on the wires due to other organic compounds in the drift gas, which can cause dark currents on the signal lines [131]. For an Ar:CO₂ mixture, however, whisker growth is not expected and has not been reported to be observed [132]. Thus, the introduction of ethanol was very unlikely to reduce the level of noise in the OLYMPUS drift chambers, and the instability of the ethanol level certainly was more of a detriment than was balanced by the minor benefit of decreased drift speed.

¹³Teledyne LeCroy, Chestnut Ridge, NY, USA

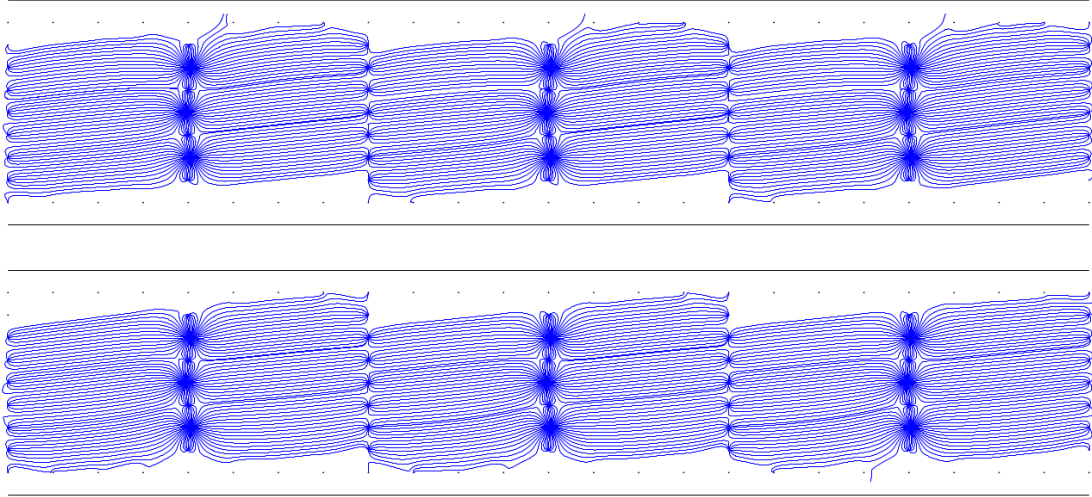


Figure 3-12: A view along the direction of the wires forming the rectangular drift cells, with the lines of electron drift induced in the cells by the voltages on the wires. Note that the lines predominantly tend towards the three sense wires on which signals were recorded. The drift lines are tilted relative to the axes of the cells due to the interaction of the OLYMPUS magnetic field with the drifting electrons, creating a drift component in the direction of $\mathbf{E} \times \mathbf{B}$ [38].

3.5 12° Tracking Telescope Luminosity Monitors

To provide one method of luminosity measurement for the experiment, a dedicated telescope tracking system was developed for the reconstruction of elastic $e^\pm p$ scattering events in which the lepton is scattered with $\theta \approx 12^\circ$. The system tracked leptons independently of the drift chambers, while the drift chamber data were used to reconstruct the corresponding proton near the upper end of the chambers' θ acceptance. Hit positions of passing charged particles were reconstructed in the detector plane elements of the telescope, and these hits were reconstructed to find the particles' trajectories, as described in Sections 5.2.3 and 5.2.4. The system took advantage of the rapid increase of the elastic $e^\pm p$ cross section at small θ to produce a high statistics count of events. Using the system as a luminosity measurement requires the assumption that TPE is small at forward angles, and thus absent this assumption and given another method of normalizing the luminosity between species, the 12° telescopes provide an additional tracking point for the measurement of $\sigma_{e^+p}/\sigma_{e^-p}$ forward of the drift chambers.

Two telescopes were constructed as units and then mounted to the forward side of each of the drift chambers. Each system consisted of three gas electron multiplier (GEM) detectors interleaved with three multi-wire proportional chambers (MWPCs) for tracking, with two scintillator tiles instrumented with silicon photomultipliers (SiPMs), and a Pb glass calorimeter array for triggering. The essential layout of these systems is shown in Figure 3-13, while Figure 3-14 shows a photograph of one of the telescopes with its mounting brackets and readout electronics. Six planes and two detector technologies were utilized to provide high resolution tracking of the high momentum forward events, and to provide a mechanism of cross-checks and calibration within the detector system. Ultimately, the GEM detectors were not used in the final luminosity analysis due to problems with the stability of their efficiencies (see Section 5.2.2), but were useful in the calibration of the system and are being considered for use in future experiments [133,134].

This section describes the essential details of these detector systems, while the luminosity analysis of the elastic $e^\pm p$ scattering events recorded by the 12° telescopes in conjunction with back-angle portions of the drift chamber tracking system is presented in Section 5.2. The value of $\sigma_{e^+p}/\sigma_{e^-p}$ at $\sim 12^\circ$ using alternate luminosity measurements is considered in Section 7.2.1.

3.5.1 Silicon Photomultiplier (SiPM) Scintillator Tiles

The main trigger signals for the 12° telescopes were provided by two $120\text{ mm} \times 120\text{ mm} \times 4\text{ mm}$ scintillator tiles in each telescope, consisting of solid blocks of Eljen¹⁴ EJ-204 plastic scintillator. Charged particles passing through the planes induced scintillation light, which was detected by the instrumentation of the planes to produce a recorded signal. As shown in Figure 3-13, the tiles were placed at the target ends of the telescopes and between the last two tracking planes in each telescope so that they would not be the limiting elements in the acceptance of the detectors. Each tile was instrumented with two Hamamatsu¹⁵ silicon photomultiplier (SiPM) multi-

¹⁴Eljen Technology, Sweetwater, TX, USA

¹⁵Hamamatsu Photonics K.K., Hamamatsu, Japan

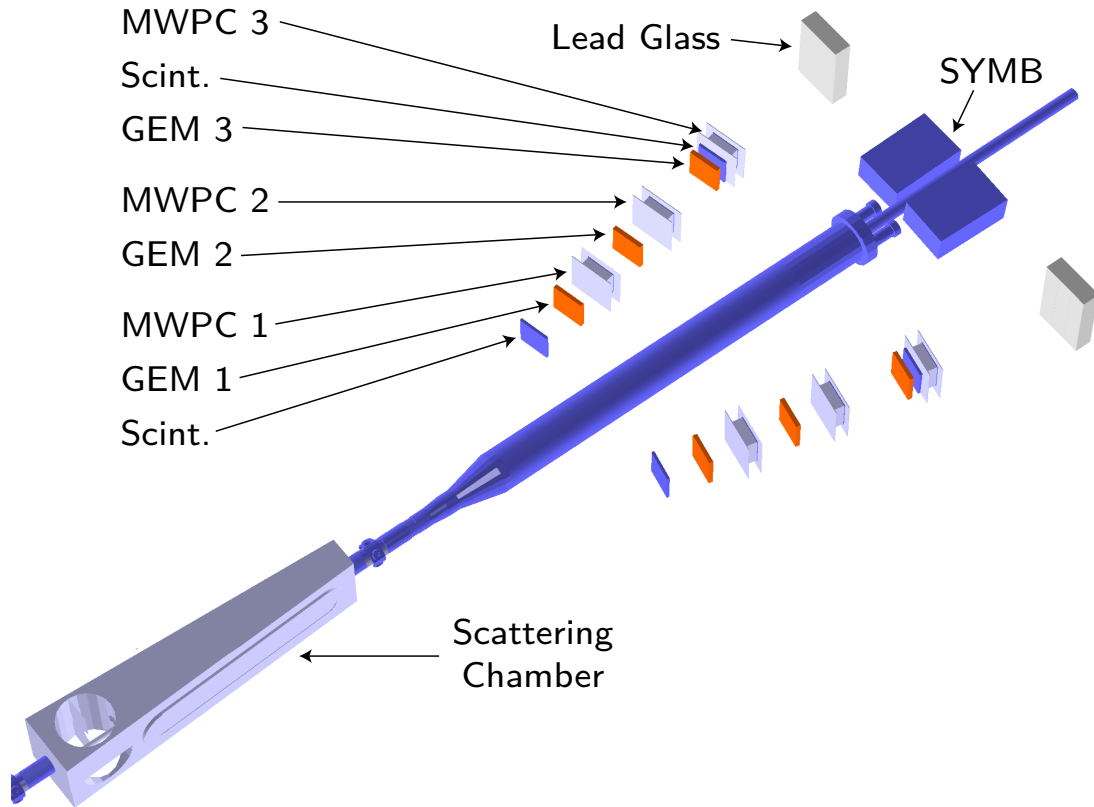


Figure 3-13: Schematic view from above of the forward detector systems, including the 12° luminosity monitor telescopes and Symmetric Møller/Bhabha calorimeter, relative to the target chamber and beamline [38].

pixel photon counters (MPPCs) mounted on opposite sides of the square tiles to homogenize the total recorded light yield across the horizontal acceptance of the tiles. Additionally, each tile was wrapped in Millipore¹⁶ Immobilon-P diffuse reflector to further boost the light yield. Analog signals from the MPPCs in each tile were summed and passed to a constant fraction discriminator to produce the effective fast trigger signal from each tile. Basic parameters of the SiPM tiles and their operation are summarized in Table 3.2.

The operation of the 12° system trigger is described in Section 3.8.2 and the performance of the scintillator tiles is analyzed in Section 5.2.5, but in general the tiles provided a very high efficiency ($>99\%$), uniform trigger for the telescopes throughout data-taking.

¹⁶EMD Millipore, Billerica, MA, USA

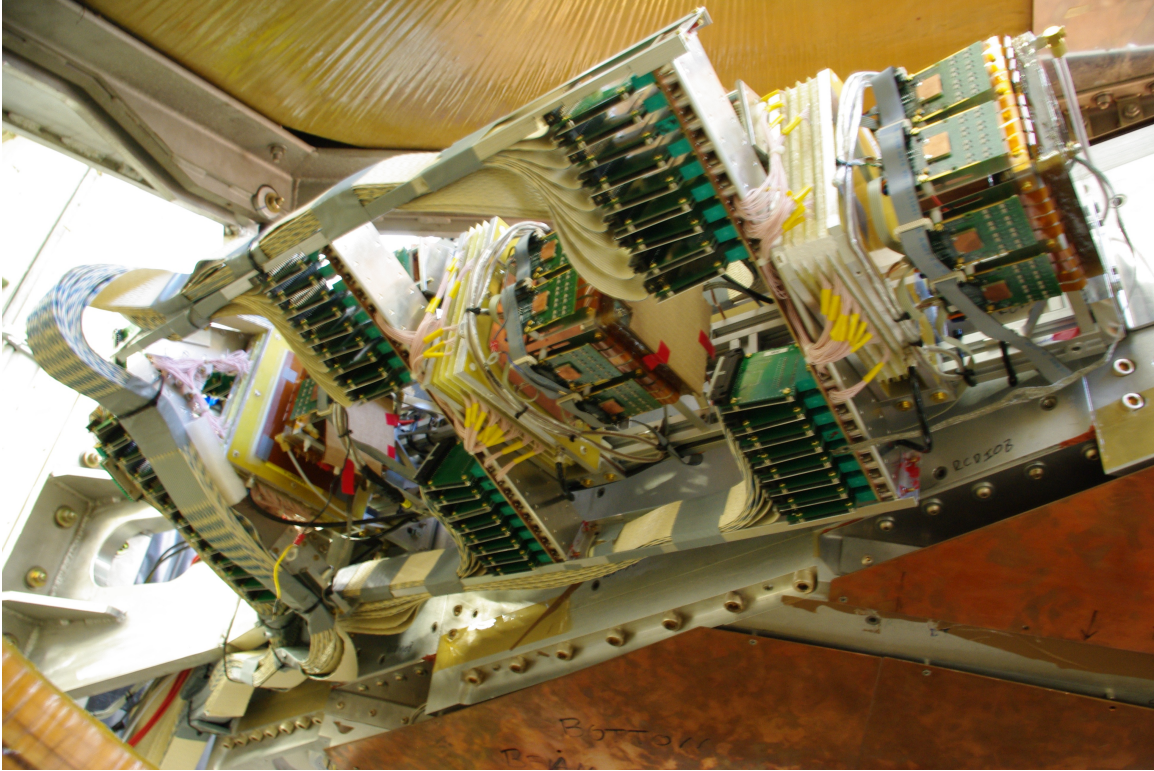


Figure 3-14: Photograph of the right-side 12° tracking telescope, showing the detector elements and their readout electronics [38].

Parameter	Value
Scintillator type	Eljen EJ-204
Size	120 mm × 120 mm × 4 mm
Reflective coating	Millipore Immobilon-P
SiPM type	Hamamatsu S10931-050P (3600 pixels)
Typical gain	$7.5 \cdot 10^5$
Typical bias voltage	72 V
Typical dark count rate	~ 0.8 MHz
Preamplification	25x

Table 3.2: A summary of essential parameters of the SiPM tiles used in the 12° telescope trigger and their operation [135].

3.5.2 Lead Glass Calorimeters

Lead glass calorimeters were mounted to the steel beams of the detector frame behind each 12° telescope to provide an independent trigger for the system for calibration and performance evaluation of the SiPM scintillator tile trigger system. Each calorimeter

consisted of three rectangular prisms of lead glass instrumented with photomultiplier tubes at one end. Particles passing through the 12° telescopes would shower in the steel beam beyond the telescope, and the calorimeters recorded the remnants of this shower exiting the beam as shown in Figure 3-15. The signal from this system was relatively noisy, with a number of events that did not correspond to trackable 12° events, due to the conditions in the detector hall, but the sample was sufficient to evaluate the performance of the SiPM tile trigger, as described in Section 5.2.5.

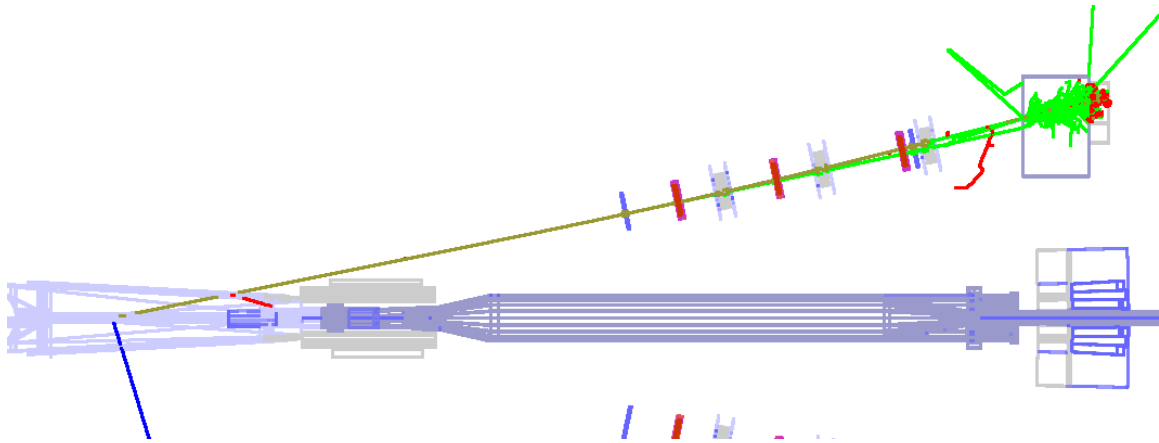


Figure 3-15: Overhead view of a simulated e^+p event in the left 12° telescope, showing the showering in the steel beam behind the telescope (mass of photons in green) and resulting energy deposits from electrons in the penetrating shower (red).

3.5.3 Gas Electron Multiplier (GEM) Detectors

Three of the tracking elements in each telescope were triple gas electron multiplier (GEM) detectors [136]. A relatively new detector technology, a GEM detector amplifies the initial ionization of gas by a charged particle by drifting the ionization electrons towards small holes ($\sim 100\ \mu\text{m}$ diameter) in a copper-coated Kapton¹⁷ foil, which is held at a fixed potential to attract the drifting electrons [57]. The high field gradients in the vicinity of the holes, shown in Figure 3-16, induce an avalanche of secondary electrons to multiply the initial ionization signal by factors on the order of 1000. Several such foils may be stacked together with order millimeter spacing

¹⁷E. I. du Pont de Nemours and Company, Wilmington, DE, USA

and stepped potentials to further multiply the signal while avoiding high potential gradients across the whole detector which could cause unwanted discharge. The final multiplied electron signal is typically collected on a readout plane beyond the final multiplication foil, which is arranged in a pixel or strip layout to provide precise hit position information by leveraging the high statistics of the position distribution of the arriving electrons.

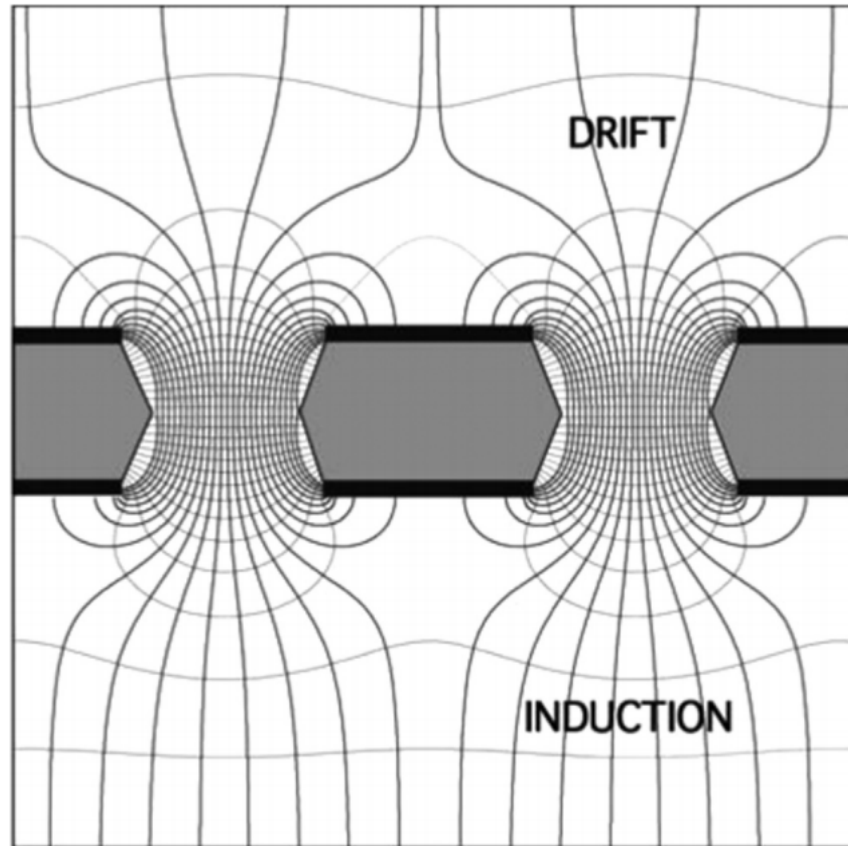


Figure 3-16: Electric field in the vicinity of holes of a GEM foil. Note the high field gradients in the immediate vicinity of the small holes. (Figure reproduced from [136].)

The OLYMPUS GEM detectors were designed at the MIT-Bates Linear Accelerator Center and assembled at Hampton University. Each detector unit consisted of three GEM foils (with the amplification holes) in between a cathode and readout foils. The total active area of each detector was $100\text{mm} \times 100\text{mm}$. The readout board and GEM foils were spaced 2 mm from one another, with a 3 mm gap between the cathode and the first multiplication foil, the arrangement of which is shown in Fig-

ure 3-17. The five foils were enclosed in a pressurized volume filled with a premixed Ar:CO₂ 70:30 gas mixture such that none of the foils were subjected to a pressure gradient that could cause deformation. The GEM foils, manufactured by TechEtch¹⁸, consisted of 50 μm -thick Kapton coated with 5 μm of copper on each side. The holes in the foil were 70 μm in diameter, arranged in a triangular pattern over the entirety of the foil with 140 μm spacing. The readout boards (also from TechEtch) consisted of strips and pads of copper arranged to provide two dimensional information from charge collection on a Kapton substrate. The pattern of strips and pads on a readout foil is shown in Figure 3-18. The pitch of pads/strips along each direction was 400 μm and the relative sizes of the strips and pads was optimized to balance the charge sharing between the strips and pads. Each readout board had 250 strip/pad channels along each of the two plane dimensions.

The signals from the readout pads and strips of a single plane were routed to four readout cards (two per dimension), each with 128 channels (leaving 12 total unused channels on each GEM detector). Each card included an APV25-S1 analog pipeline chip [138], which sampled each of the 128 channels at a 40 MHz rate. When triggered, the pipeline was read out in a single multiplexed data line to the data acquisition system managed by a multi-purpose digitizer (MPD) [139]. The digitizer included VME-based fast ADCs and a field-programmable gate array (FPGA) for the creation and readout of the GEM's data signal.

The analysis of the GEM detector data, including the development of a new dedicated hit-finding algorithm for the detectors, is discussed in Section 5.2. While the GEM detectors were not used in the final analyses of this work (as discussed in Section 5.2.2), an effort was undertaken to understand their output for the purposes of using GEM data for calibration when possible and to facilitate their possible use in future experiments.

¹⁸TechEtch, Inc., Plymouth, MA, USA

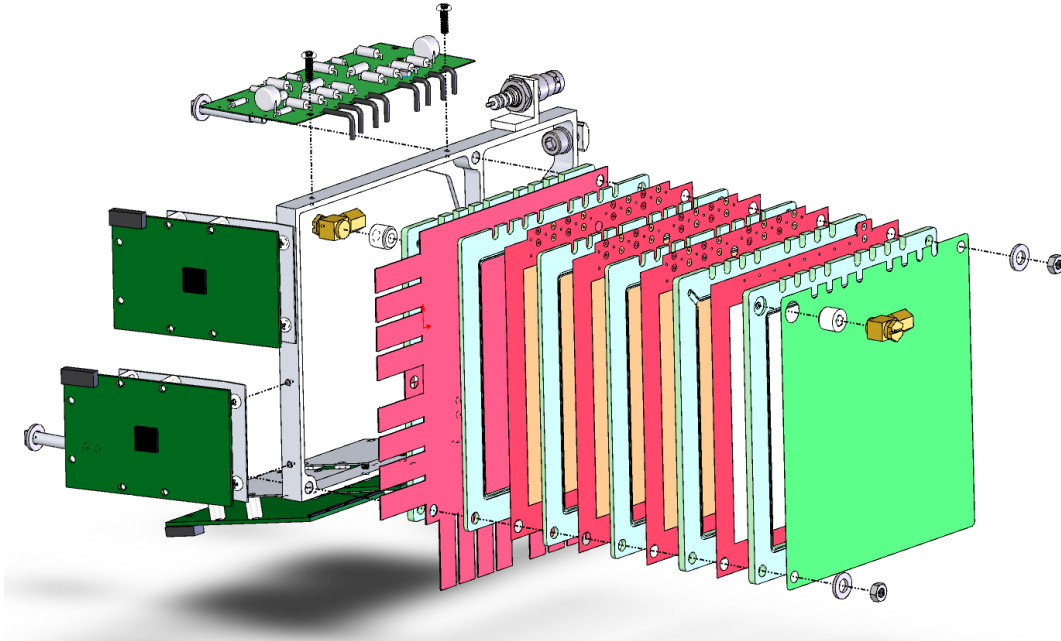


Figure 3-17: Exploded view schematic of one of the OLYMPUS triple-GEM detectors, showing the component layers from the readout electronics and foil on the left, the three GEM foils with their support frames in the middle, and the cathode foil and pressure containment layer on the right [38].

3.5.4 Multi-Wire Proportional Chambers (MWPCs)

The remaining three tracking planes in each telescope consisted of multi-wire proportional chambers (MWPCs), constructed at the Petersburg Nuclear Physics Institute (PNPI). Each detector consisted of three planes of anode sense wires, each with a cathode wire plane on each side at 2.5 mm spacing. Similar to the drift chambers in principle, particles passing through the MWPC planes induced ionization in the gas filling the detectors. This created electrical signals on the sense wires as the electrons and ions drifted towards the wires, which were held at high voltage. For the MWPCs, however, no timing or other signal information was maintained and thus only hit/no hit information was available from each wire. The sense wires in each of the three anode planes were 25 μm in diameter, consisted of gold-plated tungsten, and were spaced by 1 mm along the plane. The cathode wires were 90 μm -diameter beryllium

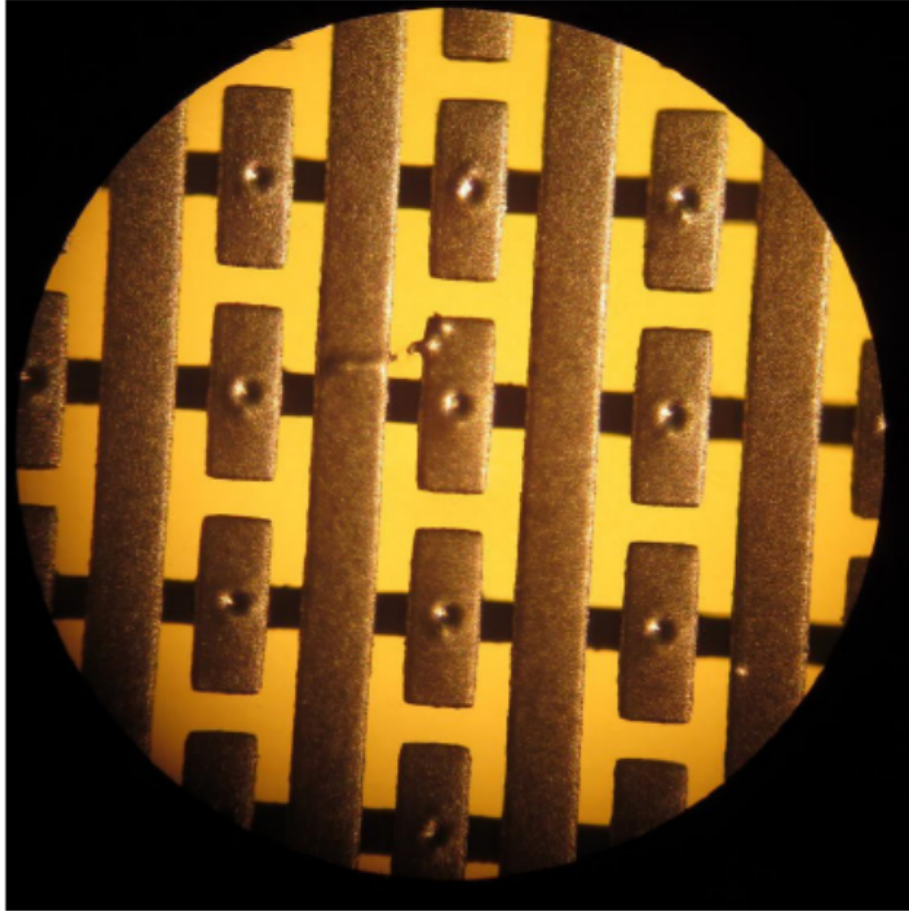


Figure 3-18: Micrograph of the GEM readout plane layout, showing the perpendicular strip/pad pattern with the pads connected by vias beneath the strips. Note the small defect near the center, a repaired short between a pad and strip that was repaired by breaking the connection [137].

bronze wires and were spaced by 0.5 mm. The middle anode wire plane was oriented so that the wires were vertical, while the wires in the other two planes were oriented at $\pm 30^\circ$ from vertical to provide two-dimensional reconstruction information, while prioritizing the resolution in the horizontal position as it was most important to momentum reconstruction. The wires were connected to a CROS-3 readout system, detailed in Reference [140], that interfaced with the main OLYMPUS DAQ.

The anode planes were contained within a pressure volume filled with an Ar:CO₂:CF₄ 65:30:5 mixture to provide the medium for ionization. This gas mixture and the voltage anode plane operation voltage (3200 V) were chosen by consideration of simulations of the detectors using the GARFIELD gas ionization and drift software

package [141] and experience operating similar detectors at the HERMES experiment [142].

Hit information from the MWPCs consisted of “yes/no”-type decisions from the wires in each plane, which limited their resolution but greatly simplified their operation and readout. Combined information from all three planes provide better hit resolution in the horizontal direction and strong noise rejection. The performance of the MWPCs and analysis of their data, including their critical role in the determination of the 12° luminosity estimate, are discussed in detail in Section 5.2.

3.6 Symmetric Møller/Bhabha Scattering Luminosity Monitor

As a second source of luminosity monitoring, OLYMPUS included a forward ($\theta \approx 1.3^\circ$) calorimeter system designed for the detection of symmetric Møller/Bhabha (SYMB) scattering events. The detector was designed to register scattering events involving the atomic electrons of the hydrogen gas in the target and beam leptons in which the outgoing particles scatter at symmetric angles from the direction of the beam. Three principal processes contribute to this measurement between the two beam species:

1. elastic $e^-e^- \rightarrow e^-e^-$ scattering (Møller scattering) [143],
2. elastic $e^+e^- \rightarrow e^+e^-$ scattering (Bhabha scattering) [144], and
3. $e^+e^- \rightarrow \gamma\gamma$ annihilation.

Additionally, and critically to the final method of luminosity determination from this system as described in Section 5.3, the detector also registered the very far forward leptons from $e^\pm p$ events. As particles entered the SYMB detector, they induced Čerenkov radiation, which was detected by the photomultipliers that instrumented the system. At such small θ , the cross sections for this processes are very large (on the order of a barn/sr), and thus the SYMB calorimeter was subject to very high rates.

As such, the detector operated at a much higher rate than the rest of the detector, internally counting events using a digital histogramming system to count events in which energy was registered in one or both sides of the calorimeter. The nature of these histograms and the conditions under which they are filled is described in Section 3.8.3. This section covers the essential details of the SYMB and its operation, while Reference [145] provides a full description of the system. The analysis of the SYMB data and the resulting luminosity estimate is summarized, although not detailed, in Section 5.3.

Figure 3-13 shows the placement of the SYMB system near the beamline and approximately three meters from the target chamber, while Figure 3-19 shows a more detailed schematic of the components of the system. The detectors were constructed at Johannes Gutenberg-Universität using expertise and materials from the A4 experiment [146, 147]. Two calorimeters were constructed, each consisting of a 3×3 array of PbF_2 crystals. Each crystal was approximately $26 \text{ mm} \times 26 \text{ mm} \times 160 \text{ mm}$ in size. In the 3×3 array, the long dimension of the crystals was placed parallel to the direction of incoming particles and corresponded to approximately 15 radiation lengths. The 78 mm square cross section of the array contained approximately two Molière radii [148]. Examples of the crystals and one of the SYMB nine-crystal assemblies are shown in Figure 3-20.

Since PbF_2 is a pure Čerenkov radiator, the response time of the crystals is extremely fast (as there is no scintillation delay), making it an ideal material for a high-rate electromagnetic calorimeter [149]. Millipore reflective paper was wrapped around each individual crystal to increase the contained light yield. Each of the 18 crystals was instrumented with a Philips¹⁹ XP 29000/01 PMT to collect light produced in the crystals, chosen for their fast (20 ns) response time. This response time was the limiting factor in the SYMB operation rate, and thus the detector could operate at up to 50 MHz. Each PMT was connected to a dedicated ADC channel to measure the effective energy deposited for an event. Lead collimators, 100 mm thick with 20.5 mm diameter holes, were placed in front of each array to shield the crystals

¹⁹Koninklijke Philips N.V., Amsterdam, the Netherlands

and define the acceptance for symmetric events. Since the collimator holes defined the acceptance of the calorimeters, they were carefully surveyed.

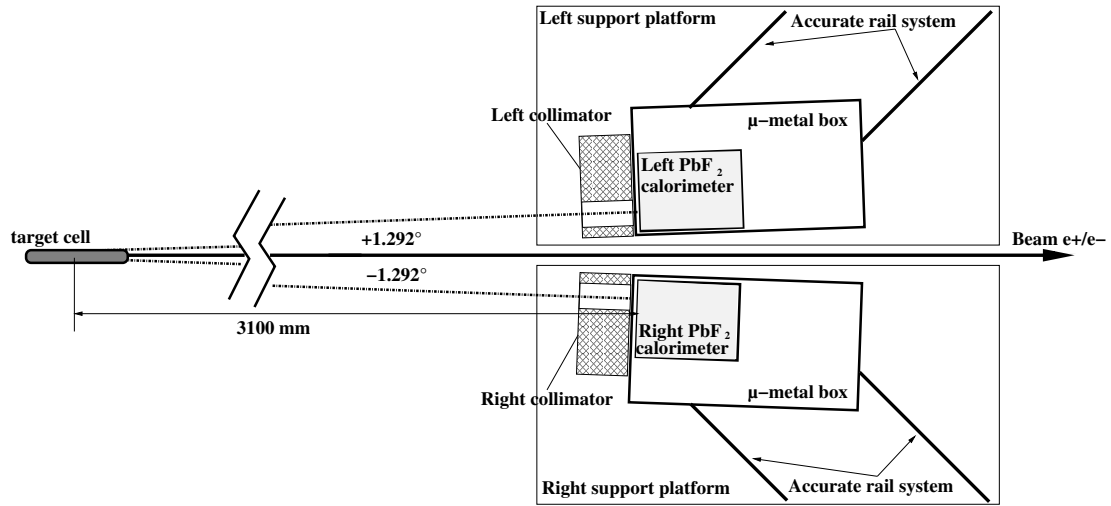


Figure 3-19: Schematic overhead view of the SYMB detector system, showing the approximate placement of the collimators, crystal arrays, and shielding boxes of the detector. Note that the horizontal scale of the figure is broken in the beamline region to illustrate the placement of the detector relative to the target [38].

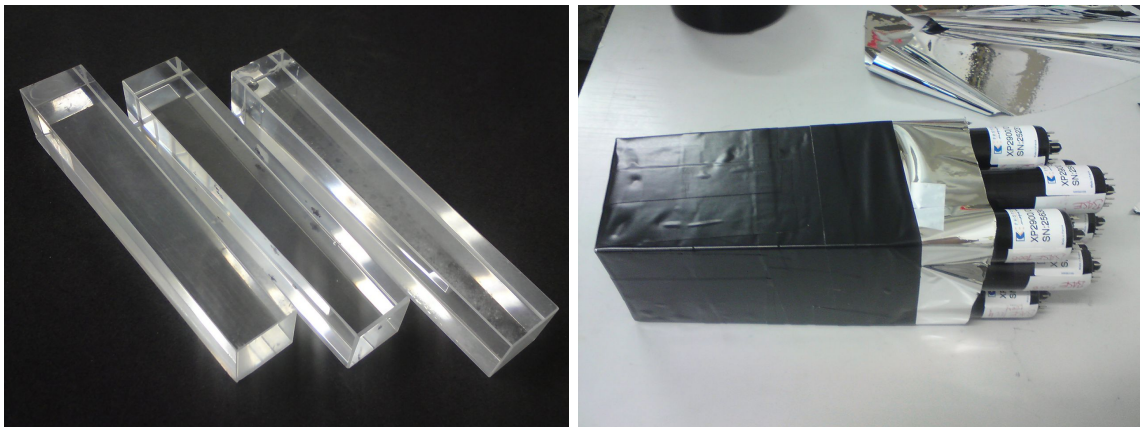


Figure 3-20: Three of the PbF_2 crystals of the SYMB detector (left) and one of the nine-crystal calorimeter assemblies instrumented with PMTs (right) [38].

3.7 Slow Control System

Elements of the experiment slower than the event trigger rate were controlled by a slow control system that monitored, set, and recorded several parameters at all times during the operation of the experiment. These parameters included voltages set via communication with high voltage supplies, temperature readings, the target gas supply system settings, DORIS beam parameters, and a variety of other settings. The software linking the slow control system to the hardware elements of the experiment was implemented using the Experimental Physics and Industrial Control System (EPICS) [150]. In addition to the EPICS system, a server was implemented for the system in Python using the FLASK micro-framework²⁰. Finally a JavaScript- and HTML-based graphical interface for this server provided the ability to control the system from any computer with secure access to the internal network at DESY (and appropriate logins for the OLYMPUS system). The software was run on three dedicated Linux VME computers, with appropriate interface cards for the various hardware elements of the experiment. The user interface included the ability to change settings such as voltages, gas flow, vacuum controls, etc., real-time plots and warnings regarding the operational conditions of the detector and beam, as well as a variety of presets for all parameters appropriate for different running conditions. This made the experiment easy to monitor and operate, not only from the control room at DORIS (which was staffed at all times during the experiment), but from anywhere with Internet connectivity. Additionally, the slow control continuously sampled readout information from various systems and recorded these in a PostgreSQL database, which was properly synced with the data acquisition system to associate the history of the readout with the recorded detector data.

3.8 The OLYMPUS Trigger and Readout

The relatively high luminosity associated with the fixed-target nature of the OLYMPUS experiment, in conjunction with the fact that a complete detector readout re-

²⁰<http://flask.pocoo.org/>

quired much more time (~ 0.1 ms) than the beam bunch spacing, required the experiment to employ a trigger system to select events of interest for readout from the fast detector system information of the experiment and reject events that would not correspond to elastic $e^\pm p$ events. The primary trigger signals were the discriminated signals from the ToF scintillators and the 12° telescope scintillators, although information from the drift chambers, lead glass calorimeters, and DORIS accelerator information also contributed to the system. Notably, the DORIS bunch clock provided the reference time signal for the ToF and drift chamber TDCs. When a trigger condition was met, information from all relevant detector channels was read out and the system was gated (i.e., prevented from collecting further events) until the readout was complete. The time the trigger was closed for readout amounted to “dead time”, which was typically $\sim 30\%$ during normal OLYMPUS operation. Thus, in order to maximize the usefulness of the dataset, the trigger was implemented to increase the fraction of recorded events that included reconstructible elastic $e^\pm p$ events, while simultaneously providing a sufficient number of events for various testing and calibration purposes.

In addition to the main trigger, which focused on selecting elastic $e^\pm p$ events, a number of other triggers provided more open configurations at a prescaled rate. The trigger was implemented using a VME FPGA, which permitted the combination of up to 16 fast input signals to produce up to 16 output trigger conditions in parallel that could be passed to the data acquisition system. Additionally, each of the output conditions could be prescaled to reduce to the rate at which an individual condition produced a detector readout below the natural rate of occurrence for that condition. This was useful for certain test trigger conditions, which would have dominated the data sample without prescaling. The critical elements of the trigger system and conditions are described in the following subsections.

3.8.1 Main Kinematic Trigger and Second-Level Drift Chamber Trigger

The main OLYMPUS trigger combined information from the ToF scintillators and the drift chambers to produce events with an enhanced purity of elastic $e^\pm p$ events. The basic trigger condition required that a ToF bar on each side of the detector recorded a hit (defined as coincidence between the top and bottom PMTs of each bar), such that the left and right bar pairing corresponded to a conceivable left/right pairing for the kinematics of elastic scattering from the gas target. The map of such allowed pairings is shown in Figure 3-21. The allowed left/right pairings were determined by Monte Carlo simulation of both e^-p and e^+p events. All pairings that occurred for elastic events in the simulation of either species were allowed for all runs, and an additional buffer of one bar on each side of the allowed block of bars on the opposite side corresponding to a specific bar was added to avoid rejecting good elastic $e^\pm p$ events. The primary advantage of this system was that it disallowed events that paired very forward bars on each side, since these bars had the highest hit rates but kinematically could not correspond to elastic events. This trigger was not prescaled (i.e., it was allowed to induce data readout at its natural rate of occurrence).

Additionally, during Run I it was determined that the restrictions of the kinematic left/right ToF pairings in the trigger still resulted in a high number of events with insufficient data in the drift chambers to permit reconstruction. Thus, for the primary production run, a “second-level” trigger element was added to the main trigger which required that at least one wire in each of the middle and outer drift chamber regions on each side recorded a good time for an event to be accepted. Since events without such information could not be reconstructed anyway, this condition did not reject any events that could be considered part of the final data sample. The condition reduced the false trigger rate due to ToF noise, beam hall radiation conditions, etc. by approximately a factor of ten, which greatly improved the dead time of the experiment to allow a much higher efficiency of luminosity collection.

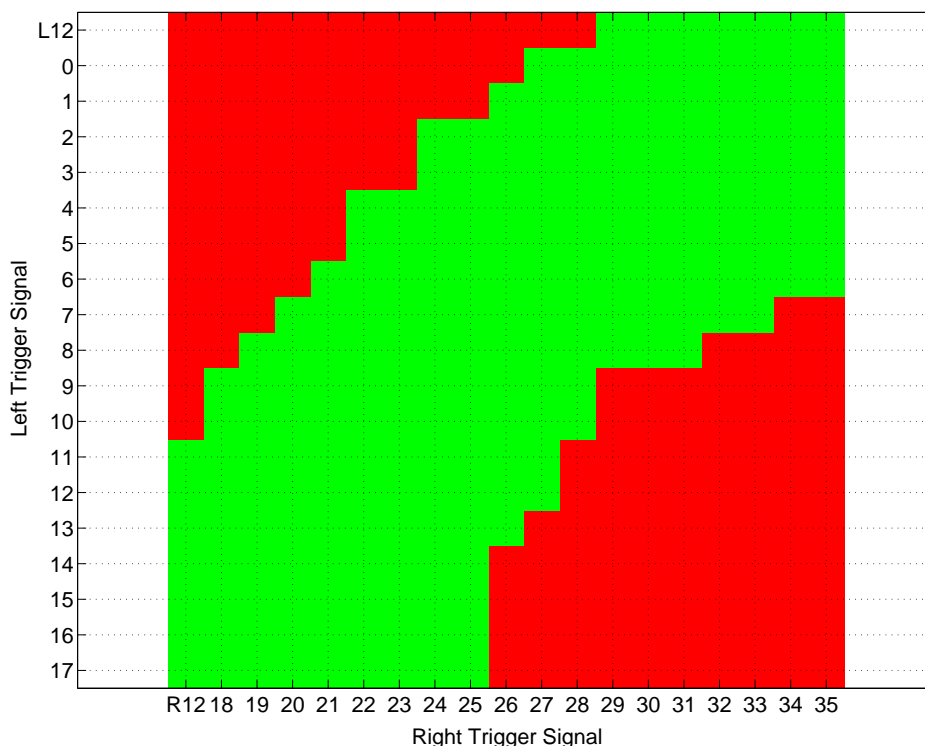


Figure 3-21: Map of the corresponding left and right fast trigger signal pairs from the OLYMPUS ToF bars (labeled by index) and 12° telescope scintillators (labeled L12 and R12, for left and right) that would result in a detector readout (green) versus event rejection (red) for the main kinematic and 12° luminosity triggers. This configuration was used for the majority of production data-taking runs.

3.8.2 12° Telescope Trigger

The second primary element of the trigger system was the dedicated trigger for the 12° telescopes, which required the coincidence of both SiPM scintillator tiles (Section 3.5.1) in one of the 12° arms and a ToF hit (top/bottom PMT coincidence) in one of the back seven bars on the opposite side. These conditions are shown as “L12” and “R12” in Figure 3-21. This trigger was also not prescaled so as to produce the highest possible statistics for the 12° elastic $e^\pm p$ luminosity measurement. The system could also be triggered using the lead glass calorimeters mounted behind the telescope, although this trigger was prescaled due to its high rate of undesired events and was used predominantly for measurement of the SiPM tile efficiencies (Section 5.2.5).

3.8.3 SYMB Readout

The readout of the SYMB calorimeter was handled independently of the main trigger system due to the way in which the SYMB detector produced digital histograms of events internally. More detail on this system may be found in Reference [145]. The detector was designed to rapidly sum the light yield in the nine crystals on each side of the calorimeter, apply basic conditions to the recorded yield in each side, and then record the event in a digital histogram if all conditions were met. Each digital histogram was essentially a 2D histogram of the energy recorded by each side of the detector system (represented by the total ADC count). The readout system was based on the similar system used for the A4 experiment, where the crystals used in the SYMB detector were originally designed and used [146, 147]. The detector could operate at a rate up to 50 MHz, which was predominantly limited by the 20 ns response time of the PMTs used to instrument the PbF_2 crystals. Two basic conditions were applied to the SYMB PMT signals to generate a readout in the digital histograms:

1. that the total energy deposited in the nine crystals of one of the calorimeters exceeded a given threshold, and
2. that the central crystal of the array meeting the threshold requirement have the largest recorded energy deposition of the nine (the “local max” requirement).

If either side of the detector met these requirements, both sides were read out to fill either the left- or right-master histogram depending on which side met the conditions. If both sides simultaneously met the conditions, the coincidence histogram was filled. These histograms were filled at a rate much higher than the main trigger rate, and thus the data acquisition system did not record the histograms on an event-by-event basis. Instead, the integrated histograms were read out approximately every 70,000 events (or at the end of a run) to limit the readout time spent on SYMB data acquisition.

3.8.4 Additional Triggers

Other triggers used during the experiment, typically designed to provide information for tests, calibration, etc. for the detectors, were prescaled to reduce their rate of occurrence in the dataset or were used for occasional dedicated tests runs. Such triggers included:

1. conditions involving looser requirements on combinations of ToF hits, including allowing hits with only one PMT firing in a bar (either with or without a coincident hit in the opposite side of the detector), useful for calibration of the ToFs,
2. triggers allowing the readout of the 12° telescopes with only registered SiPM or lead glass hits (i.e., with no requirement of a ToF bar),
3. a “clock” trigger for random readout of the detector, and
4. dedicated triggers for recording of cosmic ray events or other special event topologies.

Such triggers will be described as necessary in the description of any calibrations for which they were used. In general, these special triggers were employed with varying prescale factors throughout the experiment, but the main triggers (the kinematic and SiPM tile 12° trigger) were run without prescaling for all data production runs.

3.8.5 Readout

The readout system was implemented by the Universität Bonn group, based on experience developing similar systems for operation of the ELSA accelerator and its experiments [121, 151]. The system ran on VME CPU modules, and operated as a “synchronous system”; when a trigger occurred all detectors were read out simultaneously and no further triggers were accepted until the readout was complete. While such a system increased the dead-time of the experiment (the fraction of the running time in which the trigger was gated and events were not accepted), the advantage of

avoiding possible synchronization of data errors was judged to be of sufficient benefit to the experiment to justify the increased dead-time. The readout systems for the detectors were arranged in a master-slave architecture, in which a master module managed a number of slave modules responsible for interaction with particular systems and handled the gating of the trigger until all slave modules completed their readout. The data acquisition system collected all relevant detector readout data for a given event (ADC counts, TDC counts, slow control parameters, etc.), and produced an output ZEBRA format file [152]. This ZEBRA file was then converted to a ROOT tree format to facilitate easier access to the data [52]. More information on this system can be found in References [38] and [151].

3.9 Experiment Operation

During data-taking, a two or three person team operated the experiment 24 hours a day from the control room in the DORIS ring building, which was shared with the DESY accelerator operators to facilitate communication between the OLYMPUS and accelerator operators. The OLYMPUS shift crew was responsible for operating the slow control system and monitoring its various readouts, as well as continuously monitoring the data using low-level analysis that was conducted as data were taken. A dedicated run plan dictated the configuration of the beam, detector, etc., to maintain stable running during the main production periods. The experiment collected approximately 4.5 fb^{-1} of data during Run II (which comprises the data set for this work), of which approximately 3.1 fb^{-1} is considered excellent data in which the configuration and condition of the detector were optimal. It is this latter dataset that is used in this work for the analyses presented, although at a later date an effort may be made to include portions of the data not used. The collection of luminosity over time for Run II is shown in Figure 3-22.

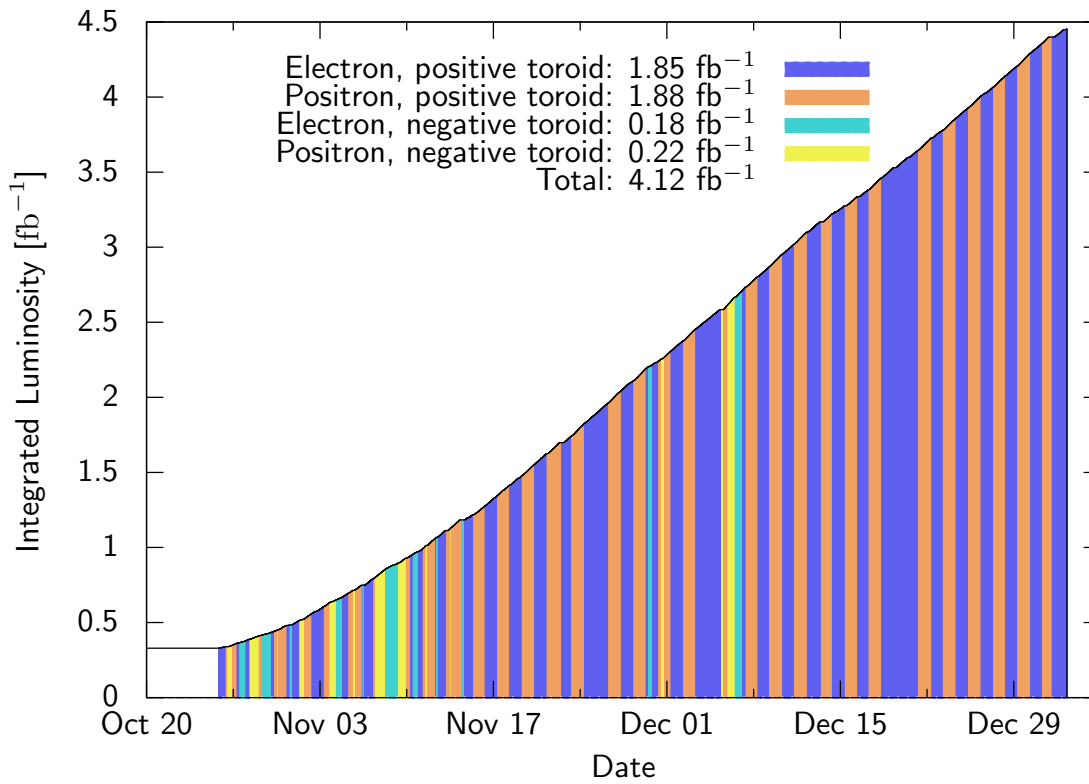


Figure 3-22: The integrated luminosity collected by the experiment, as measured by the slow control (Section 5.1), during the second OLYMPUS run, separated by the various beam/toroid configurations [38].

Chapter 4

Analysis Strategy, Detector Calibration, and Monte Carlo Simulation

In the original design of the OLYMPUS experiment [120], the plan for the operation and analysis of the experiment involved regularly switching the polarity of the toroidal magnet and computing $R_{2\gamma}$ as a super-ratio of the experimentally measured elastic event counts $N_{e^\pm p, \pm B}$ in the four combinations of species and toroid polarity, normalized to the luminosity collected for each orientation:

$$R_{2\gamma} = \frac{\sigma_{e^+p}}{\sigma_{e^-p}} \approx \sqrt{\frac{N_{e^+,+B}N_{e^+,-B}}{N_{e^-,+B}N_{e^-,-B}} \cdot \frac{\mathcal{L}_{e^-,+B}\mathcal{L}_{e^-,-B}}{\mathcal{L}_{e^+,+B}\mathcal{L}_{e^+,-B}}}. \quad (4.1)$$

Measuring $R_{2\gamma}$ using the method of Equation 4.1 confers several advantages, primarily relating to the cancellation of systematic effects due to the differences in the relative acceptance of e^+p and e^-p events due to physical detector bounds and detector efficiency. This cancellation occurs due to the fact that an e^+p event of given kinematics traversing the detector in positive field polarity take the same path through the detector as an e^-p event with the same kinematics in negative polarity (and vice versa), while two such events in traversing the detector in the same field polarity take slightly different paths through the system due to their opposite bending, and thus

are subject to different acceptances, detection efficiencies, etc. Since the acceptance of the OLYMPUS detector for exclusive $e^\pm p$ events is primarily dominated by the acceptance of the lepton, the slight difference in proton acceptances for $e^- p$ and $e^+ p$ events of the same vertex kinematics that does not cancel between the field polarity configurations was expected to be negligible.

This approach, while ideal in principle, suffers from a number of complications that make it impractical:

1. In the negative field polarity Møller scattering electrons are swept into the first layers of the drift chamber tracking system, causing a saturation of certain regions of the detector and spoiling the cancellation of tracking efficiency between the two polarities, as described in Section 3.4.1.
2. The reversal of the magnetic field reverses the direction of the $\mathbf{E} \times \mathbf{B}$ ionization electron drift in the drift chambers, significantly changing the calibration of recorded drift time-to-distance (TTD) from the wire at which a particle passed. This required change in detector calibration between polarities again spoils the ideal cancellation of efficiencies. See Figure 3-12 for an illustration of the effect on the drift lines and Section 4.2.1 for a description of the TTD calibration.
3. The negligibility of the different acceptance for protons from $e^+ p$ and $e^- p$ events of the same kinematics in opposite toroid polarities depends on having uniform efficiency for track reconstruction throughout the acceptance. As will be discussed in Section 6.1, this was not the case for OLYMPUS (and would likely be an impractical requirement due to the small likelihood of individual channels, voltage supplies, etc. in a 954-channel system performing identically).

For these reasons, it was determined that OLYMPUS could achieve better systematic uncertainties by taking data with a single toroid polarity setting, and making a detailed effort to properly account for the acceptance differences of $e^- p$ and $e^+ p$ events in simulation.

Conducting a measurement of $R_{2\gamma}$ based on Equation 1.1 demands careful consideration of all aspects of the detector system and the analysis that affect the relative

acceptance of e^-p and e^+p events and proper implementation of such effects in the Monte Carlo simulation. This chapter describes the essential strategy used in the OLYMPUS analysis to achieve this goal, including essential information on detector survey and calibration, a brief introduction to event reconstruction in the main spectrometer, and a description of the advanced Monte Carlo simulation employed in the analysis. Chapters 5 and 6 provide more detailed information on the specifics of the luminosity and main cross section ratio analyses, including the measurement and simulation implementation of effects such as detector efficiencies, resolutions, etc. for individual detector systems.

4.1 Calibration of the Spectrometer Position and Magnetic Field

Due to the fact that OLYMPUS operated using a single field polarity, knowledge of the positions of the detectors, their solid angle coverage, and the magnetic field throughout the detector volumes was crucial to properly determining the acceptance of the OLYMPUS detector for e^+p and e^-p events. The acceptance of the detector was determined by careful survey of both the detector positions and the magnetic field, and great care was taken to properly represent the results of these measurements in the representations of the detector system used for the Monte Carlo simulation and particle track reconstruction. This section describes the essential methods of the position and field surveys and their implementations in the OLYMPUS analysis.

4.1.1 Detector Position Survey and Modeling

The primary optical surveys of the detectors, target chamber, and beamline elements were conducted by the DESY survey and alignment group (MEA2) [153]. The surveys were conducted using a laser tracker system, which provided precise measurement of a polar and azimuthal angle relative to the mounted position of the tracker and a laser-ranged distance from the tracker to reflective prism targets placed on all elements

of the detector, beamline, support frames, detector hall walls and floors, etc. The position of the laser tracker relative to the center of the OLYMPUS coordinate system (Section 3.1) could be reconstructed via measurements of known points throughout the detector hall, which were conducted regularly throughout the survey and anytime the laser tracker was moved. This allowed reconstruction of any measured point in the OLYMPUS coordinate system from the information provided by the laser tracker. All detector elements, the target chamber, and beamline elements were surveyed at least twice: once in late 2011 prior to Run I and again after Run II in Spring 2013. Certain individual detector elements were surveyed more frequently in the interim to check for shifting positions.

Physical objects that were part of the detector, target system, beamline, etc. were modeled for the analysis using Geometry Description Markup Language (GDML), an XML-based language for the description of geometries that is compatible with both the ROOT and GEANT4 frameworks [52, 154, 155]. This allowed the use of a single geometry model in all OLYMPUS analysis applications (simulation, track reconstruction, visualization, etc.), greatly reducing the possibility of geometric errors in the analysis. The solid models of experiment elements in the geometry model were constructed on the basis of both survey data and original design specifications for the elements. The placement and orientations of the elements in the geometry were determined from the survey data. The survey data were converted to coordinates in the OLYMPUS global coordinate system, and a global fit was performed for the corresponding points on the modeled detector elements to determine their positions and rotations. Redundancy and overdetermined placements in the survey dataset allowed for the identification and removal of inconsistencies and erroneous survey data. The final survey fit provided accurate placement of objects in the solid model to better than 100 μm for most elements, although some elements with less-determined survey data (such as the GEM planes) had slightly higher uncertainties [156]. Complete details on the implementation of the OLYMPUS solid model may be found in Reference [55].

4.1.2 Beam Position

At all times during OLYMPUS data-taking, the position of the DORIS beam was monitored by two beam position monitors (BPMs), placed slightly upstream and downstream of the target chamber along the beamline. This provided a measurement of the central position of the DORIS beam at two points near the OLYMPUS target with an uncertainty of $\sim 100\ \mu\text{m}$. The high degree of precision was obtained by conducting a detailed survey of the positions of the BPMs, as described in the previous section, and then performing a series of calibration measurements after they had been removed from the beamline [157]. The calibration was conducted by mounting the BPMs with a current carrying wire passed through them which simulated the beam current. The position of this wire was varied and the BPM readout was matched to the surveyed position of the wire. The wire position was varied well beyond the range of beam positions that occurred during OLYMPUS data-taking, but measurements were focused on the regions most relevant to the experimental conditions. The surveyed wire positions were fitted in a similar fashion as the detector survey data so as to produce a mapping between the BPM readout data and beam positions in the OLYMPUS global coordinate system. Additional tests, such as reversing the direction of current in the wire, were conducted so as to simulate the oppositely-charged beam species to provide estimates of systematic effects.

4.1.3 Magnetic Field Survey and Modeling

Since electrons and positrons bend in opposite directions in a magnetic field, precise knowledge of the OLYMPUS magnetic field was critical to determining the detector acceptance for implementation in the simulation and tracking. To achieve this, a detailed survey of the OLYMPUS magnetic field was conducted in situ before moving the toroid coils after the experiment. The detector elements (chosen to be non-magnetic and thus neither influence or be influenced by the field) were removed, permitting access to probe all areas within the volumes corresponding to the detector acceptance. This effort is described in detail in References [128] and [53], but is briefly

summarized here.

The measurement was conducted by constructing a system in which a three-dimensional Hall probe was mounted to a system of translation tables and support brackets that allowed movement of the probe throughout the volume relevant to OLYMPUS track trajectories, from the target chamber to the locations of the ToF scintillators (the outermost detectors). Positions were systematically scanned in 50 mm steps in the inner tracking region (which affects trajectories most strongly) and 100 mm steps in the outer region in all three spatial dimensions. Approximately 36,000 points were surveyed. During this survey, the position of the Hall probe was constantly monitored using a system of theodolites so that its position at each measurement point could be reconstructed. After the measurements were performed, a fitting procedure similar to that used for the detector elements was used to reconstruct the probe positions corresponding to the field measurements.

Since the implementation of the field for tracking and reconstruction requires knowledge of the field at all locations (rather than a grid of points), a model was developed to compute the field at any location in the detector system. This model consisted of approximating the OLYMPUS toroid coils as filaments and computing the field due to the current using the Biot-Savart law. This allowed the computation of the magnetic field at arbitrary location and additionally provided the capability of numerically computing the spatial derivatives of the field components. The placement of the toroid coils in the model was determined by initially allowing their positions to float and fitting their positions and rotations so as to best fit the survey data position/field points. This fit achieved an average residual of 18.7 G, and was in general much better throughout the critical tracking volumes. The coil model, however, was not a good approximation near the coils (where the approximation of modeling the toroid elements as thin filaments broke down) and thus the field was interpolated directly from the data in such regions.

The model calculation, however, was too slow to be used directly for simulating or reconstructing particle trajectories for the OLYMPUS analysis, and so a

fast and precise interpolation scheme was developed¹. The coil model was used to pre-calculate the magnetic field vector and its spatial derivatives on a regular 50 mm × 50 mm × 50 mm grid covering the entire spectrometer volume, so that the field could be interpolated between surrounding grid points.

The interpolation scheme had to balance several competing goals:

- minimizing the memory needed to store the field grid,
- minimizing computation time for field queries, and
- faithfully reproducing the coil model in both the field and its derivatives.

To achieve this, an optimized tricubic spline interpolation scheme was developed based on the routine of Lekien and Marsden [158]. For each point P in the grid, 24 coefficients were calculated using the coil model (8 per component of the vector magnetic field):

$$C_{i,P} = \left\{ B_i, \frac{\partial B_i}{\partial x}, \frac{\partial B_i}{\partial y}, \frac{\partial B_i}{\partial x \partial y}, \frac{\partial B_i}{\partial z}, \frac{\partial B_i}{\partial x \partial z}, \frac{\partial B_i}{\partial y \partial z}, \frac{\partial B_i}{\partial x \partial y \partial z} \right\}$$

for $i \in \{x, y, z\}$. (4.2)

For the interpolation, it is convenient to consider the grid in terms of boxes defined by eight grid points, as shown in Figure 4-1, and define box-fractional coordinates $x_f, y_f, z_f \in [0, 1]$ parallel to the global axes spanning each box. Each point in the grid is labeled with an integer index j , such that stepping from point P_j one unit in x reaches point P_{j+1} . Stepping one unit in y from point P_j reaches P_{j+n_x} , where n_x is the size of the grid in the x direction. Stepping from point P_j one unit in z reaches point $P_{j+n_x n_y}$, where n_y is the size of the grid in y direction. Then, a local tricubic spline can be defined for each field component in the box:

$$B_i(x, y, z) = \sum_{l,m,n=0}^3 a_{i,lmn} x_f^l y_f^m z_f^n \quad i \in \{x, y, z\}, \quad (4.3)$$

¹The remainder of this section is predominantly reproduced from Reference [128], which was written by and describes the work of the author.

where the coefficients $\{a_{i,lmn}\}$ are functions of the set of the 64 parameters $\{C_{i,P}\}$, where P is any of the eight grid points at the vertices of the box. This function is a 64-term polynomial for each box and is C^1 at the box boundaries. The coefficients $\{a\}$ can be computed from the parameters $\{C_{i,P}\}$ following the prescription in Reference [158]. This prescription, however, requires three 64×64 matrix multiplications per box. Once completed for a given grid box, these multiplications can be stored for future use, but this adds to the size of the grid in memory, approaching a factor of 8 for large grids.

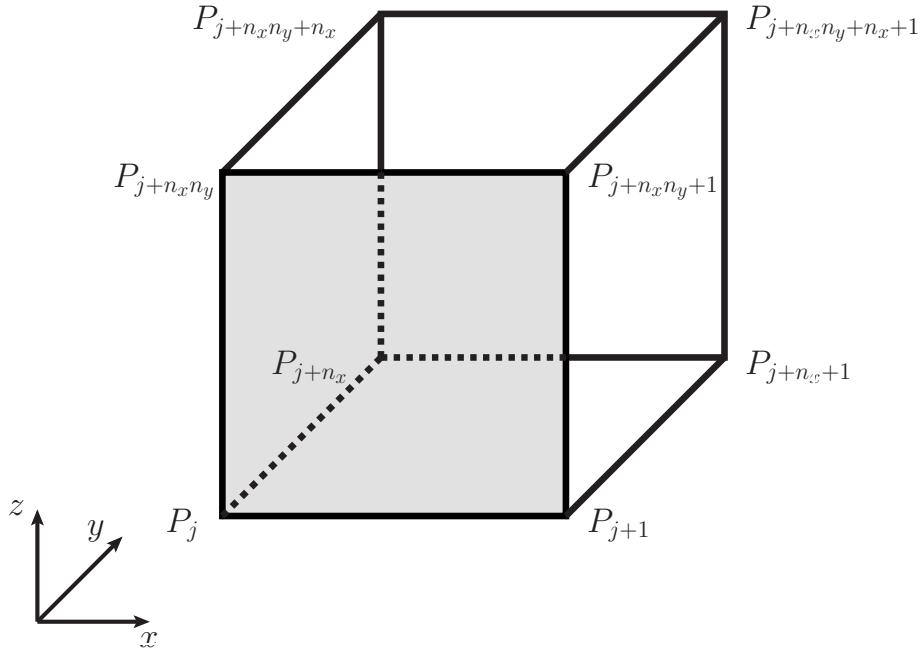


Figure 4-1: A generalized box in the interpolation grid identified by its lowest-indexed grid point P_j , where n_x and n_y are the x and y dimensions of the grid in units of grid points.

To avoid these costs, the spline was refactored so that the parameters $C_{i,P}$ can be used directly as coefficients. The resulting basis functions take the form:

$$f_0(x_i) = (x_i - 1)^2 (2x_i + 1) \quad (4.4)$$

$$f_1(x_i) = x_i (x_i - 1)^2 \quad (4.5)$$

$$f_2(x_i) = x_i^2 (3 - 2x_i) \quad (4.6)$$

$$f_3(x_i) = x_i (x_i - 1) \quad (4.7)$$

where $i \in \{x_f, y_f, z_f\}$. The interpolation then takes the form:

$$B_i(x, y, z) = \sum_{l,m,n=0}^3 b_{i,lmn} f_l(x_f) f_m(y_f) f_n(z_f) \quad i \in \{x, y, z\}, \quad (4.8)$$

where each coefficient $\{b_{i,lmn}\}$ is one of the parameters $C_{i,P}$. The correspondence between $\{b_{i,lmn}\}$ and $C_{i,P}$ is shown in Table 4.1.

	B_i	$\frac{\partial B_i}{\partial x}$	$\frac{\partial B_i}{\partial y}$	$\frac{\partial B_i}{\partial x \partial y}$	$\frac{\partial B_i}{\partial z}$	$\frac{\partial B_i}{\partial x \partial z}$	$\frac{\partial B_i}{\partial y \partial z}$	$\frac{\partial B_i}{\partial x \partial y \partial z}$
P_j	000	100	010	110	001	101	011	111
P_{j+1}	200	300	210	310	201	301	211	311
P_{j+n_x}	020	120	030	130	021	121	031	131
P_{j+n_x+1}	220	320	230	330	221	321	231	331
$P_{j+n_x n_y}$	002	102	012	112	003	103	013	113
$P_{j+n_x n_y+1}$	202	302	212	312	203	303	213	313
$P_{j+n_x n_y+n_x}$	022	122	032	132	023	123	033	133
$P_{j+n_x n_y+n_x+1}$	222	322	232	332	223	323	233	333

Table 4.1: Mapping of the coefficients $\{b_{i,lmn}\}$ (defined in Equation 4.8) to the field values and derivatives at the grid points contained in the box with lowest-indexed point P_j . Entries in the table are the values of lmn corresponding to each combination of point and coefficient on the interpolation box.

With this interpolation scheme, the procedure for querying the field map consisted of determining the grid box containing the queried point, computing the box fractional coordinates of the queried point in that box, and then applying the tricubic spline interpolation for each of the three field components independently. Special care was taken to optimize the speed and number of arithmetic operations in the routine (e.g., by pre-computing factors such as the basis functions that are used repeatedly and by converting division operations to multiplications whenever possible). Additionally, the coefficients for each grid point were arranged in a single array so that, for any box in the grid, the 192 coefficients associated with the 8 points of the box occurred in 16 continuous blocks of 12 coefficients, permitting rapid reading of the entire array and facilitating single instruction, multiple data (SIMD) computing, further increasing the speed of field queries. This scheme provided a precise and fast field implementation for the detector model for both simulation and track reconstruction.

4.2 Event Reconstruction

For exclusive elastic $e^\pm p$ event reconstruction, data were combined from the drift chambers and ToF scintillators, in conjunction with the trajectory bending caused by the magnetic field, to provide complete reconstruction of particle trajectories (the event vertex and momentum vector at the vertex). While track reconstruction algorithms for these detectors existed from the BLAST experiment [159], OLYMPUS operated with higher particle energies, different background conditions, different drift gas properties, and more demanding precision goals than BLAST. Thus, required new tracking algorithms were required.

In essence, track reconstruction in the OLYMPUS detector amounted to finding the best solution for a particle trajectory given a set of loci that is derived from data from the drift chambers and time-of-flight scintillators given the knowledge of the magnetic field throughout the volume of the detector. The locus of points corresponding to a ToF hit consisted of a horizontal band of points across a bar with a good top-bottom PMT hit combination, reconstructed from the time difference of the hits in the top and bottom PMTs of the bar. These ToF hits were relatively low resolution ($\sigma \approx 10$ cm in the vertical direction and limited to width of the bar in the horizontal direction), but provided valuable information when properly weighted in the track reconstruction. The locus of points from a wire chamber hit consisted of two lines parallel to the wire with a valid time recorded, approximately equidistant from the wire in the plane parallel to the wire chamber faces. The locus consisted of two lines due to ambiguity of a single time in representing a hit that passed either upstream or downstream of the wire. This ambiguity was resolved for each wire hit through a combination of the 0.5 mm stagger between successive wire planes, use of hits in adjacent cells to limit a track location, and global fit information. The conversion of the drift time recorded on a wire to the distance of the locus from the wire is in general a complicated problem, and is discussed in the next section.

Ideally, a reconstructed track in the OLYMPUS detector had valid wire times in all 18 wire planes and a good ToF hit fitting the trajectory suggested by those wire

hits. Often a track had multiple valid hits in a single wire plane due to the track crossing the boundary between two wire chamber cells and ionizing gas in the active regions of both, which provided a valuable constraint on the location of the track by automatically resolving the wire-side decision for that plane. In practice, inefficiencies in the chambers caused a track to have fewer than 18 hits in the drift chambers, but typically a track could be reconstructed with fewer hits as in the example event reconstruction shown in Figure 4-2.

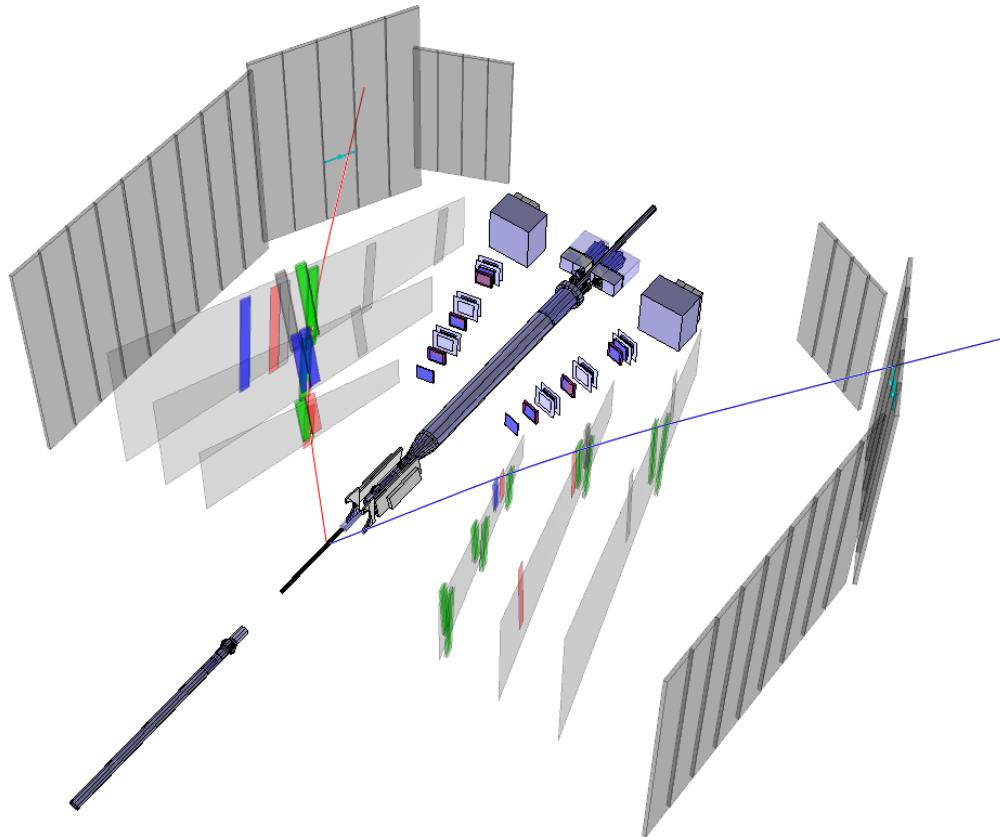


Figure 4-2: A reconstructed elastic e^-p event where the electron (red track) was detected in the left drift chamber and the proton (blue track) in the right drift chamber. The cyan lines in the ToF bars represent the horizontal lines corresponding to the loci of points corresponding to the PMT time difference used to estimate the vertical position of the ToF hit. The color-filled sections of the drift chamber planes indicate wires with valid times for the event, color-coded by the number of wires with valid times in a given cell (green indicates all three wires in a cell fired, blue two wires, and red one). The scattering chamber and toroid coils have been removed from the display for clarity.

4.2.1 Time-to-Distance (TTD) Conversion for the Drift Chambers

The conversion of recorded drift times (effectively the elapsed time between the ionization of the gas in the drift chamber to the signal time on the wire after drift) to the corresponding distance from the wire at which the track passed in the drift chambers (the time-to-distance (TTD)) was a complicated function of the electric fields generated by the wires, the magnetic field in the vicinity of the individual wires, the angle at which the track passed relative to the normal of the relevant wire plane, and individual irregularities of the wires. Due to the complexity of the problem, several models were tested for the TTD conversion. These models varied from models of very few parameters fit only to simulations of the drift gas using the Monte Carlo frameworks GARFIELD and MAGBOLTZ [141, 160] to spline models of hundreds of parameters fit iteratively to the experiment data. Ultimately, it was found that a model between these two extremes yielded the best results, both in terms of final tracking resolutions and ability to properly reconstruct the maximum number of tracks.

The goal of the TTD function is to convert the time recorded by a wire to the position in the plane of the wire at which the track passed. Figure 4-3 shows an example of a simulated track passing through an OLYMPUS drift chamber cell as viewed looking along the wires. Using the coordinate system specified in the figure, the goal of the TTD is to reconstruct the position of the particle trajectory in the $y = 1$ cm, $y = 2$ cm, and $y = 3$ cm planes. Assuming the ideal condition in which there are no noise times for a wire, the earliest time on a wire will correspond to an ionization from the passing track. Even ignoring the stochastic nature of the points along the trajectory that have ionizations, the earliest ionization point with the shortest drift time to the wire is in general not in the wire plane and is a function of the local magnetic field (which gives rise to the $\mathbf{E} \times \mathbf{B}$ drift in the local y direction) and the angle relative to the local y axis at which the track passes.

The basic behavior of drifting electrons in an OLYMPUS drift cell may be un-

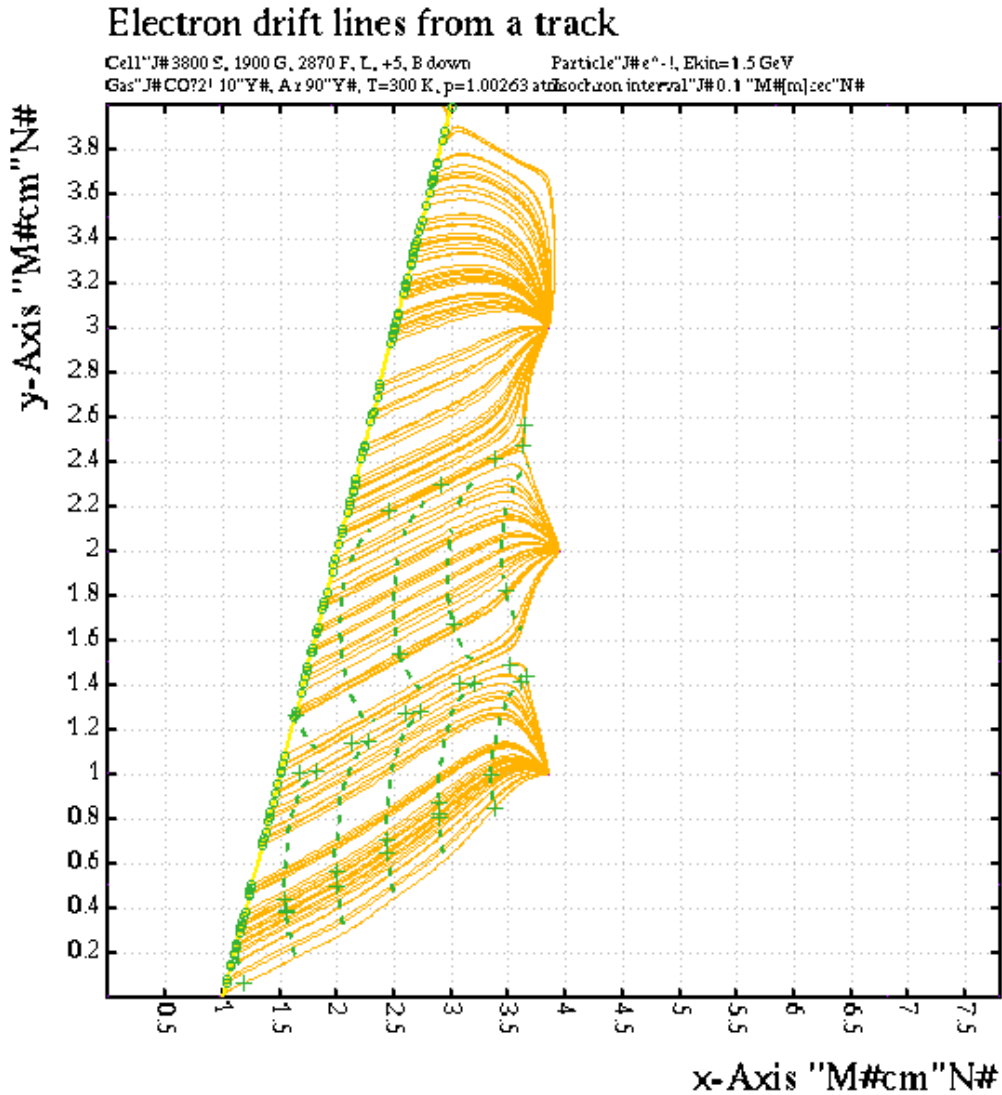


Figure 4-3: Simulated lines of electron drift (yellow) from points of ionization along a particle trajectory (open green circles) to the wires in a simulated OLYMPUS drift chamber cell using GARFIELD for the drift simulation and MAGBOLTZ for the determination of the drift gas properties [141,160]. The drift lines are angled relative to the symmetric axes of the drift cell due to the $\mathbf{E} \times \mathbf{B}$ drift induced by the local magnetic field. The three points at which drift lines converge correspond to the positions of the sense wires. The green dashed lines represent isochrons, lines of equal drift time to a given wire.

derstood by considering the electric field the electrons experience as they traverse the cell, as shown in Figure 4-4. For the bulk of the cell, the arrangement of wires provides an approximately uniform drift field of ~ 600 V/cm, which in conjunction with the resistance to drift of the gas, gives rise to an approximately constant drift

velocity for the electrons. In this region, the TTD function is approximately linear for all other conditions such as magnetic field strength and track incidence angle held fixed. The TTD function must model different behaviors near the sense and ground wires. Near the sense wire, the drift field rapidly increases, causing the drift electrons to accelerate towards the wire. This effectively compacts the drift distances from the region near the wire into a shorter range of times than in the linear region. Near the ground planes, the relatively weak field causes electrons in this region to slowly accelerate, spreading many similar distances from the wire to a wide range of drift times.

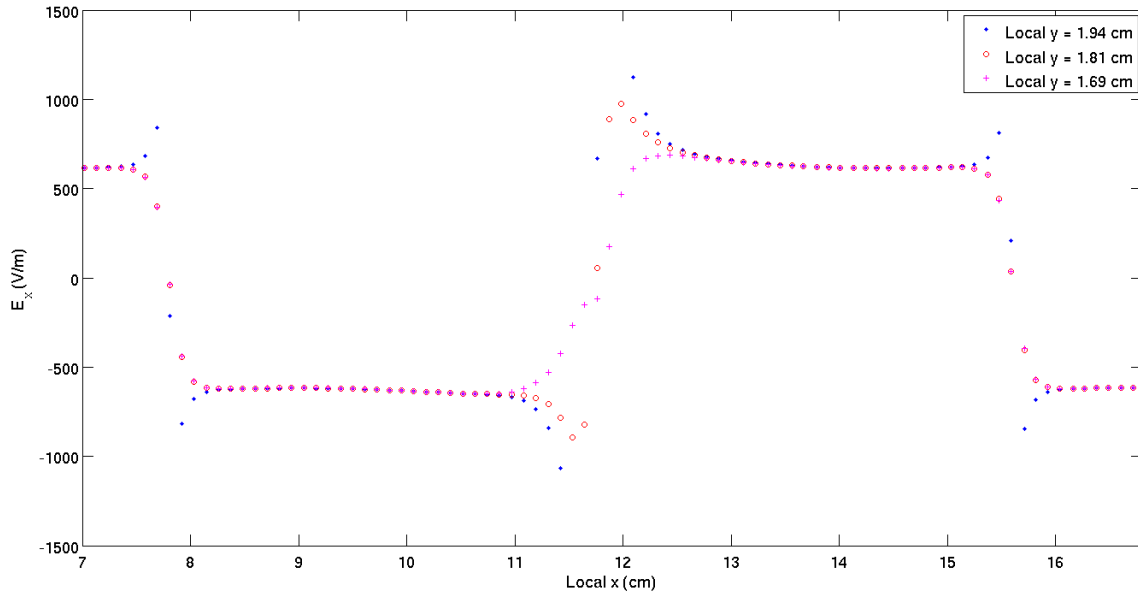


Figure 4-4: Calculated electric field strength in the local x direction for a middle wire in a simulated OLYMPUS drift cell. The wire in question is at $x \approx 12$ cm and the correspond ground wires are are $x \approx 8$ and $x \approx 16$ cm. For the bulk of the cell the electric field is roughly constant, but changes rapidly in the vicinity of the sense wires and ground planes.

The final TTD model used in the OLYMPUS analysis accounted for these effects by modeling distance from the wire as a function of recorded drift time as a cubic function near the wire, a linear function in the bulk of the cell, and steeper linear plateau near the ground planes. Additionally, this function was adjusted by the trigonometric factors introduced by the angle of the Lorentz drift and the angle of the track relative to the wire plane. The function was given additional freedom along

the length of each wire by making all parameters of the function polynomials in the global ϕ of the track. More details on the derivation and exact forms of these functions may be found in Reference [53].

Rather than attempt to determine the parameters of the functions in each region based on the ideal physics of the drift cell (i.e., the Lorentz angle, the drift velocities, the radius of the cubic acceleration region, the position of the start of the plateau region, etc.), the parameters were iteratively fit to data tracks. This allowed considerably more freedom in accounting for imperfections in cell voltages, wire time offsets, and the effects of the magnetic field in three dimensions. This also allowed for better handling of the fact that, as discussed in Section 3.4.3, the fraction of ethanol in the drift gas fluctuated and thus caused changes in the TTD relation. To account for this, the data runs were examined by hand and grouped according to the width of their drift time distributions. A fit of the TTD model to a GARFIELD simulation was used as a seed for the first iteration of tracking the data. Each individual wire was fit to two functions for the TTD on the upstream and downstream sides of the wire for each group to account for imperfections in individual wires and cells. This seed was constructed for the TTD group with the distribution width closest to average width among the groups and then the iterated solution for that group was used as the seed for the next nearest groups in widths and those groups were iterated to produce a solution, which was then used to seed the next group, and so on. Each group was iterated (tracked using the results of the previous TTD fit and then refitted to the TTD model) at least twice, after which it was found that the fit residuals did not typically continue to improve. Typically, average residuals between the TTD function and the reconstructed track distances were on the order of a few tenths of a millimeter. Examples of the resulting TTD functions are shown in Figure 4-5.

4.2.2 Track Reconstruction

With the TTD functions established, wire hit loci could be passed to a tracking algorithm for the full reconstruction of particle trajectories. This process is covered in considerably more detail in References [53] and [54], but is briefly described here for

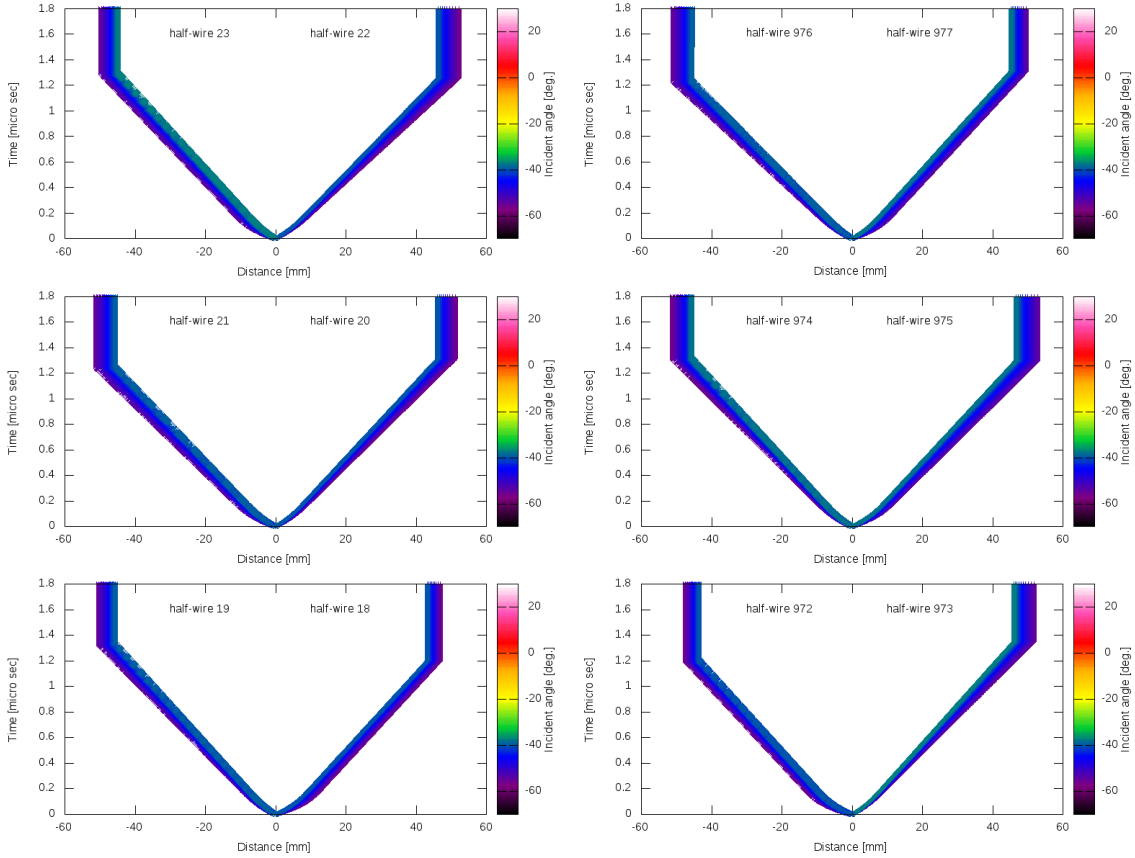


Figure 4-5: Example TTD fit results for two cells that were near the downstream ends of the drift chambers in the same positions left and right of the beamline for fixed track ϕ . Note the spread in the TTD over several millimeters caused by the angle of incidence of the track. For this case, the functions in the corresponding left and right cells are extremely similar, as would be expected in the absence of any imperfections in wire voltages, placement, etc.

completeness. Multiple tracking algorithms were developed for OLYMPUS, in part as a control on systematic uncertainties due to tracking efficiency and in part due to the challenging nature of OLYMPUS tracking (caused by the high rates of noise hits in the inner portions of the drift chambers, the ambiguity of the upstream/downstream decision for hits on an individual wire, etc.).

The tracking algorithms used two common components, which were designed to reduce noise and increase the speed of track reconstruction. The first of these was a pattern library of the combinations of wire hits that could reasonably correspond to a track of given kinematics so as to eliminate wires from consideration that were not

included in a possible track combination and to avoid attempting to track events in which no pattern was present [161]. This pattern library was generated from a very large set of simulated events extending throughout and beyond the kinematic ranges and particle species possible for the OLYMPUS running conditions. This additionally prevented tracks from events with combinations of noise hits from mimicking elastic tracks that could contaminate the sample and were difficult to simulate. A toy example of a matched pattern and a rejected event are shown in Figure 4-6. To account for inefficiencies in the wire chambers, patterns were allowed a tolerance of missing one complete cell layer (i.e, one of the six) in matching library patterns.

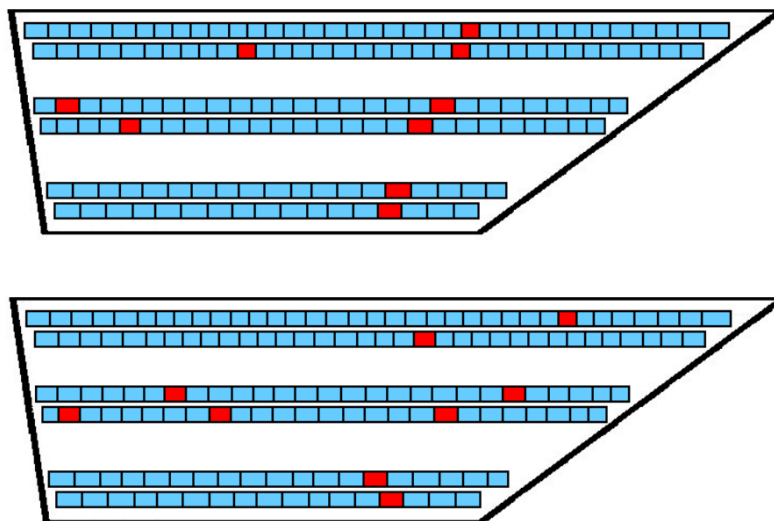


Figure 4-6: Toy example of tracking pattern matching for the OLYMPUS track reconstruction algorithms. In the top figure, the six cells obvious to the eye as corresponding to a track form a pattern match while the noise hits from the from the three cells to the left of the pattern were not passed to the track fitter. In the bottom figure, no pattern was matched and thus no attempt was made to track the event [162].

The second common component was a model fit to simulation data that provided positions in the wire planes corresponding to initial track parameters known as *Fast-track*. Other tracking routines (including that used in the 12° system (Section 5.2.4)) iteratively simulate particle trajectories to minimize the residuals between the trajectory and hit positions. Such an approach, however, would be much too slow for the OLYMPUS reconstruction. To avoid the need of iteratively propagating simulated

trajectories, a dense library of simulated events was generated and a generalized spline of the initial simulated track parameters was fit to the positions of the trajectories in each wire plane. Then, when reconstructing tracks, the spline function was queried for a given set of kinematic parameters to interpolate the resultant wire plane locations of the trajectory. In addition to providing much higher speed than simulated propagation, the spline function also allowed the computation of derivatives with respect to track parameters which is useful for many tracking algorithms.

With these tools in place, multiple algorithms were considered for the final fit of trajectories to data. The method used for the main final analysis was based on the Elastic Arms Algorithm (EAA) [163, 164]. The essential principle of the algorithm is to begin with template tracks (i.e., the “arms”) and deform them through an iterative effective temperature cooling procedure to produce a global best fit the data. Numerous additions to this procedure were made in order to optimize the algorithm for the purposes of OLYMPUS, which are discussed in References [53] and [54]. In general, this algorithm performed well for OLYMPUS, which is discussed quantitatively in Section 6.1.3.

The other algorithms created for OLYMPUS included early iterations in which iterative simulated propagation was used (the predecessor of the 12° system tracking algorithm discussed in Section 5.2.4) and approaches involving a local fitting of track elements to collections of hits to then build complete trajectories. While these algorithms were used as checks of the main EAA algorithm, they were not used for the final analyses presented in this work and thus are not discussed further here.

4.3 The OLYMPUS Monte Carlo Simulation

As noted previously, the analysis strategy of OLYMPUS required that the simulation be an accurate and detailed representation of the experiment and the experimental conditions in all conceivable ways. In particular, the results of simulation were converted to the format of the raw data (i.e., TDC counts, ADC counts, etc.) after application of the relevant resolutions on such quantities and then reconstructed using

exactly the same methods as used on raw data. In this way, biases from simulation approximations were minimized, providing a robust framework for the comparison of data and simulation. This section describes the procedure by which “simulated raw data” were produced from the Monte Carlo framework; the reconstruction and analysis proceeded as described for the raw data for all elements of the experiment.

One of the notable advantages of this approach is that it permits a complete treatment of the effects of radiative corrections on the final data analysis, since the size of the radiative corrections for any experiment depends on the acceptance and resolution of the detector systems used and the way in which events are selected from the data sample. This arises from the fact that radiative events are only distinguishable from purely elastic events if they result in a change to the momentum of the particle from its elastic momentum by an amount that can be distinguished by the detector according to its resolution. Additionally, since radiative events may change trajectories they may be pushed in and out of the acceptance or into regions of different detection efficiency relative to the pure elastic trajectory. The OLYMPUS analysis accounts for all such effects by full representing the detector in simulation including its physical acceptance, efficiencies, and resolutions and by applying identical analyses to the data and simulation so that the effects of the choices made in the selection of elastic events are equally represented in data and simulation. Although full Monte Carlo treatment of radiative corrections is common in modern higher energy experiments, most existing treatments of radiative corrections for $e^\pm p$ scattering are designed for single-arm (inclusive), high momentum resolution experiments and only allow for an adjustment of the size of the correction based on a single event selection parameter (typically effectively amounting to the deviation of the lepton energy from the purely elastic energy) [98–100, 165, 166]. The full Monte Carlo method used for OLYMPUS provides a higher level of confidence in the proper handling of radiative effects, especially those that are opposite in sign for electrons and positrons, than classical methods by allowing radiative corrections to be properly treated in an exclusive event selection and reducing the uncertainties associated with the single-arm momentum resolution of the experiment. The VEPP-3 TPE experiment utilized a

similar approach to radiative corrections as OLYMPUS and developed an $e^\pm p$ radiative event generator [115, 167], while the CLAS TPE experiment applied a more classical approach to radiative corrections to their data [114, 166].

4.3.1 Procedure

The procedure of simulating events and producing simulated detector data proceeded in three steps:

1. generation of event vertices (initial positions and momenta of particles in the event),
2. propagation of all generated particles through the detector geometry using GEANT4 with all relevant physics processes activated [155], and
3. digitization of the energy depositions, positions, etc. recorded by GEANT4 into “raw data” quantities.

The propagation step of the procedure utilized the well-verified physics processes simulated by GEANT4, and depended critically on the detailed representation of the detector in the simulation as discussed in Section 4.1. The event generation and digitization procedures were developed particularly for the purpose of the OLYMPUS simulation and are discussed in the following sections.

4.3.2 Event Generation

The first step in the OLYMPUS simulation was to generate event vertices by a Monte Carlo procedure. In general, this amounted to specifying a physical process to occur in the detector system, drawing an event vertex from a specified target distribution, and drawing the momenta of all particles involved in the process from the distributions relevant to the physics process. Options for the target distribution included realistic distributions generated from simulation of the target system (Section 5.1.2), fixed-vertex, events generated isotropically in the target region, and approximations to the

simulated target distribution. Options for the particle/momentum distributions included purely elastic $e^\pm p$ (Born approximation) kinematics, various test generators with isotropic momentum/angle distributions, an implementation of the ESEPP generator produced by the VEPP-3 TPE experiment [167], a new radiative $e^\pm p$ generator developed for OLYMPUS (see next section), as well as generators for $e^\pm e^-$ events for the SYMB system that included a new radiative generator for such processes [168].

Notably, most of the OLYMPUS generators were *weighted* in that each event in simulation carries a scalar weight, which represents its contribution to the integral over all Monte Carlo events that is compared with data. This approach provides two significant advantages:

1. events may be drawn more isotropically in phase space and then weighted appropriately so as to reduce the statistical error of the simulation in areas of phase space where the true cross section is small (such as high θ in $e^\pm p$ scattering) without simulating far more events than necessary in high cross section regions, and
2. an event can carry multiple weights corresponding to different models of radiative corrections, protons form factors, physical approximations, etc., allowing a single sample of simulation events to test multiple physics models simultaneously without propagating, digitizing, and reconstructing the simulation events multiple times.

The first advantage allowed OLYMPUS to achieve a very high statistical precision on the simulation throughout the entirety of the accepted phase space so as to make the statistical uncertainty due to the Monte Carlo effectively negligible next to the data statistical and systematic uncertainties. The second provided a rich platform for the use of various radiative corrections models, form factor models, etc. with the OLYMPUS data, which simplifies the comparison of OLYMPUS results with previous experiments and provides a strong indicator of the systematic uncertainties on the OLYMPUS results associated with such effects.

For production simulation, i.e, the simulation results designed for the direct

data/Monte Carlo comparison, the target distribution was specified as the resulting distribution from the molecular flow Monte Carlo simulation described in Section 5.1.2 and the physics processes were determined by the OLYMPUS radiative event generator.

The OLYMPUS Treatment of Radiative Corrections and Radiative Event Generator

As previously noted, an new radiative $e^\pm p$ event generator was developed for use with the OLYMPUS simulation framework. The development, testing, and application of this generator are discussed in great detail in References [53] and [54], while only the essential details are provided here. This generator was designed to implement a variety of prescriptions for radiative corrections and the proton form factor, while providing a direct interface with the OLYMPUS analysis framework. In general, previous prescriptions for radiative corrections to elastic $e^\pm p$ scattering took the basic form:

$$d\sigma_{\text{exp.}} = d\sigma_{\text{Born}} \cdot (1 + \delta(\theta, \Delta E)), \quad (4.9)$$

where $d\sigma_{\text{exp.}}$ is the experimentally measured elastic cross section, $d\sigma_{\text{Born}}$ is the Born (single-photon exchange) cross section, and δ is the radiative correction factor, which is typically computed as a function of the scattering angle θ and the effective energy resolution for the distinction of radiative events for the experiment ΔE . Typically, results for elastic $e^\pm p$ scattering were reported as the extracted Born cross section after the subtraction of the correction δ for comparison between experiments. The first of the prescriptions for computing the correction δ was developed by Mo and Tsai in the 1960s [98, 99]. Additionally, Meister and Yennie developed an approach based on the early work of Tsai that made additional approximations for the purposes of facilitating computation [165]. These correction prescriptions were the standard for nearly four decades until Maximon and Tjon published a new prescription in 2000 that reduced the number of approximations made relative to Mo and Tsai, accounts approximately for the structure of the proton via the introduction of the

dipole form factor (Equation 2.21), and reformulates the contributions due to soft two-photon exchange [100]. Each of these prescriptions was designed for single-arm (inclusive) experiments, and are thus formulated to rely on a cut in the lepton ΔE . A prescription developed by Ent *et al.* in 2001 reformulates the procedure of Mo and Tsai to produce a method that allows the calculation of δ as a function of the missing energy reconstructed from exclusive detection of the lepton and proton, extending the applicability of such models to coincidence experiments [166].

An extension to models for elastic $e^\pm p$ radiative corrections, first proposed by Yennie *et al.* in 1961 [169], replaces the $(1 + \delta)$ correction with a factor of $\exp(\delta)$, a procedure known as *exponentiation*. As demonstrated in Reference [169], this allows for the correction to account for the emission of multiple soft photons (i.e., that do not distinguishably change the event kinematics) and prevent the infrared divergence that occurs for the $(1 + \delta)$ prescription, which effectively only treats single photon emission. The soft approximation breaks down, however, as ΔE increases, necessitating a transition to consideration of such higher ΔE events as hard bremsstrahlung processes.

The OLYMPUS radiative generator incorporates a wide variety of these prescriptions via the calculation of multiple weights. The details of the implementations of these methodologies is discussed in References [53] and [54], but the essential capabilities provided by the generator include the following:

1. implementation of the prescriptions of Mo and Tsai, Meister and Yennie, and Maximon and Tjon,
2. exact tree-level calculation of the bremsstrahlung matrix element (avoiding the soft photon approximation made by previous approaches),
3. separate weights for exponentiated and non-exponentiated corrections,
4. treatment of the vacuum polarization diagrams either from calculations including all leptons in the loop or using a data-driven approach (which, in principle, includes all possible particles in the loop) [170, 171],

5. weights representing the Born and soft-photon approximations, and
6. and proper application of radiative corrections for different proton elastic form factor models.

These various assumptions are represented across multiple weights computed for each simulated event, allowing the OLYMPUS data to be analyzed under a wide variety of radiative corrections models and physical assumptions, facilitating both comparison to previous elastic $e^\pm p$ data and providing extensive insight into the systematic effects of radiative corrections for the final OLYMPUS results.

The generator was tested extensively prior to use for the final OLYMPUS analysis, including comparisons to the ESEPP generator [167] and comparisons to the model of Maximon and Tjon [100] in the appropriate regions of phase space, as described in References [53] and [54]. In general, the OLYMPUS radiative generator performed extremely well under all tests and provided a robust platform for the analysis of OLYMPUS results.

4.3.3 Digitization of the Detector System

In general, every effort was made to represent the elements of the OLYMPUS experiment in simulation to accurately represent the conditions under which the experiment operated. This involved accounting for a number of factors via the generation of simulation events for each individual data run (each of which included $\sim 1 \cdot 10^6$ triggers) that properly accounted for any effects such as beam position, target gas temperature, etc. that were subject to time variation. Such parameters were provided to the simulation from the slow control data for each data run, and they were used to adjust the conditions such as the target gas density, the position of the beam with respect to the locations of generated events, the magnetic field strength, etc. on an event-by-event basis to properly negate the possibility of such effects altering the final data/simulation comparison.

Regarding the digitization of detector elements, individual systems were treated so as to properly account for their resolutions and efficiencies (as measured from

experimental data) in the generation of simulated hits. The exact procedures used for different systems are discussed in the relevant sections describing the analyses using each detector, but in general this was achieved by applying appropriate uncertainty to simulated TDC and ADC values, testing simulated hits against data-driven maps of simulated efficiency, and the elimination of data from the final analysis corresponding to times when detectors were behaving unpredictably and could not be properly modeled in this fashion. This approach created a detailed model of the OLYMPUS experiment in simulation, accounting for detector imperfections, a wide variety of time-varying effects that could otherwise introduce systematic uncertainties, and a method of completely accounting for effects of detector acceptance and elastic event selections in the treatment of the radiative corrections applied to the experiment results.

Chapter 5

Determination of the Luminosity

As noted in Chapter 1, the OLYMPUS result on $\sigma_{e^+p}/\sigma_{e^-p}$ depends equally on two key elements of the data: the measurement of relative $e^\pm p$ rates as a function of angle and the measurement of the relative luminosity collected between the two species modes. Ideally, each of these quantities should be known individually to better than $\pm 1\%$ total (statistical and systematic) uncertainty so as to provide an overall uncertainty of less than $\pm 1\%$ on the final measurement. To this end, OLYMPUS employed three functionally independent methods of luminosity determination:

1. calculation of the luminosity from the effective target density and beam current (the “slow control luminosity”),
2. dedicated (separate from the main tracking system) forward ($\epsilon \approx 0.98$, $\theta \approx 12^\circ$) elastic $e^\pm p$ event reconstruction (the “ 12° luminosity”),
3. and very forward ($\theta \approx 1.3^\circ$) integrating calorimetric measurements of elastic $e^\pm e^-$ (Møller and Bhabha scattering [143, 144]), $e^+e^- \rightarrow \gamma\gamma$ annihilation, and elastic $e^\pm p$ events (the “Symmetric Møller/Bhabha (SYMB) luminosity”).

Each of these methods was sensitive to different physics processes and systematic uncertainty contributions, making them a comprehensive and complementary set of measurements for the luminosity determination. In particular, the slow control determination provided a real-time estimate of the luminosity during data-taking independent of event reconstruction. The 12° system provided a direct normalization

of elastic $e^\pm p$ with detectors independent from the drift chambers in a region where two-photon exchange (TPE) is expected to be small. The SYMB calorimeter used extremely forward $e^\pm p$ scattering (where TPE is expected to be extremely small) in conjunction with the independent $e^\pm e^-$ process to provide an overall normalization decoupled from the TPE measurement of interest.

Throughout this chapter, reference will be made to the “absolute luminosity” and the “species-relative” luminosity ratio measurements, with important distinctions drawn between them. For clarity, the absolute luminosity \mathcal{L}_{e^\pm} for a given period of data-taking refers to the value of the integrated luminosity that would be used in extracting the absolute cross section of elastic events:

$$\sigma_{e^\pm p}(\epsilon, Q^2) = \frac{N_{e^\pm p}(\epsilon, Q^2)}{\mathcal{L}_{e^\pm}}, \quad (5.1)$$

where $N_{e^\pm p}(\epsilon, Q^2)$ is the number of elastic $e^\pm p$ events reconstructed in a given data bin characterized by the phase space point (ϵ, Q^2) (assuming perfect acceptance) and $\sigma_{e^\pm p}(\epsilon, Q^2)$ is the total integrated cross section for elastic $e^\pm p$ scattering into that phase space bin. The species-relative luminosity ratio is then defined as the dimensionless ratio of the absolute luminosities for each lepton species:

$$R_{\text{lumi}} = \frac{\mathcal{L}_{e^+}}{\mathcal{L}_{e^-}}, \quad (5.2)$$

and ultimately it is this quantity that appears in Equation 1.1 and is critical to the determination of $R_{2\gamma}$. Notably, many systematic uncertainties cancel in the ratio of the luminosities to allow much more precise determination of R_{lumi} than of the individual luminosities. This is discussed in detail in Section 5.2.8. Since the OLYMPUS data are in principle valuable for certain measurements involving the absolute cross section (such as elastic form factor measurements), the absolute luminosity is considered in addition to R_{lumi} to provide it for possible future use.

The author’s primary effort regarding the luminosity analysis consisted of the determination of the slow control and 12° luminosity estimates, and thus this chapter will cover each of those in detail in Sections 5.1 and 5.2. Additionally, Section 5.1.2

addresses the efforts that were made to properly determine and simulate the shape of the target gas distribution generated by the OLYMPUS target system. This had important implications for the relative acceptance of the two lepton species in the various detector systems. Section 5.3 provides a brief discussion of the SYMB system luminosity analysis and the results arising from it. Section 5.4 summarizes the results of the different luminosity analyses and sets the stage for the primary OLYMPUS results on $\sigma_{e^+p}/\sigma_{e^-p}$.

5.1 Slow Control Luminosity and Target Gas Distribution Determination

The slow control luminosity determination served to provide a real-time estimate of the luminosity determination during OLYMPUS data-taking independent of any of the event triggers and reconstruction. While not as precise, either for the absolute or species-relative luminosity, the slow control estimate provided an important baseline for run simulations and a cross check for more precise measurements. Additionally, as part of the slow control luminosity determination, concerted efforts were made to understand the shape of the target gas distribution used in the experiment, which affected both the luminosity and main $\sigma_{e^+p}/\sigma_{e^-p}$ results via the varying acceptance for e^-p and e^+p events as a function of position in the target. This was achieved by developing a gas molecular flow Monte Carlo simulation with accurate representations of the both the target system geometry and the physics of the gas within the system. This section will cover the various elements of the slow control luminosity determination in detail, paying particular attention to the target gas simulation.

5.1.1 Principle of the Measurement

The slow control luminosity determination makes use of the basic definition of instantaneous luminosity for a fixed target experiment [172]:

$$\frac{d\mathcal{L}_{\text{SC}}}{dt} = \frac{I_{\text{beam}}(t)}{e} \int_{\text{target}} \rho_p(z, t) dz = \frac{2I_{\text{beam}}(t)}{e} \int_{\text{target}} \rho_{\text{H}_2}(z, t) dz, \quad (5.3)$$

where $I_{\text{beam}}(t)$ is the beam current, e the electron charge, $\rho_p(z, t) = 2\rho_{\text{H}_2}(z, t)$ represent the density of protons/hydrogen molecules in the target along the beam, and the integral runs over the length of the beam in the target z . Thus, a good estimate of the luminosity using this method includes measurement of the beam current as a function of time and a model for the number and spatial distribution of molecules present in the target as a function of the target input gas flow, temperature, and geometry.

During data-taking, the target and beam conditions were monitored using the slow control system described in Section 3.7. On an event-by-event basis, the increment to the integrated slow control luminosity was calculated as the following variation of the integral of Equation 5.3:

$$\Delta\mathcal{L}_{\text{SC}} = Q_{\text{H}_2} \cdot \frac{I_{\text{beam}}}{e} \cdot \Delta t_{\text{DTC}} \cdot n_T \cdot \sqrt{\frac{75 \text{ K}}{T}}, \quad (5.4)$$

where Q_{H_2} is the input flow rate of H_2 molecules into the target cell in standard cubic centimeters per minute (sccm)¹, I_{beam} is the beam current in A, e the electron charge in C, Δt_{DTC} the trigger livetime (i.e., the elapsed time after being “dead-time-corrected” (DTC) for the time during detector readout when the event triggers were not open), n_T the effective total thickness of the gas target in cm^{-2} presented to the beam as calculated by the target simulation described in Section 5.1.2 for 75 K and 1 sccm H_2 flow rate, and T is the target temperature in K. Note that the integrated

¹The unit standard cubic centimeter per minute is defined as the flow rate of 1 cubic centimeter of gas at temperature 0 °C and pressure 1.01 bar passing a given point per minute. For reference, this defines 1 sccm = $4.477962 \cdot 10^{17}$ particles/s. For 1 sccm of H_2 flow, note that the rate of proton flow is twice the gas particle flow.

luminosity scales linearly with the beam current (number of beam particles on target), trigger live time, and gas flow rate into the target (number of particles in the target), as would be intuitively expected. The $1/\sqrt{T}$ dependence of the target thickness arises from the fact that the H_2 molecules rapidly thermalize with the target walls, and thus their average velocity goes as the \sqrt{T} behavior of the mean of the Maxwell-Boltzmann distribution [173, 174], effectively changing the average amount of time that a single hydrogen molecule spends in the target by the inverse factor (further discussed in Section 5.1.2). The total integrated slow control luminosity for a running period is simply the sum over the values of $\Delta\mathcal{L}_{\text{SC}}$ for each event in the period. Also, note that Δt_{DTC} may be replaced by Δt , the simple elapsed time, to convert to a measure of the “delivered” integrated luminosity, but that the “collected” luminosity is more relevant since this corresponds to the time when the detector was actually active and thus corresponds to the luminosity that the detector system measures.

5.1.2 Simulation of the Target Gas Distribution

The target gas distribution used in the OLYMPUS simulation was determined using a newly-developed, standalone Monte Carlo simulation of the molecular flow of hydrogen molecules within the target system. This section reviews the physics of gas flow relevant to the system, explains the limitations of standard gas density calculations that make them insufficient for the requirements of the experiment, and describes the new simulation.

Relevant Details Regarding the Target System

The internal components of the target system are shown in Figure 3-6, including the various system components in which hydrogen gas was contained and subject to exposure to the beam. Qualitatively, gas density was highest in the region of the target cell directly below the inlet and tapered towards the edges of the system where gas could escape into the beamline via holes in the wakefield suppressors or their connections to the beamline at the ends. The flow rate was controlled by mass flow

controllers (as detailed in Section 3.3) and experimental data were only taken when the gas flow was in a steady state (rate of input from the inlet matching the rate of gas collection by the pumps), as indicated by the achievement of steady pressure in the target system. The temperature of the target cell assembly was measured as part of the slow control system by seven equally-spaced thermocouples along the system parallel to the beam. Unfortunately, not all of these thermocouples were calibrated for absolute temperature measurements.

Physics of the Target System Gas

Examining the components of Equation 5.4, the Δt_{DTC} was provided by the OLYMPUS trigger system (Section 3.8), I_{beam} was provided by the DESY accelerator system, and Q_{H_2} and T were monitored by the target and gas flow system (Section 3.3 and Reference [124]). The effective target thickness, however, is a much more complicated factor, involving the dynamics of gas flow in conjunction with the specifics of the OLYMPUS target geometry and vacuum system. The physics of gas flow varies considerably as a function of the gas pressure, nature of the conduit, and nature of the gas. A complete discussion of these phenomena may be found in Reference [175], but a brief discussion of the topic is provided here to establish the physics important to the flow regimes present in the OLYMPUS target. The flow regimes of sparse gases are typically classified by the *Knudsen number* [176,177]:

$$\text{Kn} = \frac{\lambda}{D}, \quad (5.5)$$

the dimensionless ratio of the mean free path λ between gas molecule collisions and the typical diameter D of the conduit. For $\text{Kn} \gtrsim 0.5$, the behavior of the gas is dominated by its interaction with the conduit and intermolecular interactions are considered negligible, a region known as *molecular flow* where the dynamics of the gas flow simplify considerably. Ideally, the OLYMPUS target system would be in this regime since this would make an accurate representation of the target gas much more feasible. To determine if this was the case, the hydrogen may be approximated as an

ideal gas with velocities distributed according to the Maxwell-Boltzmann distribution. In this case, the mean free path may be analytically calculated:

$$\lambda = \frac{k_B T}{\sqrt{2}\pi\xi^2 P} = 2.33 \cdot 10^{-20} \left[\frac{\text{Torr} \cdot \text{cm}^3}{\text{K}} \right] \frac{T}{\xi^2 P}, \quad (5.6)$$

where k_B is the Boltzmann constant, P the gas pressure, and ξ the effective molecule diameter. This approximation was verified experimentally by Sutherland and others in thermodynamic conditions similar to those in the OLYMPUS target [178].

The region of highest pressure in the target gas system, and thus lowest mean free path, is the narrowest aperture (examining only the parts near the cell that immediately affect the distribution of gas in the cell). This region corresponded to the inlet tube, as shown in Figure 3-6. The inlet was several centimeters long and of diameter $D = 0.5$ cm, and was cooled by the cryogenic system to temperatures as low as 35 K (in the absence of beam heat load on the system). While the pressure inside the inlet is difficult to estimate and was not directly measured, note that for the hydrogen molecular diameter experimentally determined to be $\xi = 4.04$ Å [179] and the conservative (resulting in the lowest mean free path) case of $T = 35$ K:

$$\lambda P = 5 \cdot 10^{-4} \text{ cm} \cdot \text{Torr}. \quad (5.7)$$

Thus, to consider the gas to be in the molecular flow regime ($\text{Kn} = \frac{\lambda}{D} \gtrsim 0.5$) requires:

$$P \lesssim 2 \cdot 10^{-3} \text{ Torr}. \quad (5.8)$$

Since this is three orders of magnitude larger than the pressure measured in the scattering chamber during normal running conditions (a region of only approximately 1–2 orders of magnitude greater in volume than the inlet) [124], it is reasonable to assume that the gas was characterized by molecular flow throughout the target system.

Molecular Flow

As noted, in the molecular flow regime it is assumed that interaction between molecules in the gas are negligible and interactions with the walls of the conduit dominate the behavior of the flow. In particular, for the case of the OLYMPUS target system where the gas is relatively low in density and the conduit walls (the target cell, inlet, wakefield suppressors, etc.) are being actively cooled, the gas rapidly thermalizes to the temperature of the conduit. The gas can be understood as a collection of individual molecules that propagate along straight lines between collisions with the walls of the conduit with speeds distributed according to the Maxwell-Boltzmann distribution of temperature T (hence the $1/\sqrt{T}$ dependence of Equation 5.4). Note that the collisions at the walls of the conduit are not reflection-like (i.e., angle of incidence equal to the angle of reflection), since the walls are fundamentally “rough” on the scale of molecular collisions. The rebounds from the wall are typically modeled to be distributed as the cosine of the angle from the surface normal vector independent of the incident angle, with no preference for the azimuthal angle relative to the normal vector (known as “Knudsen’s cosine law” [180]). Note that the preference is to rebound normal to the surface, with vanishing probability to rebound along the surface. While it is not excluded that there may be a finite time between collision with the wall and the reemission of the molecule, this effect will equilibrate and become negligible after the gas flow is well established and many molecules are in the system.

Conductance Modeling

Having established the molecular flow nature of the flow of the gas through the target system, the traditional approach to determining the resultant gas density inside the target cell is to define the *conductance* C of the target cell (with dimensionality of volume per unit time), analogous to an electrical conductance. By construction, this conductance obeys a corresponding molecular flow analog of Ohm’s law:

$$C = \frac{Q_T}{\Delta P}, \quad (5.9)$$

where Q_T is the *throughput* (with dimensionality pressure times volume per unit time) and ΔP the pressure difference across the system. A more useful quantity than the throughput is the *pumping speed* S , defined as the throughput divided by the pressure at the entrance to the system (in this case the inlet of the target cell)². Defining P_{in} as the inlet pressure to the target cell and P_{out} as the pressure at the exit to the cell, then $S = Q_T/P_{\text{in}}$ and:

$$C = \frac{SP_{\text{in}}}{P_{\text{in}} - P_{\text{out}}} = \frac{S}{1 - \frac{P_{\text{out}}}{P_{\text{in}}}}. \quad (5.10)$$

This result is important in that it implies that for $P_{\text{out}} \ll P_{\text{in}}$, the pumping speed goes to the conductance, independent of the precise value of the conductance. Thus, while the pressure in the target inlet tube and at the exit to the target cell are not well known, it is satisfied that $P_{\text{out}} \ll P_{\text{in}}$ and so the conductance of the system may be calculated to determine the rate at which molecules pass through the cell (and thus the density of molecules inside the cell).

The computation of the conductance of an arbitrary conduit, however, is quite difficult. Typically, such calculations require computation of integrals over all possible straight-line particle trajectories between collision points, rely on assumptions that the geometry has uniform cross section, and ignore boundary conditions (i.e., assume the conduit is very long). Analytical calculations for several simple geometries may be found in Reference [175]. For the original OLYMPUS simulation, the target density was modeled using the Steckelmacher analytical computation of the conductance for a long tube of elliptical cross section [181] to model the OLYMPUS target cell. Since the model had constant cross section, the resulting predicted gas density distribution was triangular, peaking at the inlet and linearly declining to zero at each end of the target cell (similar to a voltage dropping across a long, uniform resistor), shown as the “Old Slow Control MC” distribution in Figure 5-2. While initially expected to provide a sufficiently good model of the true target density, comparison of analyses of simulation and data via tracking in multiple detectors indicated that the simulated triangular

²The name “pumping speed” arises from the fact that the system of interest often terminates at a vacuum pump, but this need not be the case and the term can describe the rate of gas flow through any conduit.

target model did not predict the shape of the measured distribution well near the ends of the cell and underestimated the density of the target by approximately 20%.

In retrospect, this model failed due to the fact that it ignored the end conditions of the target cell, which directly connect to wakefield suppressors. While the wakefield suppressors were manufactured with holes to allow the escape of gas (see Figures 7–9 in Reference [124]), the model severely underestimated the containment of gas by these elements and could not make any prediction regarding the shape of the gas distribution in the regions near the ends of the cell. Additionally, the effective conductance for gas escape was not the same at each end of the cell due to the connection of the collimator, and thus the distribution of gas was additionally not symmetric about the inlet port. It was, however, completely impractical to use analytical methods to compute the conductance of the complete target system geometry, due to both the elliptical cone shapes of the collimator bore and wakefield suppressors and the lack of gas escape handling in such calculations.

Simulation of Molecular Flow and Conduit Geometry

Due to the fact that the acceptance of e^-p and e^+p events in the detectors can differ as a function of target vertex position and the desire to have the slow control luminosity calculation more accurately represent the overall target thickness, a new method was developed for computing the target density to ensure an accurate representation in the simulation. As discussed, the complexity of the complete geometry made any attempt at an analytical approach infeasible, which naturally suggests Monte Carlo simulation methods. While there exists commercial software for molecular flow [182], this software is quite expensive and designed for engineering applications that do not necessarily have similar conditions to internal gas targets in nuclear and particle physics experiments. For this reason, a new, standalone molecular flow and geometry simulation known as “TargetSim” written in C++ was developed for the purpose of the OLYMPUS experiment³.

³The source code for TargetSim, along with basic documentation, is available from the author for academic applications.

In general, TargetSim follows the approach of propagating particles (i.e., molecules or atoms of gas) of given mass through a modular geometry. Molecules traverse the geometry starting from a source distribution defined by the user (i.e., a position and velocity distribution for particles entering the system). Each input particle is individually tracked to its next collision with a wall of the geometry or until it reaches a designated exit of its current geometry unit. At the exit to a geometry unit, a particle may pass into another geometry unit, in which case its next intersection or exit point is calculated for that unit, or out of the system (i.e., to a location where it will reach a vacuum pump). At each wall collision point, the gas molecule is assumed to thermalize with the local temperature of the wall, and is then re-emitted with speed distributed according to the Maxwell-Boltzmann distribution and direction according to Knudsen's cosine law. This process is iterated for each particle until it reaches a system-exit condition. Such a propagated path in the OLYMPUS target system is shown in Figure 5-1.

Along the particle's path, the time occupation of the particle in three-dimensional spatial bins is recorded. Then, at the end of the trajectory, the time occupation histogram may be divided by the total time the particle spent in the system to create a position density distribution histogram for a single particle. For a collection of many particles, the average of such distributions will converge to the position distribution of the target system under steady-state conditions. Furthermore, the average time a particle spends in the system may be used in conjunction with the steady-state input flow rate to determine the average number of particles inside the system at a given time, and thus to place an overall normalization on the position distribution as a function of flow rate for direct implementation in the simulation and slow control luminosity calculation.

The definition of the geometry in TargetSim is a user input to the program, which must include the following information for each unit in the geometry:

1. equations or inequalities defining the surfaces of the geometry that a particle may strike,

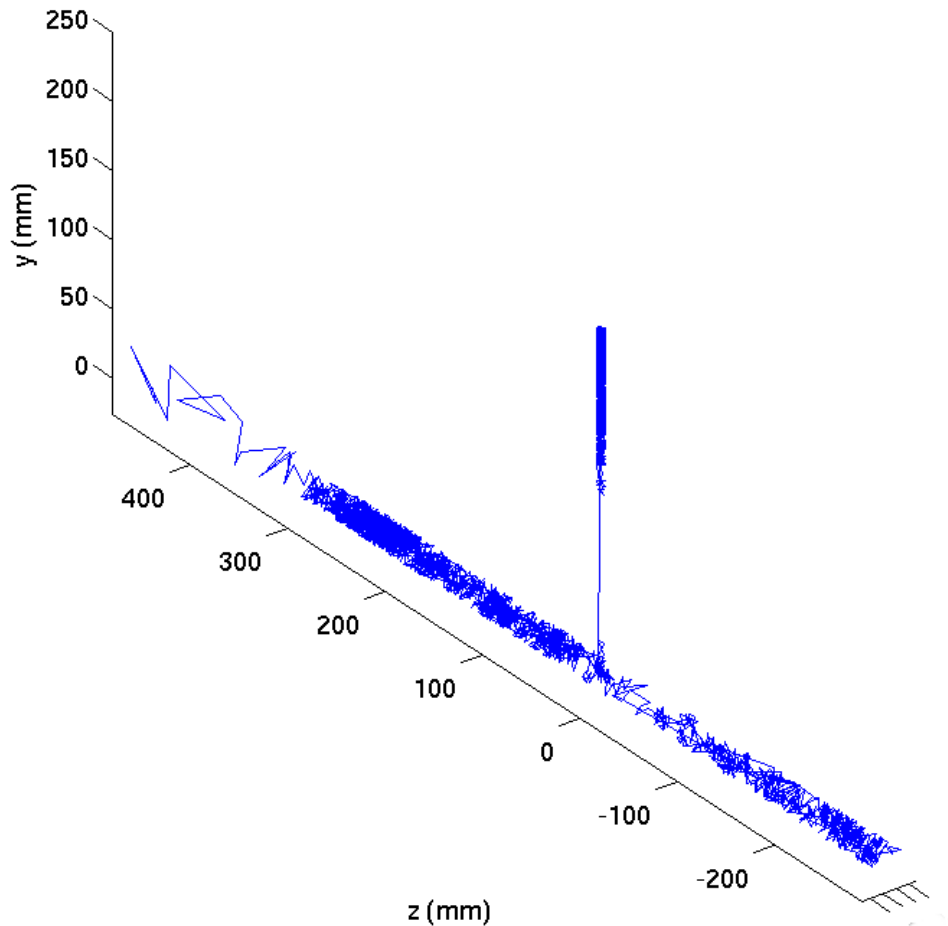


Figure 5-1: Simulated path of a hydrogen molecule inside the OLYMPUS target system, beginning at the top of the inlet, passing into the upstream portion of the target cell, and eventually leaving the system through the downstream wakefield suppressor. Coordinates are approximately the OLYMPUS global coordinates.

2. a method of calculating the surface normal vector at any point on the strikable surfaces of the geometry,
3. a defined temperature function for each strikable point on the geometry,
4. an analytical or numerical method for computing the intersection of a line (i.e., a particle trajectory) with the strikable surfaces, and

5. conditions defining which points on the strikable surfaces are exit points and into which geometry unit or system exits those exit points pass the particle.

Geometry units are defined as instances of a general C++ geometry unit class with member variables and functions that provide the above information to a propagator function which handles the Monte Carlo drawing of new particle directions, generates the time occupation histograms, and records other requested information about the particle trajectory. The version of TargetSim used for OLYMPUS includes implementations of cylindrical tubes, elliptical tubes, and elliptical cones as geometry units (including some elements with holes that correspond to system exit locations). In principle, however, any geometry description that can be implemented to satisfy the requirements above can be used as a geometry unit, thus making TargetSim extremely flexible to handle a variety of molecular flow systems.

Simulation Implementation and Results

For the OLYMPUS implementation of TargetSim, gas particles were generated at the top of the cylindrical hydrogen inlet tube, 250 mm above the top of the elliptical target cell, at room temperature with trajectories distributed as $\cos \theta$ relative to the downward pointing vector along the inlet tube, which has been shown to be a good approximation for molecular flow in a long cylindrical tube [183]. The geometrical elements included in addition to the inlet were the elliptical target cell, the elliptical cone internal bore of the collimator, and the three wakefield suppressors (all shown in Figure 3-6). The system exit conditions were at the holes of the wakefield suppressors and the ends of the wakefield suppressors that attach to the beamline. Simulations in which the cylindrical beamline was expanded beyond the wakefield suppressors and in which the target chamber was implemented as a box containing the system were conducted so as to assess the probability of a particle reentering the system after one of the aforementioned exit conditions. This effect was found to be negligible, and so to increase the speed of the simulation, additional beamline and target chamber elements were not included in the geometry. The surfaces of the system were assumed to be at constant temperature, as suggested by the limited calibrated temperature

information available from the thermocouples.

The results of the simulation for typical OLYMPUS running conditions are shown in Figure 5-2, including a comparison to the results of the Steckelmacher elliptical tube conductance calculation. As can be seen, the target simulation predicts the $\sim 20\%$ increase in density relative to the conductance calculation that was suggested by other detector systems, and predicts a more complicated shape for the target gas distribution extending beyond the ± 300 mm of the target cell. Note that the upstream ($-z$) end of the distribution is especially important to the 12° luminosity telescope measurement since events from this range may be in the telescope tracking acceptance. The simulation reproduces the $1/\sqrt{T}$ dependence of the gas occupation of the target expected from the Maxwell-Boltzmann distribution of velocities. Thus, this factor may be computed analytically, as previously claimed in the discussion of Equation 5.4 so as to avoid requiring simulations at each individual measured temperature from the dataset.

To implement the results of the target simulation in the main OLYMPUS simulation to properly represent the vertex distribution of tracks, the shape of the distribution was parametrized using piecewise polynomial fits to its shape. The distribution was normalized by using the effective total target thickness of $n_T = 7.9095 \cdot 10^{15}$ protons/cm⁻² predicted by the simulation at $T = 75$ K and $Q_{\text{H}_2} = 1.0$ sccm and then correcting for the measured flow and temperature as a function of time using Equation 5.4. Comparison of the parametrization of the simulation to data is complicated by the fact that the extended angular acceptance of the OLYMPUS tracker distorts the reconstructed z vertex position. By narrowing the event selection to a small θ range, however, data and the raw target distribution prediction may be approximately compared. Such a comparison is shown in Figure 5-3, for reconstructed elastic events selected for lepton θ within 0.5° of 32° . In general, the simulation predicts the shape of the distribution very well, including the slopes on each side of the triangle and the behavior near the ends of the cell.

Due to the strong indications that TargetSim produces a better target distribution prediction (both in terms of shape and normalization) than previous methods, the

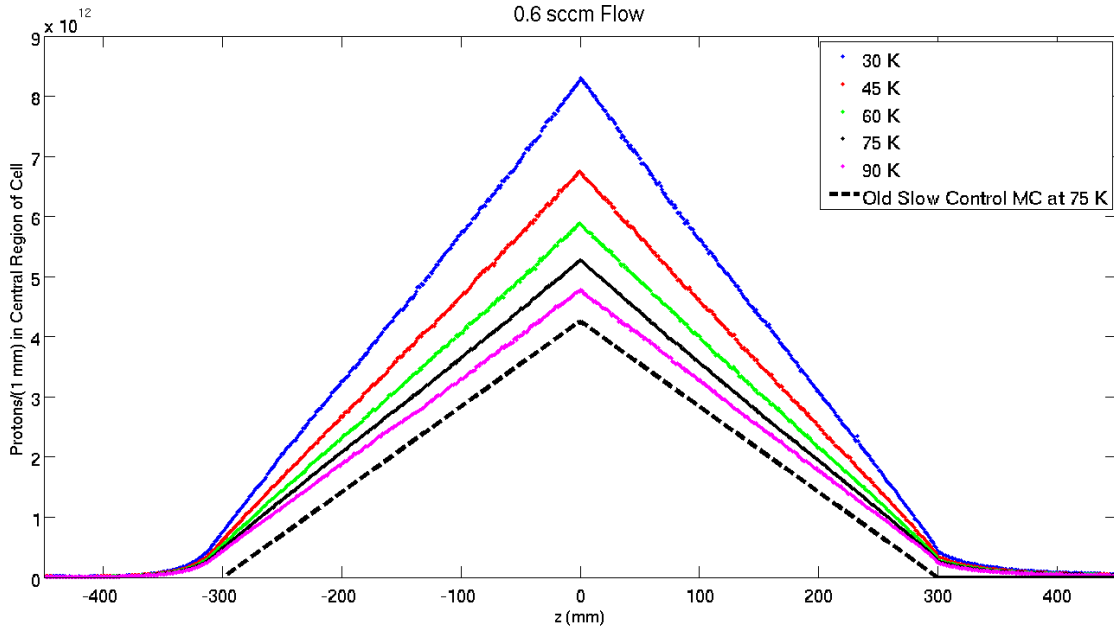


Figure 5-2: Predicted target gas density distributions for the region of the system near the beam from TargetSim, for 0.6 sccm input flow and a range of typical constant temperatures for running conditions, compared to the prediction from the elliptical tube conductance calculation of Reference [181] (“Old Slow Control MC at 75 K”). Note that while the central regions of the simulation predications are approximately triangular as predicted by the conductance, the distributions are greater in magnitude and asymmetric relative to the triangular conductance prediction due to the increased and asymmetric resistance to flow of the additional target system components on each end of the cell.

results of TargetSim were incorporated into all generated simulation datasets for the OLYMPUS experiment.

5.1.3 Systematic Uncertainty and Discussion of the Slow Control Luminosity

Note that, despite the apparent success of TargetSim in predicting the shape and normalization of the gas density of the target, several uncertainties make it unreasonable to use the slow control luminosity on its own as a precise luminosity determination. As previously noted, the temperature measurements along the target cell were not well calibrated, and thus it is impossible to determine the exact temperature of the

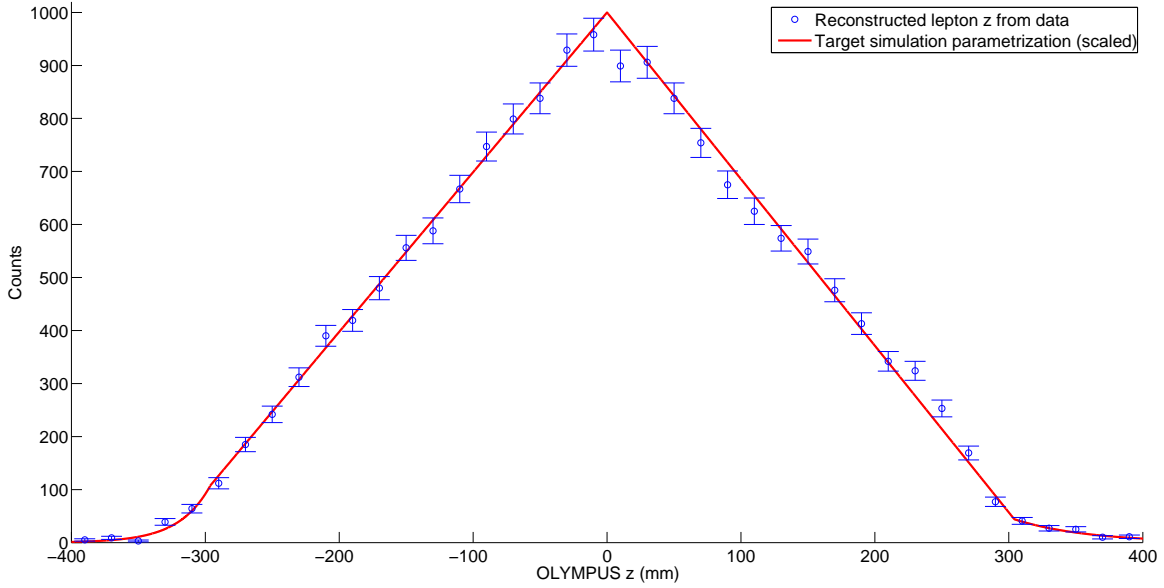


Figure 5-3: Track vertex z distribution for elastic events with lepton θ within 0.5° of 42° , compared to the predicted distribution from the raw target simulation distribution. Note that the simulation distribution is normalized to have equal integral to the data distribution for comparison of the distribution shapes in this plot.

target cell as a function of time and whether or not the temperature was uniform across the system at any given time. Even a very plausible 5 K shift in temperature alters the absolute slow control luminosity by $\sim 3.2\%$. Given that the target temperatures during electron running were ~ 10 K higher than during positron running due to different beam conditions, any non-linearity or other misunderstood aspects of the temperature measurement could induce a false asymmetry in the slow control luminosity measurement on the order of a percent. While beam energy was well constrained, the input flow was calibrated by filling buffer volumes in the gas supply system, a process with only percent level precision and that doesn't account for any losses in the several-meter-long input line from the supply system to the gas inlet. Adding these to the fact that the simulation is not yet definitively experimentally verified, it is reasonable to ascribe a systematic uncertainty to the slow control luminosity of $\delta_{\text{SC,abs}} = \pm 5\%$ absolute and $\delta_{\text{SC,rel}} = \pm 2\%$ relative.

While not viable as a standalone precision measurement, the slow control lumi-

nosity provided a valuable approximate benchmark for the other luminosity monitors, and more importantly the results of TargetSim provided a more accurate representation of the target gas distribution for use in the simulation. The versatility and generality of the TargetSim code make it a good candidate for use in future experiments with molecular flow regime gas targets and other applications.

5.2 Luminosity Determined Using the 12° System

To take advantage of the rapidly increasing elastic lepton-proton scattering cross section at small lepton scattering angles (θ) a dedicated tracking system consisting of two six-plane telescopes was constructed as a means of providing a luminosity normalization point for the measurement of $\sigma_{e^+p}/\sigma_{e^-p}$ in the main tracking volume. While subject to possible differences in the e^-p and e^+p elastic cross sections due to TPE, these effects are universally expected to be small (i.e., less than the experimental precision) at the kinematics accepted by the telescopes. This uncertainty is addressed in Section 5.2.8 and an extraction of the value of $\sigma_{e^+p}/\sigma_{e^-p}$ from the system using an independent luminosity determination from the SYMB is presented in Section 7.2.1.

The detectors and trigger of the 12° telescopes are described in Chapter 3, while this section addresses the analysis of the data from the system. The analysis included full representation of the system in the OLYMPUS Monte Carlo simulation, hit reconstruction, track reconstruction, and event selection to produce final yield of elastic $e^\pm p$ events for the luminosity determination. Additionally, this section discusses the performance of the system, the comparison of reconstructed data to Monte Carlo simulation, and the resulting luminosity extraction.

Please note that throughout this section, “12°” will be used as a shorthand to refer to events in which the lepton is reconstructed in the aforementioned tracking telescopes and to the detector system as a whole, even though the actual lepton scattering angles accepted by the telescope varied over a range of several degrees around $\theta = 12^\circ$.

5.2.1 Principle of the Measurement

Since the cross section for elastic $e^\pm p$ scattering increases rapidly as θ decreases, scattering events at forward angles are a natural choice for statistically precise luminosity measurements due to the high rate of events that can be sampled. With this principle in mind, OLYMPUS included dedicated forward tracking elements to expand the acceptance for elastic $e^\pm p$ events to scattering angles as small as 9° for positrons and 11° for electrons. The most backward-going recoiling protons from elastic $e^\pm p$ events where the lepton is accepted by the 12° telescope had $\theta \approx 76^\circ$, meaning they were within the drift chamber acceptance described in Section 3.4. This allowed the exclusive reconstruction of elastic events, providing a strong lever against background contamination while maintaining a high statistics data sample. Figure 5-4 shows an event display of such an event from the data set.

In essence, the determination of the luminosity from the 12° system involved the reconstruction of possible particle hits and tracks in the telescopes and drift chambers for events passing the 12° trigger (Section 3.8.2), and then testing the resulting $e^\pm p$ pairs (selecting on the beam species for elastic kinematics via a series of cuts (Section 5.2.6)). Similar to the main $e^\pm p$ analysis method (Section 6.2), this procedure was followed for both experimental data and digitized Monte Carlo data. Then, for a given simulated integrated luminosity \mathcal{L}_{MC} corresponding to a set of data (correctly simulated beam parameters, detector efficiencies, etc.), the measured integrated luminosity in the 12° system for the set of data is simply a function of the number of elastic events N accepted in data and simulation and the simulated luminosity:

$$\mathcal{L}_{12^\circ} = \frac{N_{\text{data}}}{N_{\text{MC}}(\mathcal{L}_{\text{MC}})} \cdot \mathcal{L}_{\text{MC}}. \quad (5.11)$$

While simple in principle, this method requires a deep understanding of the conditions under which data were taken so that the simulation properly replicates any conditions that could have affected the elastic event yield. While the simulation makes every attempt to faithfully reproduce the data, as described in Section 4.3, simulation parameters are in general considered as possible sources of systematic uncertainty

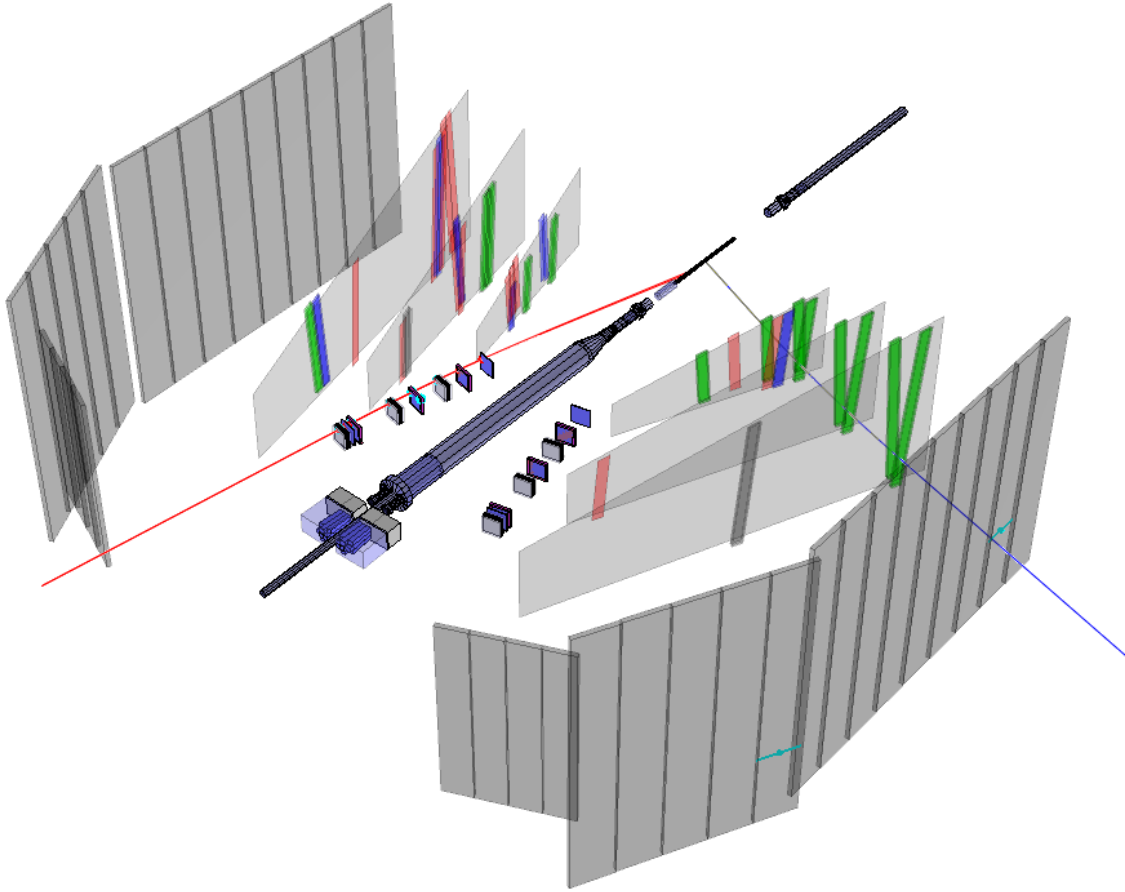


Figure 5-4: A reconstructed elastic e^-p event where the electron (red track) was detected in the right 12° telescope and the proton (blue track) in the left drift chamber. Note the proper rejection of uncorrelated hits in the drift chamber to find the good selection of hits that corresponded to the proton track. The scattering chamber and toroid coils have been removed from the display for clarity.

and are exhaustively analyzed in Section 5.2.8.

In a single data run file (typically with $\sim 1.0 \cdot 10^6$ triggers, lasting ~ 20 minutes), approximately 10,000 total accepted e^-p events or 19,000 accepted e^+p events (due to the differences in the trigger noise conditions between beam species) were recorded. Since simulation could be run to arbitrary statistical precision, the data rate determined the overall statistical uncertainty on the 12° luminosity estimate: approximately 1%/run or 0.5%/hour. Combining the entire data run, the statistical precision is on the order of 0.01% and is thus negligible compared to various systematic uncertainties.

Constraints of a Single Arm Measurement

For the purpose of the analysis presented in this work, the luminosity was determined via the use of exclusively reconstructed $e^\pm p$ events rather than with inclusive events in which the lepton is reconstructed in one of the 12° telescopes, but no requirement is placed on the proton. While the latter has the advantage that it would completely separate the 12° measurement from dependence on drift chamber data and make its independence as a monitor more robust, the differing beam environments between e^- and e^+ running made a single-arm inclusive measurement extremely difficult. In particular, during electron running the rate of hits in the ToF bars that were part of the 12° system trigger were considerably higher than during positron running, which led to an increased rate of triggers from non-elastic events for e^- running.

When attempting a single-arm analysis, it was found that the ratio of the positron rate to the electron rate was approximately 2% lower than the ratio found by an exclusive analysis due to this increased background in the electron sample. While using information such as ToF meantime and energy deposition could recover some of this difference, it could not discriminate against events with multiple ToF hits in the 12° trigger window and the simplicity of the ToF-only data did not provide a strong separation of good elastically scattered protons. Additionally, as will be discussed in Section 5.2.2, the final analysis made use only of the MWPCs as tracking elements. Due to this, the resolution on the kinematic parameters of the reconstructed lepton was quite limited. This made a background subtraction scheme like the one used for the main analysis (Section 6.2.3) a dubious approach. Due to this, it was determined that the systematic uncertainty inherent in an inclusive measurement was greater than the systematic uncertainty introduced by requiring proton track information from the drift chambers. Thus, this work predominantly considers the exclusive measurement.

Possible Contribution of TPE

Fundamentally, the measurement of the luminosity using elastic $e^\pm p$ scattering in the 12° system as a normalization point for the measurement of $\sigma_{e^+p}/\sigma_{e^-p}$ is limited by

the fact that it involves the same physics process that is being examined for TPE contributions. While the vast majority of theoretical and phenomenological models predict that TPE should be small (or at least negligible compared to systematic effects) in the kinematic region accepted by the 12° system [37, 39–47], there exists very little experimental evidence to validate these predictions. The effect of this assumption is considered as a systematic uncertainty for the luminosity determination, and is discussed in detail in Section 5.2.8. Also considered in this work, however, is the measurement of the value of $\sigma_{e+p}/\sigma_{e-p}$ in this kinematic region, using the SYMB system to provide the luminosity normalization, and this is discussed in Section 7.2.1.

5.2.2 Discussion of the Exclusion of the GEM Detectors

As previously noted, the GEM detectors that were part of the 12° telescopes were not utilized in the luminosity analysis presented in this work. When closely examined in the course of studying their performance during data-taking, it was found that they exhibited a strong, time-dependent variation in their efficiency for detection of particles on the order of 10%. The essence of this issue is illustrated in Figure 5-5, which shows the variation in the number of six-plane accepted tracks (i.e., events in which each GEM contributed a hit) relative to the number of accepted tracks using only the MWPC hits. While it would be expected that few six-plane tracks would be found (both due to the smaller acceptance covered by all six planes relative to the MWPCs only and the influence of single plane inefficiencies), it would be expected that the value of the ratio would be constant to within statistical variation over the course of data-taking. Furthermore, this variation in efficiency was found to be almost entirely correlated between the GEM planes within a telescope (i.e., all three GEMs dropped in efficiency together, possibly on an event-by-event basis). This was discovered by noting that the structures present in Figure 5-5 persist even when relaxing the tracking conditions to demand only four planes. To require four planes, however, at least one GEM must supply a hit for the track. Requiring even a single GEM induced the structure in the measured yield of elastic events, indicating that the efficiency of the GEM planes varied in a strongly correlated way.

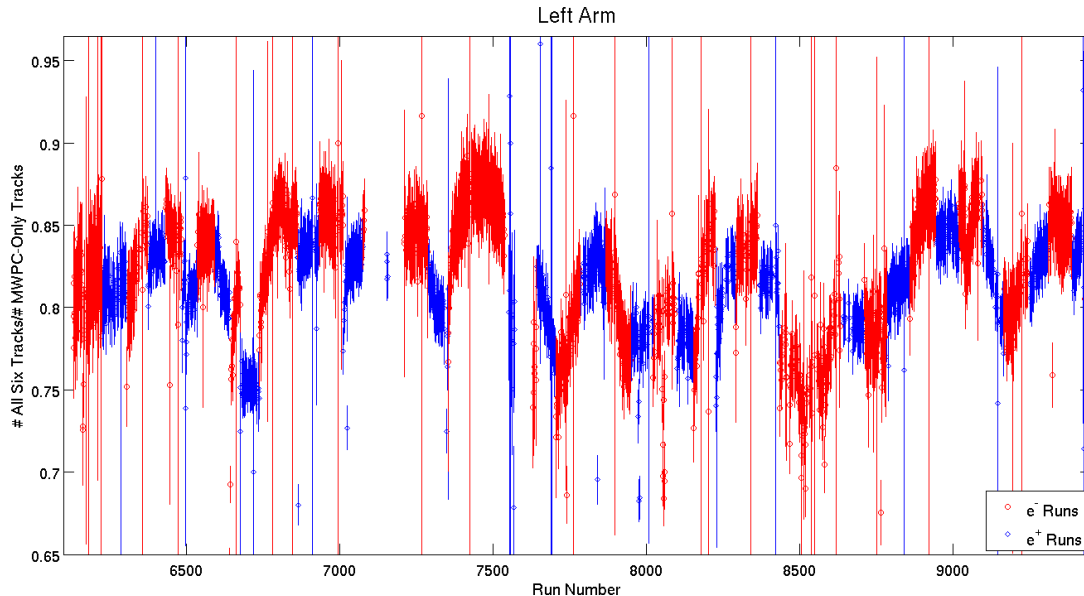


Figure 5-5: Ratio of accepted six-plane 12° system tracks in the left arm to the number of accepted MWPC-only three plane tracks as a function of OLYMPUS run index. The strong structures that vary with run index indicated a severe problem with the GEMs, which prevented their use for the final luminosity analysis.

When this was discovered, a large effort was undertaken to attempt to determine its cause and rectify the issue to permit the use of the GEMs in the 12° analysis. The algorithms for hit-finding in the GEMs (Section 5.2.3) and track reconstruction in the 12° telescopes (Section 5.2.4) were completely redone in an attempt to solve the problem. A great deal of improvements were made through this process, including improving the overall efficiency of the GEM planes and tracking, but no changes that were made significantly affected the observed time dependence in the GEM hit yields. While the various changes in the efficiency over time could be roughly correlated with changes in beam conditions, these effects were not sufficiently quantifiable to produce a solution. Based on this, it is theorized that the root cause of the issue was a saturation effect in the GEM readout electronics that caused a varying, unknown deadtime for GEM hits, which gave rise to the observed inefficiency effects. Ultimately, the exact cause of this time-varying efficiency was not definitively identified, but seemed to be associated with the readout system of the GEMs and its behavior as a function of hit rate/beam conditions. This should be diligently kept in mind when considering

the use of the OLYMPUS GEMs in future experiments [133, 134].

Due to the correlation in this efficiency variation, the GEMs were fundamentally prevented from measuring event rates (absolute or relatively). Any attempt to correct for the time-variation (i.e., by varying the simulated efficiency of the telescope and/or planes over time) would amount to a manual scaling of the simulated yield, effectively nullifying the measurement of the elastic rate as an indicator of the luminosity. While it is conceivable that GEM hits could be used if present without requiring them, this still would require implementing the time variance in the efficiency in simulation in order to replicate the tracking resolution of the data in the simulation. Due to the uncertainty this would introduce if not properly accounted for (and the fact that it would still introduce a manually-inserted variation in detector response into the simulation), it was decided that the GEMs could not be part of the actual yield determination in the 12° system. Hit information from the GEMs was still useful in tracking for applications in which absolute rate information was not required, such as measuring the efficiencies of the MWPCs and SiPM scintillators (after checking to ensure no cross-system correlation was present) and measuring detector misalignment using tracks.

5.2.3 Hit Reconstruction

The first step in reconstructing particle trajectories for particles in the 12° system was to generate hit positions in the detector planes from the system's raw data. A new hit-finder for the GEMs was written "from-scratch" for the GEMs, partially in an attempt to remedy the issues described in Section 5.2.2. While the new algorithm did not remedy the time-dependent issue, it did significantly improve the performance of the GEMs in many regards. Due to this, and the fact that the GEMs may be used in future experiments, this new hit-finder is described here. For the MWPCs, a functional hit-finder was available based on the code used for the HERMES experiment MWPCs [184], and so only the basic elements of this algorithm and the improvements made are discussed.

GEM Detectors

While the GEMs were not used in the final analysis, a large effort was undertaken to improve their hit-finding routines relative to the original algorithms used, not only in the process of attempting to solve the issues discussed in Section 5.2.2, but also to increase their resolution and efficiency for usage in calibration analyses. The two crossing patterns of the readout planes of the GEMs (described in Section 3.5.3) essentially provided independent 1D hit information. An example of such a 1D hit is shown in Figure 5-6. The basic strategy used in hit-finding for GEM detectors like the ones used in OLYMPUS is to find hit candidates (peaks/maxima) in the 1D data samples, and then combine 1D hits in the same planes to form 2D hit candidates. Note, however, that the number of candidates scales multiplicatively with the number of 1D hits from each axis. To combat this, most GEM systems (including the OLYMPUS detectors) are designed to share the charge signal as equally as possible between the dimensions of the readout so that the magnitude of the 1D hits can be compared so as to indicate better which pairs of 1D hits go together to properly form a 2D hit [185,186].

The OLYMPUS GEMs presented several specific challenges with regard to hit-finding that were addressed in the improved hit-finder (relative to the original software used on the experiment) that is described here:

1. strips with weak amplification and/or bad data transfer, which occurred both randomly among the ADC channels and in a periodic pattern at the edges of the four connectors used used to read out each APV (see as a grid pattern in Figure 5-7),
2. different ADC baseline/pedestals between the two APVs covering a single plane dimension, which made it difficult to reconstruct hits at the boundary between two APVs (seen in the blue points in Figure 5-6),
3. channel-to-channel ADC pedestal variation on top of the common-mode variation, and

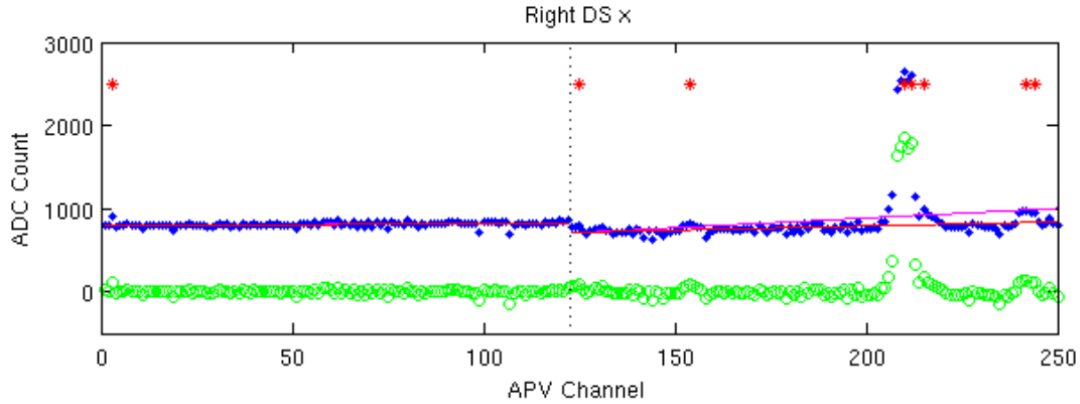


Figure 5-6: An example of how a charged particle passing through one of the OLYMPUS GEM planes creates a signal visible in the 1D data from one of the strip/pad patterns on the readout plane. The blue points correspond to the raw ADC counts registered on each ADC change (each channel corresponds to a single readout strip or connected strip of pads), and the green represents the ADC data after a baseline/pedestal subtraction. Red points indicate a first pass attempt at identifying local maxima in the data as a first step in hit-finding. In this event, a clearly identifiable hit occurs around APV Channel 210 with a possible smaller hit around Channel 240. The vertical dotted line represents the break between the two separate APV cards used to readout a single dimension of the plane.

4. other large-scale problems such as failed APV cards on the middle GEM in the left telescope.

The new hit-finding algorithm addressed these issues to significantly increase the overall efficiencies of the detectors and to reduce the structural inefficiencies shown in Figure 5-7, but did not affect the time-dependent behavior of the GEM hit yields discussed in Section 5.2.2.

The new GEM hit-finder proceeded as follows⁴:

1. Raw channel-by-channel ADC counts were mapped to their corresponding local coordinates in the GEM planes (x and y).
2. A first pass was made over all events in a given data run file in which a 12° trigger fired in which a line was fit to the ADC count as a function of channel number (properly ordered) for each APV card (two cards per dimension per

⁴The source code (C++) for this hit-finding algorithm, along with basic documentation, is available from the author for academic applications.

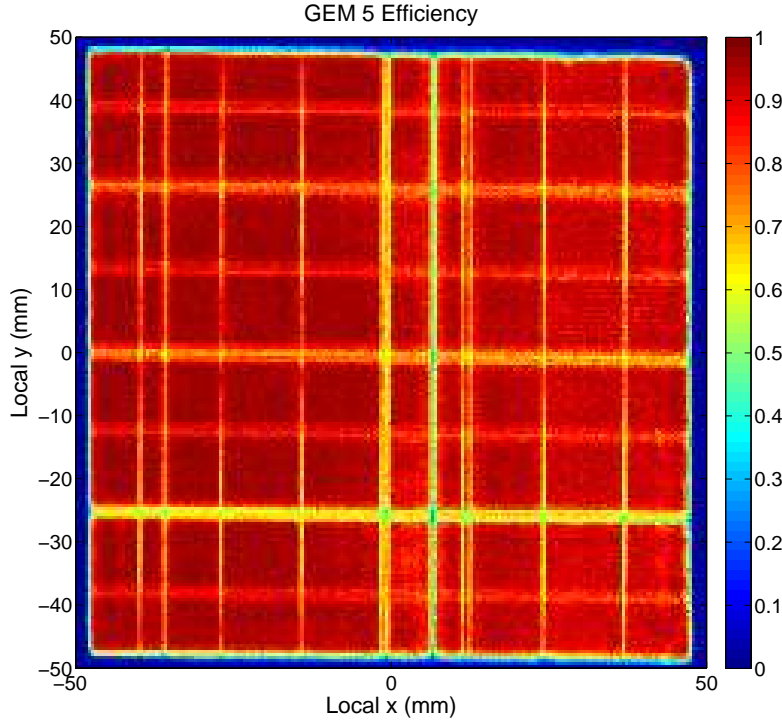


Figure 5-7: Efficiency for hit reconstruction of GEM 5 (the furthest downstream GEM in the right telescope), using the previous hit-finding algorithm. Note the periodic occurrence of inefficient regions, as well as other random strips with low efficiencies caused by the issues discussed in the text. The improved efficiency of this GEM, as well as of the others, is shown in Figure 5-14.

plane) to calculate the common-mode pedestal for the channels. A rudimentary 1D peak-finding algorithm was used to remove points near a possible hit so as to avoid biasing the baseline fit. This procedure is illustrated by the magenta (without peak removal) and red (with peak removal) lines shown in Figure 5-6. The previous hit finding algorithm did not correct for possible hits in the baseline removal, which made the procedure prone to rejecting hits, especially near the edge of an APV card. This created regions of strong inefficiency along the central axes of the planes.

3. After the first pass over the data, the mean and variance over all baseline fits of the separation of a single ADC channel count from the fit baseline on each event were calculated. While the baseline fluctuated event-by-event, it was

found that single channels exhibited predictably low or high counts relative to neighboring channels with a width that varied by channel as well, as can be seen in Figure 5-8. The mean deviations and width of the distributions for each channel saved to adjust the pedestal subtraction from the value suggested by the baseline subtraction alone. No such channel-to-channel correction was made in the previous algorithm, which allowed the new algorithm to recover hits from channels with lower average counts and reject spurious highs from high-count channels.

4. The data were then passed-over a second time, again event-by-event. Each ADC channel was adjusted by the baseline+deviation pedestal computed in the first pass. Local maxima in the ADC channels were identified (using thresholds based on the widths from Step 3), and all pairings of x and y minima were considered. Pairings were scored based on the relative match of the x and y signal strengths as well as the absolute total strength of the pairing. The user then chose how to select which hits to pass to the tracking algorithm from among the scored hits (e.g., with minimum accepted scores, passing the highest-scoring hits, etc.). A visualization of identified hits with comparison to the hits identified by the old algorithm is shown in Figure 5-9.

This new hit-finder succeeded in increasing the overall efficiencies of the GEMs by 5-10% and greatly reduced the structure in the efficiencies across the planes. The resulting efficiencies are shown in Figure 5-14 in Section 5.2.5. While the time-dependence of the GEM efficiencies did not ultimately arise from a hit-finding issue, this improved hit-finder was useful in allowing the GEMs to provide better data for calibration of the 12° system and should be useful for future experiments that use the OLYMPUS GEMs.

MWPC Detectors

Due to the relative simplicity of the MWPC hit information (see Section 3.5.4), hit-finding for the MWPCs did not require the same complexity of analysis as the GEM

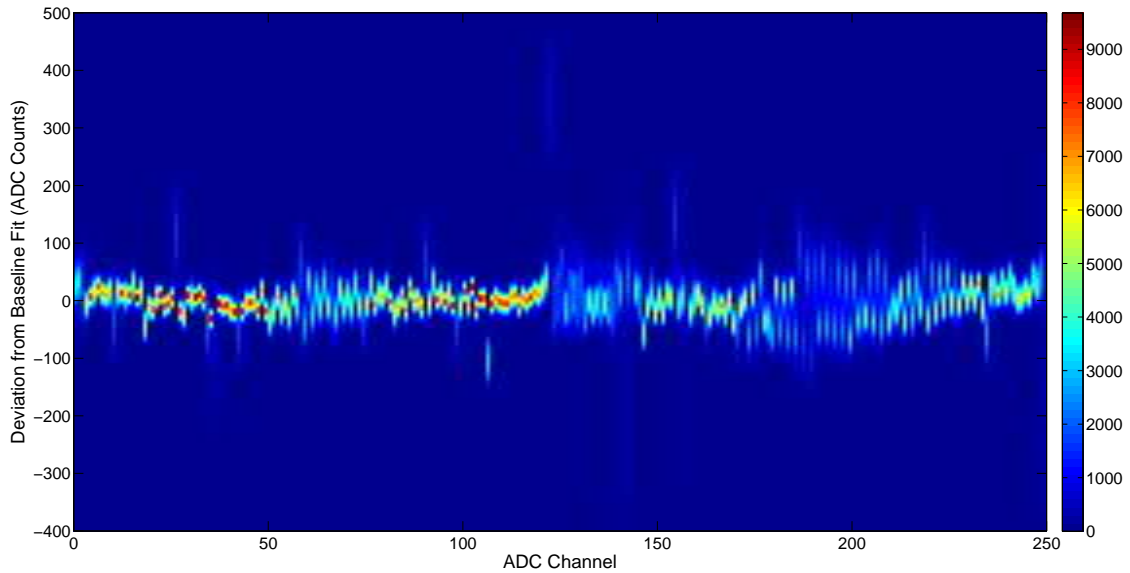


Figure 5-8: Histogram of the average deviation of the ADC count in each channel along one dimension of one of the GEMs. As can be seen channels typically exhibited a clear mean deviation that could be used to correct the pedestal subtraction for that channel and a definable width that could be used to set the noise threshold for hit candidates for each channel.

hit-finder. Initial hit decisions for single wires were produced by software adapted from the software used for the HERMES experiment MWPCs [142, 184] adapted by the PNPI group. While, in principle, single wire 1D hits could be passed to the track reconstruction algorithm used for the 12° system, the combination of information from the three wires in a chamber provided an important means of rejecting noise hits. Recalling that the MWPC wires in chamber were arranged in three planes such that the wires were oriented at -30° , 0° , and $+30^\circ$ relative to vertical in the three planes, local coordinates U , X , and V may be defined perpendicular to the wire orientations in each plane, in addition to local x and y coordinates perpendicular to the sides of the chamber face. This system is illustrated in Figure 5-10. The single wire hit decisions were given corresponding $U/X/V$ coordinates, which can then be converted to the plane coordinates via the following linear combinations:

$$x_X = X, \tag{5.12}$$

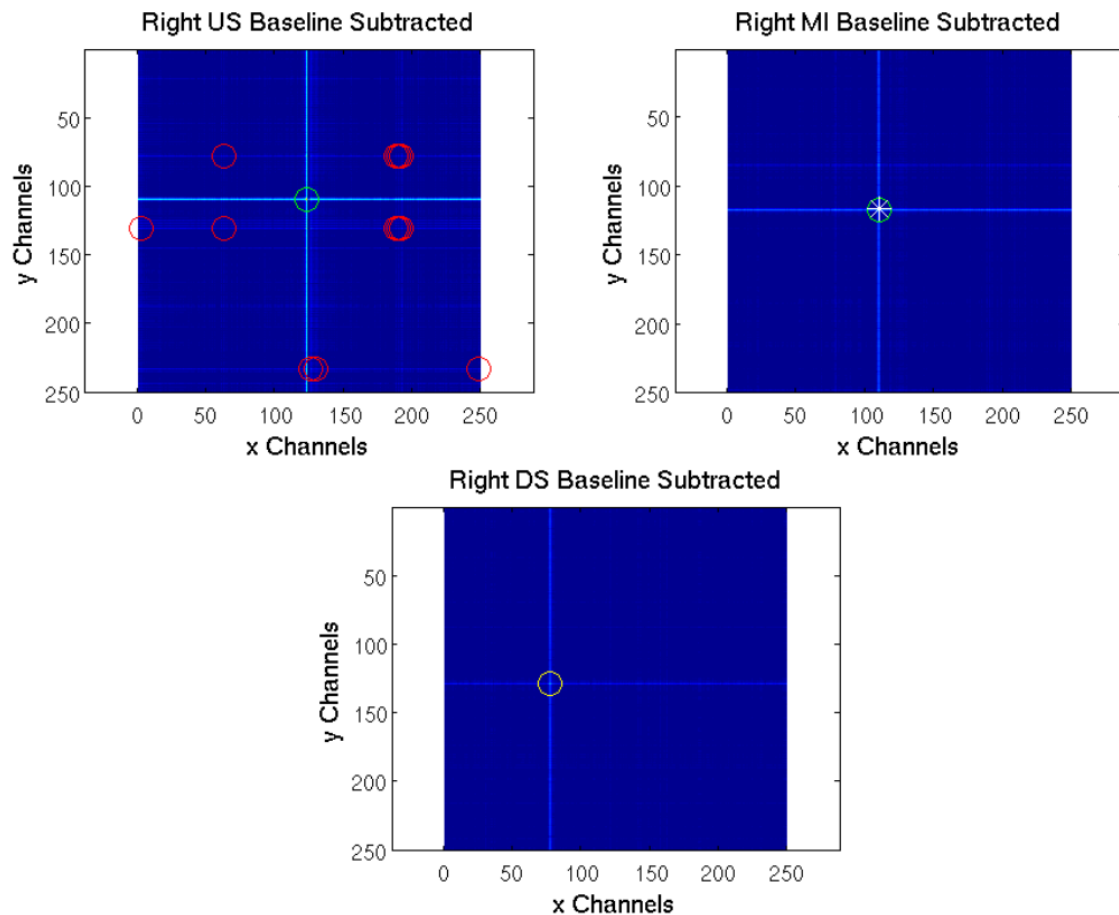


Figure 5-9: Data from the right GEM telescope for a single event (2D histograms of ADC counts) showing the hits identified by the original GEM hit-finding algorithm (white stars) and the new algorithm (circles, colored red, yellow, or green by increasing hit score). The three strongest hits from each plane reconstruct well to an elastically scattered lepton that would have been missed by the old algorithm due to the missed hits in the upstream (US) and downstream (DS) planes. The upstream hit was missed in the old algorithm due to its x location near the APV card boundary, while the downstream hit was missed due to its relatively weak signal and being near the y APV card boundary. For the latter, the new baseline subtraction methods allowed the hit to be separated from the noise.

$$x_{UV} = \frac{U + V}{\sqrt{3}}, \quad (5.13)$$

$$y_{UV} = U - V. \quad (5.14)$$

Note that there are only three linearly independent combinations that form x and y since there are three inputs U , X , and V (e.g.; $y_{XV} = \sqrt{3}X - 2V = \sqrt{3}(x_X - x_{UV}) + y_{UV}$). In constructing MWPC hits, all combinations of hits on the U , X , and V

planes within a single chamber on a given event were considered. Any combinations with $|x_X - x_{UV}| > 4$ mm were rejected as bad combinations. The 4 mm cutoff was chosen by studying tracks that were reconstructed with the other five planes of the telescope, and identifying hits in the unused sixth plane that appeared correlated with the track (i.e., that were good hits). The boundary was chosen to ensure that such good hits were not cut. While this cut was wide, it was chosen to exclude as few good hits as possible since hits from all three MWPCs in a telescope were required for tracks in the final analysis. The resulting higher hit multiplicity was handled by the tracking algorithm described in the next section.

The final local hit coordinates for a given plane that were passed to the tracking algorithm were a weighted average of the independent x constructions (since x corresponded to the bending direction of the field and thus was the direction in which maximum resolution was desired), while y_{UV} was used for the y coordinate. That is:

$$x = \frac{2x_X + 3x_{UV}}{5}, \quad (5.15)$$

$$y = y_{UV}. \quad (5.16)$$

5.2.4 Tracking in the 12° Telescope

While the reconstruction of the scattered proton in 12° events was conducted using the main drift chamber tracker described in Section 4.2, the 12° telescopes utilized a separate tracking system that allowed greater flexibility than the main tracker. This was possible due to the relative simplicity of reconstruction in the 12° telescopes compared to the drift chambers in which the reconstruction is complicated by the uncertainty in the drift time-to-distance calibration and the duplicity of each recorded hit. While the drift chamber tracking was constrained to generate event vertices along the line of the beam due to its kinematic look-up library (“fasttrack”), the 12° tracker had full freedom to determine all five kinematic parameters of tracks passing through the telescopes. This allowed the surveyed positions and orientations of the 12° system

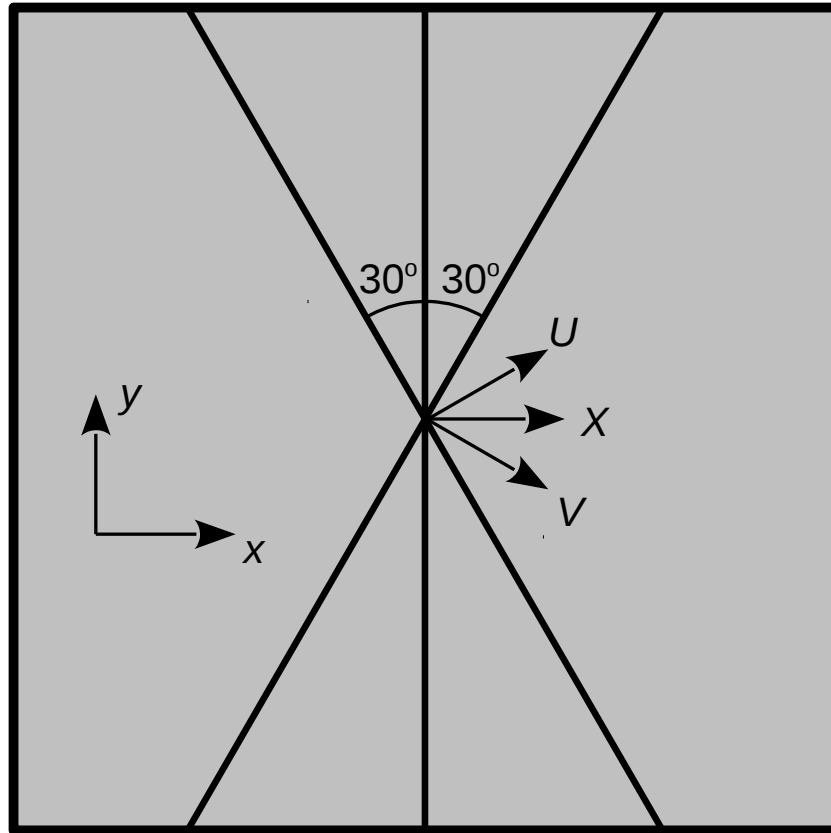


Figure 5-10: Local coordinate system used for the MWPC detector hit finding. The U , X , and V coordinates measure distances along the perpendiculars to the different wire orientations, which may be converted via linear combinations to the local coordinates x and y that are used for the final hit positions. The local x coordinate points away from the beamline in both telescopes, while y points up in the left MWPCs and down in the right MWPCs.

to be well-verified, since the tracking was able to reproduce measured beam positions and expected target distributions with no input of such information.

The first stage of the 12° tracker was a candidate forming algorithm, which was necessary due to the very high rate of particles scattered in the regions forward of the drift chambers (either from the target region or upstream of experiment) that caused a high rate of noise hits in the 12° detector planes. For the tracking used in the final analysis, only the MWPC hits were used and so track candidates were first formed of all possible combinations of a hit in each of the three planes in the telescope for a given event. For each of these three hit combinations, the sagitta (i.e., the distance

of the middle hit from the line connecting the hits in the inner and outer planes) was computed. Using a large library of simulated events created using the radiative elastic event generator for both lepton species, the expected distribution of the value of the sagitta of MWPC tracks for good events was constructed. The distribution of sagittas in simulation is shown in Figure 5-11. While the peak value of the sagitta for elastic events was slightly offset between the two species due to the magnetic field, both peaked near 2 mm and had similar widths. Visual inspection of events with sagittas greater than 5 mm indicated that the vast majority of these events involved hard scattering from a metallic element of the detector, and thus these events were not good events for the purpose of the analysis. Thus, for both species a cut was placed at 5 mm for the maximum value of the sagitta for a candidate to be passed to the track fitting algorithm. In data, this cut 25%–30% of three-hit candidates (predominantly with sagittas greater than 10 mm, a region where simulation indicates there were no good events). When tracking with the GEMs additional information regarding the correlation of hits positions in adjacent GEM/MWPC pairs could be used to further clean the track candidate sample; this is not discussed in detail here as it was not a component of the final analysis.

The hits belonging to a selected candidate were passed as local coordinates in the detector planes to the tracking algorithm. The tracking algorithm utilized the GEANT4E extension to GEANT4, that propagated tracks through the simulated OLYMPUS geometry and magnetic field according to the most probable energy loss rather than determining energy losses via Monte Carlo [155, 187]. In this scheme, a track propagated through a given geometry and field with given initial conditions behaves deterministically as it traverses the detector system. This propagation was iterated with the initial conditions (θ , ϕ , $|\mathbf{p}|$, y , and z at the event vertex) free to vary so as to minimize the residuals between the recorded hit positions in data and the propagated hit positions generated by the GEANT4E simulation. The minimization of the residuals was conducted using a Levenberg-Marquardt minimization routine, as implemented by the C/C++ Minpack libraries [188–190]. While a relatively slow method of tracking compared to other algorithms, the relatively small number of 12°

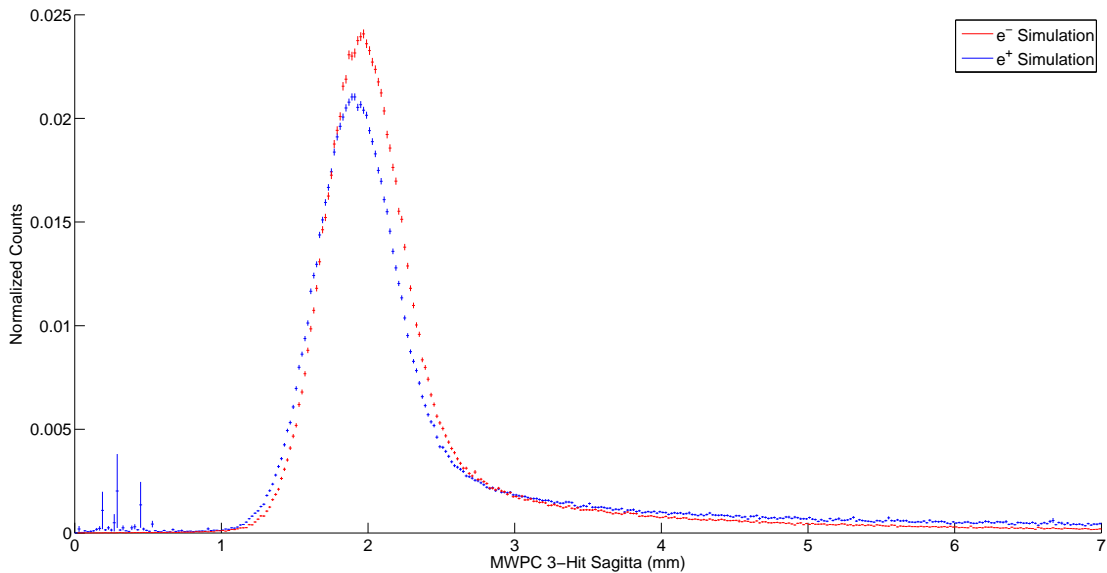


Figure 5-11: Distribution of the sagittas for track candidates consisting of three MWPC hits in simulation for each species in simulation. The clear peak value, similarity of the distributions to those seen in data, and verification that events in the long tail of the distribution corresponded to unwanted events permitted the sagitta to serve as a useful cut against unwanted hit combinations to save time when tracking events.

events (compared to those handled by the drift chamber tracking) in the OLYMPUS trigger sample allowed the use of the tracker to take advantage of its complete kinematic freedom in performing alignment calibrations, assessing resolutions, etc.

5.2.5 System Performance

This section discusses various relevant aspects of the performance of the 12° system during the OLYMPUS data runs and the methods used to make the performance assessments. In general, the system performed consistently and well throughout data-taking (with the exception of the previously mentioned GEM issues). The redundancy of the system with the inclusion of GEM data allowed precise assessment of the efficiencies and resolutions of the trigger and MWPC planes, providing high confidence in the simulation implementation of those detectors.

Detector Efficiencies

To provide an accurate measure of both the absolute and species-relative luminosities, it was critical to determine and properly simulate the efficiencies of the various components of the 12° system. In general, these efficiencies were measured to very high precision using fully reconstructed events with the detector of interest removed, which was made possible by the high redundancy of the 12° telescopes. The methods and results of the efficiency determinations for each subsystem are described in this section.

SiPM Scintillator Planes The performance of the SiPM trigger planes was evaluated using the lead glass calorimeters and the associated trigger described in Sections 3.5.2 and 3.8.2. Since electron and positron events were distributed differently across the trigger planes, it was important to measure any inconsistencies in efficiency across the planes for implementation in the simulation.

A large sample of lead glass trigger events was compiled, and all possible six-plane tracks from the 12° telescopes in this sample were constructed. Six-plane tracks were used so as to achieve the best projected position resolution for the tracks in the scintillator planes. The standard elastic sample cuts for the 12° analysis (described in Section 5.2.6) were used to ensure that the tracks represented good, relevant events for the purpose of the study. For each track, the trajectory of the track was propagated using the GEANT4E tracker to the planes of the scintillator tiles. For each plane, if the plane recorded a hit for that event the corresponding position bin was marked efficient for the event. Approximately 3 million tracked events per telescope were used to generate the efficiency maps shown in Figure 5-12, which were implemented in the digitization of the 12° trigger for the simulation. In the regions of the planes corresponding to the kinematic acceptance of the telescopes for tracks, the efficiency of the planes was in excess of 97% and typically higher ($\gtrsim 99\%$). By comparing subsets of the data sample, it was determined that no significant time dependence or beam species/running condition dependence affected the SiPM plane efficiencies.

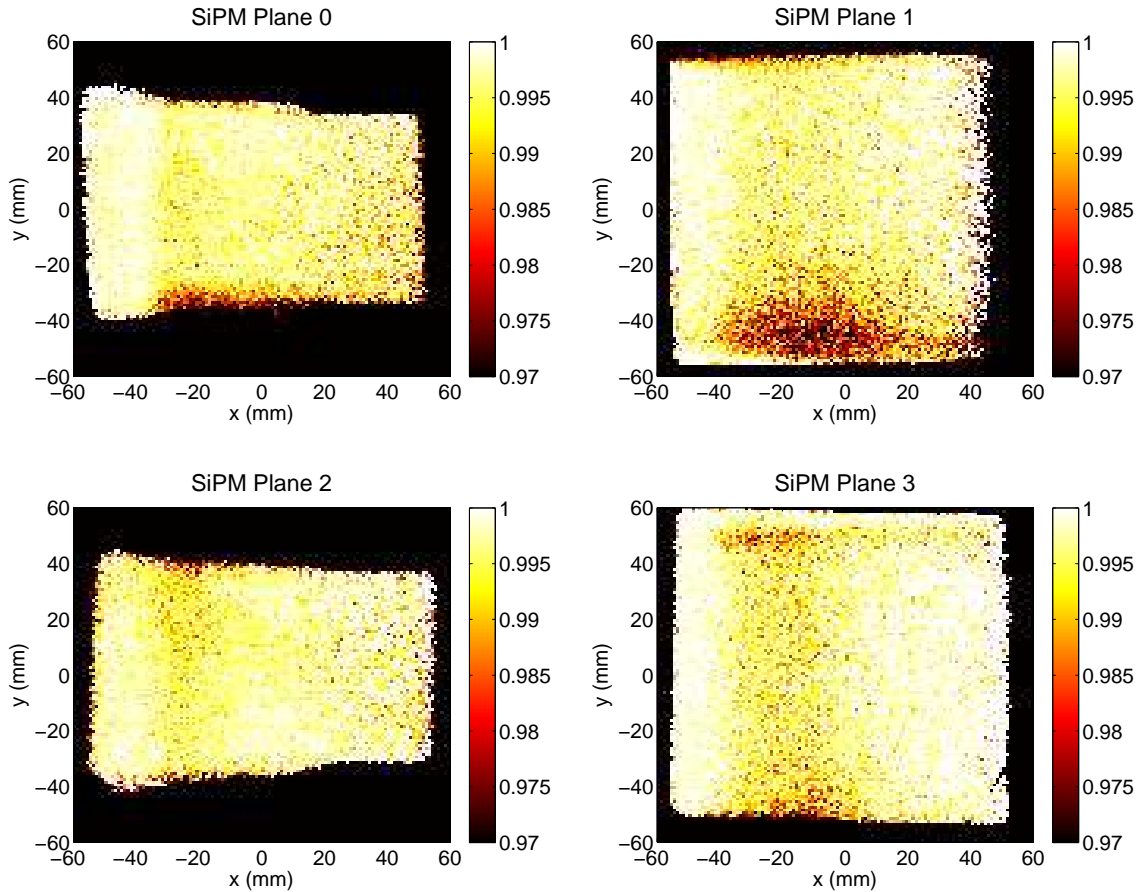


Figure 5-12: Efficiency maps for the four SiPM-instrumented scintillator tiles used for the 12° trigger. The x and y coordinates in each plot represent the local detector coordinates of each plane, which follow the convention in which x points away from the beamline and y points up in the left sector and down in the right. Note that due to acceptance constraints (determined by the outermost detectors in the telescopes (MWPCs 2 and 5)), the inner planes (0 and 2) in each telescope are not completely illuminated by tracks.

MWPC Detectors As the MWPC planes were critical to the ultimate measurement of the luminosity in the 12° system, proper implementation of their efficiencies in the simulation was also critical for the same reasons as for the SiPM plane efficiencies. Due to the redundancy of the 12° tracking system, it was straightforward to measure the MWPC plane efficiencies using the main trigger and tracking with hits from the other five planes in the telescope aside from the plane being assessed. For a large fraction of the data set (including data from all time periods used in the

final analysis), tracks were reconstructed in the 12° system using all five-plane combinations to check the efficiency of the sixth unused plane in each set using the same methodology as described for the SiPM planes. The MWPC planes were found to have extremely high and consistent efficiency, both across the face of each plane and as a function of time. Notably, the three planes in the right sector telescope had five known inactive wires (due to bad connections, malfunctioning ADC channels, etc.) that were easily identified by this analysis, serving as a proof of the validity of the analysis. Figure 5-13 presents the efficiency maps for each plane.

GEM Detectors The same method used for the MWPC efficiencies was applied to measure the efficiencies of the individual GEM planes, the results of which are shown in Figure 5-14. While the efficiency with the new hit-finding algorithm was improved significantly over that with the old algorithm (Figure 5-7, the time-dependence problem of the overall efficiency was not solved, as previously discussed. Some “striping” from weak channels remained in the new efficiency maps (as well as small regions of lower efficiency due to defects in the readout planes in GEMs 1 and 4, as well as the larger region in GEM 1 due to a known bad APV), but in general the new hit-finder recovered a significant number of hits in the regions in which the GEM data was challenging.

Hit Resolution

The hit resolution in the MWPCs was fundamentally limited by the discrete nature of the detector’s readout, which provided hits at specific wire locations spaced by approximately 1 mm. While the placing of the wires was not exact (due to the wires being soldered by hand to the detector frames), the uncertainty on this placement ($\mathcal{O}(0.1\text{ mm})$) was considerably less than the wire spacing and randomly distributed about the nominal placement, and thus effectively negligible to the overall hit position resolution. Propagating an uncertainty of 0.5 mm on each individual MWPC plane coordinates (U , X , and V) through Equations 5.15 and 5.16, and approximately accounting for the correlation of hits in the three planes results in the approximate

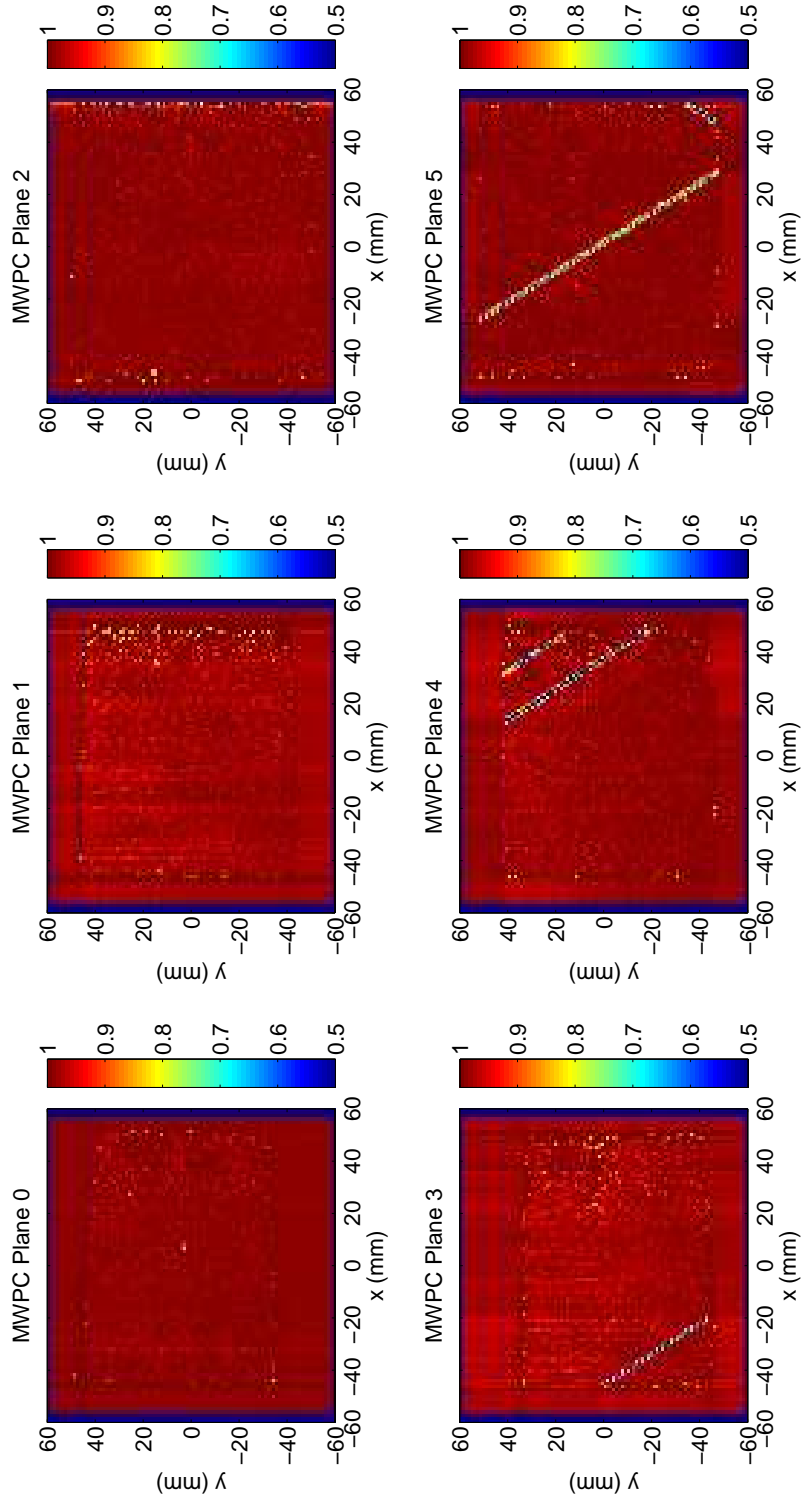


Figure 5-13: Efficiency maps for the six multi-wire proportional chambers used in the 12° luminosity telescopes. The x and y coordinates in each plot represent the local detector coordinates of each plane, which follow the convention in which x points away from the beamline and y points up in the left sector and down in the right. It is notable that all six chambers exhibit remarkably consistent and high ($>98\%$) away from the five known inactive wires in the right side detectors (Planes 3-5).

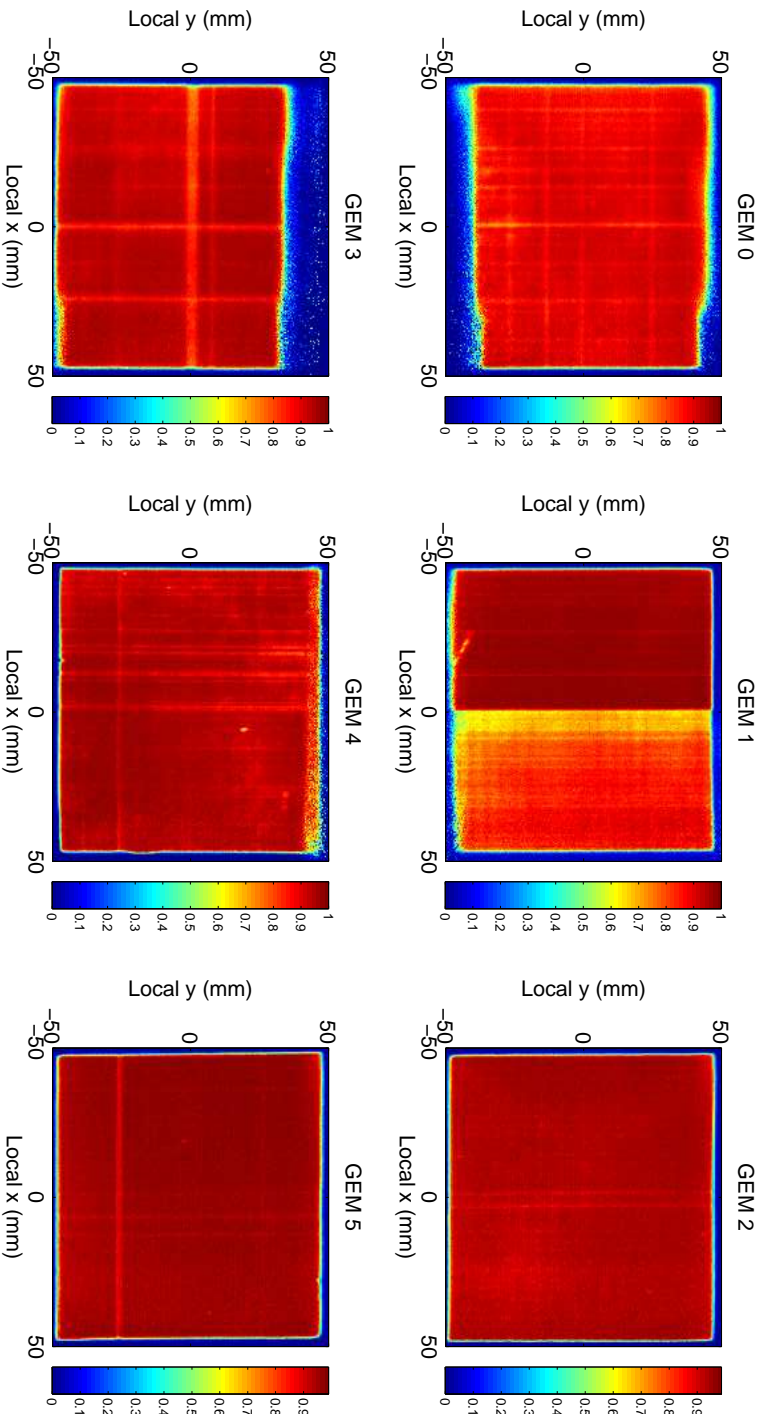


Figure 5-14: Efficiency maps for the six GEMs used in the 12° luminosity telescopes, using the new GEM hit-finder described in Section 5.2.3. Note that GEM 1 operated with a known bad APV for its $+x$ data (and no instrumentation for its y data), and the inner GEMs (0 and 3) were not completely illuminated due to constraints in the acceptance from the other detector and trigger planes. The efficiency with the new algorithm was significantly better than that with the previous hit-finding method (Figure 5-7). The efficiency data shown here was sampled for specific runs, but was found to vary approximately uniformly across each plane as a function of time as discussed in Section 5.2.2. The x and y coordinates in each plot represent the local detector coordinates of each plane, which follow the convention in which x points away from the beamline and y points up in the left sector and down in the right.

reconstructed hit uncertainties of:

$$\Delta x \approx 0.25 \text{ mm}, \quad (5.17)$$

$$\Delta y \approx 0.50 \text{ mm}, \quad (5.18)$$

in the local MWPC coordinates. In general, this calculation was found to be consistent with both data and simulation. Regarding the GEM hit resolution, a careful study was not completed for this work since the GEM hit-finder was not fully optimized after it became clear that the use of the GEMs in final luminosity analyses was precluded. In general, however, resolutions of order $50 \mu\text{m}$ are likely achievable.

Lepton Tracking Efficiency

A lower bound on the lepton tracking efficiency was found by comparing the number of simulation events for which the generated kinematics were within the cuts described in Section 5.2.6 and a candidate set of hits was produced according to the scheme discussed in Section 5.2.4 to the number of successfully tracked leptons from such candidates. This study found that the tracking algorithm produced a valid lepton track for 96.67% of such candidates, with a very small lepton species difference (discussed in Section 5.2.8). Note, however, that this is a conservative lower bound on the tracking efficiency since many of the events missed correspond to events in which the lepton underwent a hard scatter from an element of the target or detector system. This process occurs in both simulation and data, and such events cannot be reasonably reconstructed and used in an elastic $e^\pm p$ event sample. Visual inspection of such events indicated that tracks missed in the inefficient sample very frequently corresponded to such hard-scatter anomalies.

Lepton Tracking Resolutions

The resolution of the tracking in the 12° system (as it pertains to the analysis in which the GEM detectors were not included) was fundamentally limited by the resolution of the MWPC hit reconstruction rather than limitations of the tracking scheme. Table

5.1 summarizes some of the main tracking resolution parameters estimated from the combined dataset used in the analysis. The resolutions were not found to vary between beam species, and the simulation digitization was developed so as to properly replicate the data resolutions to the extent possible. Examples of the distributions of parameters presented in the table may be found in Section 5.2.7. Since the MW-PCs were designed to sacrifice resolution in the vertical direction for extra sensitivity to the horizontal direction (the direction of the field bending), the resolution in reconstructed θ was considerably better than that in ϕ . In general, the momentum resolution is quite wide. While this complicates event selection, it also reduces uncertainties due to radiative corrections that could otherwise be large due to the relatively narrow acceptance of the telescopes. Naturally, reconstructed parameters involving $e^\pm p$ pairs convolve the resolutions of the 12° and drift chamber tracking, which is briefly discussed in Section 4.2 but covered in more detail in References [53] and [54]. Inclusion of the GEM detectors improves the resolution by a significant factor (nearly an order of magnitude in some parameters), but no complete quantitative study of this has been completed.

Parameter	Estimated Resolution
Vertex y position	3.5 mm
Vertex z position	50 mm
Lepton momentum	310 MeV
θ	0.1°
ϕ	0.4°

Table 5.1: A summary of approximate estimates of the resolution achieved for several kinematic parameters for the tracking of $e^\pm p$ leptons in the 12° telescopes.

5.2.6 Method of Analysis

While single-arm inclusive measurements of the luminosity using the 12° system were investigated, it was ultimately determined that an exclusive measurement (requiring the detection of the protons in the $e^\pm p$ scattering events) was the method that could achieve the smallest overall systematic uncertainty in the final absolute and relative

luminosity determinations. This is primarily due to the fact that in a single-arm measurement, contamination from background (i.e., non-elastic $e^\pm p$ events that mimic the signal of such an event (a ~ 1.9 GeV forward lepton with a rearward ToF hit)) would be an appreciable fraction of the sample. While a simple cut on the meantime of the ToF hit rejected a large fraction of this background, the relatively poor resolution associated with tracking only with the three planes of the MWPCs in each telescope made it difficult to properly model and subtract the remaining background due to random ToF hits in the appropriate timing window. Since it was known that rates of random ToF hits during electron beam operation were notably higher than during positron running, it was determined that an inclusive measurement would entail a larger systematic uncertainty than an exclusive measurement (which introduces uncertainty from the tracking of the proton). An exclusive measurement does, however, heavily suppress the background leaving a very clean $e^\pm p$ sample. Tests following the background subtraction scheme described in Section 6.2.3 determined that for the exclusive selection of 12° events the background fraction was $\mathcal{O}(0.1\%)$ and that the species-relative difference in the background was on the order of the statistics of the entire dataset ($\mathcal{O}(0.01\%)$) and thus negligible.

The final analysis combined leptons tracked using the methods described in Section 5.2.4 and protons tracked in the drift chambers using the elastic arms algorithm tracking scheme discussed in Section 4.2.2. The methodology and application to both simulation and data are described in the following sections. This scheme produced the values of the event counts N_{data} and N_{MC} that were used in Equation 5.11 to determine the integrated luminosity.

Exclusive Event Selection Scheme

The exclusive event selection proceeded as follows, looping over all data and simulated event triggers:

1. Determine if the trigger condition met the 12° trigger requirements (Section 3.8.2), and reject the event if not.

2. Using the information from the trigger (which determined which 12° telescope was active for the event), search for hit in one of the valid trigger ToF bars (Figure 3-21) with a large enough meantime ($\gtrsim 12$ ns) to allow the possibility that the hit corresponded to an elastically scattered proton. This cut was chosen so as to be only a very wide selection against fast lepton backgrounds from the target and to err on the side of inclusiveness rather than rejecting possible protons. If no such ToF hit was present, the event was rejected.
3. Create all possible pairing of properly charged leptons according to the track bending (i.e., e^+ or e^- determined by the beam species) in the specified telescope and identified proton tracks in the opposite side drift chambers. If no such pair exists, reject the event.
4. Select the pair from among the created pairs (multiple-pair events accounted for $\ll 1\%$ of events at this step), which minimizes the resolution-weighted sum of the cut parameters listed in the next step.
5. Check if the event passes the following cuts (the chosen values of these cuts based on a comprehensive systematic uncertainty analysis are described in the fiducial and elastic cut portions of Section 5.2.8):
 - (a) Fiducial cut on the reconstructed position of the event vertex in global y as determined by the lepton track (the proton tracks did not have flexibility in this dimension)
 - (b) Fiducial cut on the reconstructed position of the event vertex in global z as determined by the average of the two tracks
 - (c) Elastic kinematics cut on the coplanarity ($\Delta\phi \approx 180^\circ$) of the two tracks
 - (d) Elastic kinematics cut on the correlation of the placement of the global z event vertex of the two tracks (Δz)
 - (e) Elastic kinematics cut on the beam energy reconstructed from the angles of the two tracks, assuming elastic kinematics ($E_{\text{beam},\theta} \approx 2010$ MeV)

- (f) Elastic kinematics cut single-arm missing energy of the lepton over the square of the energy as computed by the expected elastic energy from the reconstructed θ ($\Delta E'_\theta/E'^2 \approx 0$)

6. Add the event to the count of elastic events N if all steps are passed.

Note that only one cut that considers reconstructed momentum was used due to the relatively poor momentum resolution of the MWPCs and the difficulty of precisely tracking particles in the back-angle portions of the drift chamber where the tracks traverse the wire layers nearly perpendicularly (resulting in few crossings between cells, which help to provide more precise track positions for tracking). In the course of determining the final event selection method, a number of cut schemes were tested and the boundaries of the cuts were systematically tested as described in Section 5.2.8. This methodology was chosen for its robustness to the weaknesses of the 12° measurement (poor momentum resolution) and its stability under variance of the cuts.

Simulation of 12° Events

Simulated 12° events (used to produce N_{MC}) were treated identically to data events, following the analysis strategy discussed in Chapter 4. The simulation was conducted in the same framework as described for the main analysis in Section 4.3, and the creation of digitized hits in the ToFs and drift chambers (i.e., values from simulation converted to mimic the structure of the experimental data) was conducted using the same methods as for the main $\sigma_{e+p}/\sigma_{e-p}$ analysis. The digitization of the 12° system elements was straightforward, due to the discretized nature of the MWPC U , X , and V plane hits discussed in Section 5.2.3. Recorded energy depositions from the primary particles were associated with discrete wire positions and then simulated MWPC hits were reconstructed in an identical fashion as data hits. Based on the distribution of hits from data that registered on multiple adjacent wires, simulated MWPC hits were allowed to also register on multiple wires and rates randomly drawn from the data distribution. SiPM plane digitization for the trigger was also straightforward, in that

it only involved matching the energy deposition threshold in simulation to a value similar to experimental conditions. Due to the fact that good 12° events produced SiPM hits well above the experimental threshold, the choice of this threshold in simulation was effectively negligible. After hits were constructed in the SiPM planes and MWPCs, they were tested by position against the efficiency maps presented in Section 5.2.5 using a random number drawn against the efficiency. Hits passing the efficiency test were packaged in the same format as the hits produced from data, and from this point simulation data were treated identically to experimental data, ensuring a robust comparison.

5.2.7 Comparison of Data and Simulation

This section provides several figures showing distributions of various kinematic parameters reconstructed by the 12° telescope analysis for both lepton species in data and simulation so as to provide a basic overview of the nature of the data and establish the validity of the data/simulation comparison. While plots of all kinematic parameters would fill many pages, several representative plots that are particular relevant to the analysis are shown. In general, the data/simulation agreement is very good to within resolutions and the conservative cuts applied to the data avoid regions of disagreement due to slight differences in resolution. Note that since the final 12° luminosity measurement (Section 5.2.9) found a result several percent above the slow control estimate for the absolute luminosity (which was used to generate the simulation), the integrals of the distributions shown differ by that factor. Uncertainties caused by these residual data/simulation differences were accounted for when considering the systematic uncertainties due to the various applied cuts. The distributions presented are:

- Q^2 reconstructed from the lepton angle (Figure 5-15),
- vertex z reconstructed by the lepton track (Figure 5-16),
- reconstructed lepton momentum (Figure 5-17), and

- $\Delta E'_\theta/E'^2$, the single arm lepton missing energy relative to the expected energy at the reconstructed θ (Figure 5-18).

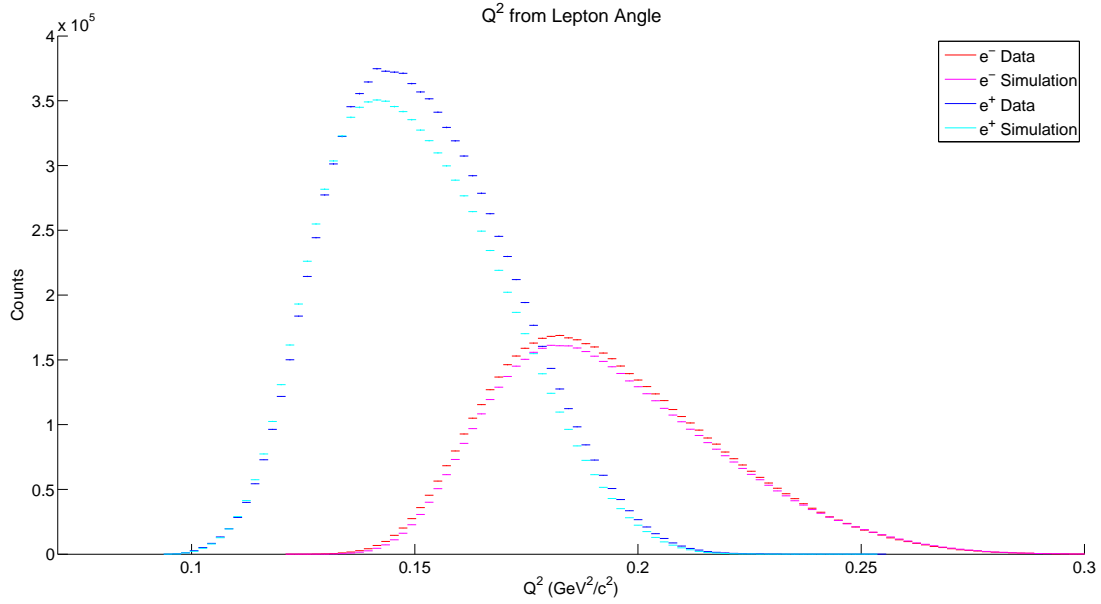


Figure 5-15: Distributions of reconstructed Q^2 for 12° leptons of each species, in data and simulation for the entirety of the data sample.

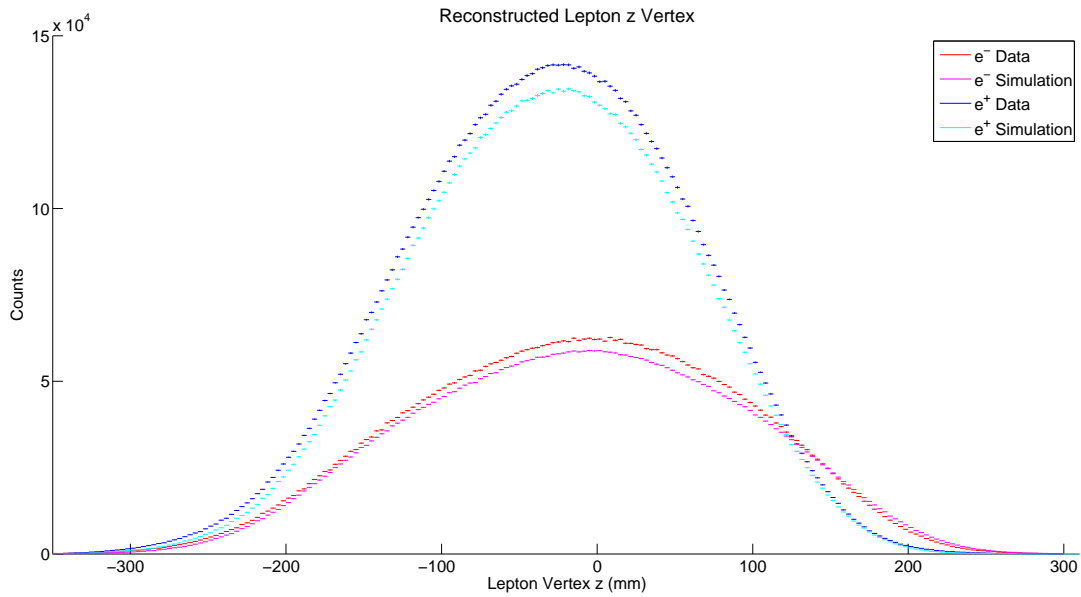


Figure 5-16: Distributions of reconstructed vertex z for 12° leptons of each species, in data and simulation for the entirety of the data sample.

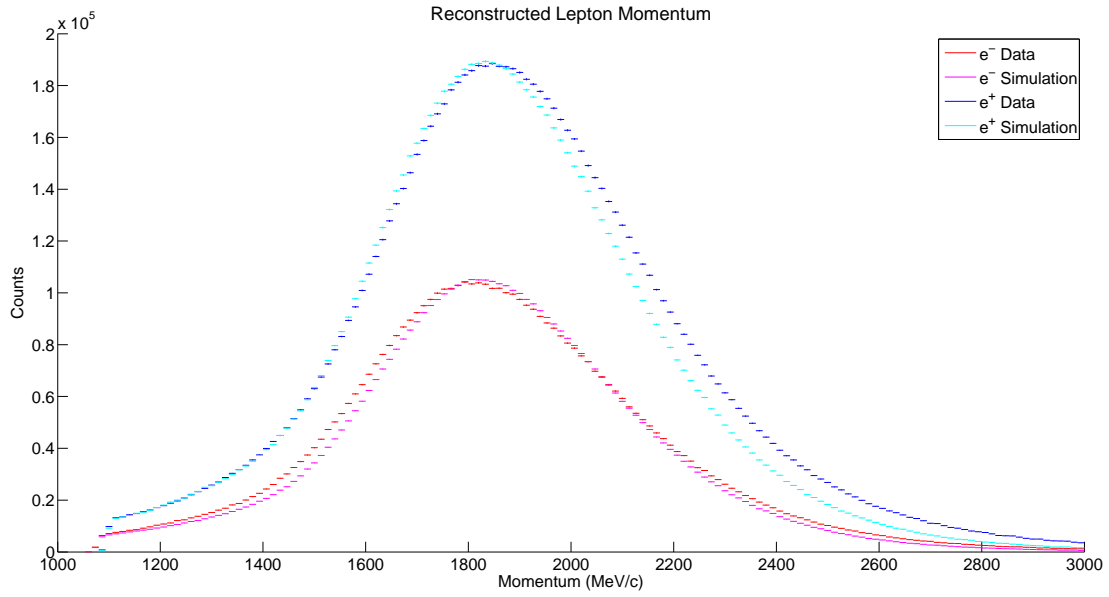


Figure 5-17: Distributions of reconstructed momentum for 12° leptons of each species, in data and simulation for the entirety of the data sample.

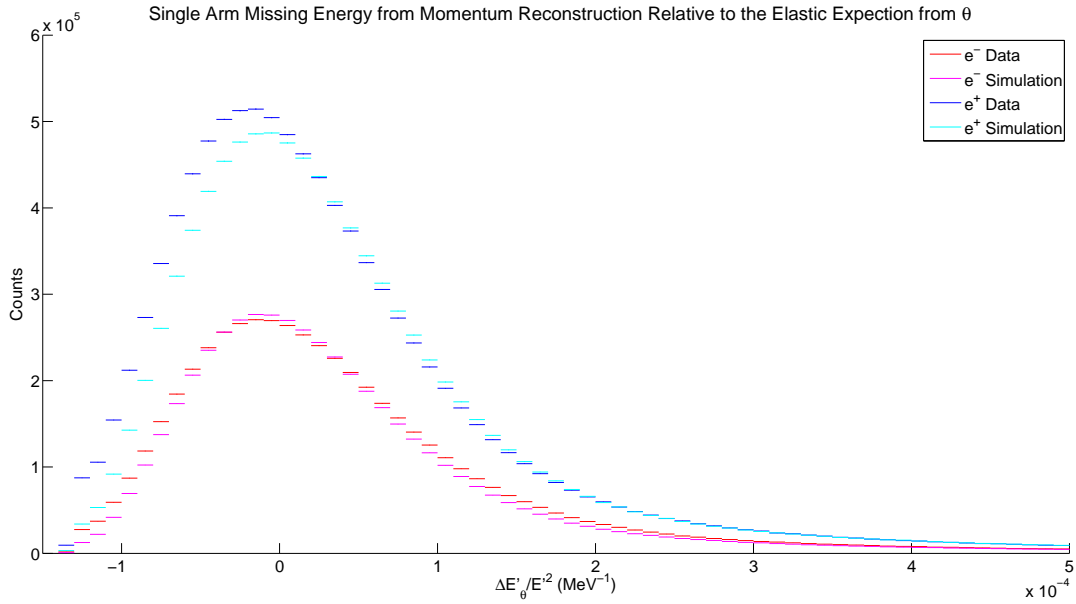


Figure 5-18: Distributions of the single-arm missing energy $\Delta E'_\theta/E'^2$ for 12° leptons of each species, in data and simulation for the entirety of the data sample.

5.2.8 Systematic Uncertainties

Since any uncertainty in the luminosity determination directly affects the uncertainty on the final $\sigma_{e+p}/\sigma_{e-p}$ ratio result, it was critical to consider all possible causes of systematic uncertainty in the extraction of the 12° luminosity, especially any such factors that affect the relative luminosity of the lepton species. Naturally, the uncertainty of the species-relative luminosity determination is considerably smaller than the uncertainties of an absolute luminosity determination due to the numerous systematic effects that are the same for both species, making the 12° an effective system for the task at hand (although not necessarily a precise absolute luminosity monitor). Note that no systematic effects that explicitly arise from the GEM detectors are formally discussed or computed since the GEM data did not directly contribute to the luminosity measurements in this work. The systematic uncertainties for the 12° system are discussed in the following sections, and the absolute and relative luminosity uncertainties are summarized in Table 5.2. A discussion of the interpretation and implications of these estimates may be found at the end of this section following a discussion of the details of each contribution estimate.

Regarding the methods used to compute the systematic uncertainties and the way in which they should be interpreted, the values presented in this section are estimates of the maximum range that the values of the extracted absolute and relative luminosities could have due to conservative estimates of the plausible range over which each effect may vary. Due to this, these are not to be interpreted as Gaussian uncertainties in most cases (as many of the effects are non-Gaussian), and, in general, the interpreted Gaussian uncertainties corresponding to the values in Table 5.2 are less than or equal to the presented values (as is discussed at the end of this section). Only effects found to amount to a contribution of 0.01% or greater are discussed here, since this is the order of the overall statistical uncertainty of the dataset of 12° events.

Uncertainty Source	Relative (%)	Absolute (%)
ToF trigger efficiency ($\delta_{\epsilon_{\text{ToF}}}$)	± 0.19	± 0.25
SiPM trigger efficiency ($\delta_{\epsilon_{\text{SiPM}}}$)	± 0.01	± 0.10
MWPC plane efficiency ($\delta_{\epsilon_{\text{MWPC}}}$)	± 0.01	± 0.05
Magnetic field (δ_B)	± 0.15	± 0.35
Lepton tracking efficiency ($\delta_{\epsilon_{e,\text{track}}}$)	± 0.18	± 0.86
Proton tracking efficiency ($\delta_{\epsilon_{p,\text{track}}}$)	± 0.10	± 0.80
Beam position/slope (δ_{BPM})	± 0.01	± 0.01
Beam energy ($\delta_{E_{\text{beam}}}$)	± 0.02	± 0.02
Detector position (δ_{det})	± 0.02	± 0.20
Fiducial cuts (δ_{fid})	± 0.12	± 0.22
Elastic cuts (δ_{elas})	± 0.27	± 1.63
Radiative corrections (δ_{rad})	± 0.08	± 0.45
Elastic form factors (δ_{ff})	± 0.14	± 1.20
TPE at $\theta = 12^\circ$ (δ_{TPE}^*)	± 0.10	± 0.10
Total including TPE uncertainty ($\delta_{12^\circ, \text{TPE}}$)	$\pm 0.47\%$	$\pm 2.44\%$
Total without TPE uncertainty (δ_{12°)	$\pm 0.46\%$	$\pm 2.44\%$

Table 5.2: A summary of the contributions to the systematic uncertainty in the determination of $\sigma_{e^+p}/\sigma_{e^-p}$ and of the absolute single-species luminosity in the 12° monitors in percent, as discussed in detail in Section 5.2.8. Absolute uncertainties are averaged between the species for the purpose of quoting a single number. These uncertainties may be considered to be independent, in general, and thus are added in quadrature to produce the total uncertainty estimate. Note that the TPE uncertainty (marked by *) contributes when the 12° result is used as a determination of the relative luminosity for the $\sigma_{e^+p}/\sigma_{e^-p}$ result, but is not included for a measurement of TPE at $\theta \approx 12^\circ$ using an independent luminosity extraction.

ToF Trigger Efficiency

Due to the fact that protons from e^+p and e^-p scattering events are distributed differently among the ToF scintillator bars at backwards angles (Figure 5-19) and the fact that a recorded ToF hit is required for the 12° trigger (Section 3.8.2), any unaccounted for anisotropy among the efficiencies of the ToF bars would introduce a shift in the relative $\sigma_{e^+p}/\sigma_{e^-p}$ measurement. Since the 12° trigger is only concerned with the efficiency of generating hits for protons of relatively low momentum ($\sim 10^2$ MeV/c) in the ToFs (which deposit a large amount of energy in the scintillator) and since those protons strike the central region of the bar (the most efficient region for generating a signal in both photomultipliers), the expected efficiency for the ToF

element of the 12° trigger is essentially unity from physics considerations alone. Due to issues with the PMT couplings and electronics used to readout the ToF bars, however, some inefficiencies were likely present in the experiment that are difficult to account for in the simulation, which assumes a nearly perfect efficiency for 12° event protons.

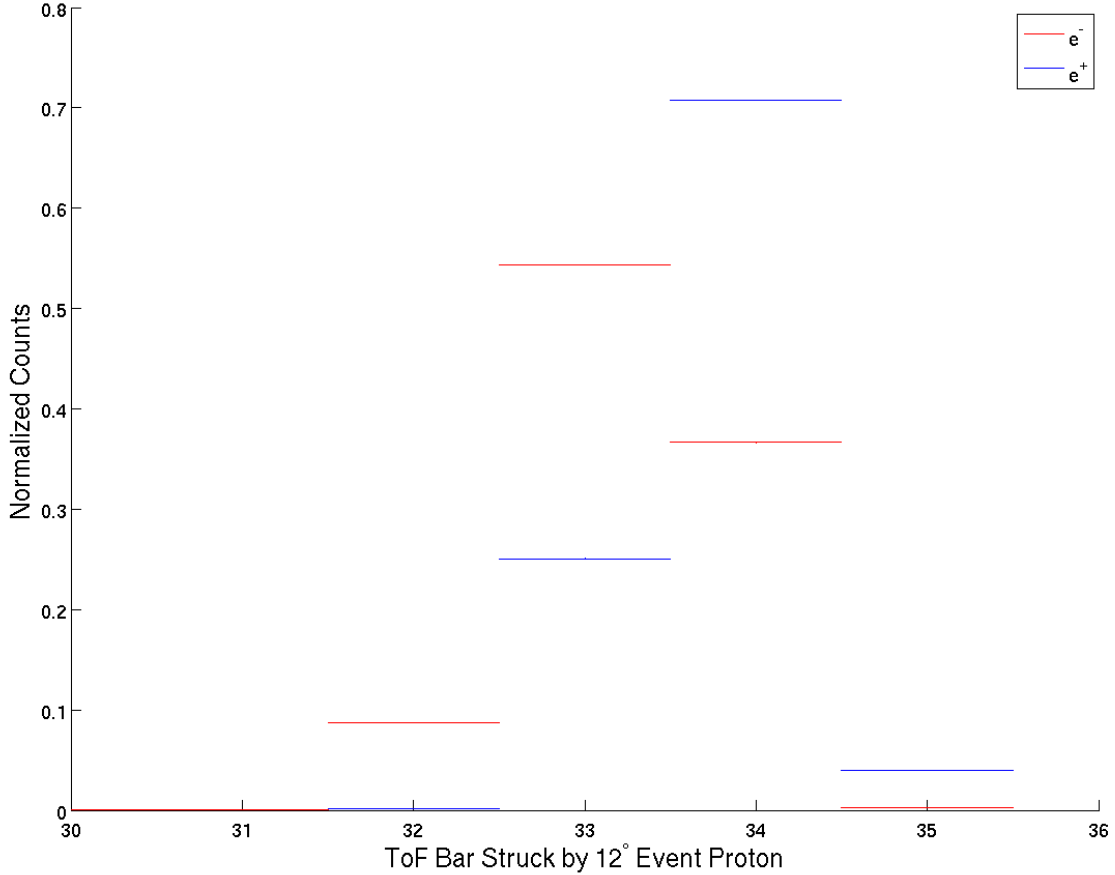


Figure 5-19: Distributions of the ToF bars struck by the protons in elastic e^+p and e^-p events in which the lepton was recorded by the left 12° telescope, normalized for comparison between events of the different lepton species. Note that 12° e^+p events have protons at more backward angles (higher ToF index) than e^-p events due to the toroidal field which caused positively charged particles to be out-bending. Due to the differences in these distributions, any anisotropy in ToF bar efficiencies could introduce a systematic shift in the $\sigma_{e^+p}/\sigma_{e^-p}$ determination in the 12° system.

Via estimates of the ToF efficiencies from both dedicated triggers (Section 3.8.4) and “scintillator sandwich” measurements, it was determined that the efficiency for

proton detection can be conservatively estimated to be in excess of 99.5% for the protons of interest [191]. Due to the fact that the Monte Carlo assumed near perfect efficiency for the events of interest, the effect of unaccounted for inefficiencies in the simulation could be estimated by rejecting events in specific bars with an artificial efficiency of 99.5%, and examining the effect on the electron-positron ratio and the absolute luminosity estimates. This rejection was computed for all subsets of the seven bars that are a part of the 12° trigger for each side (i.e., reducing the efficiency of all single bars, pairs of bars, triplets of bars, etc.). The resulting effect on the $\sigma_{e^+p}/\sigma_{e^-p}$ ratio is shown in Figure 5-20. Since the maximal error on the ratio can occur for multiple combinations of small numbers of bars, the systematic uncertainty of $\sigma_{e^+p}/\sigma_{e^-p}$ in the 12° system was conservatively assigned to be the maximum value of the deviation in the ratio under this method ($\delta_{\epsilon_{\text{ToF,rel}}} = 0.19\%$). The uncertainty of the absolute luminosity for each species from this effect was taken to be the mean effect from all 0.5% efficiency drop combinations, i.e., $\delta_{\epsilon_{\text{ToF,abs}}} = 0.25\%$.

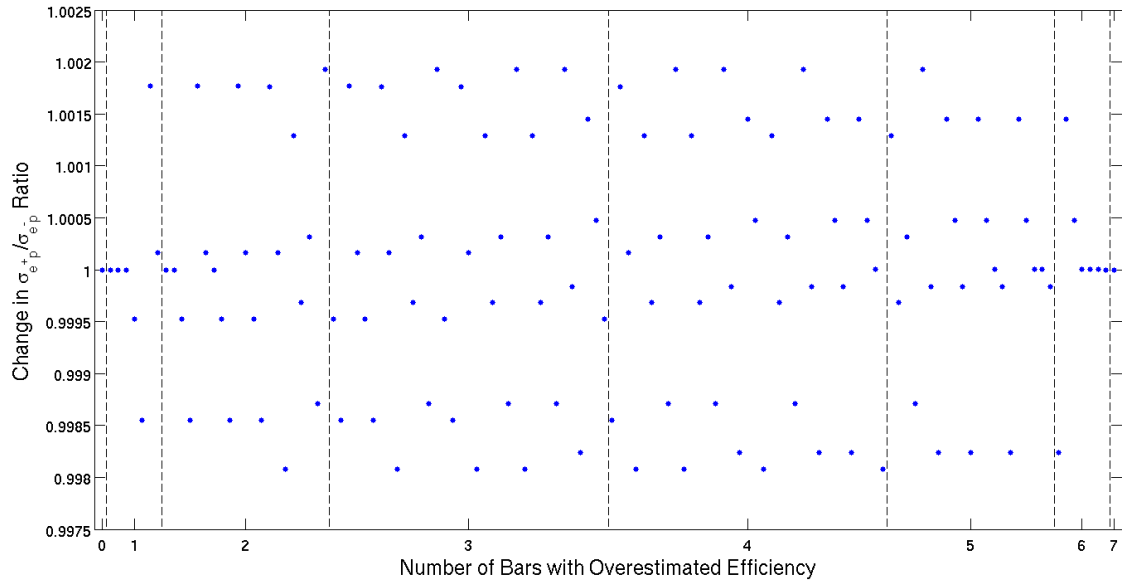


Figure 5-20: Estimated possible effect on the extracted 12° luminosity ratio due to uncertainty in the efficiency of the ToF trigger. The uncertainty of 0.5% in the efficiency of each bar was applied for each subset of bars involved in the trigger, as described in the text. The maximal deviation was $\delta_{\epsilon_{\text{ToF,rel}}} = 0.19\%$.

SiPM Trigger Efficiency

While electron and positron tracks in the 12° telescopes illuminated approximately the same total regions of the SiPM planes due to the telescope acceptance being constrained by other elements, the distributions of the illumination of the planes by the two different species may be different due to the change in the cross sections for elastic scattering across the ranges of θ accepted for each species. The SiPM plane efficiencies computed in Section 5.2.5 and shown in Figure 5-12 are in general quite good ($>99\%$) throughout their active regions. The small anisotropies in the efficiency could lead to an artificial difference in the extracted electron and positron luminosities. The anisotropies in the SiPM plane efficiencies are on the percent level, and taking the behavior of SiPM Planes 1 and 3 as the worst case scenarios, a model of a 1% efficiency drop with an uncertainty of the drop in efficiency of 0.5% in a band of local x of width ~ 30 mm provides a conservative test case for determining the effect on the 12° trigger. The relative normalized illumination of the SiPMs between e^+ and e^- hits differs by at most 0.1%, as determined by simulation. So, assuming the maximally asymmetric case between species, in which the lepton hit distributions differ by 0.1% in the aforementioned model uncertain region (corresponding to 30% of the detector plane), the resulting change in the ratio of the number of accepted hits between lepton species is shifted by less than 0.01%. Thus, even for a very conservative estimate in the uncertainty in the knowledge of the SiPM plane efficiencies, the high efficiency, uniformity of the efficiency, and small acceptance of the telescopes (making the hit distributions for each species very insensitive to differing slopes in the cross sections for each species as a function of θ), the effect on the relative extracted luminosity is small and may be conservatively quoted as $\delta_{\epsilon_{\text{SiPM,rel}}} = 0.01\%$.

Assigning an overall conservative uncertainty of 0.1% to the overall efficiencies of the individual SiPM planes from the statistics of the estimate in Section 5.2.5 and track reconstruction, this directly contributes an overall trigger efficiency uncertainty of $\delta_{\epsilon_{\text{SiPM,abs}}} = 0.1\%$ to the absolute luminosity measurement.

MWPC Plane Efficiency

The uncertainty introduced due to MWPC plane inefficiency is similar in nature to that introduced by the SiPM plane inefficiency, but the MWPC planes, especially in the left telescope, exhibited even more consistent efficiency than the SiPM planes, as discussed in Section 5.2.5 and shown in Figure 5-13. In the left telescope (MWPC Planes 0–2) the anisotropies are on the scale of a few tenths of a percent and millimeter width, but are relatively randomly distributed across the planes rather than the larger scale bands in the SiPMs. Given this difference, but still accounting for the fact that all three MWPCs in a telescope must have hits to generate a track, the uncertainty of the relative luminosity determination is estimated to be no more than half the value more rigorously computed for the SiPMs: $\delta_{\epsilon_{\text{MWPC,rel,left}}} = 0.005\%$.

For the right side MWPCs (Planes 3–5), the situation is somewhat different due to the presence of the inactive wires, which amount to hard acceptance edges for 12° events. While the possibility of using two-wire hits to mitigate the effect of inactive wires was explored, it was found that the spurious hits due to noise introduced by accepting such hits would amount to a more detrimental effect than implementing a model of the inactive wires in the simulation to account for their effect. To estimate the possible errors introduced by uncertainty in the simulation model, first note that the inactive wires correspond to about 0.8% of the total active area of the three planes. Then, if the illumination of these regions differs between species on the level of 0.1% and the uncertainty in the placement and inefficiency of these regions (hits may be constructed in these regions due to hits on the surrounding wires in the plane containing the inactive wire) is assumed to be $\pm 5\%$ for the sake of providing a wide estimate, the induced asymmetry remains smaller than the quoted left side relative uncertainty.

As an additional test, the simulation of the MWPC inactive wires was tested in two separate ways. In the first method (the method ultimately used for the analysis), simulation hits were treated on the wire-plane level (as data hits are treated in the main analysis) and thus the inactive wires provided no hit information and lowered

the efficiency in the region of the hit reconstruction planes surrounding them. In the second method, the inefficiency due to the wires was implemented via the maps shown in Figure 5-13. The difference in the overall accepted track rates in the simulation between these methods was found to be on the order of 0.01%. While the wire-plane hit reconstruction digitization method demonstrably better mimics the data (both in terms of methodology and comparison between the resultant of hit and track distributions), the difference between the methods is taken as the uncertainty in this case. Since the estimates for the left and right side differ but are each small effects in the overall uncertainty, for the simplicity of assigning a single number to the MWPC efficiency effect, the uncertainty is estimated as: $\delta_{\epsilon_{\text{MWPC,rel}}} = 0.01\%$ for both sides. Since this is a considerably smaller than other uncertainties, this choice does not significantly impact the final systematic uncertainty estimate.

The MWPC efficiencies were computed with extremely high statistics and with very precise five-plane tracking, as discussed in Section 5.2.5, and thus the overall uncertainty of the MWPC efficiencies is at most 0.02%. Since all three MWPC planes in a telescope are required to reconstruct an accepted 12° event, the absolute luminosity uncertainty from this source is conservatively estimated as $\delta_{\epsilon_{\text{MWPC,abs}}} = 0.05\%$.

Magnetic Field

As described in Section 4.1.3 and Reference [128], a large effort was undertaken to properly model the magnetic field of the OLYMPUS spectrometer for simulation and track reconstruction since any uncertainty in the field directly corresponds to uncertainty in the acceptance of electron and positron scattering events. Uncertainty in the field in the 12° telescope region can occur due to uncertainty in the measurement of the vector components of the field, uncertainty in the reconstructed position of the Hall probe used for the measurements, and errors/residuals in the field model used to fit and interpolate the field for the simulation and reconstruction.

The region surrounding the 12° telescopes is among the hardest to model due to the telescopes occupying the region near the “pinch” of the toroid (i.e., the region

where the coils most-closely approach each other). As noted in the description of the field model, regions near the coils are sensitive to the thin filament model used to approximate the toroid coils resulting in residuals between the field model and the survey measurements. Field components in the OLYMPUS y direction are the strongest experienced by 12° tracks and affect the in/out-bending of tracks. Field components in the OLYMPUS x result in approximately azimuthal bending. Components of the field along z are nearly parallel to 12° tracks and are less than 50 G throughout the region experienced by 12° tracks, and thus any uncertainties in this field are negligible. Additionally, the x component of the field is also very small in this region, especially in the area near the target cell where deflections would most strongly affect the telescope acceptance. Simulations indicate that shifts of even $\sim 100\%$ in the magnitude of B_x are lesser effects than realistic uncertainties in B_y , and thus are sub-dominant effects.

Having established B_y as the most critical element of the field for the 12° system, the magnitudes of uncertainties in this region were examined. Figure 5-21 shows the field model calculation for the magnitude of B_y in the region, while Figure 5-22 shows the residual in B_y between the field model and the survey measurements. Comparing the gradients in B_y experienced by 12° tracks between survey points (spaced by either 5 or 10 cm), and noting that the uncertainty of the position of the survey points is at least an order of magnitude smaller than the spacing, any shift in the field grid relative to the true position may be neglected compared to the residuals between the survey and the model shown, which are on the order of tens of gauss (or a few percent of the magnitude of B_y). It should be noted, however, that the residuals are not uniformly distributed, and exhibit two key elements that lessen their effect:

1. residuals along the first meter of the track, where deflections most strongly affect the acceptance, are extremely small compared to the pinch region, and
2. tracks experience regions of approximately equal in magnitude positive and negative residuals as they approach the telescopes leading to at least some cancellation of effects on the acceptance due to these regions.

Thus, a model for determining the uncertainty in acceptance due to field uncertainties that systematically scales the field on the order of a percent represents a conservative estimate of the acceptance uncertainty since a full systematic shift in all field components separates the acceptances of the two lepton species to a significantly higher degree than the observed deviations in the field model.

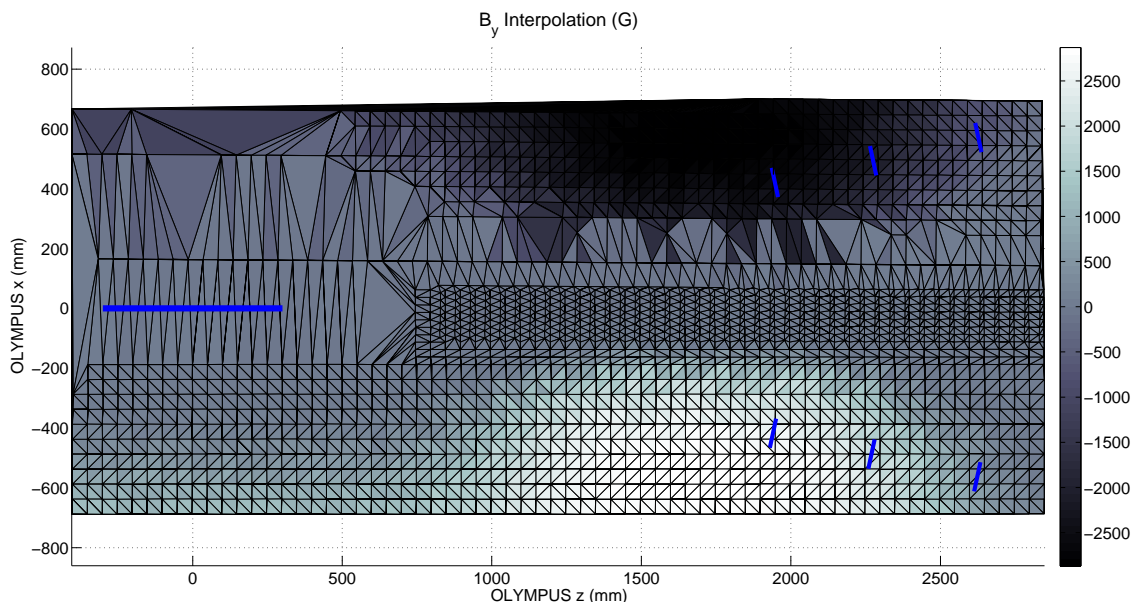


Figure 5-21: Field model interpolation calculation for B_y in the region important for the 12° telescopes, on a triangulated grid of the survey measurement points. Approximate positions of the target cell and MWPC tracking planes are marked in blue for reference.

To examine the effects of field scaling uncertainty, simulations were conducted in which a set of generated events was propagated using several scaled fields (implemented by varying the toroid current over $\pm 5\%$ from its nominal value) but reconstructed using the nominal field model. The effects on the species-relative and absolute luminosity extractions are shown in Figures 5-23 and 5-24, respectively. Linear models were found to be good descriptions for the variation in the extracted relative luminosity and the individual species absolute luminosities as a function of toroid current, and the resulting fits are shown in the figures. The integrated average residual seen by 12° track is considerably less than the 18 G average RMS residual quoted in Reference [128], indicating that a shift of the field model of 0.5% in the

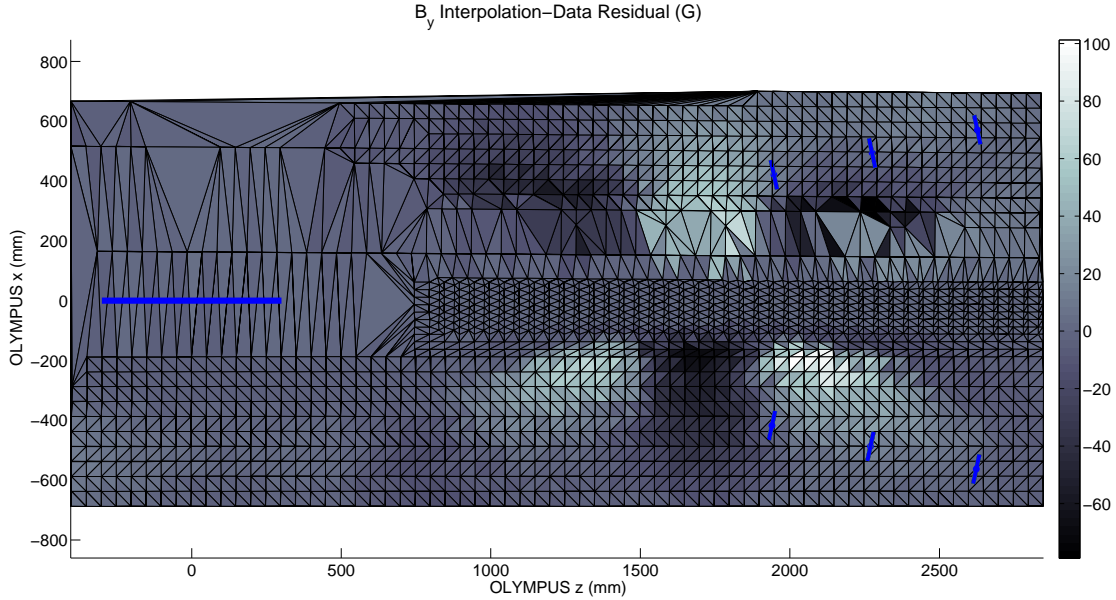


Figure 5-22: Residual between the field model interpolation calculation for B_y and the measurements at surveyed points in the region important for the 12° telescopes, on a triangulated grid of the survey measurement points. Approximate positions of the target cell and MWPC tracking planes are marked in blue for reference.

tracking/bending regions (i.e., a shift in the toroid current of 25 A) represents a conservative estimate of the field error. Thus, using the results of the simulations shown in Figures 5-23 and 5-24, the relative and absolute systematic uncertainties due to the field may be estimated as $\delta_{B,\text{rel}} = \pm 0.15\%$ and $\delta_{B,\text{abs}} = \pm 0.35\%$, respectively.

Lepton Tracking Efficiency

Given the way in which the leptons in the 12° arm were tracked with the GEANT4E tracker and the minimal number of hits available for each track in the final 12° analysis (three total hits in a telescope from the three MWPC planes), a track could be fit to the vast majority of 12° events having a hit in each of the three planes that passed the track candidate selection criteria (Section 5.2.4). This was due to the kinematic flexibility of tracker to fit to the three points aside from rare failure modes of the either GEANT4E or the Levenberg-Marquardt minimization routine. Anytime a lepton track was produced for an event, it was considered individually and with all possible proton track pairings, and thus the systematics of the quality of

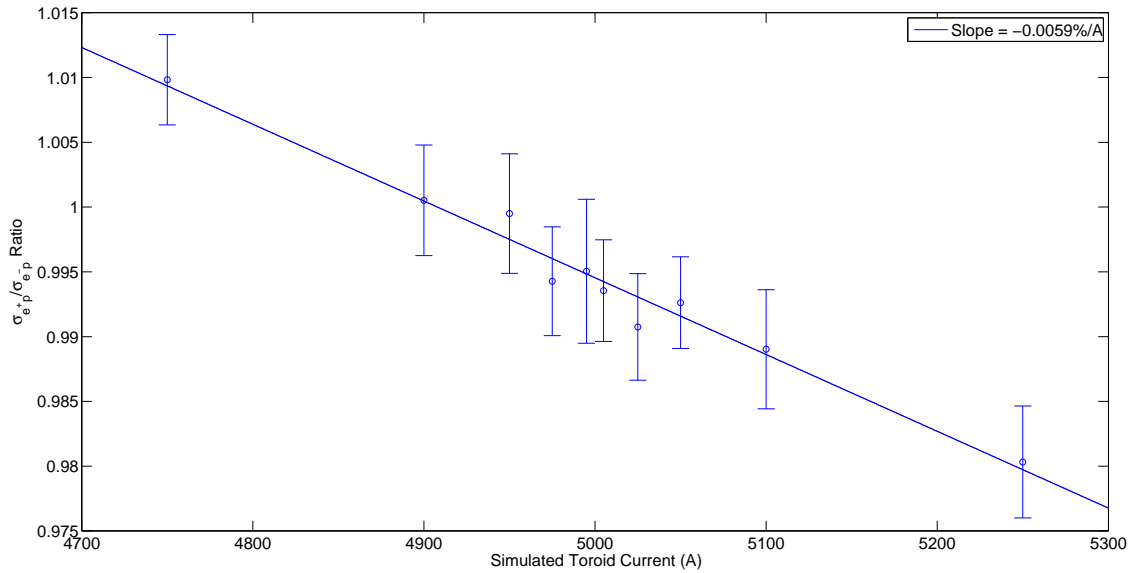


Figure 5-23: Effect of scaling the magnetic field (from the nominal setting of 5000 A for the toroid current) on the extraction of $\sigma_{e^+p}/\sigma_{e^-p}$ in the 12° system. Note that the error bars on the points are statistical, but that the statistical uncertainty between points is highly correlated due to the fact that each point arises from the same generated events.

the reconstruction are captured in the consideration of the effects of the elastic and fiducial cuts applied to the tracks.

To estimate the possible effect on the relative luminosity extraction, the rate of successful tracking for track candidates was examined for each species in the simulation. Note that not all hits produced in simulation are components of a desired lepton track due to hits produced by secondaries, unusual hard scattering that causes tracks to deviate heavily from standard trajectories, etc., and thus some rejection of events is expected. For positron runs the simulation candidate-to-track efficiency was found to be 96.76%, while for electrons the efficiency was slightly lower at 96.58%. While it is extremely unlikely that this difference is entirely due to an asymmetry in rejection of good events, as indicated by visual inspect of such events, the contribution to the systematic uncertainty due to this effect is conservatively estimated as the difference in these efficiencies: $\delta_{\epsilon_{e,\text{track,rel}}} = 0.18\%$

An exact determination of the effect on the absolute luminosity extraction is

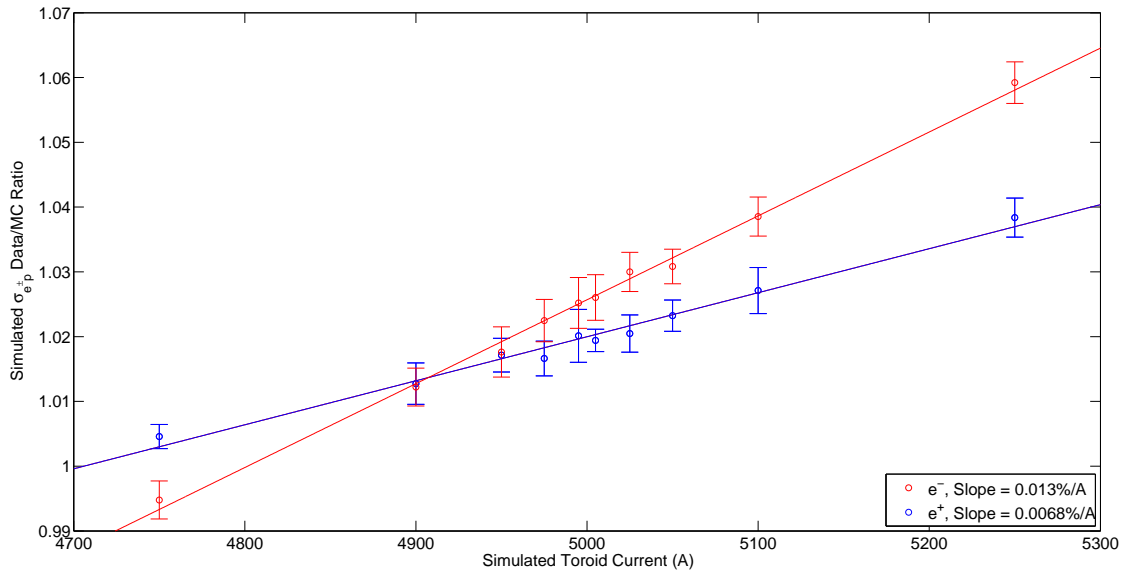


Figure 5-24: Effect of scaling the magnetic field (from the nominal setting of 5000 A for the toroid current) on the extraction of the absolute luminosities in the 12° system. Note that the error bars on the points are statistical, but that the statistical uncertainty between points is highly correlated due to the fact that each point arises from the same generated events.

difficult since the tracking inefficiency is not necessarily representative of the fraction of “good events” lost due to lepton tracking failures. To assess the fraction of events in the sample of missed tracks that likely would have been counted as a good event if reconstructed, approximately 100 such events were inspected by eye using the visualization routine for the simulation propagation (see Appendix A). Making a generous assessment, perhaps a quarter of such tracks were within the acceptance of the telescope but ultimately not reconstructed. Thus, the uncertainty of the absolute luminosity from this effect is taken to be a quarter of the overall inefficiency:

$$\delta_{\epsilon_{e,\text{track,abs}}} = 0.86\%$$

Proton Tracking Efficiency

While the effect of proton tracking has been minimized to the extent possible in the analysis due to the difficulty of tracking the high θ protons in 12° events (as discussed in Section 5.2.6), the uncertainty in the reconstruction efficiency for the

exclusive events may provide some species-relative effects due to the difference in the relative distributions of the protons in e^+p and e^-p scattering (i.e., the protons from each event type are distributed differently in the drift chamber and thus sample different cells). As discussed in Section 4.2, two methods of track reconstruction were utilized for the OLYMPUS drift chambers and thus available for reconstruction of the protons in 12° events: EAA and SA. The EAA tracker used for the reconstruction of the leptons in the main 12° analysis is quite efficient in the region relevant to 12° events, but the SA tracker suffers from notable inefficiencies in the region. Due to this, the SA tracker is not useful for a final analysis, but may be used to estimate the magnitude of the effects of drift chamber and tracking inefficiency on the 12° result.

To make such an estimate, the 12° analysis was re-run using protons reconstructed using the SA tracker and the resulting difference between the SA and EAA analyses was used to estimate the effect of proton tracking efficiency. Note that at the time this analysis was performed the SA tracker was not in its final state and improved somewhat in its performance at back angles for subsequent analyses. While the absolute values of the measured $e^\pm p$ cross sections drop on the order of a percent in the SA analysis due to the missing protons, the change in the relative measurement is not as drastic and can be used as an estimate in the uncertainty caused by a large inefficiency in the proton reconstruction on the relative measurement. The induced differences in the value of $\sigma_{e^+p}/\sigma_{e^-p}$ at $\theta \approx 12^\circ$ due to the two different tracking methods are shown in Table 5.3. The size of the effect was found to be on the order of 0.1%. Since the SA tracking used for this analysis represents a significantly worse proton reconstruction capability than the EAA tracking used for the main 12° analysis, this was taken as a conservative estimate of the effect of proton tracking on the luminosity ratio extraction: $\delta_{\epsilon_{p,\text{track,rel}}} = 0.2\%$. For the estimate of the effect on the absolute extraction, approximately half of the decrease in the absolute extraction between SA and EAA reconstruction was taken as a rough estimate of this uncertainty: $\delta_{\epsilon_{p,\text{track,abs}}} = 0.8\%$.

Event side	$\sigma_{e^+p}/\sigma_{e^-p}$ with EAA	$\sigma_{e^+p}/\sigma_{e^-p}$ with SA	Difference
Lepton left	1.000	1.002	0.2%
Lepton right	0.994	0.993	0.1%

Table 5.3: Difference in the determination of $\sigma_{e^+p}/\sigma_{e^-p}$ in the 12° system between EAA and SA proton tracking.

Beam Position and Slope

The quoted uncertainty of the OLYMPUS beam position reconstruction from the beam position monitor surveys and model fits was $100\ \mu\text{m}$ on the absolute beam positions and $20\ \mu\text{m}$ on the species-relative shift error [192]. To assess the sensitivity of the 12° system to errors in the knowledge of the beam position, simulated data sets were generated at a variety of beam shifts that exceeded the aforementioned expected position uncertainty by an order of magnitude (i.e., shifts of several mm). Figures 5-25 and 5-26 show the shifts in the absolute rates for each lepton species in each 12° telescope for shifts in the beam x and y positions, respectively, while the other position dimension is held fixed. Taking the largest slopes as a conservative estimate of the effects of beam position results in an uncertainty in the absolute rate due to beam position uncertainty of approximately $0.027\%/ \text{mm}$ and an uncertainty in the species-relative luminosity of $0.033\%/ \text{mm}$. In addition to the data shown in the figures, several other beam positions and slopes on the order of several mm at each BPM were tested as well and observed to exhibit no effects larger than those shown in the figures. It is also notable that the 12° system is insensitive to any uncertainties in the shape of the beam profile (i.e., something deviating from the Gaussian envelope described in Section 3.2.2) since such effects are on much smaller length scales than the beam shifts described in this section.

Since the uncertainty in the beam position reconstruction (both absolute and relative) is approximately an order of magnitude less than 1 mm, the systematic uncertainties of the relative and absolute luminosity measurements in the 12° system due to the beam position and slope is very conservatively estimated to be $\delta_{\text{BPM,rel}} = \pm 0.01\%$ and $\delta_{\text{BPM,abs}} = \pm 0.01$. Thus, the 12° monitors were extremely robust to

changes in beam position and slope providing a good complement to the SYMB system, which exhibits a much more notable dependence on beam shifts.

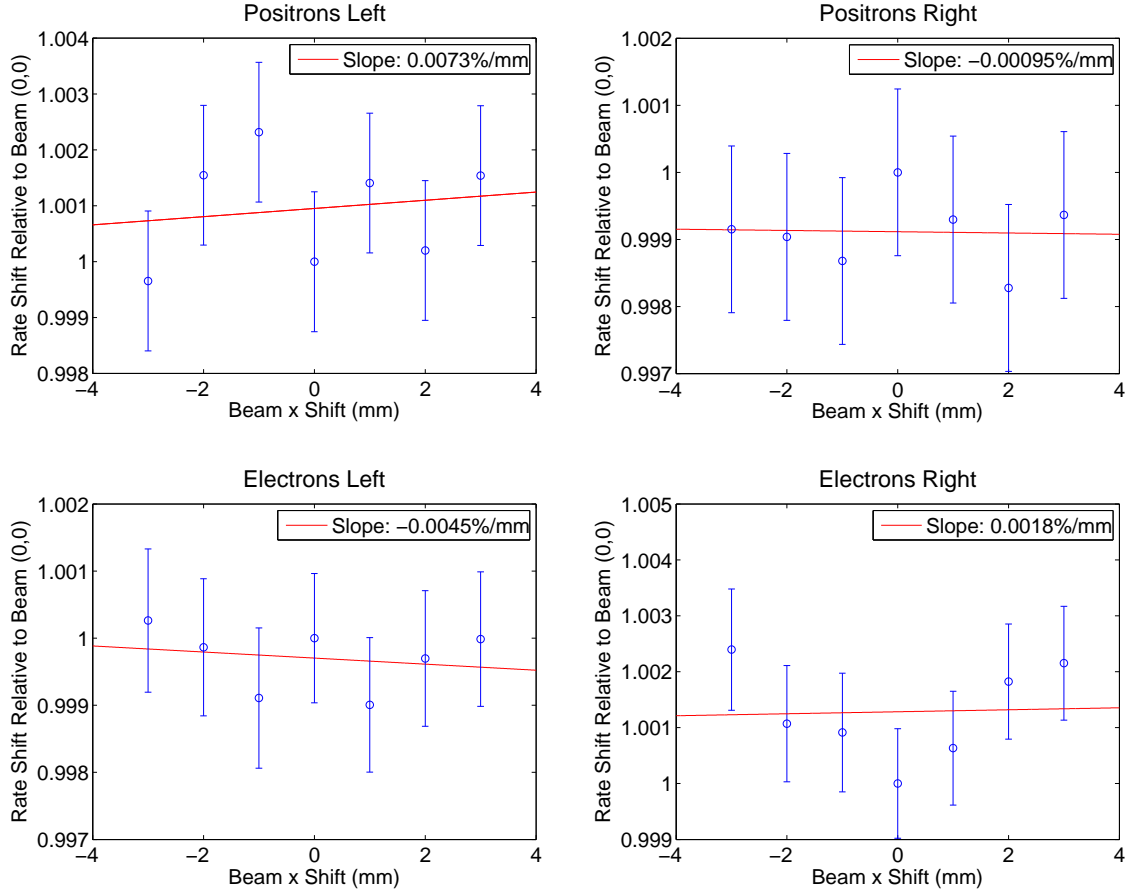


Figure 5-25: Effects of varying the simulated beam x position on the rates for each species in each 12° telescope for fixed $y_{\text{beam}} = 0$. Note that the error bars are slightly overestimated due to correlation between the Monte Carlo data sets. For each combination, the shifts in rates are at most on the order of 0.1%/mm in both the absolute and species-relative measurements.

Beam Energy

The 1σ uncertainty of the DORIS beam energy was determined by the DESY accelerator group to be ± 0.1 MeV for each species ($E_{\text{beam}} \approx 2010$ MeV) [193]. While the two species beams had slightly different measured energies ($\Delta E \approx 0.5$ MeV), this was accounted for in the generation of simulated events using the measured values

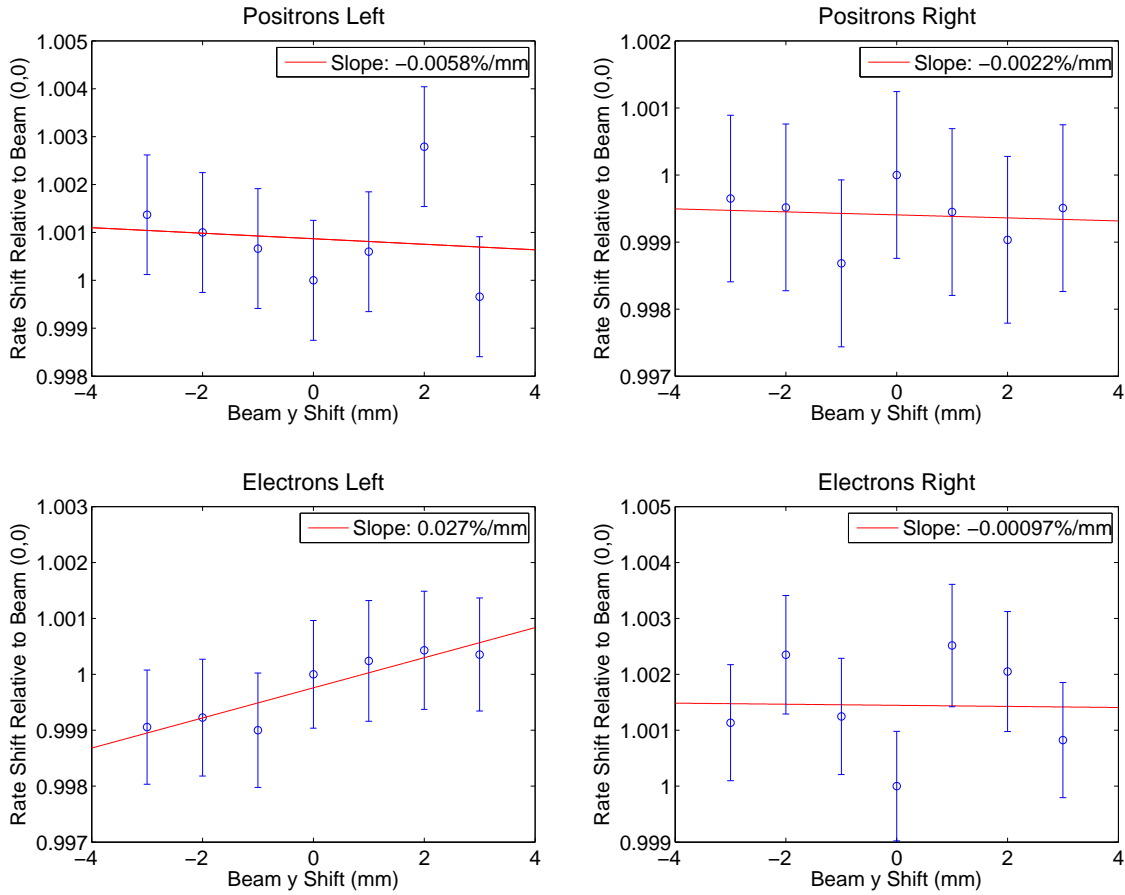


Figure 5-26: Effects of varying the simulated beam y position on the rates for each species in each 12° telescope for fixed $x_{\text{beam}} = 0$. Note that the error bars are slightly overestimated due to correlation between the Monte Carlo data sets. For each combination, the shifts in rates are at most on the order of $0.1\%/mm$ in both the absolute and species-relative measurements.

of the DORIS dipole magnet current saved in the slow control database throughout data-taking. Thus, it is the uncertainty on the knowledge of the relative absolute energies (rather than the absolute energy) difference that affects the uncertainty of the final results. The 0.1 MeV uncertainty on the individual beam energies was estimated by testing the DORIS beam with various perturbations and was continuously stabilized with a system of correction magnets. Due to the importance of precision for the OLYMPUS results, this control of the beam energy was significantly better than the ~ 5 MeV ($\sim 0.1\%$) beam energy uncertainty that was present when DORIS was

operated as in e^+e^- collider mode for the ARGUS experiment [118,194]. To estimate the magnitude of the effect of this uncertainty on the extracted luminosity in the 12° system, the Rosenbluth cross section (Equation 2.16) was computed as a function of θ for the nominal beam energy and beam energies $\pm 1\sigma$ from it. Note that shifts in radiative corrections due to the beam energy are considerably smaller effects, and thus the variation in the Rosenbluth cross section is a sufficient approximation for this estimate. Figure 5-27 shows the ratio of this cross section at $+1\sigma$ beam energy to that at -1σ , i.e. the effective shift that would occur in the ratio if one lepton species has a beam energy lower than expected from the energy measurement by 0.1 MeV and the other higher by 0.1 MeV. The maximum deviation of this ratio in the 12° acceptance is approximately 0.04%, and the uncertainty of $\sigma_{e+p}/\sigma_{e-p}$ at 12° may thus be reasonably estimated as $\delta_{E_{\text{beam,rel}}} = 0.02\%$ with a similar effect on the absolute cross section: $\delta_{E_{\text{beam,abs}}} = 0.02\%$

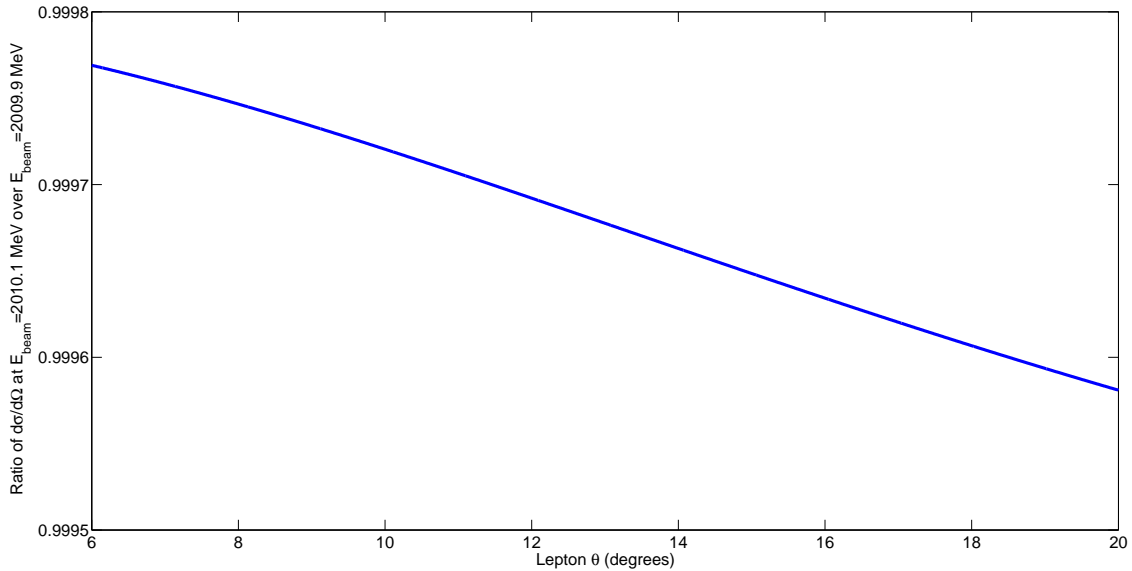


Figure 5-27: Ratio of the Rosenbluth $e^\pm p$ cross section (using the Bernauer form factor parametrizations [37]) in the vicinity of the 12° acceptance for a beam of $E_{\text{beam}} = 2010 + 0.1$ MeV to that at $E_{\text{beam}} = 2010 - 0.1$ MeV, i.e. $\pm 1\sigma$ around the nominal beam energy.

Detector Position

Due to the large number of degrees of freedom available for uncertainties in the positions of detectors relevant to 12° event reconstruction (positions and rotations of each of the MWPC and SiPM planes, and additional degrees of freedom from the ToFs and drift chambers), it was not practical nor instructive to approach this uncertainty via a simulation-based method. Notably, the acceptance of the 12° system is almost entirely dependent on the position of the outermost plane used in each telescope (i.e., MWPC planes 2 and 5) since they cover the smallest solid angle ranges relative to the other detector elements (both in the 12° and the proton tracking detectors). Thus, the dominant uncertainties from acceptance issues related to poorly reconstructed detector positions arise from the outermost planes. While there could be additional uncertainties from poor track reconstruction due to uncertain knowledge of the offsets between planes, these were minimized by aligning the detectors relatively using both events at nominal magnetic field and straight tracks from zero field runs tracked in the rest of the planes excluding the one being studied. For this reason, uncertainties in the placement of the outermost planes may be considered the dominant source of detector position systematic error. Since for even only one plane there are six degrees of freedom in the placement of the detector, a simulation-based approach still would require a relatively impractical computing investment and thus a method involving considerations of the effects of geometry and the $e^\pm p$ cross section is used instead.

First, considering the rotational degrees of freedom of the detectors, basic geometrical arguments may be used to estimate the size of the effect. Leptons striking the 12° detector planes do so approximately perpendicularly to the plane, and so any rotation of the plane relative to this standard incidence angle would reduce the effective acceptance of the plane. While, of course, not all 12° tracks strike the planes truly perpendicularly, this approximate case is sufficient for estimating the size of the effect. For a small rotation by angle ψ about an axis in the plane of the MWPC detector, the acceptance area presented to an incoming track varies as $\cos \psi$. Given that uncertainties of the rotations are on the order of 0.2° for the MWPC survey [195],

this would correspond to a change on the order of less than a part in 10^5 in the acceptance. Thus, the uncertainty due to errors in the rotational placements is nearly certain to be minimal for both the relative and absolute luminosities.

To consider the positional degrees of freedom the detectors, geometric considerations in conjunction with a Rosenbluth cross section calculation (similar to that conducted for the beam energy uncertainty estimate) were used. The residuals of the MWPC position reconstruction from the survey were approximately $200\ \mu\text{m}$ [195], and thus shifts of that order were considered for each of the three available degrees of freedom. The outermost MWPCs were nominally located 2.68 m from the center of the target along the $\theta = 12^\circ$ lines in the OLYMPUS x - z plane, and the survey positions differed from these values on the order of several mm. At this position, the MWPC planes' extent ($110\ \text{mm} \times 110\ \text{mm}$) covers a geometrical solid angle (not necessarily corresponding to a track phase space solid angle) range of $\phi = \pm 5.6^\circ$ and $\theta = 12 \pm 1.2^\circ$. Shifting the detector towards or away from the target along the 12° line changes these ranges on the order $0.04\%/ \text{mm}$, as can be seen in Figure 5-28, and so is on the order of hundredths of a percent for shifts on the order of $200\ \mu\text{m}$. Similarly, the results of shifting the detector up or down are shown in Figure 5-29. In this case, the results are even smaller, amounting to changes of order 10^{-7} for shifts of hundreds of micrometers. Since shifts in neither of these directions significantly change the cross section of $e^\pm p$ events sampled (the first does not change the mean or central value of θ , while the second is predominantly a shift in ϕ under which the cross section is invariant), these geometrical factors are a good estimator of the cross section change due to such shifts.

For the final direction of position shift for an MWPC plane, perpendicular to the $\theta = 12^\circ$ line in the $y = 0$ plane (i.e., the local x of the detectors), more care must be taken since this involves a shift in the θ acceptance of the detector and thus a change in the sampled cross section, which rapidly changes as a function of θ . Additionally, different θ ranges are sampled for each species, further adding possible sources of uncertainty. For reference, the normalized θ distributions accepted for each species are shown in Figure 5-30.

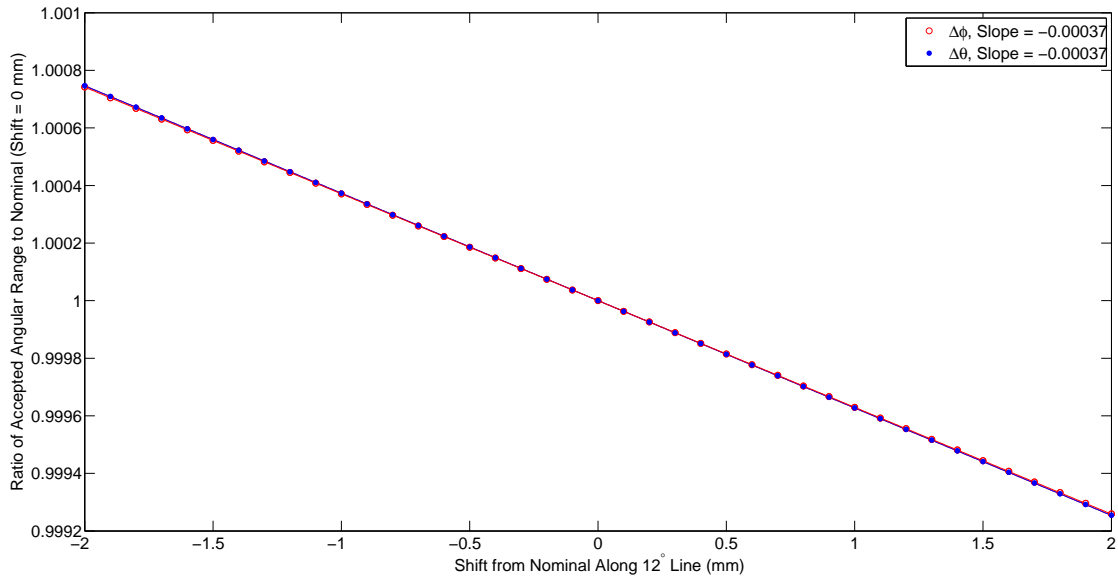


Figure 5-28: Effect on the solid angle encompassed by the outermost MWPC planes when shifted toward or away from the target cell center along the 12° line. The effect in both θ and ϕ is approximately 0.04%/mm.

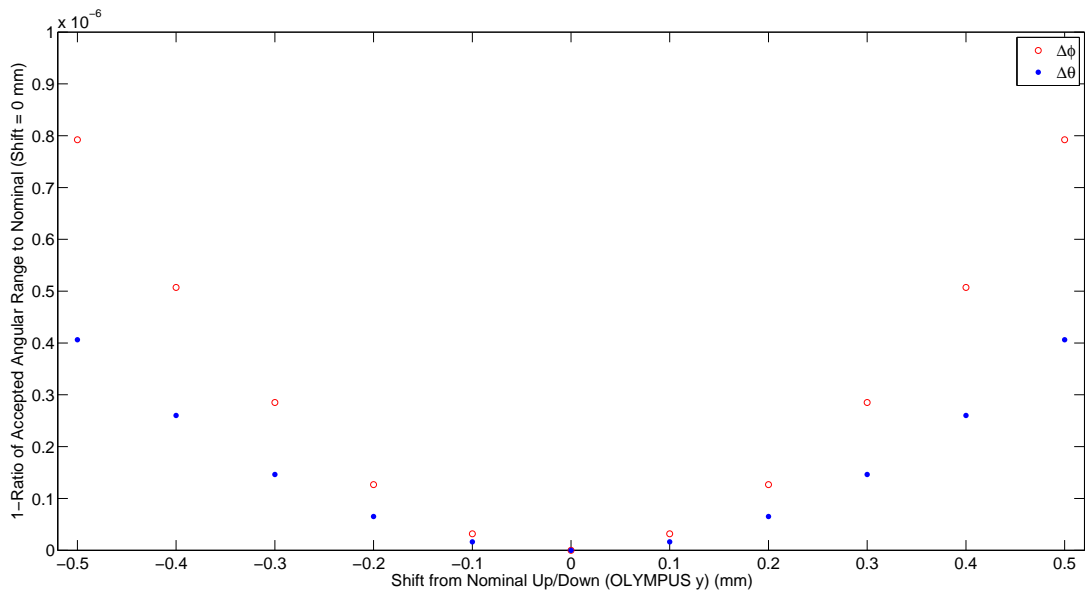


Figure 5-29: Effect on the solid angle encompassed by the outermost MWPC planes when shifted up or down. The effect in both θ and ϕ is $\sim 1 \cdot 10^{-7}$ for shifts on the order of 200 μm .

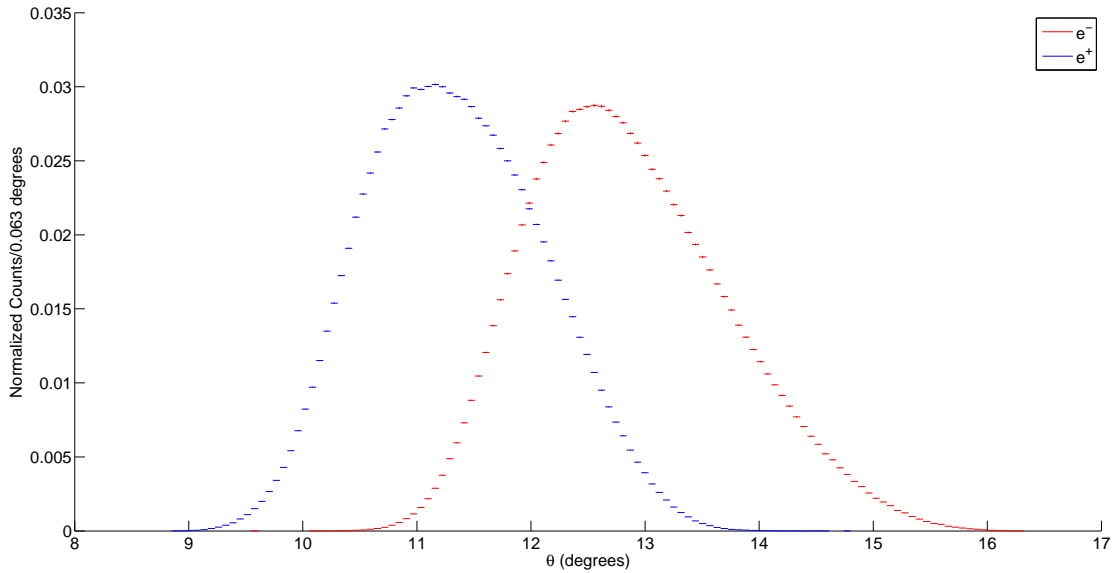


Figure 5-30: Normalized distributions of the lepton θ for electron- and positron-proton elastic scattering events accepted by the 12° system.

A shift in this direction corresponds to a shift of a $0.02^\circ/\text{mm}$ in θ for small shifts with a negligible change in the total θ coverage (and, of course, no change in ϕ). Since the distributions shown in Figure 5-30 are of approximately the same width, the cross-section at the mode angle for each species acceptance is taken as an approximate stand-in for the cross section in the acceptance and the resultant shifts in the e^+p and e^-p cross sections for θ shifts on the order of several hundredths of a degree were computed using the Rosenbluth formula. The effects on the error that would be expected due to such shifts on the simulated cross section, and thus on the luminosity, are shown for the individual lepton species and the ratio of the species in Figure 5-31. Since a $200\ \mu\text{m}$ shift corresponds to a shift of approximately 0.004° , the resultant relative effects due to this uncertainty on the luminosity extractions are 0.014% .

Combining the various effects discussed in this section, and noting that for both the relative and absolute luminosities shifts in effective θ are the dominant contributors, the estimate for the systematic uncertainties due to detector position are $\delta_{\text{det,rel}} = 0.02\%$ and $\delta_{\text{det,abs}} = 0.20\%$.

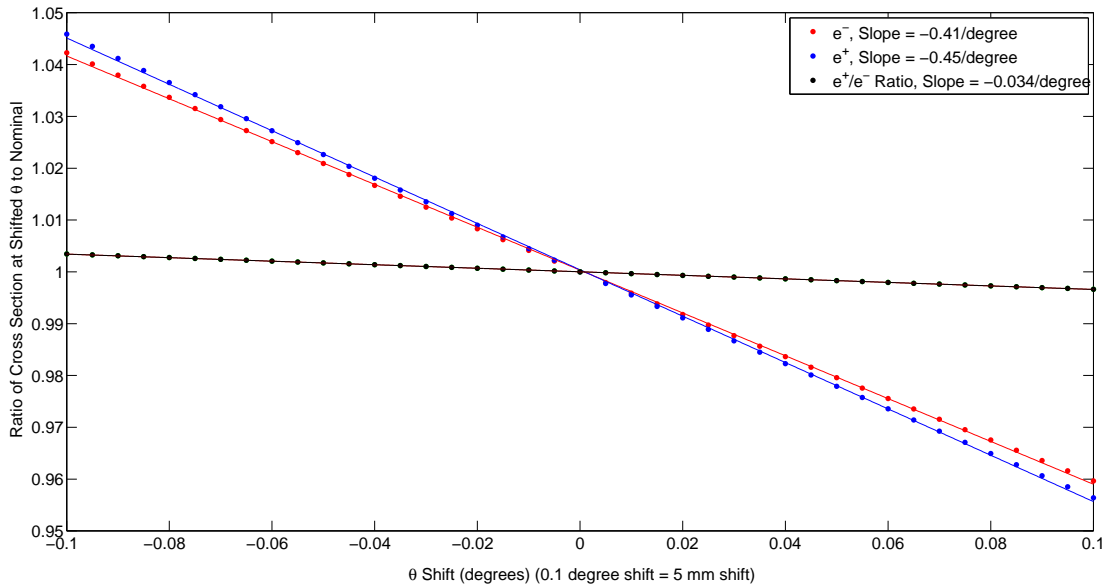


Figure 5-31: Effect on the simulated cross section in the 12° acceptance, and thus on the luminosity extraction, due to shifts in the θ acceptance of the detectors away from nominal for each species individually and the ratio. Note that expected shifts from survey uncertainties are considerably smaller than the range of shifts presented.

Fiducial Cuts

Since the 12° telescopes had limited acceptance and poor reconstruction resolution due to the use of only the MWPC planes in the final analysis, fiducial cuts were only made on the reconstructed y and z positions of the lepton vertex in the OLYMPUS global coordinate system as described in Section 5.2.6. Note that any attempt to make a fiducial cut in ϕ is extremely dangerous since deviations of the OLYMPUS magnetic field from a perfect toroidal field experienced by 12° tracks focus electrons and defocus positrons in ϕ and thus any fiducial cut within the reconstructed distributions explicitly introduces a false shift between the species. The possible systematic effects of this focusing, however, are accounted for in the previous considerations of the effect of the magnetic field and shifts in the detector position/acceptance.

For both the y and z fiducial cuts, the cuts were made at the widest reasonable values due to the system's lack of position reconstruction resolution and based on the simulation distributions that were generally free of background and mis-reconstructed

tracks. Thus, to test the effects of these cuts each value was further constrained to reasonably tighter cuts in each case. A sample histogram of reconstructed y vertex positions (for left going electrons) with a Gaussian fit is presented in Figure 5-32, which is representative of these distributions in the different configurations. Note that the nominal fiducial cut was symmetric and placed well into the tails of the distributions at ± 12 mm to avoid cutting good events in the tails. The effect of varying the y fiducial cut is shown in Figure 5-33. Taking the smallest reasonable cut as ± 8 mm, since at cuts smaller than that the good Gaussian region of the distribution is cut into, the maximal effect of reasonable cuts on the absolute luminosity is 0.2% while the relative luminosity is changed by at most 0.07%.

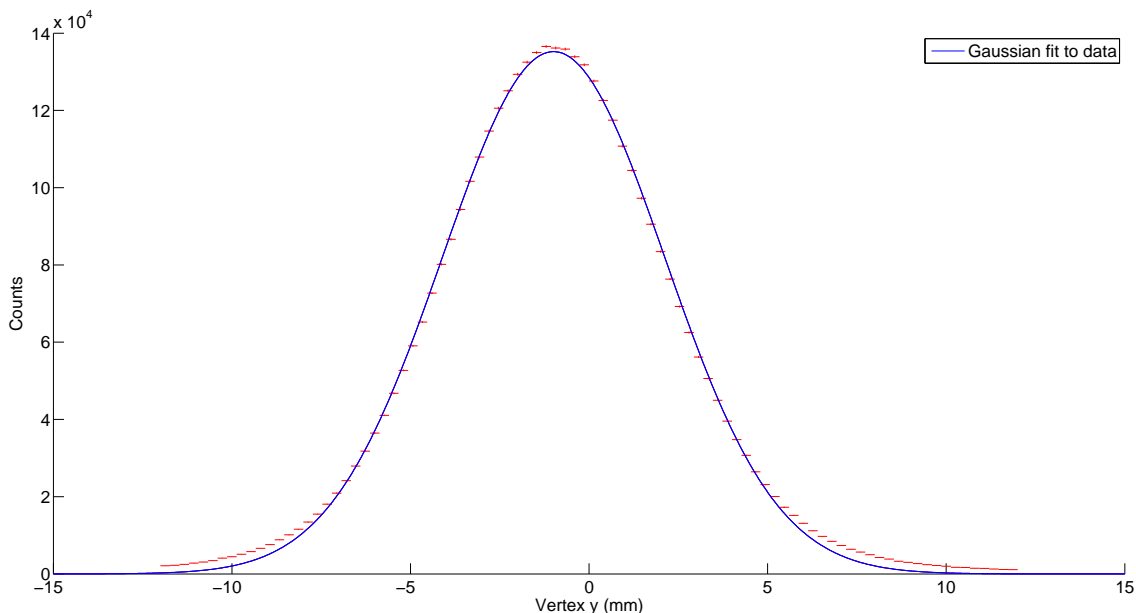


Figure 5-32: Distribution of reconstructed y vertex positions for left-going 12° electrons with a Gaussian fit applied for reference.

The question of the z fiducial cut is somewhat more complicated than the y cut due to the fact that the target distribution has an irregular shape (described in Section 5.1.2) and the poor 12° resolution caused by the limitation to three-plane tracks in combination with the small-angle lever arm for this reconstruction. Additionally, the acceptance of the 12° events is constrained by the target chamber on the downstream side, leading the magnetic field to create a difference in the reconstructed z

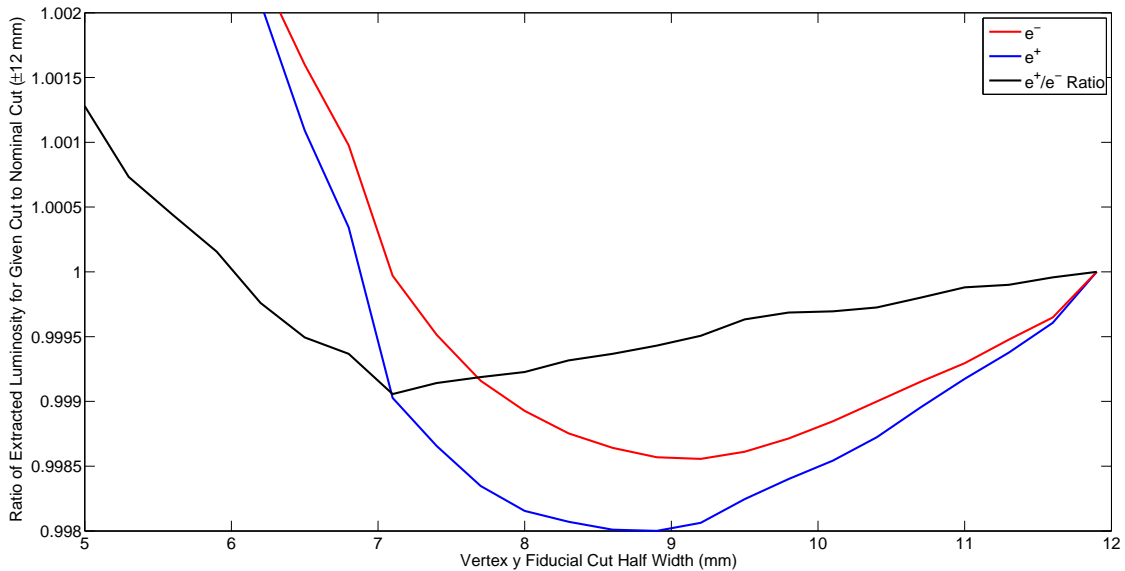


Figure 5-33: Ratio of the absolute and species-relative luminosities extracted in the 12° for varying y fiducial cuts to the value at the nominal cut of ± 12 mm. Cuts smaller than 8 mm begin to cut into the Gaussian region shown in Figure 5-32 and are thus not considered reasonable cuts.

distributions for each species. The reconstructed distributions for each species are shown in Figure 5-16. The nominal fiducial cut was placed as $-380 \text{ mm} < z < 250 \text{ mm}$. Due to the fact that the 12° system has an unrestricted view of the upstream end of the target, the cut on that end has considerably less effect than the upstream cut as can be seen in the distributions. To estimate the effect of the downstream cut, the distributions were examined and an upper bound of $z = 225 \text{ mm}$ was determined to be a reasonable estimate of the tightest reasonable cut. The results are summarized in Table 5.4. The effect on both the absolute and relative luminosities was found to be on the order of 0.1%.

Taking the two fiducial cut effects together by combining them in quadrature, the contributions to the absolute and relative uncertainties are estimated as $\delta_{\text{fid,abs}} = 0.22\%$ and $\delta_{\text{fid,rel}} = 0.12\%$.

Luminosity measurement	Nominal/Tight Cut Ratio
e^+ Absolute	1.0003
e^- Absolute	0.9991
e^+/e^- Relative	1.0012

Table 5.4: Change to the absolute and relative 12° luminosity extractions that occurs when making an upstream z fiducial cut at 225 mm relative to the nominal cut at 250 mm.

Elastic Cuts

Due to the relatively poor resolution of the 12° telescope for most kinematic variables, the philosophy for the final analysis regarding cuts on such variables was to keep such cuts wide so as to avoid cutting into regions of good data. The fact that background contributions were very small in exclusively reconstructed 12° events permits such a philosophy, but it is important to assess the possible effects of such cuts by examining the effects of tightening cut boundaries. As described in Section 5.2.6, the four kinematic elastic cuts made in the 12° analysis were:

1. coplanarity ($\Delta\phi$),
2. vertex z correlation (Δz),
3. beam energy reconstructed from the two track θ values assuming elastic kinematics ($E_{\text{beam},\theta}$), and
4. and the single-arm missing energy of the lepton over the square of the energy as computed by the expected elastic energy from the reconstructed θ ($\Delta E'_\theta/E'^2$).

Following a similar procedure as was used for the assessment of the fiducial cuts, the boundaries for each of these cuts was tightened over a reasonable range and the effect on the resultant luminosity extraction was computed. Since each of these cuts was quite broad, tightening the cuts has a larger systematic effect on the luminosity extraction than broadening the cuts (since relatively few events are outside the cuts), and thus the following studies primarily concern examination of the effects of tighter cuts.

The nominal coplanarity ($\Delta\phi$) cut was placed conservatively at $\pm 4.5^\circ$ around 180° due to the lack of resolution in the lepton ϕ reconstruction and general uncertainty in the quality of proton reconstruction. This cut was tightened to $\pm 3.0^\circ$ in four steps to examine the uncertainty associated with this cut, where $\pm 3.25^\circ$ was judged to be the narrowest reasonable cut. The results of this study are shown in Figure 5-34. Tightening the cut lowers to the absolute luminosity estimate (as the data resolution in ϕ is slightly broader than in simulation), but leaves the relative luminosity stable. The maximum effect on the luminosity from this cut is determined to be 0.01% relative and 0.15% absolute.

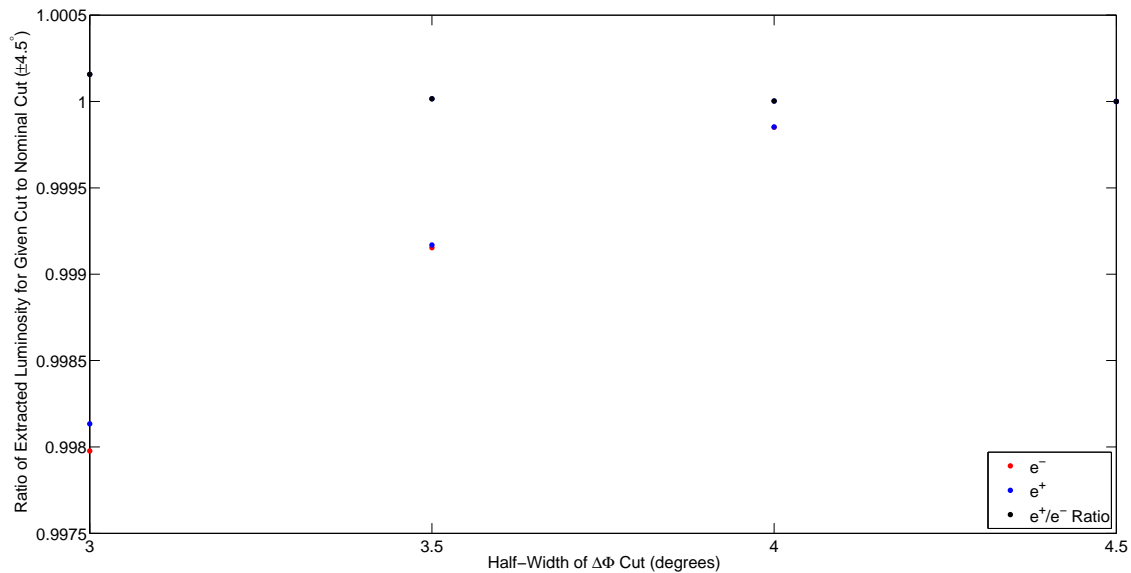


Figure 5-34: Ratio of the absolute and species-relative luminosities extracted in the 12° system for varying $e^\pm p$ track coplanarity ($\Delta\phi$) cuts to the value at the nominal cut of $\pm 4.5^\circ$.

Varying the cut on the vertex z correlation between the lepton and proton track from the nominal value of ± 200 mm produced effects similar to those observed for the coplanarity cut. Figure 5-35 shows the results of the z cut study, in which the cut was varied towards the minimum reasonable value of ± 130 mm. From this information, the maximum effect on the luminosity extraction is estimated as 0.05% relative and 0.8% absolute.

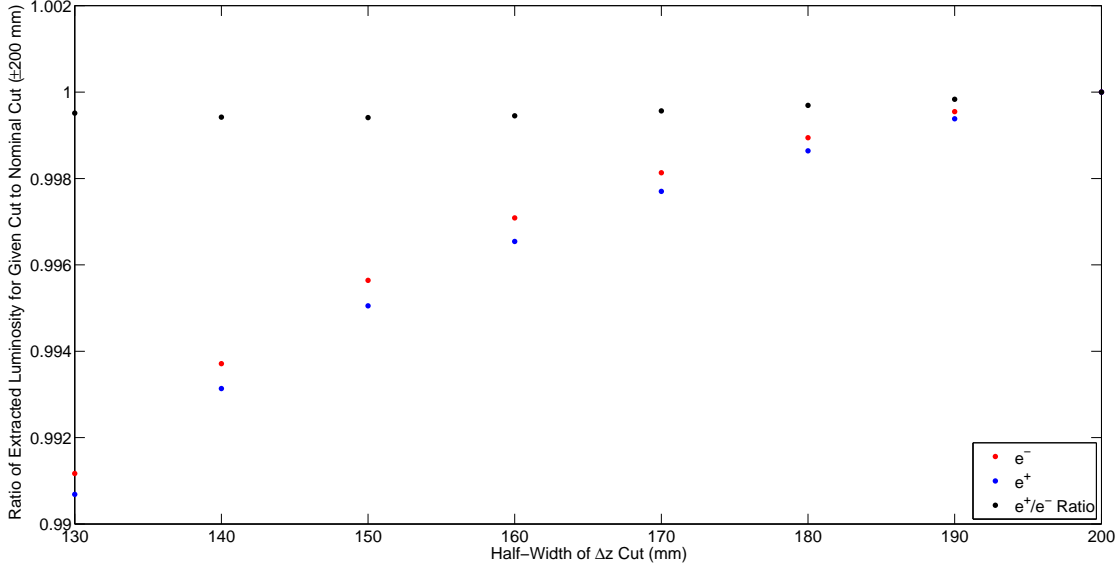


Figure 5-35: Ratio of the absolute and species-relative luminosities extracted in the 12° for varying vertex z correlation cuts (Δz) to the value at the nominal cut of ± 200 mm.

The final two cuts ($E_{\text{beam},\theta}$ and $\Delta E'_\theta/E'^2$) are heavily correlated as they both involve the expected elastic energy of the lepton from the lepton θ . First they will be considered separately in a fashion similar to the previous two cut studies, and then their correlation will be discussed to determine the overall contribution from these cuts to the systematic uncertainty. For the $E_{\text{beam},\theta}$ cut, the range of the cut was varied from the nominal value of 1950 ± 650 MeV down to 1950 ± 300 , while the nominal cut of $\Delta E'_\theta/E'^2 < 5 \cdot 10^{-4}$ MeV $^{-1}$ was varied down to $\Delta E'_\theta/E'^2 < 2 \cdot 10^{-4}$ MeV $^{-1}$. Since these cuts are very sensitive to multiple aspects of the detector resolution, the studied cut range was extended well beyond values considered reasonable. Figures 5-36 and 5-37 show the results of the studies for the $E_{\text{beam},\theta}$ and $\Delta E'_\theta/E'^2$ cuts, respectively.

For the $E_{\text{beam},\theta}$ cut (Figure 5-36), the effect on the relative luminosity is quite flat even for the tightest cuts, and thus the contribution of error to the relative luminosity from this effect alone may be estimated to be 0.18% (the maximum deviation from unity in the study). For the absolute luminosity, the deviation from the nominal value quickens for cuts below a half-width of 450 MeV, indicating that this region is not

a valid cut region due to its sensitivity to distribution rapidly changing in this area. The deviation from unity at ± 450 MeV is thus taken as the estimate of the absolute uncertainty due to this effect: 1.40%.

Variance of the $\Delta E'_\theta/E'^2$ cut (Figure 5-37) causes a smaller absolute effect than the $E_{\text{beam},\theta}$ angles cut, but notably shows different behaviors between species. Due to the poor momentum resolution for reconstructing the leptons, a cut at $\Delta E'_\theta/E'^2 < 3.5 \cdot 10^{-4} \text{ MeV}^{-1}$ was considered the tightest reasonable cut, resulting in an uncertainty of 0.20% for the relative luminosity and 0.24% for the absolute value for this effect alone.

Comparing the values from these two effects, they individually indicate a similar magnitude of uncertainty for the relative luminosity while differing in the absolute luminosity contribution. The larger effect of $E_{\text{beam},\theta}$ on the absolute luminosity is likely due to uncertainty in the proton tracking in data, which broadens this distribution relative to simulation in which the recoil protons are more accurately reconstructed. While it is known that these effects are correlated, it is difficult to fully decouple them due to the complexity of the variables. Thus, as a very conservative estimate, they are considered independent and are added in quadrature for the final estimate for elastic cut uncertainty contribution to the luminosity.

Combining the four cut variation effects in quadrature the total uncertainties due to the elastic cuts amount to $\delta_{\text{elas,rel}} = 0.27\%$ and $\delta_{\text{elas,abs}} = 1.63\%$ for the relative and absolute extractions, respectively. The fact that these uncertainties are large relative to other sources demonstrates that the GEMs would have been a valuable contribution to the 12° measurement had it been feasible, due to the large improvement they provide to tracking resolution. It is notable that the MWPCs, originally designed to provide alignment/efficiency measurement capability for the GEMs and extra low-resolution track points, performed extremely well to provide a luminosity measurement of sufficient precision to satisfy the OLYMPUS goals.

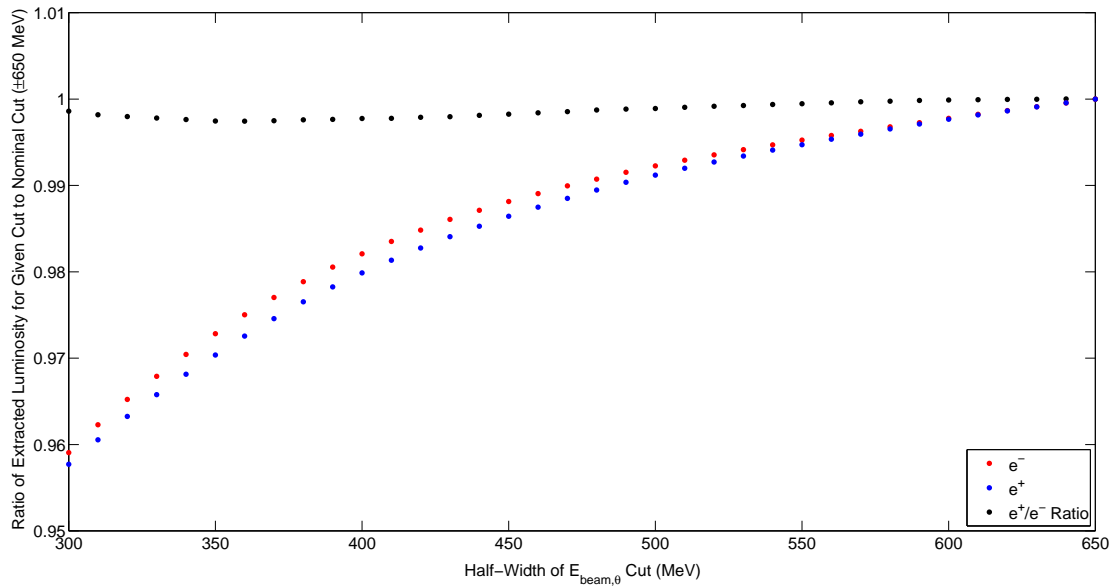


Figure 5-36: Ratio of the absolute and species-relative luminosities extracted in the 12° system for varying cuts on the beam energy reconstructed from track angles assuming elastic kinematics ($E_{\text{beam},\theta}$) to the value at the nominal cut of 1950 ± 650 MeV.

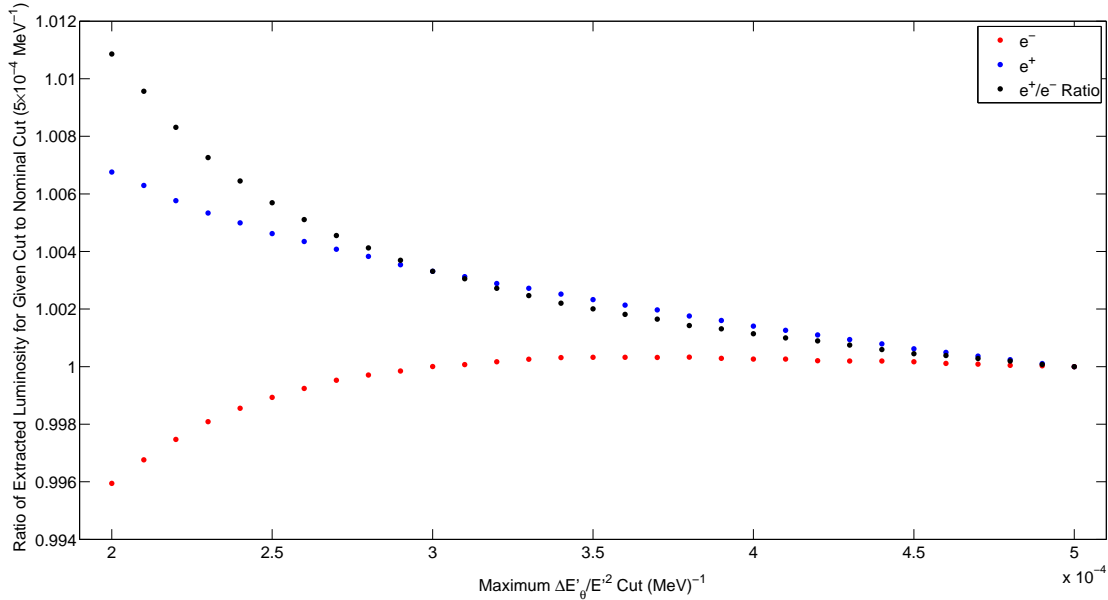


Figure 5-37: Ratio of the absolute and species-relative luminosities extracted in the 12° system for varying cuts on missing energy of the lepton relative to the expected elastic energy from the lepton θ over the square of the energy ($\Delta E'_\theta/E'^2$) to the value at the nominal cut of $<5 \cdot 10^{-4}$ MeV^{-1} .

Radiative Corrections

To assess the effect of radiative corrections on the extracted relative and absolute luminosities, the experiment's simulation included a number of radiative corrections schemes, implemented via multiple stored event weights as described in Section 4.3.2. Figure 5-38 shows the effect on the extracted species relative luminosity for the available radiative corrections schemes, while Figure 5-39 shows the effect on the absolute luminosity extractions for each species. The simulated data shown in the figures includes most of the Run II dataset (several thousand runs) and therefore the statistical uncertainty, which is also highly correlated between the points, is extremely small relative to the variation in the points due to the weights. Several models included in the radiative corrections (in particular the Born approximation and soft photon approximation (SPA)) are included only for comparison with historical experimental data and are not considered realistic models. Additionally, the inclusion of full vacuum polarization effects derived from $e^+e^- \rightarrow$ hadrons cross sections is preferred to the inclusion of only lepton vacuum polarization effects [170, 171, 196]. Further details on the different radiative corrections schemes included in the figures may be found in Section 4.3.2.

After discounting the previously aforementioned unrealistic models, the spread in the remaining results was used to estimate the systematic uncertainty introduced by radiative corrections. The maximally different results occurred between the Mo & Tsai (Reference [99]) correction under the photon ΔE method and the methods with full vacuum polarization included for both the absolute and relative measurements. The radiative correction uncertainty was thus conservatively taken to be the maximal spread: $\delta_{\text{rad,rel}} = \pm 0.08\%$ and $\delta_{\text{rad,abs}} = \pm 0.45$.

Elastic Form Factors

Due to the fact that the Q^2 range accepted by the 12° telescopes for each of the lepton species is slightly different in the single toroid polarity, there is an uncertainty introduced from the uncertainty in the magnitude of the proton elastic form factors

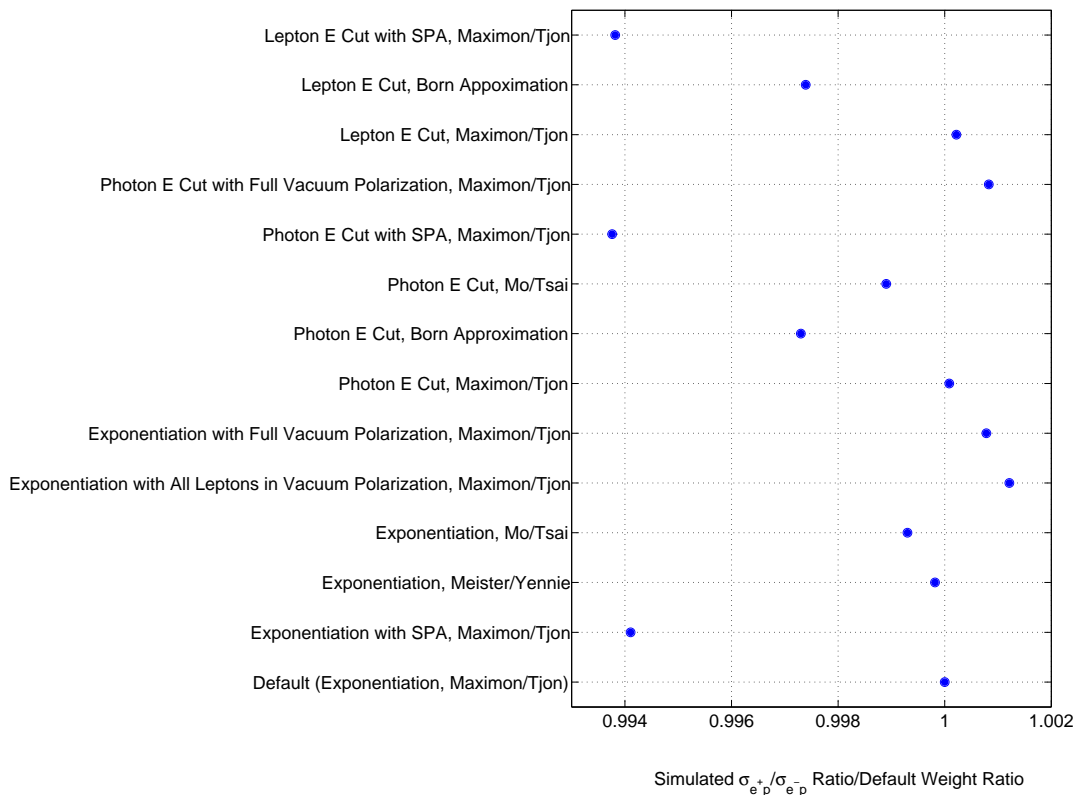


Figure 5-38: Effects of applying different radiative corrections schemes to the simulation on the resulting extracted relative 12° luminosity. The maximal deviation between realistic models was $\delta_{\text{rad,rel}} = \pm 0.08\%$. Details on the three main correction schemes included above (Maximon & Tjon, Meister & Yennie, and Mo & Tsai) may be found in [100], [165], and [99], respectively, and a more detailed discussion of these methods may be found in Section 4.3.2.

and the variation in the form factors at small Q^2 . Figure 5-40 shows the distribution in Q^2 of events of each lepton species in the 12° telescopes, which notably exhibits a shift of approximately $0.3 \text{ GeV}^2/c^2$ between the two event types. Thus, the form factor (a function of Q^2) will not cancel completely in the ratio of the integrated acceptances for each species. Additionally, any uncertainty in the magnitude of the form factors directly contributes systematic uncertainty to the absolute luminosity extraction.

To estimate the uncertainty in the 12° luminosity estimate due to uncertainties in the proton form factors, a similar method was used as in the previous section to estimate the effects of radiative corrections uncertainties. The OLYMPUS simula-

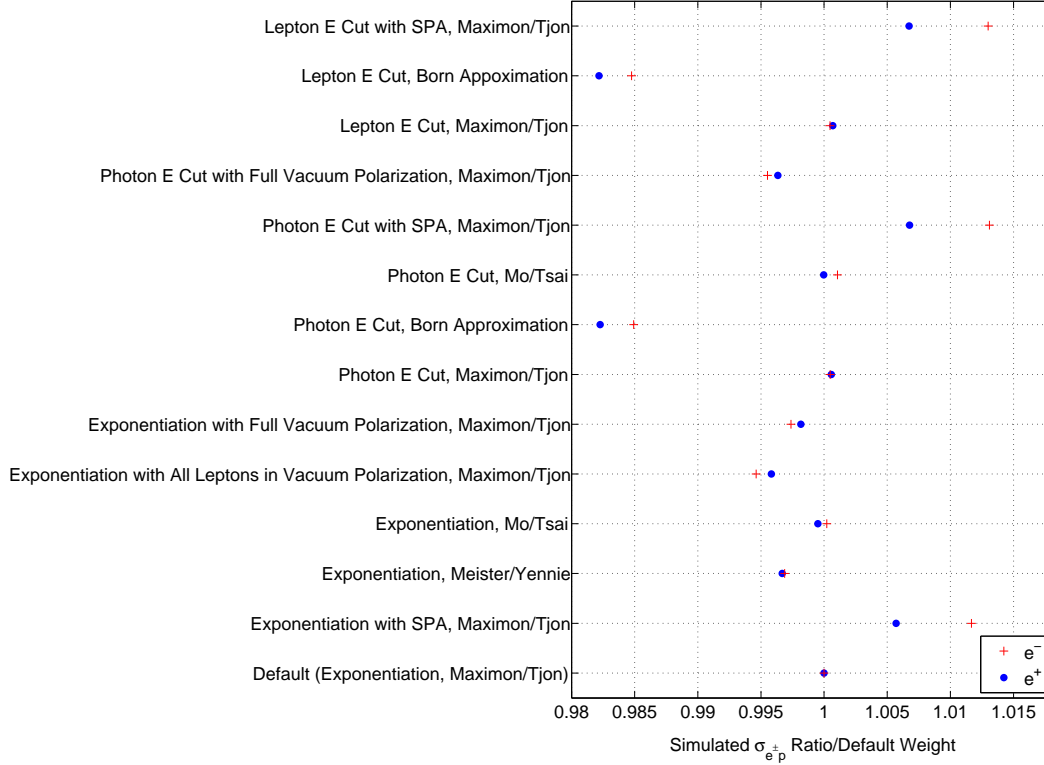


Figure 5-39: Effects of applying different radiative corrections schemes to the simulation on the resulting extracted absolute 12° luminosity for each species. The maximal deviation between realistic models was $\delta_{\text{rad,abs}} = \pm 0.45\%$. Details on the three main correction schemes included above (Maximon & Tjon, Meister & Yennie, and Mo & Tsai) may be found in References [100], [165], and [99], respectively, and a more detailed discussion of these methods may be found in Section 4.3.2.

tion includes additional event weights for several form factor models including, the Bernauer, et al. fits (Reference [37]) and the Kelly model (Reference [197]), as well as dipole and point-like proton models for reference. Most notably, the Bernauer model exhibits a structure in G_M in the vicinity of $Q^2 \approx 0.2 \text{ GeV}^2/c^2$ (Figure 20.b. in Reference [37]) that is not present in the majority of form factor fits that creates disagreement in the prediction of different form factor models within the 12° system acceptance. The spread in the resulting luminosities when using the Bernauer and Kelly models, which does not exhibit the aforementioned structure in G_M , was taken as an estimate of the systematic uncertainty due to the form factors, discounting the spread due to the unrealistic proton and dipole form factors. Figures 5-41 and

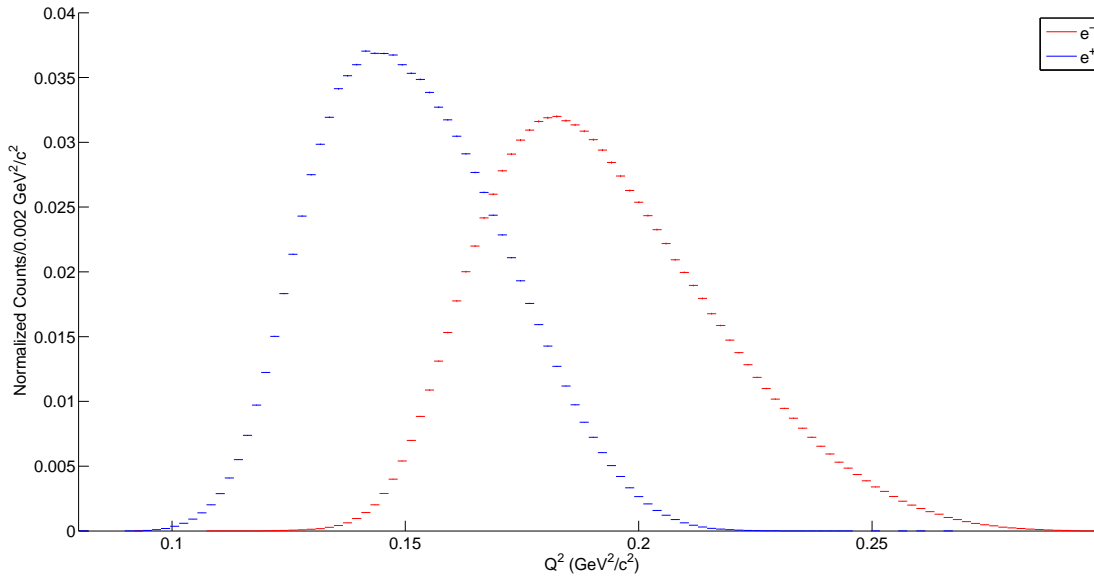


Figure 5-40: Normalized distributions of the Q^2 computed from the reconstructed lepton θ for electron- and positron-proton elastic scattering events accepted by the 12° system. Note the differences of the systematic $\sim 0.3 \text{ GeV}^2/c^2$ shift between the acceptance ranges of the two species and the longer tail at higher Q^2 values for electrons caused by the in-bending of the negatively-charged electrons from the upstream end of the target cell.

5-42 show the results of this study for the species-relative and absolute luminosity extractions, respectively, in which it was found that the uncertainties due to the form factors could be estimated as $\delta_{\text{ff,rel}} = \pm 0.14\%$ and $\delta_{\text{ff}} = \pm 1.2\%$.

TPE at 12°

As noted in Section 5.2.1, the underlying physics process measured by the 12° system is the same process ($e^\pm p$ elastic scattering) that is under examination in the main detector for TPE contributions and thus it is not excluded that a difference in the e^+p and e^-p cross sections at $\theta \approx 12^\circ$ due to TPE could exist and systematically shift any attempt to determine the relative luminosity from this measurement. To estimate the possible size of this shift, several methods may be considered:

1. comparison with the other OLYMPUS luminosity measurements (amounting to a measurement of $\sigma_{e^+p}/\sigma_{e^-p}$ at $Q^2 \approx 0.165 \text{ GeV}^2/c^2$, $\epsilon \approx 0.98$ as is discussed in

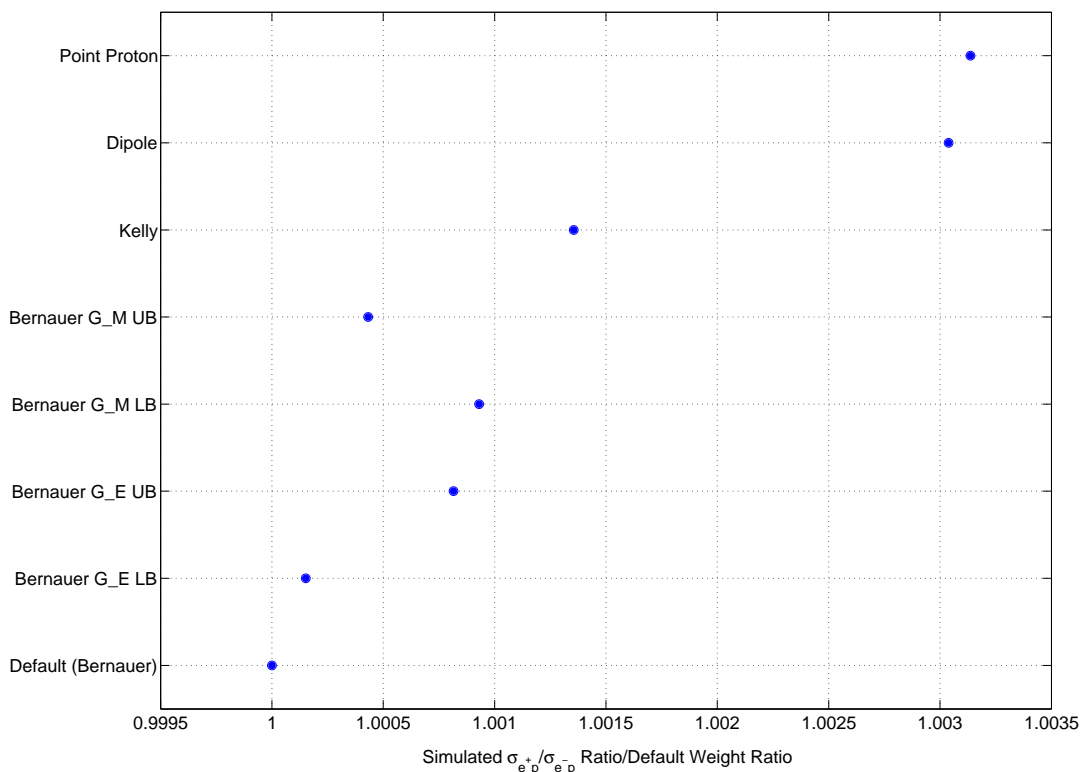


Figure 5-41: Effects of applying different form factor models to the simulation on the resulting extraction of the species-relative 12° luminosity ratio, including the unphysical dipole and point proton models. The systematic uncertainty was estimated as the spread in the Bernauer and Kelly parametrizations (References [37] and [197], respectively): $\delta_{\text{ff,rel}} = \pm 0.14\%$. Note that radiative corrections were applied to these results using the default method (exponentiation, Maximon & Tjon [100]) in each case, but that the effects of the changing form factor were accounted for in calculating the radiative corrections.

Section 7.2.1),

2. comparison with existing data, and
3. examination of the spread of theoretical predictions for the value of $\sigma_{e+p}/\sigma_{e-p}$ in 12° region.

The question of the first point is addressed in Section 7.2.1 and effectively does not treat the 12° result as a luminosity measurement, so here it is attempted to estimate this uncertainty from outside sources. From the standpoint of data constraints, the

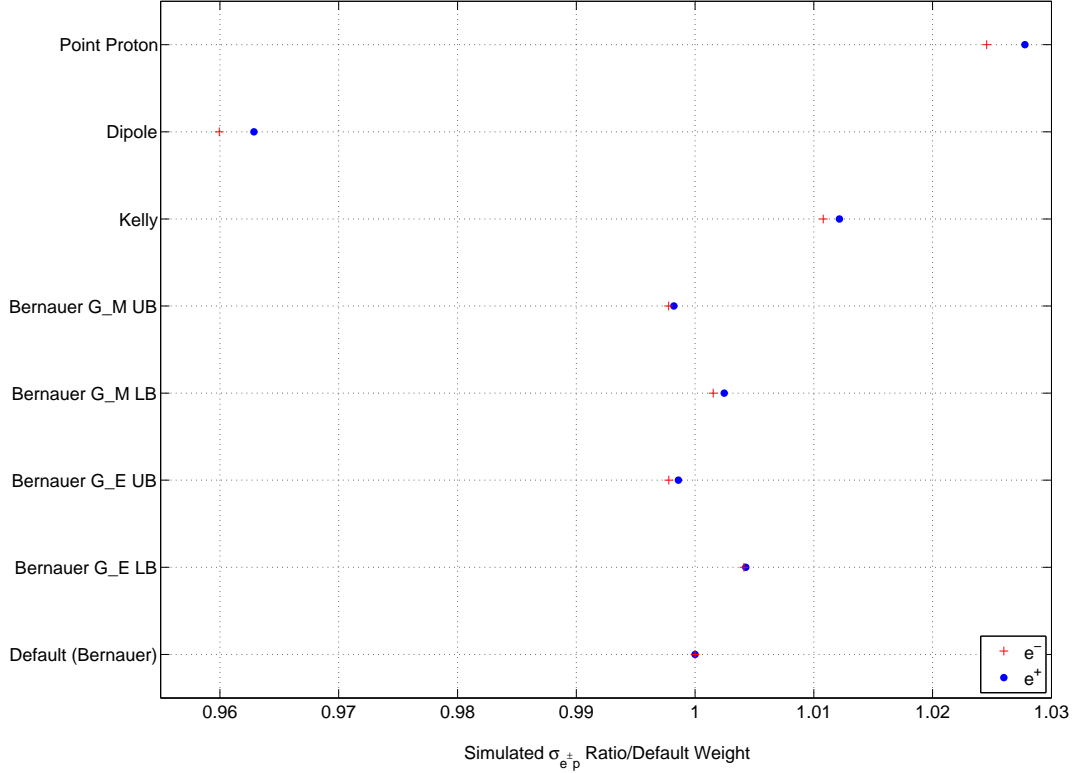


Figure 5-42: Effects of applying different form factor models to the simulation on the resulting extraction of the absolute 12° luminosity for each species, including the unphysical dipole and point proton models. The systematic uncertainty was estimated as the spread in the Bernauer and Kelly parametrizations (References [37] and [197], respectively): $\delta_{\text{ff,rel}} = \pm 1.2\%$. Note that radiative corrections were applied to these results using the default method (exponentiation, Maximon & Tjon [100]) in each case, but that the effects of the changing form factor were accounted for in calculating the radiative corrections.

VEPP-3 experiment (Reference [115]) used forward elastic $e^\pm p$ scattering for luminosity normalization in a similar fashion as OLYMPUS would use the 12° data as a standalone luminosity normalization and thus does not provide a useful constraint on the value of $\sigma_{e^+p}/\sigma_{e^-p}$ at high ϵ /low Q^2 . The CLAS experiment, which used photon-induced e^+e^- pair production to balance luminosities, provides a measurement of $\sigma_{e^+p}/\sigma_{e^-p}$ in the small angle bin with average $Q^2 = 0.232 \text{ GeV}^2/c^2$, $\epsilon = 0.915$ of $R_{2\gamma} = 0.991 \pm 0.009$ (including systematic and statistical uncertainty) and a variety of measurements at $\epsilon > 0.88$ and $Q^2 < 0.9 \text{ GeV}^2/c^2$ that all scatter around

$R_{2\gamma} = 1$ within uncertainties on the order of 1% [114, 198]. Most of the data prior to the modern experiments, predominantly from the 1960s, consists of data at low Q^2 but higher ϵ (References [48, 49, 110]) or are at much higher energies/ Q^2 (References [50, 51, 111]). One older experiment (Reference [112]), provides a measurement at a comparable kinematic point to the 12° system of $R_{2\gamma} = 1.012$, but quotes uncertainties on the order 3.0%. Thus, at best, existing data constrains this uncertainty to order 0.5%, and no precise measurement of $\sigma_{e^+p}/\sigma_{e^-p}$ at very high ϵ exists in previous data.

Examining various theoretical and phenomenological models for TPE in this region (References [37, 39–47]), most predict $R_{2\gamma}$ to be near unity but vary on the order of a tenth of a percent, as exemplified in Figure 1-2, and thus are all roughly consistent with the previously aforementioned experimental data. Taking into account these available sources of experimental and theoretical estimates, it is reasonable to apply an additional 0.1% uncertainty on the relative and absolute luminosities when the 12° is taken as a standalone normalization point for the data set: $\delta_{\text{TPE,abs}} = \delta_{\text{TPE,rel}} = \pm 0.1\%$. Any contribution OLYMPUS can make in reducing this uncertainty via the combination of multiple luminosity measurements would be valuable for the constraint of the VEPP-3 normalization point and the various models.

Additional Discussion on Systematic Uncertainties

As can be seen in Table 5.2, the 12° system total systematic uncertainty for the relative luminosity is well below 1% and thus provides a sufficiently good measurement for the $\sigma_{e^+p}/\sigma_{e^-p}$ analysis to meet the OLYMPUS goals. Additionally, the system performed admirably in providing an approximate absolute luminosity measurement (or cross section measurement if combined with an alternate luminosity measurement). Furthermore, note that the dominant systematics (ToF trigger efficiency, lepton tracking, efficiency, magnetic field, and elastic cuts) are all estimated in a non-Gaussian fashion and thus represent “box-like” limits. Those wishing to interpret the systematic uncertainty as a Gaussian 1σ error could approximate this by multiplying the standard deviation of the uniform distribution of unity width ($1/\sqrt{12}$), although this

is not necessarily a correct interpretation or good estimate of the systematic uncertainty. Certain contributions to the uncertainty are correlated between the left and right telescopes, reducing somewhat the estimate of the relative uncertainty between the telescopes. The details of this will be discussed in the comparison of the left and right side results in Section 5.2.9.

5.2.9 Results

With the complete analysis method and systematic uncertainty determination, the final results for the 12° luminosity may be considered. The results in this section are quoted as ratios of the measured 12° luminosity (calculated separately for detection of the lepton in the left and right telescopes and for the combined statistics of both sides) to the luminosity used to generate the simulation event sets (i.e., the slow control luminosity for a given run). This amounts to reformulating Equation 5.11 as:

$$\frac{\mathcal{L}_{12^\circ}}{\mathcal{L}_{\text{MC}}} = \frac{\mathcal{L}_{12^\circ}}{\mathcal{L}_{\text{SC}}} = \frac{N_{\text{data}}}{N_{\text{MC}}(\mathcal{L}_{\text{SC}})}. \quad (5.19)$$

Note that the value of $\mathcal{L}_{12^\circ}/\mathcal{L}_{\text{SC}}$ is expected to be unity only within the uncertainty of the slow control luminosity measurement, which, as discussed in Section 5.1.3, is on the order of several percent in both the relative and absolute luminosities.

To provide a scale in units of integrated luminosity, a typical data run consisted of $\sim 1.5 \cdot 10^{36} \text{ cm}^{-2}$ of recorded integrated luminosity. Thus, the entire data set used for the analysis in this work (~ 2200 runs) corresponds to $\sim 3.1 \cdot 10^{39} \text{ cm}^{-2}$ ($\sim 3.1 \text{ fb}^{-1}$) of data, approximately equally split between the two lepton species.

The results of the 12° luminosity estimates are summarized in Table 5.5, showing the measurements and associated uncertainties (as determined in Section 5.2.8) for detection of the lepton in the left and right arms as well as the measurement combining the statistics of the two samples. Figures 5-43, 5-44, and 5-45 show the run-by-run estimates for the left arm, right arm, and combined measurements respectively. For each run-by-run sample, the values are histogrammed (weighted by their statistical significance) to provide a means of determining the effective values of $\mathcal{L}_{12^\circ}/\mathcal{L}_{\text{SC}}$ for the

full dataset. Statistical errors on the datasets were computed at the 95% confidence bound on the fit to the mean of this histogram. For all estimates, the statistical uncertainty is effectively negligible relative to the systematic uncertainties. In general, the widths of the histogrammed distributions of run-by-run luminosities were found to be only slightly larger ($\sim 0.1\%$) than the mean statistical error associated with the estimate from individual runs (1.5% and 1.7% for single-telescope measurements of e^+p and e^-p runs respectively) and the distributions are well represented by Gaussian distributions, indicating that only minor time-varying systematic effects were present in the slow control luminosity. As will be discussed in Section 5.4, the SYMB run-by-run estimates show similar features as the 12° , indicating that the run-by-run variance was indeed due to effects in the slow control estimate rather than the 12° estimate.

In general, the absolute luminosities determined by the 12° systems are several percent above the slow control estimate, while the species-relative luminosity determination is within a few tenths of a percent of unity. The left and right estimates agree well to within uncertainties, providing further evidence for the validity of the measurements. These estimates provide an effective normalization for the main OLYMPUS results and, with the addition of the SYMB luminosity estimate, an additional measurement of $\sigma_{e^+p}/\sigma_{e^-p}$ in the vicinity of $\theta \approx 12^\circ$, as will be discussed in Chapters 6 and 7.

5.3 Luminosity Determined Using the SYMB System

As originally designed, the symmetric Møller/Bhabha calorimeter system was to provide a luminosity measurement completely independent from $e^\pm p$ scattering, examining only the processes $e^\pm e^- \rightarrow e^\pm e^-$ and $e^+ e^- \rightarrow \gamma\gamma$ involving beam leptons and atomic electrons from the hydrogen gas within the target. This method of measuring the luminosity would avoid any assumptions regarding the magnitude of TPE effects

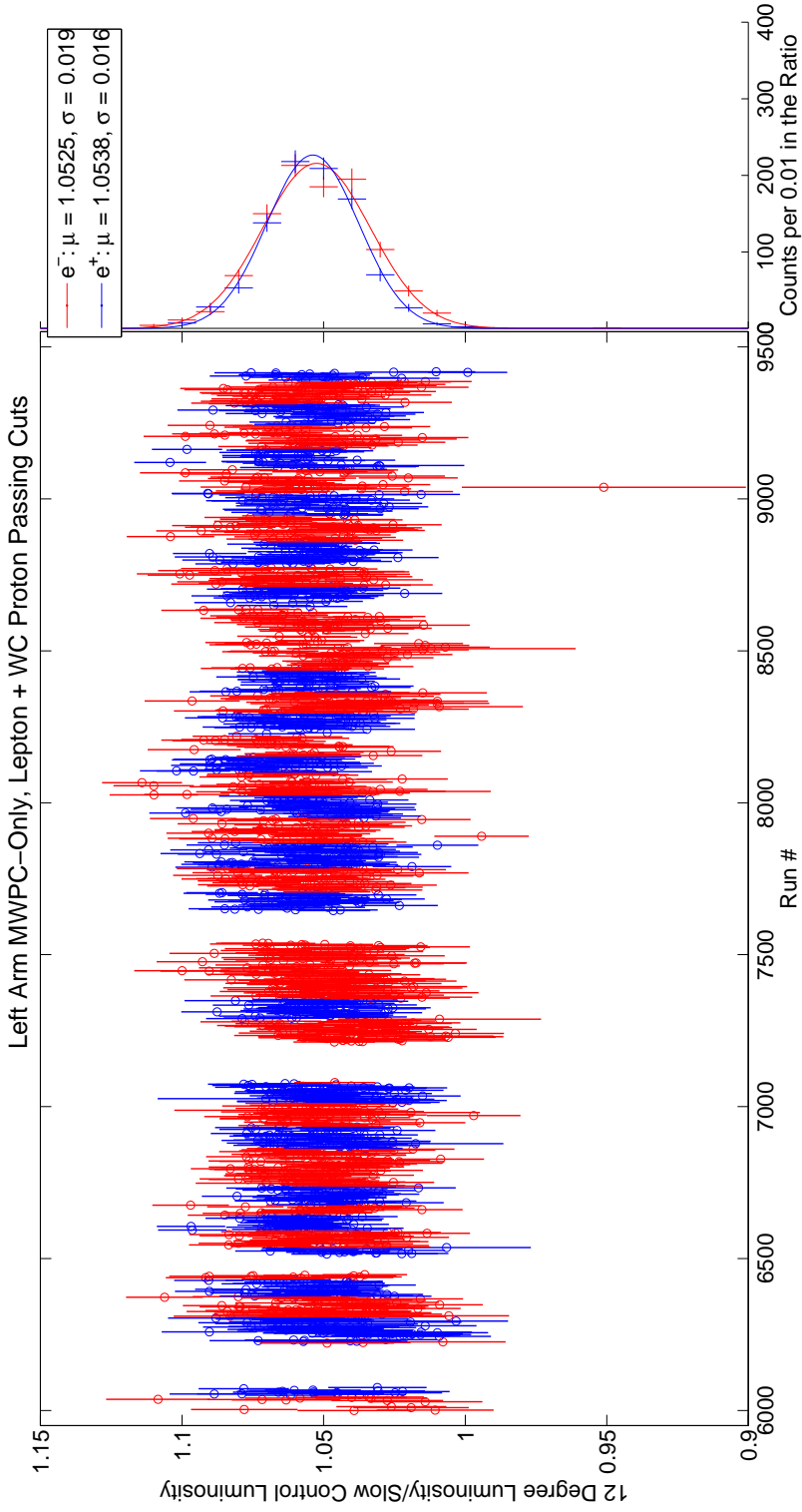


Figure 5-43: Run-by-run estimate of the integrated luminosity collected by the OLYMPUS experiment relative to the slow control estimate, as measured by examining $e^\pm p$ events in which the lepton was detected in the left 12° telescope in coincidence with a proton in the right drift chamber, subject to the analysis described in Section 5.2.6. The run-by-run values are histogrammed in the right-hand plot and fitted to Gaussian distributions for each species to produce the estimates of the luminosities for each species over the full data set.

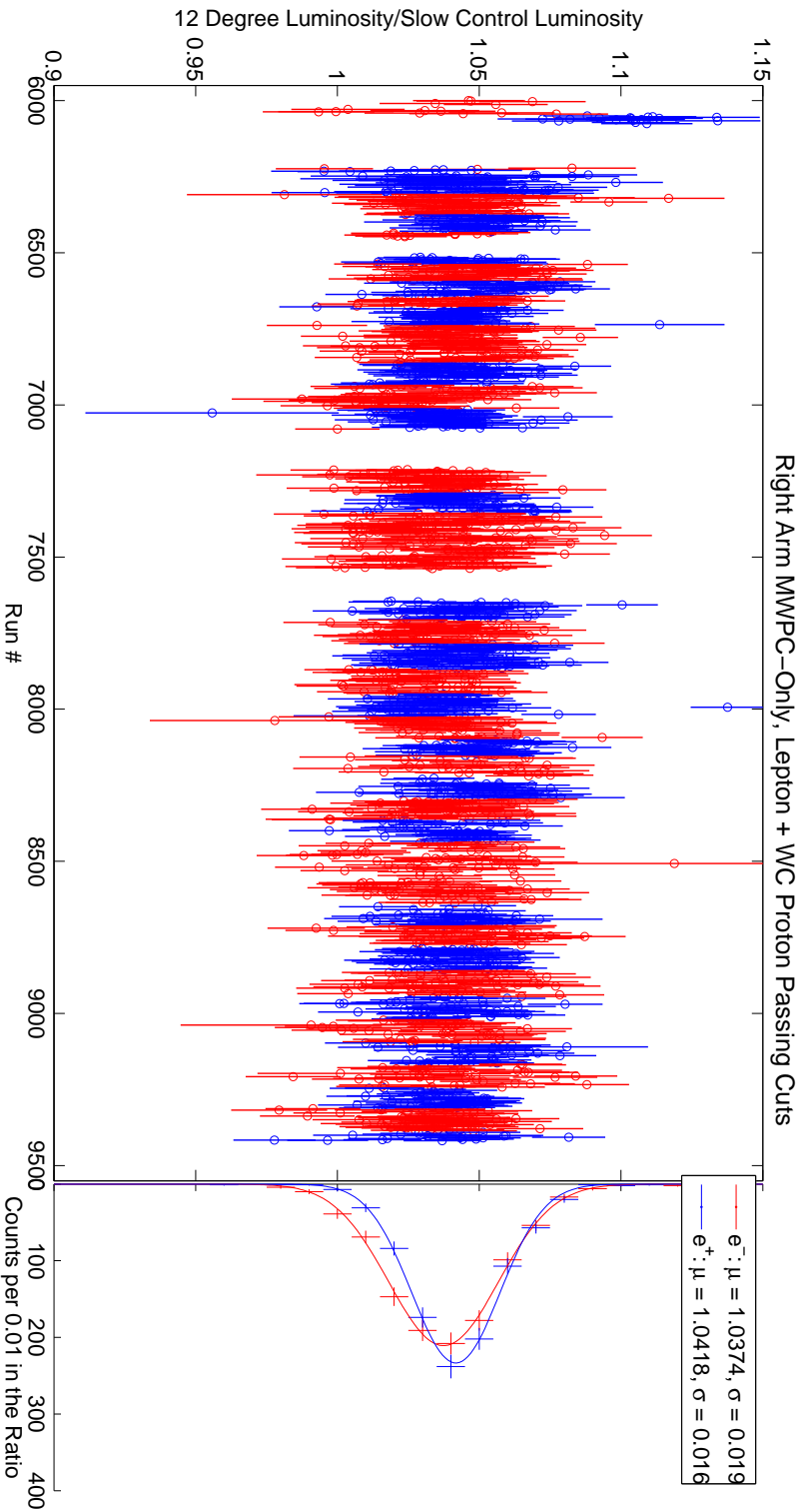


Figure 5-44: Run-by-run estimate of the integrated luminosity collected by the OLYMPUS experiment relative to the slow control estimate, as measured by examining $e^\pm p$ events in which the lepton was detected in the right 12° telescope in coincidence with a proton in the left drift chamber, subject to the analysis described in Section 5.2.6. The run-by-run values are histogrammed in the right-hand plot and fitted to Gaussian distributions for each species to produce the estimates of the luminosities for each species over the full data set. The outlier positron runs in the vicinity of Run 6050 were taken while the MWPC data acquisition was malfunctioning, and thus they are excluded from the estimate.

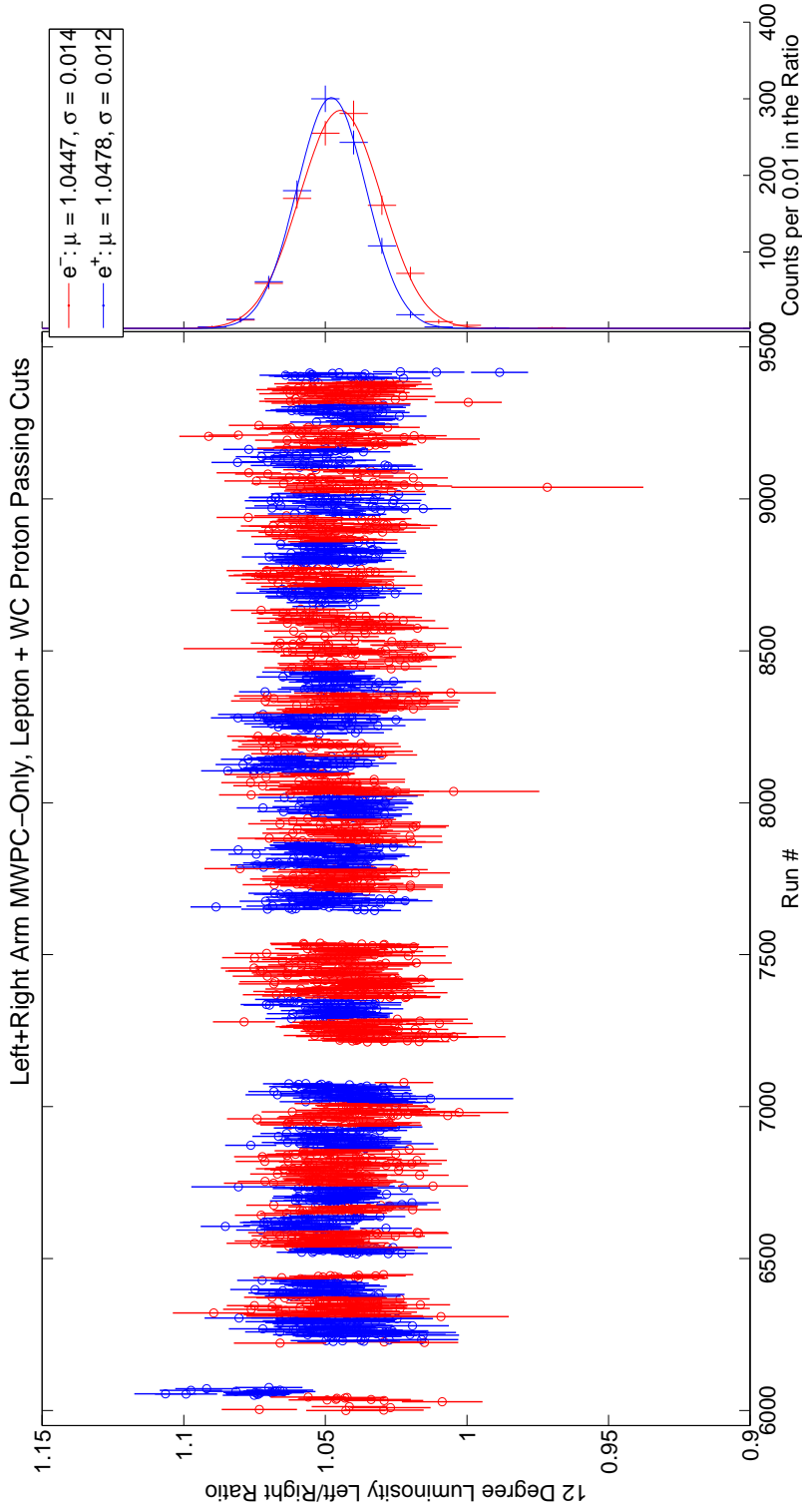


Figure 5-45: Run-by-run estimate of the integrated luminosity collected by the OLYMPUS experiment relative to the slow control estimate, as measured by examining $e^\pm p$ events in which the lepton was detected in either 12° telescope in coincidence with a proton in the opposite side drift chamber, subject to the analysis described in Section 5.2.6. The run-by-run values are histogrammed in the right-hand plot and fitted to Gaussian distributions for each species to produce the estimates of the luminosities for each species over the full data set. The outlier positron runs in the vicinity of Run 6050 were taken while the MWPC data acquisition was malfunctioning, and thus they are excluded from the estimate.

Measurement	Value
$\mathcal{L}_{12^\circ,e^+,L}/\mathcal{L}_{\text{SC},e^+}$ (e^+ Left + p Right)	1.0538 ± 0.0003 (stat.) ± 0.0244 (syst.)
$\mathcal{L}_{12^\circ,e^-,L}/\mathcal{L}_{\text{SC},e^-}$ (e^- Left + p Right)	1.0525 ± 0.0003 (stat.) ± 0.0244 (syst.)
$(\mathcal{L}_{12^\circ,e^+,L}/\mathcal{L}_{12^\circ,e^-,L})/(\mathcal{L}_{\text{SC},e^+}/\mathcal{L}_{\text{SC},e^-})$	1.0012 ± 0.0004 (stat.) ± 0.0046 (syst.)
$\mathcal{L}_{12^\circ,e^+,R}/\mathcal{L}_{\text{SC},e^+}$ (e^+ Right + p Left)	1.0418 ± 0.0003 (stat.) ± 0.0244 (syst.)
$\mathcal{L}_{12^\circ,e^-,R}/\mathcal{L}_{\text{SC},e^-}$ (e^- Right + p Left)	1.0374 ± 0.0003 (stat.) ± 0.0244 (syst.)
$(\mathcal{L}_{12^\circ,e^+,R}/\mathcal{L}_{12^\circ,e^-,R})/(\mathcal{L}_{\text{SC},e^+}/\mathcal{L}_{\text{SC},e^-})$	1.0042 ± 0.0004 (stat.) ± 0.0046 (syst.)
$\mathcal{L}_{12^\circ,e^+}/\mathcal{L}_{\text{SC},e^+}$	1.0478 ± 0.0002 (stat.) ± 0.0244 (syst.)
$\mathcal{L}_{12^\circ,e^-}/\mathcal{L}_{\text{SC},e^-}$	1.0447 ± 0.0002 (stat.) ± 0.0244 (syst.)
$(\mathcal{L}_{12^\circ,e^+}/\mathcal{L}_{12^\circ,e^-})(\mathcal{L}_{\text{SC},e^+}/\mathcal{L}_{\text{SC},e^-})$	1.0030 ± 0.0003 (stat.) ± 0.0046 (syst.)

Table 5.5: Summary of the results of the measurement of the luminosity in the 12° system for the measurements using the left and right telescopes for the detection of the scattered lepton separately, as well the combined result. Determination of the quoted systematic uncertainties is detailed in Section 5.2.8. The statistical errors represent the 95% confidence interval for the average value of the ratio computed over the entire data set. The measurements are presented as the average adjustment to apply to the integrated slow control luminosity (SCL) for the entire data set so as to compute the estimate of the integrated luminosity from the 12° measurements for each lepton species. The e^+/e^- ratios presented here would be measurements of $\sigma_{e^+p}/\sigma_{e^-p}$ assuming perfect relative slow control luminosity ($\mathcal{L}_{\text{SC},e^+}/\mathcal{L}_{\text{SC},e^-} = 1$), but are better interpreted as normalization points assuming no TPE at 12° for the relative luminosity or as measurements of $N_{e^+p,\text{data}}(\epsilon, Q^2)/N_{e^-p,\text{data}}(\epsilon, Q^2)$ at $\epsilon \approx 0.98$, $Q^2 \approx 0.165 \text{ GeV}^2$ that may be normalized by an independent luminosity measurement (e.g., that of the SYMB system (Section 5.3)) to compute $R_{2\gamma}$ as in Equation 1.1. See Section 7.2.1 for latter analysis.

in $e^\pm p$ scattering at forward angles that are necessary when using the 12° measurement as a luminosity normalization. The original measurement principle was to count such lepton-lepton scattering events in which the outgoing particles scatter symmetrically about the beam axis ($\theta \approx 1.29^\circ$ at $E_{\text{beam}} = 2.01 \text{ GeV}$) and then detected in coincidence in the left and right calorimeters via the deposit of approximately 1 GeV of energy in each and, as in the other OLYMPUS analyses, compare the measured rates to those expected from Monte Carlo simulation. The collimators in front of the calorimeters limited the acceptance of the detector to such events near the symmetric scattering angle. This method was to provide a very high statistics measurement of the integrated luminosity using the very high rate of forward lepton-lepton scattering, with statistical uncertainties far smaller than any other element of the analysis.

Unfortunately, for a number of reasons briefly described in the next section and detailed in Reference [55], this method of luminosity determination was untenable for the OLYMPUS analysis in that it would have introduced an unacceptably large systematic uncertainty to the final $\sigma_{e^+p}/\sigma_{e^-p}$ analysis.

To provide a luminosity measurement from the SYMB system that avoided the problems associated with the original method, a new analysis was developed in which the ratio of rates of multiple event types was detected in the SYMB calorimeters. In particular, two types of events were considered for the analysis:

- coincidence symmetric lepton-lepton scattering events (as would have been used in the original analysis), and
- the detection of *simultaneous* (i.e., from the same beam bunch) coincidence symmetric leptons and additionally a single lepton with energy ~ 2 GeV corresponding to a very forward elastic $e^\pm p$ scatter resulting in the deposition of ~ 1 GeV in one calorimeter and ~ 3 GeV in the other.

While this method greatly reduces the statistical power of the measurement, taking the ratio of multiple event types reduces systematic uncertainties associated with detector efficiency and eliminates the need to simulate the three separate lepton-lepton event types. This analysis, referred to as the *multi-interaction event* (MIE) method, and its results are described in Section 5.3.2 and Reference [53] provides complete detail on the method.

In general, this section provides a brief summary of the analyses and results from the SYMB system for the purpose of establishing the necessary results for the main analysis described in the remaining chapters. Complete discussions of these analyses may be found in the theses of O'Connor and Schmidt (References [55] and [53]).

5.3.1 Discussion of the Untenability of the Original Coincident Event Analysis

As originally conceived, the SYMB analysis would have involved comparing the rates of symmetric $e^-e^- \rightarrow e^-e^-$ scattering for electron beam running to the rates of

symmetric $e^+e^- \rightarrow e^+e^-$ and $e^+e^- \rightarrow \gamma\gamma$ for positron beam running, normalized to simulation of all three processes in a similar fashion as the other OLYMPUS analyses. This concept was based on a forward calorimeter luminosity monitoring scheme used by the HERMES experiment to measure the relative luminosity of positron beams of different polarizations incident on a hydrogen target via $e^+e^- \rightarrow e^+e^-$ and $e^+e^- \rightarrow \gamma\gamma$ events [199]. In converting this concept to a measurement of the relative luminosities of different beam species, however, several important differences were not properly considered. In particular, the cross sections for the aforementioned processes change rapidly as a function of θ in the region of the SYMB detectors, and additionally the cross sections for the different processes vary in θ with different slopes in the region of interest ($\theta \approx 1.3^\circ$), as shown in Figure 5-46. This difference makes the original method extremely sensitive to small shifts in beam position, beam slope, and the placement of the detectors (both in absolute space and relative between the two collimators). Additionally, the comparison of cross sections for multiple processes involves the simulation of all such processes and the application of proper radiative corrections methods for each, introducing an additional large systematic uncertainty to any luminosity result using such a method. Reference [55] provides a full analysis of these effects. It was determined that given the survey uncertainty, beam position uncertainty, available radiative corrections schemes at the time of the analysis, and other systematic effects there was at least a 2.8% systematic uncertainty in any species-relative luminosity measurement made using this method. Use of such an imprecise luminosity would spoil the resulting uncertainty on the $R_{2\gamma}$ determination well beyond the 1% uncertainty goals of the experiment. Analyses that attempted to use this method found values of $\mathcal{L}_{e^+}/\mathcal{L}_{e^-}$ that deviated by several percent or more from the measurements of all other systems, and additionally found that the measured rate varied inexplicably by several percent over time.

In addition to the inherent sources of uncertainty in this method, it is also believed that the electronics used in the SYMB detector to assess the local-max condition (requiring that the central crystal in the calorimeter have the highest energy deposited) and the left/right coincidence module may have had failure modes that affected the

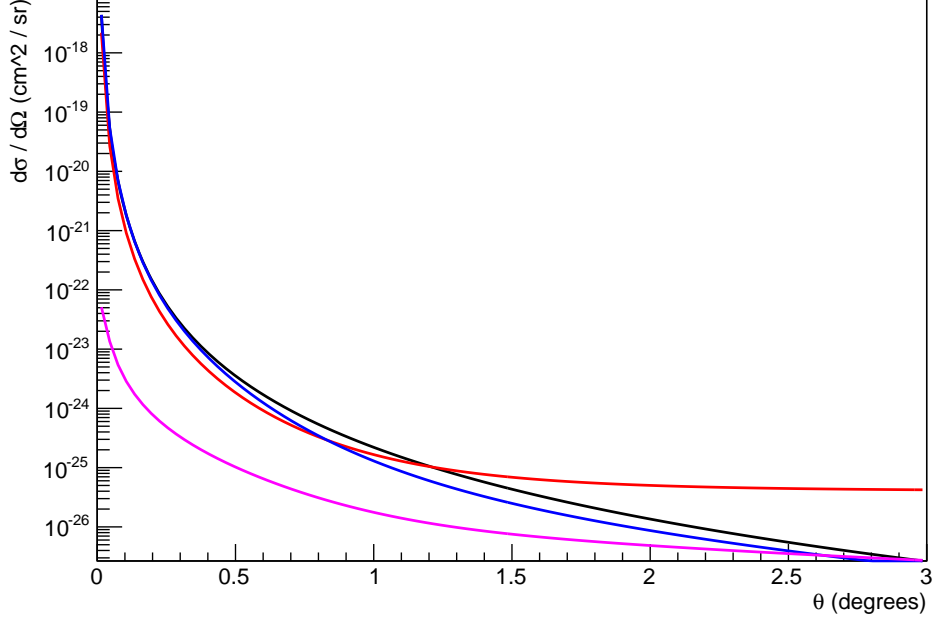


Figure 5-46: Calculated tree-level differential cross sections for Møller scattering (red), Bhabha scattering (blue), pair annihilation (magenta), e^-p elastic scattering (black) in the vicinity of the SYMB calorimeter acceptance. (Figure reproduced from [145].)

detector during data-taking. Regarding the latter, the coincidence histogram showed behavior away from the main (1 GeV, 1 GeV) peak that could not be reproduced in simulation, and was possibly due to a small timing error in the window of coincidence used by the coincidence module between the two calorimeters. Regarding the former, it was hypothesized that for events with large energy deposition in a single calorimeter, the comparator module which determines if the central crystal has the highest deposition could be saturated at its maximum value leading to an erroneous local maximum event rejection [200]. These two possible issues pose additional concerns for the coincidence measurement, and must be avoided or suppressed in any alternative methods of extracting a luminosity measurement from the SYMB.

5.3.2 The Multi-Interaction Event Luminosity Determination

With the originally proposed method for producing a luminosity analysis from the SYMB system invalidated, other methods were sought to provide a means of estimating the luminosity using the SYMB that was immune to the problems that were believed to be responsible for the failure of the coincidence method. A method was developed that took advantage of the fact that, in addition to the (1 GeV, 1 GeV) peak corresponding to coincident symmetric leptons, the SYMB single-side-master histograms showed additional peaks corresponding to other event types (e.g., occurrence of two lepton-lepton events in coincidence creating a peak at (2 GeV, 2 GeV), a lepton-lepton event in coincidence with an $e^\pm p$ event in which the $e^\pm p$ lepton deposits ~ 2 GeV in one of the calorimeters creating a peak at (1 GeV, 3 GeV), etc.). An example of the left-master histogram showing these peaks is shown in Figure 5-47. The MIE analysis compares the relative rates of symmetric lepton-lepton events and events in which a symmetric lepton-lepton event occurs in coincidence with an elastically scattered $e^\pm p$ lepton in the right side calorimeter as recorded in the left-master histogram (the (1,1) and (1,3) peaks in Figure 5-47) and normalizing to the simulated rate for the $e^\pm p$ leptons (noting that the coincidence lepton-lepton rate cancels in the ratio, eliminating the need to simulate it). This offers several important advantages over the original lepton-lepton coincidence method:

1. By taking a ratio of rates, any species-dependent detector efficiency variations are canceled to first order.
2. By using one of the side-master histograms, any unknown problems with the electronics for the coincidence histogram are irrelevant.
3. Since the high energy deposition (3 GeV) occurs in the right calorimeter while the left side receives only 1 GeV for the events of interest, the left side is not near the comparator saturation region in which its local-max condition may erroneously fail. Since the method examines the left-master plot, no requirements

are placed on the right-side deposition making it irrelevant if the right side local max comparison fails due to the high energy deposition.

4. The need to simulate the three processes of Møller scattering, Bhabha scattering, and pair annihilation is eliminated, leaving only simulation of the $e^\pm p$ lepton rate.
5. The MIE method is considerably less sensitive to effects that introduce very large systematics to the original coincidence method such as beam position and detector position since the rate of coincident leptons cancels in the ratio.

The disadvantages of the MIE method include a significant reduction in statistical precision relative to the coincidence method (since it depends on two events being recorded from a single beam bunch) and the fact that only the left-master histogram provides the necessary (1 GeV, 3 GeV) peak needed for the analysis since the right-master histogram ADC range was not set to include 3 GeV events from the left side. These drawbacks, however, are greatly outweighed by the robustness of the method.

This analysis is detailed in full in Reference [53], but the essential details are provided here for the purpose of establishing the method for use as one of the luminosity estimates for the final $R_{2\gamma}$ result.

Principle of the Measurement

As noted, the MIE method compares the number $N_{(1,1)}$ of symmetric lepton-lepton events (i.e., Møller scattering, Bhabha scattering, and pair annihilation) to the number $N_{(1,3)}$ of events where a symmetric lepton-lepton event occurs in the same beam bunch in which an elastically $e^\pm p$ lepton reaches the right side calorimeter recorded by the left master histogram, normalized to the expected cross section of $e^\pm p$ leptons in the right calorimeter from simulation $\sigma_{e^\pm p \rightarrow R}^{\text{MC}}$ and the number of beam bunches N_b in the data sample. As derived in Reference [53], this estimate must also account for the variance in integrated luminosity delivered by single beam bunches v_b , and the average cubed integrated luminosity of single beam bunches $\langle \mathcal{L}_b^3 \rangle$ that enter the formula in higher order terms due to effects caused by the fluctuation of the likelihood

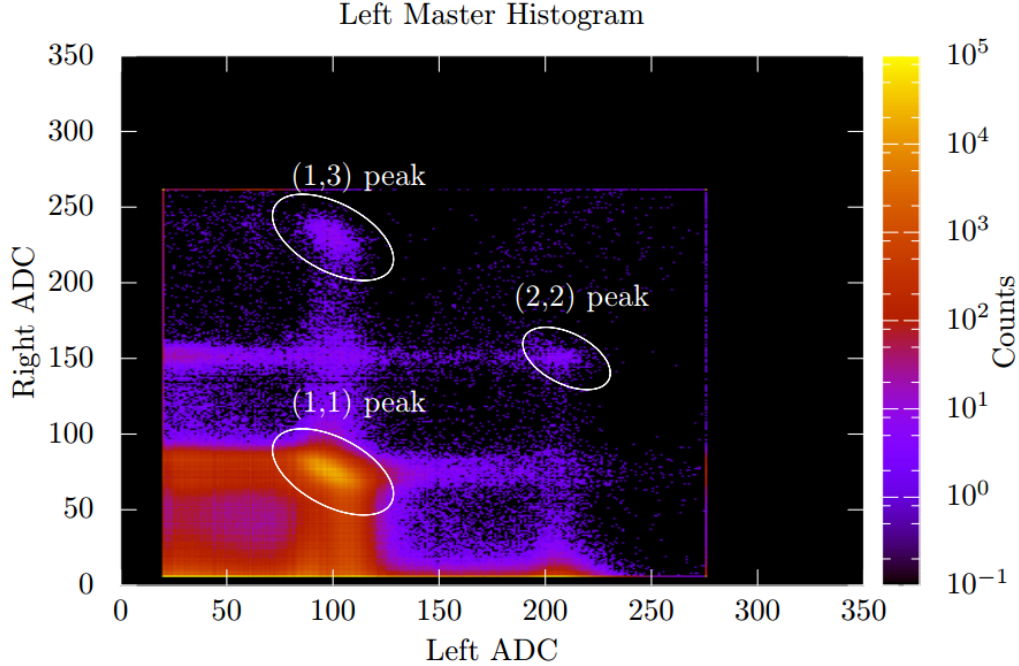


Figure 5-47: The left-master histogram from SYMB data, which was filled for any event in which the left SYMB calorimeter met its energy deposition (ADC count) threshold with the center crystal having the highest deposition regardless of the ADC count in the right calorimeter. The visible peaks correspond to the various combinations of scattering events that can occur in coincidence (i.e., from the same beam bunch), as described in the text. (Figure reproduced from [53].)

of multiple simultaneous events occurring with fluctuations in the beam bunch charge and the possibility of more than two events occurring simultaneously (which “moves” events out of the peaks of interest). In principle, these higher order terms also depend on the total luminosity (the quantity being measured) and the cross-section for all processes that may enter the measurement σ_{tot} . These may be safely estimated as the slow control luminosity and the dominant (1,1) cross section respectively since they enter only in the higher order terms making any error in their determination a small effect. The result of the derivation in Reference [53] provides the following formula for the integrated luminosity of a given data sample using the MIE method:

$$\mathcal{L}_{\text{MIE}} = \frac{N_{(1,3)}N_b}{N_{(1,1)}\sigma_{e^\pm p \rightarrow R}^{\text{MC}}} - \frac{v_b N_b^2}{\mathcal{L}_{\text{SC}}} - N_b \sigma_{\text{tot}} \left[\left(\frac{v_b N_b}{\mathcal{L}_{\text{SC}}} + \frac{\mathcal{L}_{\text{SC}}}{N_b} \right)^2 - \frac{N_b \langle \mathcal{L}_b^3 \rangle}{\mathcal{L}_{\text{SC}}} \right]. \quad (5.20)$$

For reference, the second term is approximately 1% of the leading term, while the third term is approximately 0.1%. Since the uncertainty of the measurement is on the order of the third term, consideration of higher orders was unnecessary.

The beam parameters N_b and v_b were provided by the DORIS beam parameter archives associated with the slow control system. The procedure for determining the count rates in data ($N_{(1,3)}$ and $N_{(1,3)}$) is detailed in Reference [53], but essentially amounted fitting the centroids of the relevant peaks in the left master histogram, placing rectangular box cuts around those centroids, and then integrating the boxed regions. It was determined that the choice of box size significantly affect the absolute value of \mathcal{L}_{MIE} , but did not as significantly affected the species-relative measurement $\mathcal{L}_{\text{MIE},e^+}/\mathcal{L}_{\text{MIE},e^-}$. Given that no clear method existed to determine the exact proper size of the box cut, no absolute luminosity determination is quoted for the MIE method and the size of the box cut was tested as a systematic uncertainty of the relative measurement.

Systematic Uncertainties

As previously noted, the uncertainty on the absolute measurement of the luminosity from the MIE method is quite large (at least several percent) due to the large variation in absolute count rates that occurs when the sizes of the cut boxes are varied. Additionally, there is no a priori methodology for determining the “correct” box size, and thus it is extremely difficult to place a specific estimate of the absolute luminosities. The analysis is capable, however, of producing an estimate of the species-relative luminosity with uncertainty small enough to meet the goals of OLYMPUS.

The main sources of uncertainty for the species-relative MIE luminosity estimate are summarized in Table 5.6, as analyzed in Reference [53]. The total systematic of the MIE analysis for the species-relative luminosity was found to be $\delta_{\text{MIE}} = \pm 0.27\%$, dominated by the contributions from uncertainty in the beam position and slope, uncertainty in the modeled positions and orientations of the calorimeters and collimators, and the choice of the size of the cut boxes used in the analysis. Estimates of the effects were conducted in a manner similar to those described in Section 5.2.8

for the 12° system (the exact methods are described in [53]). Due to the relatively small magnetic field in the region traversed by particles from the target to the SYMB ($\lesssim 50$ G), magnetic field plays a small role in the MIE uncertainty, while beam energy and radiative corrections are comparably-sized effects for the MIE and 12° analyses. Since the $e^\pm p$ events in the SYMB calorimeters are much further forward than those in the 12° system ($\epsilon = 0.99975$, $Q^2 = 0.002$ GeV²), any uncertainty due to TPE effects is expected to be much smaller than other effects that were tested (since the TPE uncertainty was 0.1% and the TPE contribution must go to zero at $\epsilon = 1$).

Uncertainty Source	Relative (%)
Beam position/slope (δ_{BPM})	± 0.21
Detector/collimator position (δ_{geo})	± 0.13
Cut box sizes (δ_{cuts})	± 0.10
Magnetic field (δ_B)	± 0.05
Radiative corrections (δ_{rad})	± 0.03
Beam energy ($\delta_{E_{\text{beam}}}$)	± 0.01
Total (δ_{MIE})	$\pm 0.27\%$

Table 5.6: A summary of the contributions to the systematic uncertainty in the determination of $\sigma_{e^+p}/\sigma_{e^-p}$ from the SYMB MIE luminosity estimate. These uncertainties may be considered to be independent, in general, and thus are added in quadrature to produce the total uncertainty estimate.

Due to the relative simplicity of the data output of the SYMB system, there are relatively few identifiable possible causes of systematic uncertainties for the MIE analysis. The system, however, is very sensitive to effects such as beam position and detector geometry (effects to which the 12° is quite insensitive). In general, the sensitivities to systematic effects are very complimentary between the 12° and MIE analyses, with large effects such as tracking efficiency and magnetic field in the 12° system being either irrelevant or much smaller effects in the MIE analysis. The statistical precision of the MIE analysis is comparable to the 12° analysis, and thus effectively negligible. Due to this, the 12° and MIE luminosity estimates provide an important cross check for the luminosity used in the final $\sigma_{e^+p}/\sigma_{e^-p}$ analysis and present the opportunity to present a measurement of $\sigma_{e^+p}/\sigma_{e^-p}$ in vicinity of 12° as well (Section 7.2.1).

Results

Since the MIE analysis is only able to use the left-master histogram (since the right-master histogram range was not set so as include the necessary (3 GeV, 1 GeV) peak for the MIE calculation), the MIE analysis produces a single estimate for the relative luminosity. Similarly to the 12° results (Section 5.2.9), this estimate is quoted as a ratio relative to the slow control luminosities for each species. As computed in Reference [53], the estimate of the species relative luminosities relative to slow control for the dataset of interest was:

$$\frac{\mathcal{L}_{\text{MIE},e^+}}{\mathcal{L}_{\text{MIE},e^-}} \cdot \frac{\mathcal{L}_{\text{SC},e^-}}{\mathcal{L}_{\text{SC},e^+}} = 1.0055 \pm 0.0010 \text{ (stat.)} \pm 0.0027 \text{ (syst.)}. \quad (5.21)$$

This result is very consistent with the 12° estimate and the expected uncertainties associated with the slow control determination. This result may be used either as a luminosity normalization point at very forward angles, or combined with the 12° estimate to provide a high-confidence estimate for the main result. The run-by-run luminosity estimate from the MIE method and the projected fit distributions are shown in Figure 5-48.

5.4 Discussion of the Luminosity Analyses

In general, despite the issues with the performance of the GEMs in the 12° telescopes and the SYMB coincidence event analysis, the species-relative luminosity measurements for OLYMPUS achieved the necessary level of uncertainty to permit an overall uncertainty on the measurement of $R_{2\gamma}$ of less than 1%. The excellent agreement of the MWPC-only 12° $e^\pm p$ analysis and the MIE analysis in the SYMB system provides a high degree of confidence in the luminosity measurements, since each system is subject to very different systematic uncertainties. Figure 5-49 shows the run-by-run ratio of the combined left/right 12° and MIE estimates. Notably, this run-by-run ratio shows less time variance in the individual luminosity estimates relative to the slow control luminosity, indicating that the two methods captured systematic effects that

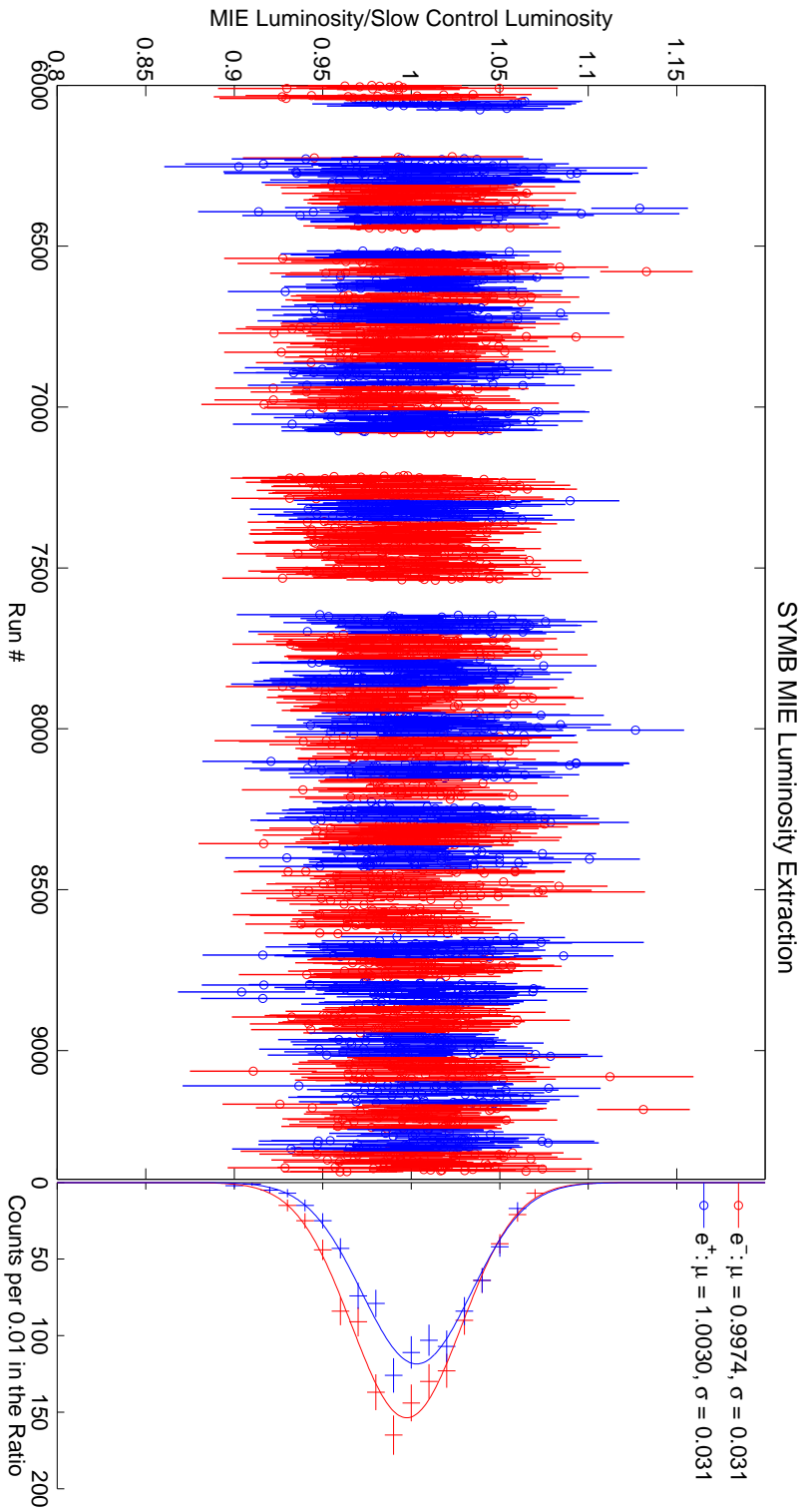


Figure 5-48: Run-by-run estimate of the integrated luminosity collected by the OLYMPUS experiment relative to the slow control estimate, as measured by the SYMB multi-interaction event analysis. The data and analysis methods are from Reference [53]. The run-by-run values are histogrammed in the right-hand plot and fitted to Gaussian distributions for each species to produce the estimates of the luminosities for each species over the full data set.

were not accounted for in the slow control estimate. While the MIE method sacrifices the complete exclusion of $e^\pm p$ scattering that would have been part of the coincidence symmetric lepton-lepton scattering method, the additional reduction in uncertainty provided by the MIE analysis via the cancellation of efficiency uncertainties in the ratio of counts and the reduction of the number of required simulated physics processes and the low uncertainty on the estimate of possible TPE for such forward scattering ($\epsilon = 0.99975$) make the estimate very robust. Additionally, the careful analysis performed for the 12° system provided not only a high precision relative luminosity measurement but also an absolute luminosity estimate for each species with uncertainty of only a few percent, which may be useful for future physics analyses with the OLYMPUS data.

For the $\sigma_{e^+p}/\sigma_{e^-p}$ analysis that follows in the remaining chapters, the luminosity measurements may be combined into a single average normalization point or taken individually to provide either an estimate of the systematic effects of the variation of the relative luminosity scale or to provide an measurement of $R_{2\gamma}$ in the vicinity of $\theta = 12^\circ$. These different cases are discussed in Section 7.2. For the case of the averaged single normalization point, the two analyses (weighted by their uncertainties) provide an estimate of the species-relative integrated luminosity relative to the slow control luminosity over the course of the full dataset under consideration of:

$$\frac{\mathcal{L}_{e^+}}{\mathcal{L}_{e^-}} \cdot \frac{\mathcal{L}_{\text{SC},e^-}}{\mathcal{L}_{\text{SC},e^+}} = 1.0048 \pm 0.0024 \text{ (combined stat. + syst.).} \quad (5.22)$$

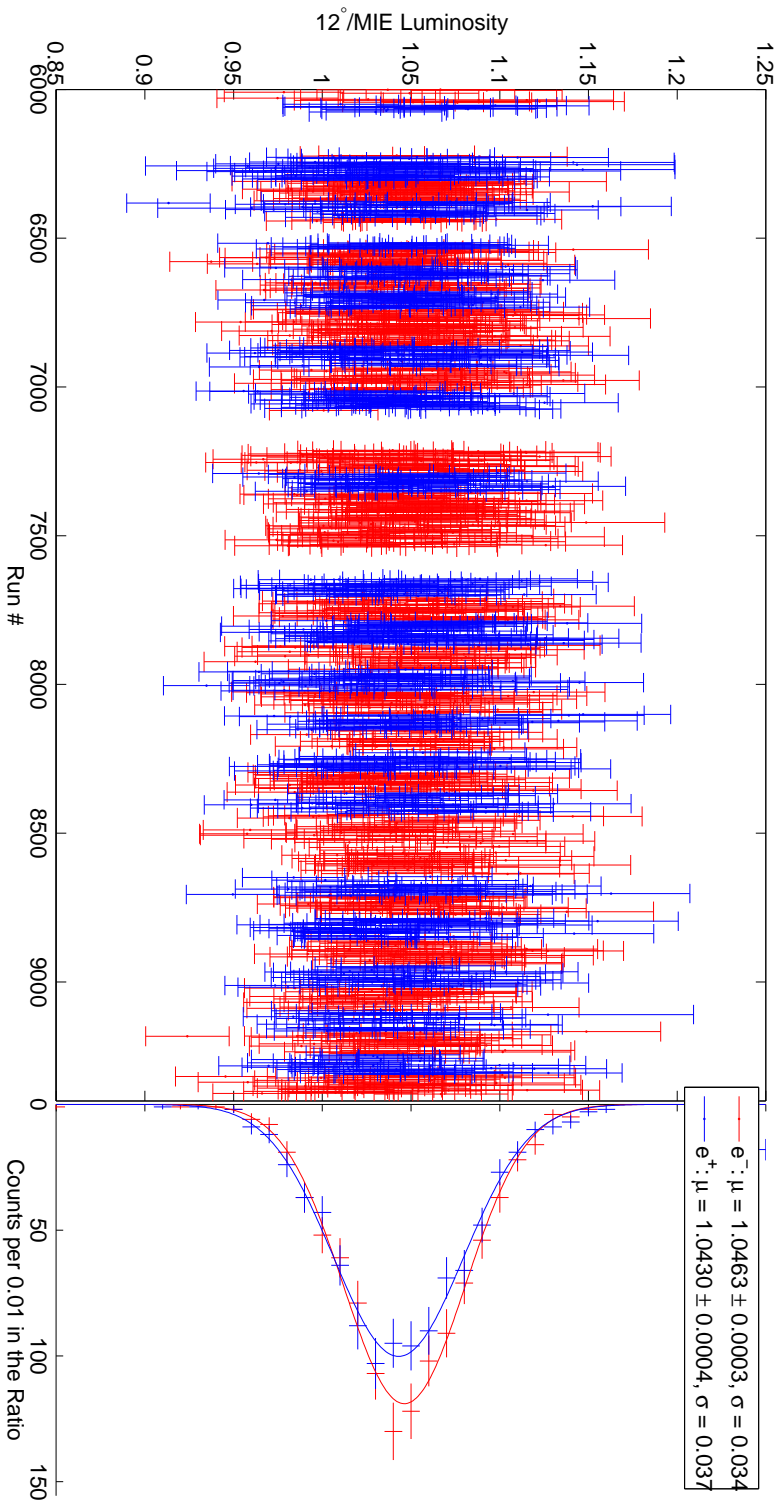


Figure 5-49: Run-by-run ratio of the combined left+right 12° luminosity (Figure 5-45) and the MIE luminosity (Figure 5-48). The run-by-run values are histogrammed in the right-hand plot and fitted to Gaussian distributions for each species to produce the estimates of the luminosities for each species over the full data set.

Chapter 6

The e^+p/e^-p Cross Section Ratio Analysis

The final piece of the OLYMPUS result for $R_{2\gamma}$ is the analysis of the elastic $\sigma_{e^+p}/\sigma_{e^-p}$ ratio in the main tracking volumes of the detector. As has been discussed previously, this involves not only a robust method of selection elastic e^+p and e^-p events from the data sample, but also proper representation of the detector system in the simulation so that the elastic selection method may be applied equally to the data and the simulation. This chapter discusses the performance of the main tracking detectors (the drift chambers and time-of-flight (ToF) scintillators), the implementation of the tracking detectors in the simulation, and a method of selecting elastic events and conducting background subtraction to produce a result for $\sigma_{e^+p}/\sigma_{e^-p}$ over the full acceptance of the detector. Additionally, a preliminary estimate of the systematic uncertainty in the $\sigma_{e^+p}/\sigma_{e^-p}$ analysis is discussed in Section 6.4. The results of this analysis are presented in Chapter 7.

Note that the analysis described here is only one of several conducted using the OLYMPUS data to produce a $\sigma_{e^+p}/\sigma_{e^-p}$ result. Multiple analyses using unique methods were conducted by different members of the OLYMPUS collaboration so as to provide an estimate of the systematic uncertainty in the result due to choices made in the elastic event selection and background selection. These analyses utilized different methods for particle-type identification, combinations of kinematic cuts to produce

the elastic event sample, models for the remaining background after cuts, and orderings of the various steps in the analysis to provide providing a robust examination of the effects of analysis decisions on the final result. Information on several of these analyses may be found in References [53], [54], and [55], and Section 7.3 discusses the comparison of the analyses.

6.1 Spectrometer Performance and Modeling in Simulation

Characterization of the detectors involved in the reconstruction of elastic $e^\pm p$ events was critical to the analysis, as it allowed a detailed implementation of the detector response in simulation so as to ensure that the simulated detector accurately represented the acceptance of the detector during the experiment. In particular, it was critical to model the efficiency and resolutions of the drift chambers and ToFs in detail so that reconstruction of simulated tracks could occur on equal footing as tracks in experimental data. This section describes the measurements and implementation of these parameters in simulation, particularly focusing on the drift chamber efficiencies.

6.1.1 Drift Chambers

Since the drift chambers were the main reconstruction detectors for OLYMPUS, it was critical to properly model them in the Monte Carlo, especially with regard to efficiencies (which affected the effective acceptance of the detector) and resolutions (which affected the validity of applying the same elastic event selections to data and simulation). Each of these quantities was measured throughout the chamber using the experimental data and globally-fit track information.

Efficiency

If the drift chambers had been highly efficient for track detection throughout their volumes, they would have affected the acceptance of the detector very minimally.

This, however, was not the case for the conditions of the OLYMPUS experiment. Furthermore, because the beam environment differed between e^-p and e^+p experiment modes (predominantly through the backgrounds caused by Møller and Bhabha scattering of beam leptons from the atomic electrons in the target gas which caused hits in the innermost drift chamber layers), it was critical to precisely measure the efficiencies in each running mode to avoid an artificial shift in $\sigma_{e^+p}/\sigma_{e^-p}$ due to an asymmetry in drift chamber efficiencies in the two modes. In particular, the efficiency of the drift chambers was lowest in the innermost layers where the wires were exposed to higher rates from particles in the target which had relatively low energy, but were not so low energy as to be completely contained away from the chambers by the magnetic field. An example of the inner chamber efficiency is shown in Figure 6-1, which was additionally reduced by a defective high voltage supply card in the central region. In the outer layers, the efficiency was typically much higher.

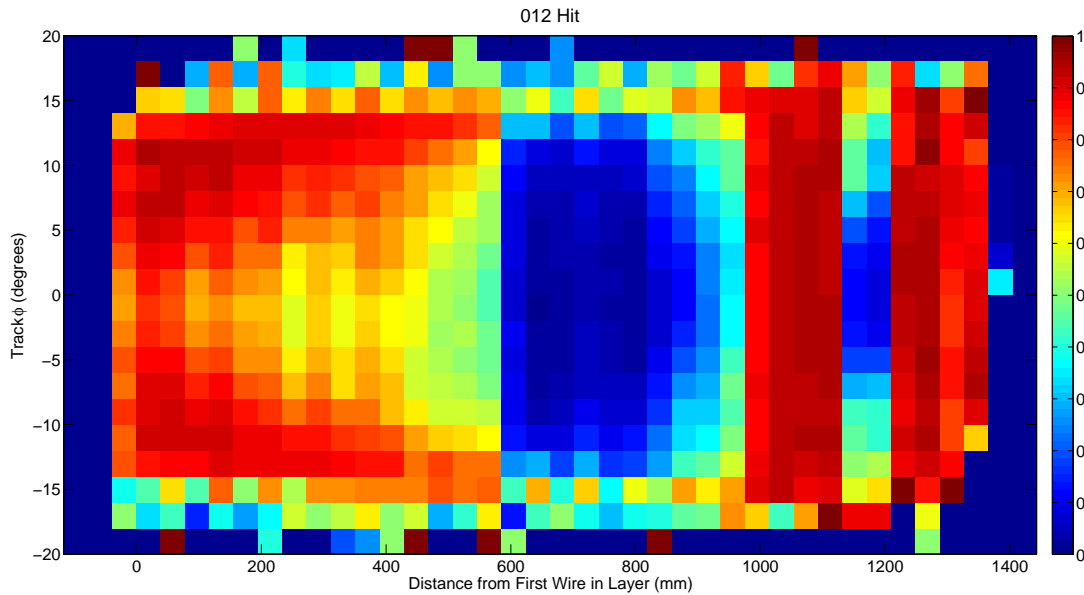


Figure 6-1: Probability for all three wires in the innermost layer of left drift chambers cells to fire for a track in e^-p running as a function of position in the drift chamber plane. In addition to a reduction in efficiency due to high rates (visible at distance of < 600 mm from the first wire), this layer contained a defective high voltage supply card that significantly reduced the efficiency of a 390 mm block in a correlated way. Additionally a single defective wire channel at distance 1170 mm reduced the all-three hit probability in that region.

An additional factor of consideration was that blocks of five adjacent wire chamber cells shared a single high voltage distribution card and discriminator card. Thus, issues with either the high voltage applied to the wires or the low voltage that powered the a discriminator card could simultaneously affect up to 15 wires, introducing the possibility of correlated inefficiencies between wires. While studies indicated that correlation did not occur between wires that did not share a card, significant efficiency correlations were observed for wires connected to the same card. Since a track in the drift chambers can be constructed without hits in each layer, it was critical to model such correlation effects so as to avoid over-predicting the number of reconstructible events in simulation.

To account for such effects, the drift chambers were not modeled with simple efficiency maps for each layer in the same fashion as the planes of the 12° telescopes (Section 5.2.5). For each cell layer in the wire chambers (three single-wire layers), eight maps were calculated corresponding to the 2^3 possible combinations of hit/no hit for the three wire layers. To determine the efficiency for a given cell layer, the data was tracked with the layer completely excluded from consideration (both in terms of contributing hits to possible tracks and in being required to match a track pattern (Section 4.2.2)). The data used for the efficiencies mapping were a sample of ~ 100 data runs of each lepton species beam sampled evening across the entirety of the dataset (approximately 10% of the full dataset used for the analysis). Each data run was tracked six times, with a different cell layer masked for each reconstruction (removing the corresponding layers on both the left and right sides). A rough elastic selection was applied to the tracks to assure reasonable track quality, and the masked layer was checked for hits corresponding to the selected track. Hits were required to be within several times the resolutions described in the next section to be counted as associated with a track and thus mark a wire efficient. This cutoff was found to be very stable once outside of the resolution peak. As described, for each layer the probability for each of the eight wire hit combinations was calculated as a function of position in the cell layer plane and maps of these probabilities were generated for each layer. In the simulation, tracks were tested at the cell layer level using a random

draw against these maps to determine which hits (if any from the track) would be passed from that cell layer to the reconstruction of simulation. Separate sets of maps were constructed for position and electron beam operation since the noise conditions in the innermost layers differed significantly enough to induce an efficiency difference. An example set of maps for an outer layer, where the efficiency was quite uniform and high, is shown in Figure 6-2.

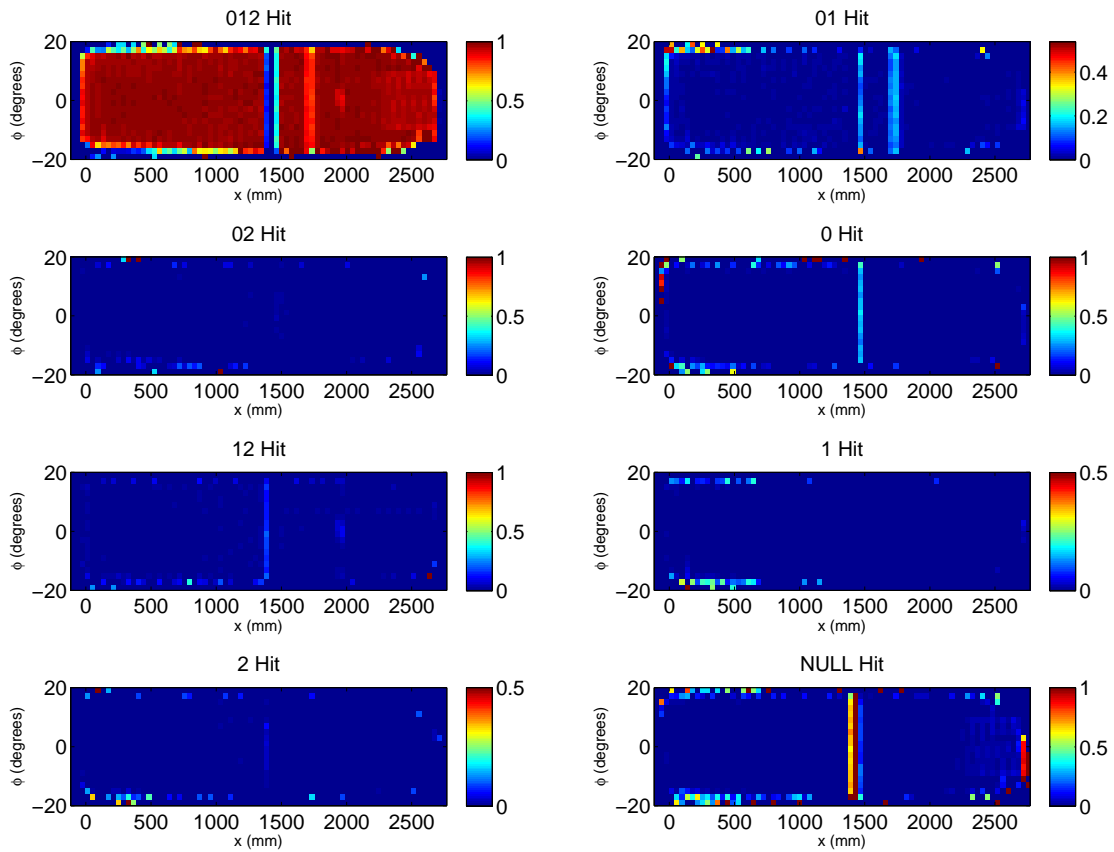


Figure 6-2: Probability maps for the eight possible combinations of hits in the outermost left cell layer during e^+p running, where x is the distance from the first wire and ϕ is the track azimuthal angle. The three layers are labeled 0, 1, and 2, and the plot titles indicate which wires are hit in a given map. Note that the dominant probability is for all three wires to fire, outside of the region of a known disconnected cell at $x \approx 1400$ mm. Additionally, lower single wire efficiencies occur at two other locations but do not cause a significant correlated probability of missing all three hits in the cell layer.

Wires that were known to be disconnected or to have malfunctioning readout equipment were excluded from the analysis of both data and simulation entirely, rather than implementing 0% efficiency in the maps. This approach is superior due to the fact that while a track may pass predominantly through the region of a deactivated wire, it may also pass through the active region of an adjacent wire and produce a hit that reconstructs to the position in the deactivated cell. This was especially common in the forward portions of the drift chambers where tracks passed wires with large angles relative to the normal vector of the wire planes. Thus, the “dead” regions due to inactive wires had soft efficiency edges rather than hard cutoffs in acceptance, which was modeled in the maps as described. This complete model of the drift chamber efficiencies permitted OLYMPUS to achieve a high degree of data/simulation agreement in final yields (up to the effect of TPE), providing evidence for the use of the method encapsulated in Equation 1.1.

Time Resolution

The inherent time resolution of the drift chambers was dominated by the physics of ionization drift rather than any time scales inherent to the capabilities of the TDCs used to measure times for each wire. Dispersion caused by random interactions of the drifting ions with the drift gas worsened the resolution roughly linearly as a function of the distance between the point of the initial ionization and the wire. The resolution was found to vary from approximately 20 ns in the vicinity of the wire to slightly more than 30 ns near the edges of the cell. The resolution was measured by examining the width of the distribution of the difference between the distance reconstructed from the globally reconstructed track involving the drift chamber time in question and the distance predicted by the time-to-distance (TTD) function for a hit, which was then converted to a time width via inversion of the TTD function (see Reference [53]). In this way, the method captures at least a portion of the uncertainty in the TTD function for a given cell in addition to resolution widening caused by the drift gas.

To apply these resolutions to simulation, simulated hits were first produced in the form of distances from drift chamber wires and then converted to times using the

inverse TTD function. This time was then smeared according to a Gaussian of the appropriate width according to its time (distance from the wire). These “smeared” time hits were then saved as the experimental data analogs of the experimentally measured drift times and passed to the track reconstruction algorithm in an identical fashion to data.

6.1.2 Time-of-Flight System

Due to the importance of the ToF system in the analysis (as the main component of the trigger), it was critical to the results of the experiment to properly calibrate and simulate the system. Timing offsets, ADC calibrations, etc. for each bar were determined using a detailed data-driven approach, which is discussed in detail in Reference [54]. The efficiency of the ToF bars was not simulated using a mapping as in other systems, but rather was modeled by measuring the response of each bar and the attenuation length of scintillation light as a function of position in the bar in data to create a model of the scintillator response and efficiency for implementation in the simulation. Such a model was necessary due to the fact that while special triggers were included at a prescaled rate in the dataset to allow for data-driven direct ToF efficiency measurements, it was found that these triggers were generally swamped by forward event noise and provided very little useful data for the majority of ToF bars.

Quantities such as timing offsets were determined using an iterative approach of matching ToF hit positions reconstructed from the PMT timing difference and positions projected from reconstructed trajectories in the drift chambers (excluding the ToF hit information from the trajectory fit). An example of the success of this methodology is shown in Figure 6-3, which shows the excellent agreement between the reconstructed track ϕ and the associated ToF hit ϕ position.

6.1.3 Reconstruction

In general, the reconstruction algorithm based on the elastic-arms algorithm (EAA) (References [163, 164]) used for OLYMPUS (Section 4.2.2), performed extremely well.

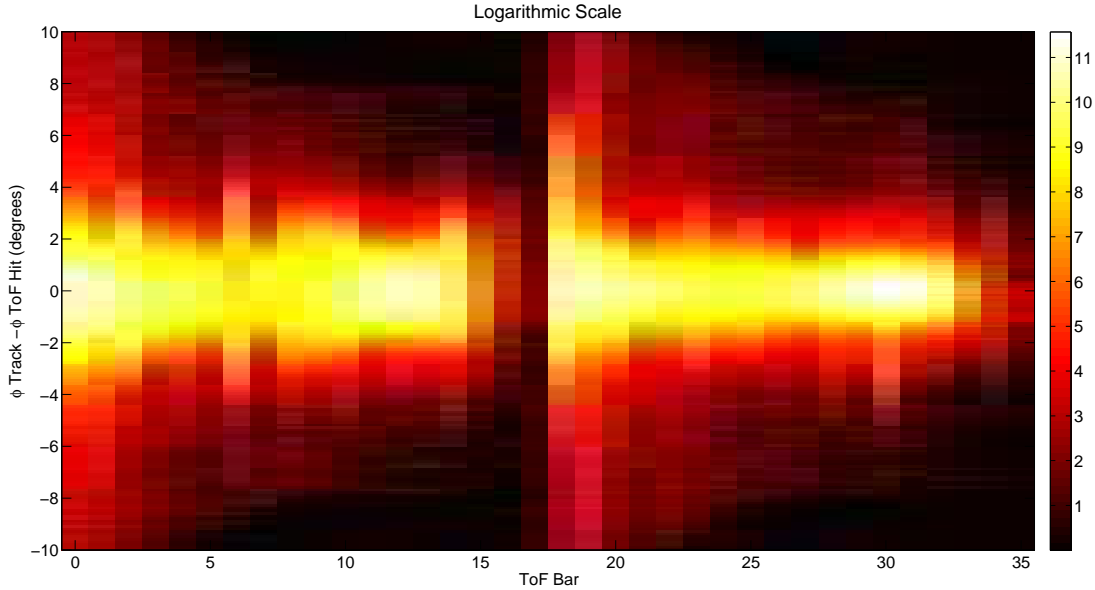


Figure 6-3: Difference between ToF hit ϕ and reconstructed track ϕ by bar for e^-p data, after event pair selection but prior to background subtraction. Note that the logarithm of the counts is shown by the color scale of the histogram so as to make the mid-angle bars with fewer counts visible in the figure. In general, the left ToF bars (indices 0-17) had poorer resolutions than the right bars (indices 18-35), but all bars were properly calibrated to match tracks on average. Such resolution differences were implemented in the simulation so as to make simulated events match data events in reconstruction and analysis.

This was achieved by a careful tuning of the EAA parameters to best model the OLYMPUS tracking environment. This process is described in detail in Reference [54]. The extensions to EAA implemented to improve its performance with regards to correctly resolving the wire side ambiguities of the drift chamber hits is described in Reference [53]. To test the efficiency of the tracker, and to provide a basis for the tuning of the EAA parameters, the capability of the tracker was tested using simulation tracks for which the true trajectories are known, but that have been converted to the data format with time smearing and the introduction of the wire side ambiguity of the drift chamber hits. Through the tuning of the parameters, tracking efficiency for such tracks (proper identification of the correct wire side for all drift chamber hits and reconstruction parameters within acceptable bounds of the known true values) was in excess of 99% for the tracking of all three relevant particle types throughout the

entirety of the acceptance. The difference in efficiencies between the different particle types was within the statistical uncertainty of the tests [201]. While there was no effective method for testing the tracking of data events in a similar fashion, the high efficiency for simulation tracking and the similarity of efficiency for all particle types provided high confidence in the robustness of the tracker. This was further buoyed by the comparison of data to simulation event selection, which indicated very good agreement (Section 6.3).

Resolutions with respect to various reconstruction parameters are discussed in Section 6.2.2 in the context of the various kinematic parameters used for the elastic event selection, and the figures of Appendix B illustrate the resolutions on a number of kinematic parameters over the full detector acceptance for both e^-p and e^+p data.

6.2 Method of the Analysis

This section describes the methodology of the elastic $e^\pm p$ event selection analysis conducted by the author and used to produce the majority of the results presented in this work. The analysis presented here is one of several $R_{2\gamma}$ analyses conducted for OLYMPUS, each of which used different choices of particle identification, kinematic cuts, background subtraction models. The variation in these analyses provides a useful measure of certain elements of the systematic uncertainty in the final result and is discussed later in this chapter. Details on the alternate analyses may be found in any of the other OLYMPUS PhD theses (References [53–55]), although other analyses were conducted that have not yet been published.

As previously noted, this analysis method was applied to both the experimental data and the events generated from simulation, which were constructed in such a way so as to precisely mimic the format of the experimental data. This allows completely equal treatment of data and simulation throughout the entire analysis (track reconstruction, particle identification, kinematic cuts, etc.). From this point forward, any use of the simulated events makes use of the default event weight (see Section 4.3.2), which was the exponentiated radiative corrections model based on the prescription of

Maximon and Tjon [100], unless explicitly noted otherwise.

6.2.1 Particle Identification and ToF Hit Association

In this analysis, the first step was to conduct particle identification, i.e., the proper association of particle trajectories reconstructed by the tracking algorithm (Section 4.2.2) with the true particle type associated with the track. The reconstruction algorithms used for OLYMPUS attempted to fit a lepton or proton to any matched pattern in the data, and thus the reconstructed data contained tracks of different particle types associated with the same drift chamber hits. First, the list of all pairs of leptons corresponding to the beam species and protons in opposite sectors as identified by the tracking algorithm was constructed. This process eliminated all leptons of the opposite charge.

For each such pair, the validity of the tracker's particle type assignment was assessed using information from the ToF scintillators. For each track, the trajectory was projected to the ToF panels and the expected bar to be hit in association with the track was calculated. Then, any actual registered ToF hits within a tolerance of the two bars surrounding the projected hit bar were considered to be a hit that could be associated with the track.

For each ToF hit, the likelihood that the hit corresponded to the identified particle of the track in question was assessed using the meantime of hit, i.e., the time recorded for the hit in the ToF bar as the mean of the times recorded for the upper and lower PMT hits corresponding to the time elapsed between the beam bunch crossing the target and the scattered particle striking the ToF (up to the correction for travel time of the beam between the crossing time location and the scattering vertex). The use of ToF ADC information was considered, but was not ultimately used for several reasons:

1. protons could deposit a range of energies in the scintillator bars (including small amounts of energies similar to lepton depositions),
2. it was difficult to assess the total energy deposition of particles that possibly

passed through the edges of two bars, and

3. generally the calibration of the ToF ADCs was not as well constrained as that of the TDCs for timing information.

The distributions of the meantimes for tracks associated with each particle type for events with each beam species are shown in Figures 6-4, 6-5, 6-6, and 6-7. The electron candidate plot (Figure 6-5) most clearly shows the band of meantimes corresponding to elastic events (since actual proton tracks tracked as leptons would be tracked with positive curvature resulting in a positron identification). Each of the other three plots shows the ambiguity introduced by tracking all events with both lepton and proton assumptions that must be deconvolved by the particle identification portion of the analysis. As suggested by the clean separation of the elastic electron meantime band (and the visible separation of bands corresponding to leptons and protons in the other plots), a simple bar-by-bar cut on meantime would achieve much of this goal. This approach worked very well in the backward regions of the detector where the meantime separation is large (as in the $12^\circ e^\pm p$ analysis (Section 5.2.6)), but struggled in the intermediate and forward regions where the meantime bands blend together.

To achieve better particle identification in the forward regions, a two-dimensional cut was developed using the reconstructed momentum of the track in question to predict the meantime according to the speed of the particle's travel from the vertex to the ToF bar ¹. Since essentially all leptons in the data sample had $\beta = \frac{v}{c} \approx 1$ a simple maximum meantime cut, tuned bar-by-bar, was sufficient for lepton identification. More interesting were the protons, whose large mass causes significant variation of β as a function of their momentum. For each track, the path length of the particle's trajectory from the scattering vertex to the ToF panels l was calculated by the tracking algorithm. Then, the value of β for each track was calculated using the momentum as reconstructed by the tracking algorithm $|\mathbf{p}|$, but assuming the particle

¹The author wishes to acknowledge R. Russell [54] for the essential method of this particle identification cut.

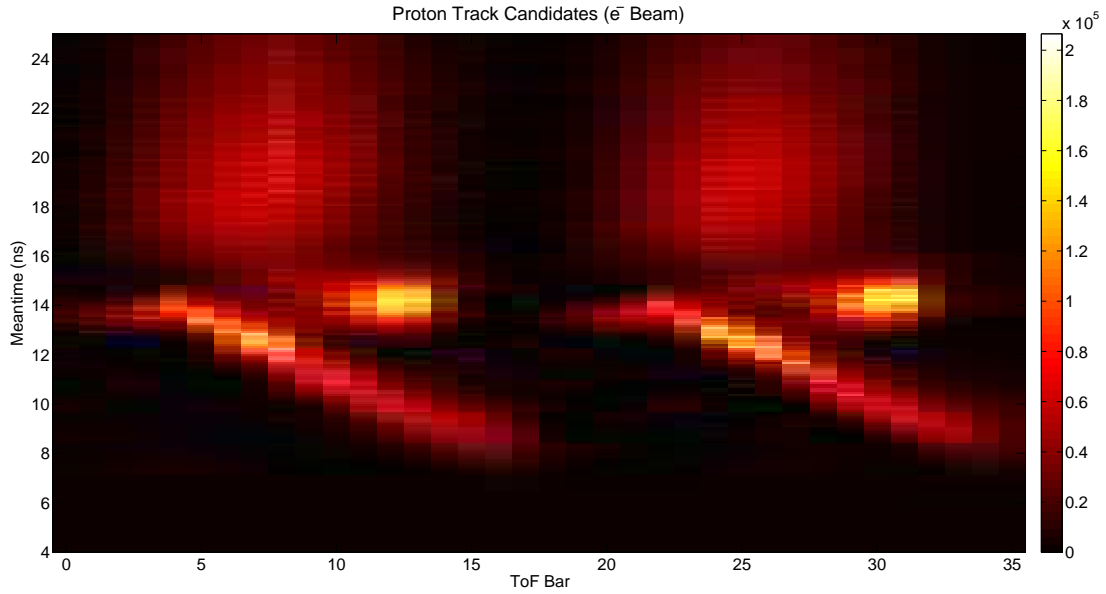


Figure 6-4: Distribution of ToF meantimes by bar for tracks identified by the reconstruction algorithm as protons in e^- beam data.

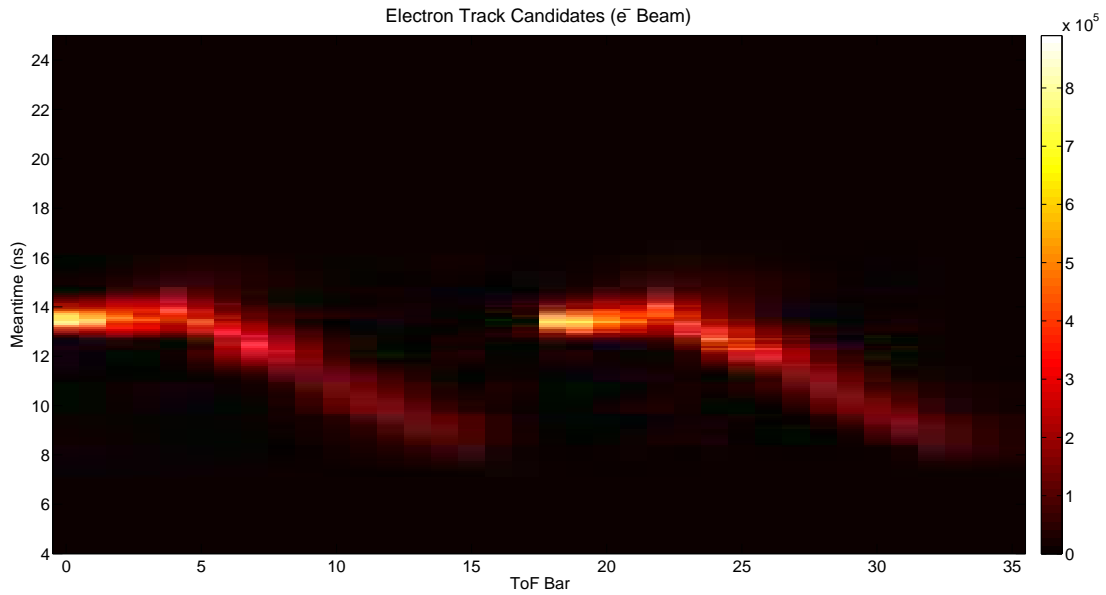


Figure 6-5: Distribution of ToF meantimes by bar for tracks identified by the reconstruction algorithm as electrons in e^- beam data.

had proton mass. That is:

$$\beta_p = \frac{|\mathbf{p}|}{|\mathbf{p}|^2 + m_p^2}. \quad (6.1)$$

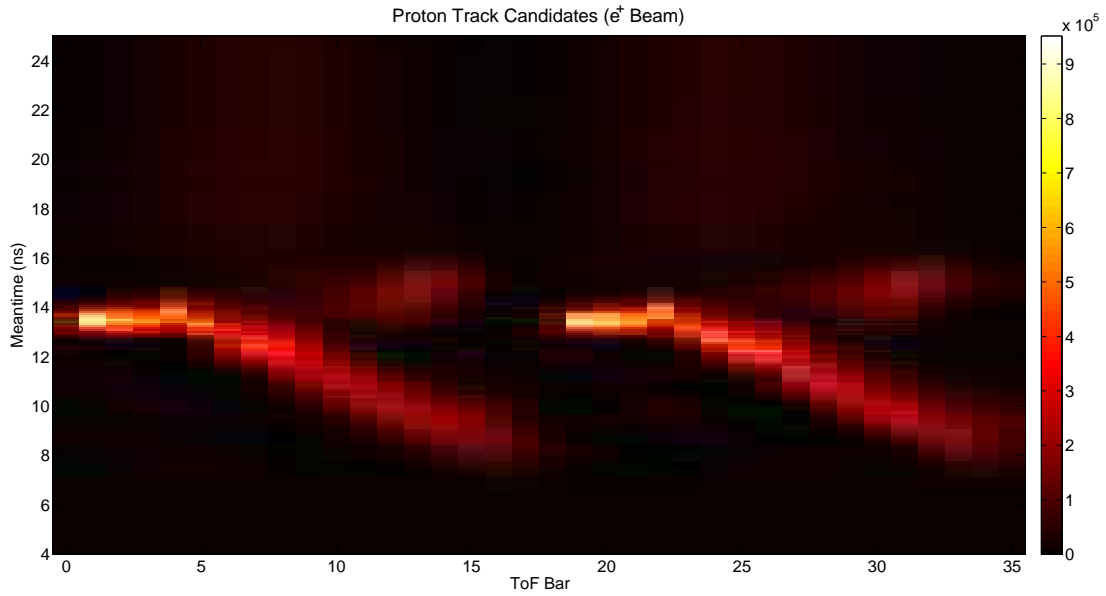


Figure 6-6: Distribution of ToF meantimes by bar for tracks identified by the reconstruction algorithm as protons in e^+ beam data.

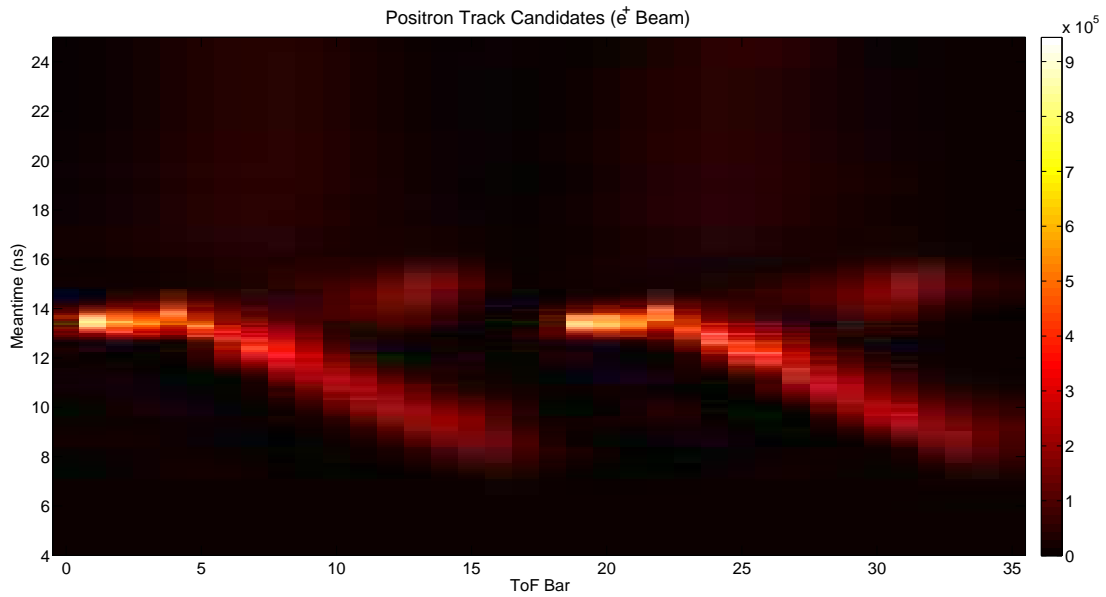


Figure 6-7: Distribution of ToF meantimes by bar for tracks identified by the reconstruction algorithm as positrons in e^+ beam data.

This was used to predict a meantime under the assumption of proton mass for the

particle:

$$\bar{t}_p = \frac{l}{\beta_p c}. \quad (6.2)$$

Track pairs were then histogrammed by the measured ToF meantime and the quantity \bar{t}_p . An example of such a histogram for a relatively forward ToF bar in e^+ beam data (where the positron-proton disambiguation is most difficult) is shown in Figure 6-8. As can be seen this histogram produces a clear separation between correctly and wrongly identified proton candidates. For each ToF bar, a linear cut between these two bands was optimized to as to produce clear separation between the bands, and thus properly identify tracks that corresponded to real protons.

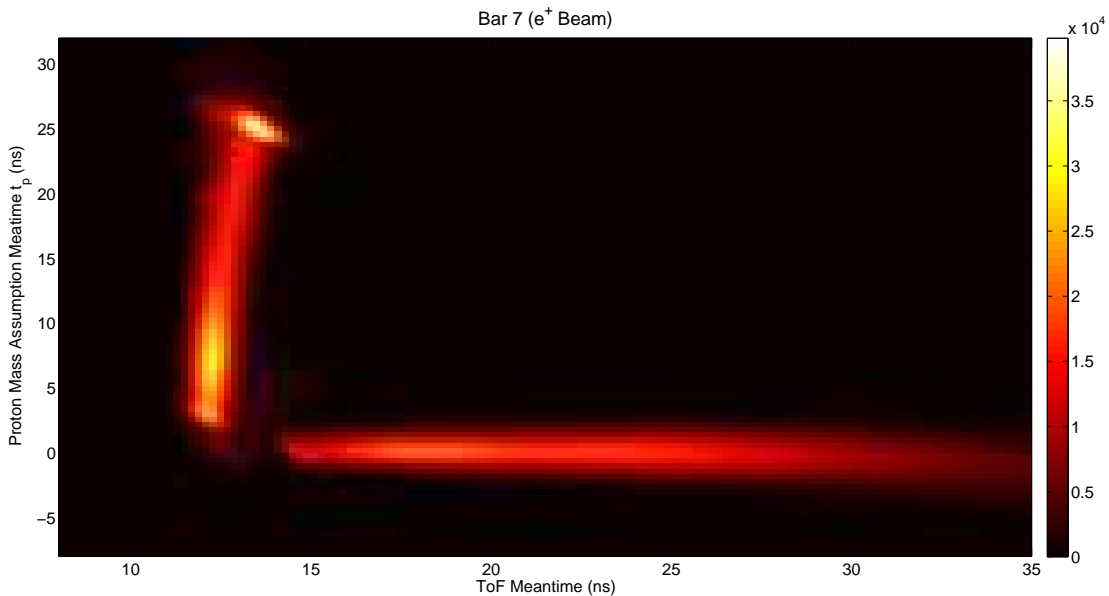


Figure 6-8: Histogram of track pairs by the associated ToF meantime and the meantime assuming the particle to have proton mass \bar{t}_p (Equation 6.2) for Bar 7 (a mid-to-forward bar on the left) in e^+ beam data. Note that the band at $\bar{t}_p = 0$ corresponding to true protons is well-separated from the wrongly identified particles in the roughly vertical band. The curvature of the vertical band bends towards the ToF meantime gap, illustrating why a simple meantime is difficult since small meantimes for real protons were obfuscated by wrongly identified tracks in the upper portion of the vertical band.

All lepton-proton pairs were analyzed in this fashion, attempting to find a ToF hit that could be properly associated with the particle type as identified by the tracking algorithm. Any $e^\pm p$ pair without a valid ToF hit combination was rejected. In the

event that a single pair was found to possibly validly correspond to multiple ToF hit combinations (an effect that occurred $< 1\%$ of the time and was typically due to a particle striking near the edge of a bar and depositing energy in the adjacent bar as well), the best combination for ToF assignment was determined as the pair of ToF hits with the best correlation of vertex times computed from the ToF meantimes and track path lengths (i.e., predicting the most similar scatter time for the two particles).

6.2.2 Elastic $e^\pm p$ Pair Selection

All track pairs with valid ToF hits were then tested by a set of kinematic and fiducial cuts designed to identify pairs with approximately elastic kinematics. The general philosophy in placing these cuts was to keep them wide (so as to avoid effects from varying resolutions) and to apply fiducial cuts only to the proton (since the acceptance of the detector for protons was identical for e^-p and e^+p events, while the lepton acceptance was different due to the magnetic field). For the same reason, the reconstructed parameters of the proton were used to derive quantities such as Q^2 and ϵ so that comparisons of e^-p and e^+p data in these parameters was on the most equal footing possible.

First, fiducial cuts were applied at $|\phi| < \pm 11.5^\circ$ from the horizontal on the proton in each sector, which avoided the acceptance edges due to the drift chamber frames throughout the acceptance, and the reconstructed vertex z of the proton at $|z| = \pm 350$ mm from the center of the target. While other analyses consider fiducial cuts that vary as a function of the scattering angle, which allowed for the recovery of more events in regions excluded by these cuts, this approach was chosen for this analysis to limit the sensitivity to errors in simulated acceptance of the target and to provide a cross-check on such methods.

Then each pair was tested against the following elastic kinematic cuts:

1. Vertex time from ToF meantime and track path length correlation (corrected for vertex position): $|\Delta t| = |t_p - t_{e^\pm}| < 5$ ns (Figures B-1 and B-2)
2. Vertex z correlation: $|\Delta z| = |z_p - z_{e^\pm}| < 175$ mm (Figures B-3 and B-4)

3. Electron-proton elastic angle correlation: $|\theta_p - \theta_{p,\text{elas}}(\theta_{e^\pm})| < 7^\circ$ (Figures B-5 and B-6)
4. Beam energy reconstructed from the track momenta: $|E_{\text{beam},p} - E_{\text{beam}}| < 1000$ MeV (Figures B-7 and B-8)
5. Beam energy reconstructed from the θ of both tracks assuming elastic kinematics: $|E_{\text{beam},\theta} - E_{\text{beam}}| < 350$ MeV (Figures B-9 and B-10)
6. Single-arm missing energy of the lepton over the square of the energy as computed by the expected elastic energy from the reconstructed θ_{e^\pm} : $\Delta E'_\theta/E'^2 < 0.0048$ MeV⁻¹ (Figures B-11 and B-12)
7. Longitudinal (beam direction) momentum balance: $p_{z,p} + p_{z,e^\pm} - p_{\text{beam}} > -500$ MeV (Figures B-13 and B-14)
8. Coplanarity $|\Delta\phi - 180^\circ| = |\phi_{\text{right}} - \phi_{\text{left}} - 180^\circ| < 7.5^\circ$ (Figures B-15 and B-16)

Appendix B presents 2D histograms of the data events by each of these cut parameters and the lepton scattering angle θ_{e^\pm} after application of all selection cuts (but before background subtraction) for each beam species, as noted for each listed cut. As can be seen in these figures, the cuts were chosen to be quite permissive in any individual cut allowing the collection of the multiple exclusive kinematic cuts to produce a relatively clean elastic sample. The remaining background was predominantly at high lepton θ , low total momentum, and very similar between the two modes of operation making it straightforward to separate and subtract in the final steps of the analysis. Note that some of these cuts are heavily correlated (such as the elastic angle correlation and the beam energy from angles), but that both cuts were applied so as to make an effective cut that was not axis-parallel in either. Each of these cut values (with the exception of coplanarity) was chosen as approximately five times RMS width of the distribution of the parameter with the other (non-correlated) cuts applied at its widest across the acceptance so as to reduce sensitivity to the detector resolutions by erring on the side of including more background. The elastic $e^\pm p$ candidate sample

passed to the background subtraction methods, however, still only contained less than 30% background throughout the whole acceptance due to the strength of the multiple cuts that were applied using the full exclusive reconstruction of the events. Other analyses chose deliberately tighter cuts fit to the distributions [53–55].

If no pairs were found with good ToF hit assignments passing all cuts, remaining pairs were assessed for inclusion in the sample if they passed at least five of the seven cuts, with strict limits still enforced for the lower bounds of the reconstructed beam energy from both angles and momenta and the longitudinal momentum balance. If multiple pairs met these criteria, the one with the most cuts passed and lowest weighted sum of cut parameters was preferred. Most commonly, this allowed an event to be selected with one or both tracks at higher than expected momentum, caused by the difficulty of resolving momentum from the bending in the magnetic field as trajectories become straighter at higher momenta. If after this reduction in cut requirements no pair remained, the event was discarded as a non-elastic $e^\pm p$ event.

In approximately two-thirds of events with a pair passing these conditions, a single pair was found. Since the likelihood for simultaneous multiple elastic events in the detector was much less than 1%, in the remaining third the pair with the minimum sum of the cut parameters weighted by the width of each cut was chosen as the elastic pair. The selected pair was referred to as an “initial pair” and was considered as part of the elastic candidate sample for background subtraction.

6.2.3 Background Subtraction

As noted, the final kinematic cut of the analysis (coplanarity of the lepton and positron tracks) was deliberately left open to allow the application of a background subtraction. Several other background models were considered, including applying background models to the z vertex correlation of the track pairs and to the elastic θ correlation of the pairs. The former approach was discarded due to the fact that the shape of a random background (the convolution of the target distribution for each track) was an irregular shape to fit and the fact that it was found that the background (as determined from the sidebands of the coplanarity distributions) was

found to have strong z vertex correlation, as shown in Figure 6-9. Regarding the latter model, the asymmetry of the distribution complicated the model, which introduced uncertainties not present in modeling the coplanarity background. Various combinations of 2D models involving pairs of the three considered distributions were also considered, although none were found to be as robust as the coplanarity method. Notably, the different OLYMPUS analyses included several different approaches to both the method of background subtraction and to the strictness of cuts prior to background subtraction (i.e., the amount of background in the sample before background subtraction and the final cut).

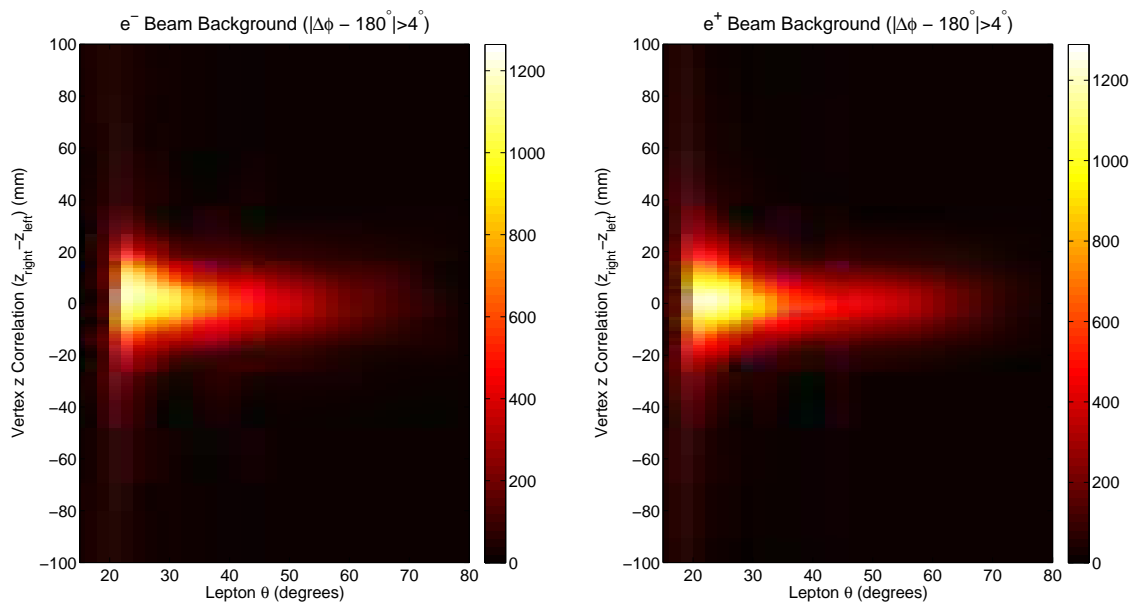


Figure 6-9: Correlation of the reconstructed z of track pairs (that of the right track minus that of the left track) for track pairs selected from the sidebands of the coplanarity distribution ($|\Delta\phi - 180^\circ| > 4^\circ$) for e^-p event selection (left) and e^+p event selection (right). Note that the background had strong vertex correlation throughout the acceptance, indicating that the background was dominated by various scattering events from the target region and that this distribution was not a useful quantity on which to perform background subtraction.

Since cuts involving the reconstructed momentum and elastic event θ correlation of the particles heavily suppressed backgrounds that would be expected to also prefer $\Delta\phi \approx 180^\circ$ (such as pion electro-production [202] and e^+e^- scattering), it was expected that the background in $\Delta\phi$ would be dominated by random track pairs.

For a given small bin in Q^2 (or θ), the corresponding ϕ distribution was essentially uniform, constrained by the frames of the drift chambers. Thus, the expected random pair background was the convolution of two uniform distributions, i.e., a triangular distribution. The initial $e^\pm p$ pair selection was binned in a 2D histogram of $\Delta\phi$ and Q^2 (as determined by the proton θ assuming the beam energy and elastic kinematics), with bin width of 0.05 GeV^2 in Q^2 (corresponding to approximately 35 bins across the full acceptance). The background fraction was computed independently for each Q^2 bin, lepton left and right, event type (e^-p or e^+p), and for both data and simulation according to the following procedure:

1. A single Q^2 bin was projected as a 1D histogram of $\Delta\phi$, as shown in Figure 6-10.
2. A Gaussian plus constant model was fit to the central region of the histogram ($|\Delta\phi - 180^\circ| < 6^\circ$) to find the peak of the coplanarity distribution. For all bins within the acceptance, this peak was found to be within 0.15° of 180° , indicating excellent ϕ reconstruction.
3. The sidebands of the distribution (outside of 4σ of the Gaussian fit of the previous step) were fit to a triangular distribution model ($a - b|x - \mu|$, where μ is the mean of the Gaussian fit in the previous step).
4. This background distribution was passed, along with the data/simulation coplanarity distribution, to the final step of the analysis, which applied the final cut on coplanarity and determined the fraction of counts within that cut corresponding to background that should be subtracted. Additionally, the 95% confidence bounds of the background model fit were retained to estimate the uncertainty in the background model.

The resulting background fractions as a function Q^2 (for the final selection described in the next section), are shown in Figure 6-11 and 6-12 for leptons going left and right respectively for both leptons species in both data and simulation. In general, it was found that e^-p data exhibited slightly higher background levels than positron

data, consistent with the beam conditions for each species. The very small ($\mathcal{O}(1\%)$) background levels in simulation may be attributed to radiative events in which a radiated photon causes a large deviation in ϕ for one of the tracks and occasional mis-reconstructed events. As expected, however, the background fraction in simulation was minimal. In the experimental data, the initial pair selection resulted in a maximum background fraction of $\sim 30\%$ within the acceptance of the detector ($Q^2 \lesssim 2.2 \text{ GeV}^2$). The different OLYMPUS analyses used different levels of strictness in their initial elastic selections, resulting in higher or lower background fractions than this analysis. This difference in modeling provides a valuable test of the robustness of the background subtraction models via comparison of the results produced by each analysis.

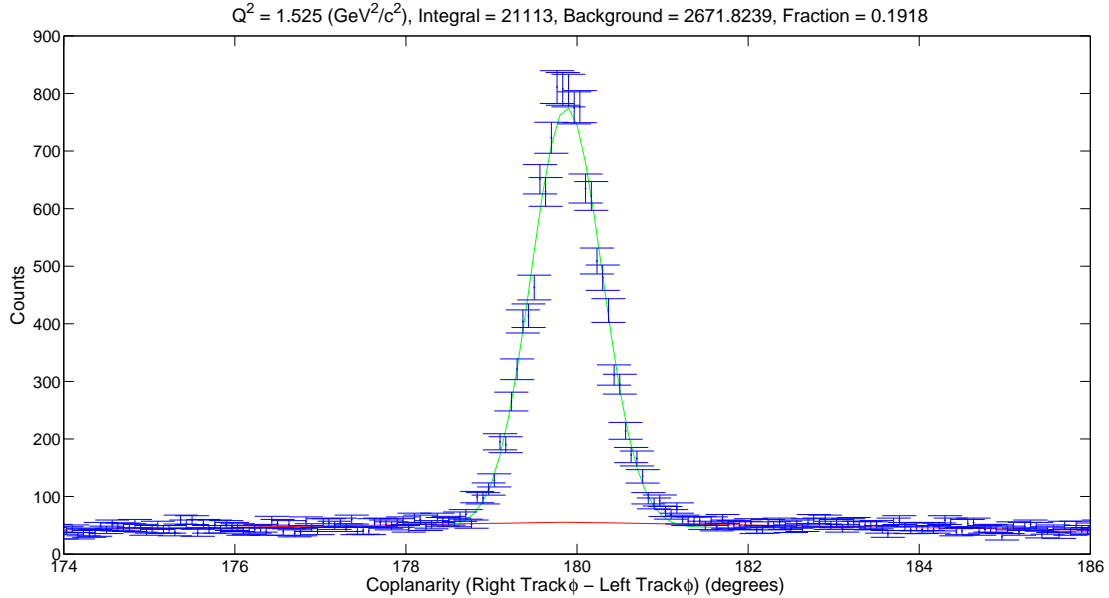


Figure 6-10: Example of the background model fit for left-going electrons for the bin centered at $Q^2 = 1.525 \text{ GeV}^2$ for the full e^-p dataset used for the analysis. The blue points represent the data (with statistical uncertainties), the green line the initial Gaussian+constant fit to the central region ($|\Delta\phi - 180^\circ| < 6^\circ$), and the red line the triangular background fit to the regions beyond 4σ of the Gaussian peak. For all bins within the acceptance, the model fit the data extremely well, producing positively sloped triangles as expected without explicitly requiring this condition.

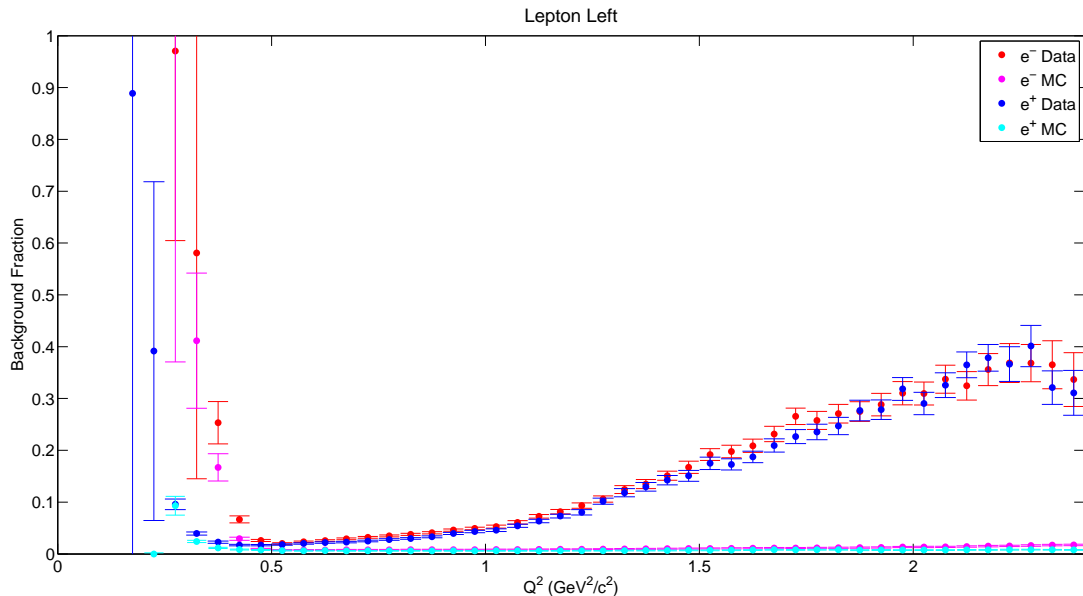


Figure 6-11: Background fraction remaining in the final elastic event selection for leptons detected in the left sector for e^-p and e^+p events in both data and simulation. The error bars represent the 95% confidence bounds on the integrals of the background distributions within the final coplanarity cut.

6.2.4 Final Processing

With the background model in place, the final event selection was made by placing the final available cut on $\Delta\phi$ and integrating the number of counts remaining to produce the data and simulation total elastic event yields. This $\Delta\phi$ cut was placed at the 3σ width of the Gaussian distribution fitted to each Q^2 bin in the background modeling process described in the previous section. These distribution widths are shown as functions of Q^2 for leptons going left and right in Figures 6-13 and 6-14 respectively. Note, that since the simulation resolution in $\Delta\phi$ was slightly better than the data resolution, the fit cut width of the data sample for each lepton species was applied to both the data and simulation of that species so as to maintain the consistent treatment of data and simulation as in the initial cuts. For each Q^2 bin of width 0.05 GeV^2 , region within the 3σ data width was integrated for both the coplanarity histogram and the background model. The integral of the background model was subtracted from the integral of the coplanarity histogram to produce the

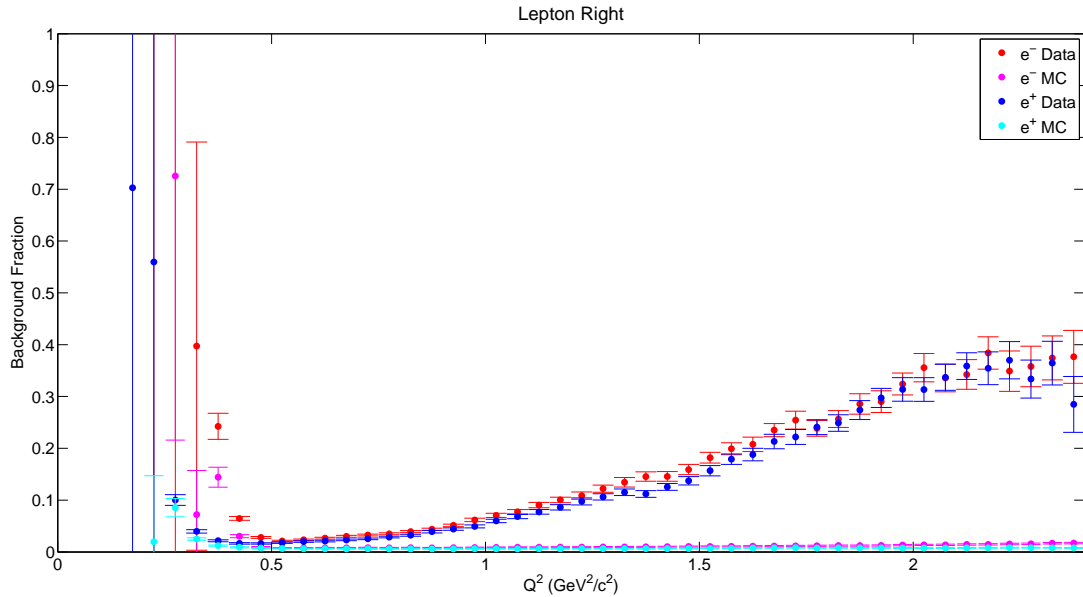


Figure 6-12: Background fraction remaining in the final elastic event selection for leptons detected in the right sector for e^-p and e^+p events in both data and simulation. The error bars represent the 95% confidence bounds on the integrals of the background distributions within the final coplanarity cut.

final yields of elastic $e^\pm p$ events that were used to generate the final results of the experiment.

6.3 Comparison of Data and Simulation

With the full analysis method applied, comparisons between the data and simulation elastic event yields after background subtraction provide insight into the quality of the data and analysis as well as a preliminary measure of the absolute elastic e^-p and e^+p cross-sections. Figure 6-15 presents the ratio of the background-subtracted data and simulation yields for e^-p and e^+p events, separated by whether the lepton was detected in the left or right sector of the spectrometer. For this figure, the simulation was conducted using the Kelly parametrization of the elastic proton form factor [77] and the Maximon and Tjon radiative corrections prescription [100]. Encouragingly, the data and simulation show agreement on the level of a few percent across the entire acceptance, which is consistent with the expectations in deviations

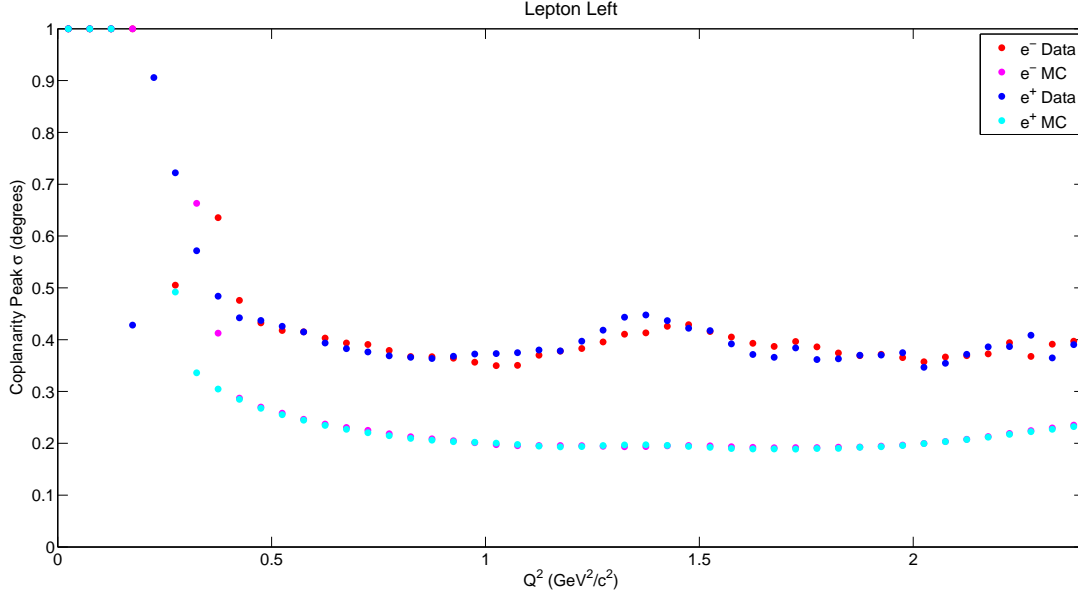


Figure 6-13: The 1σ width of the Gaussian fit to the coplanarity distribution as a function of Q^2 for leptons in the left sector. The loss of resolution in data near $Q^2 = 1.4 \text{ GeV}^2$ corresponds to the lepton passing through the inefficient region of the left-inner drift chamber (see Figure 6-1), which caused the lepton tracks to be comprised of fewer hits. The purity of the simulation data sample resulted in a maintenance of resolution in this region despite the loss of hits due to the efficiency map implementation.

due to uncertainties in the knowledge of the form factors. Differences in the ratios computed for leptons going left and right are indicative of the approximate systematic uncertainty in the determination of the absolute elastic $e^\pm p$ cross sections that are possible with the OLYMPUS data. Additionally, since the simulation events used for Figure 6-15 were generated using the slow control luminosity, the fact that the data/simulation ratio is several percent above unity across the entire acceptance is very consistent with the measurement of the absolute luminosity from the 12° system ($\mathcal{L}_{e^\pm}/\mathcal{L}_{\text{SC}} \approx 1.046 \pm 0.024$, see Section 5.2.9). Thus, careful analyses of the OLYMPUS data may be able to provide information on the absolute e^-p and $e^\pm p$ cross sections, and also information regarding the elastic form factors, with uncertainties on the order of $\sim 5\%$.

Figure 6-16 shows the ratio of the total e^-p and e^+p elastic event yields in data and simulation for three different form factor parametrizations: the Kelly model [77],

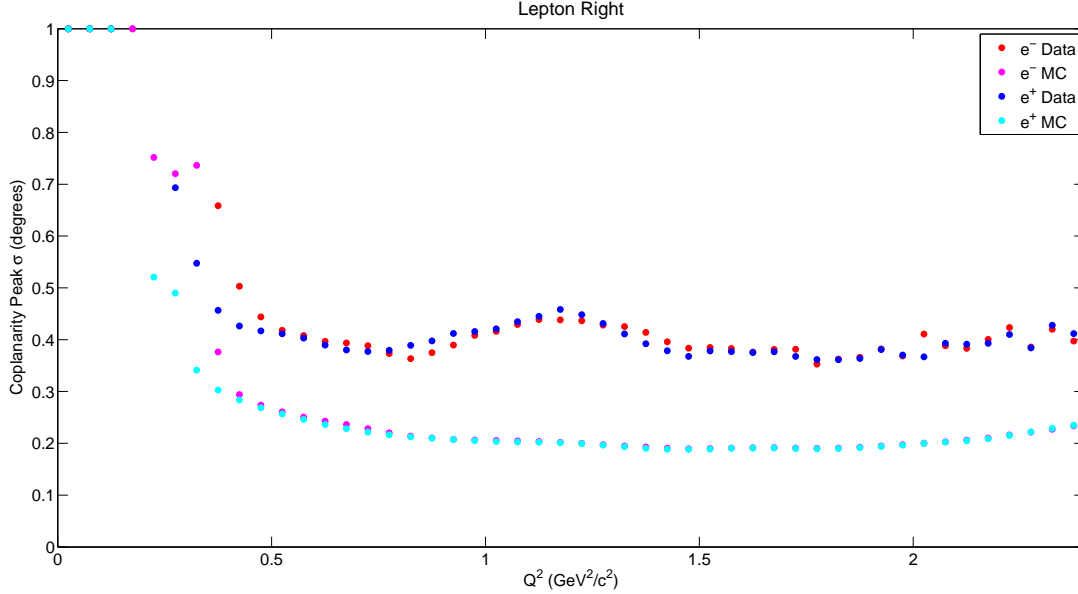


Figure 6-14: The 1σ width of the Gaussian fit to the coplanarity distribution as a function of Q^2 for leptons in the left sector. The loss of resolution in data near $Q^2 = 1.2 \text{ GeV}^2$ corresponds to the left-going proton passing through the inefficient region of the left-inner drift chamber (see Figure 6-1), which caused the proton tracks to be comprised of fewer hits. The purity of the simulation data sample resulted in a maintenance of resolution in this region despite the loss of hits due to the efficiency map implementation.

the Bernauer model [37], and the dipole form factor (Equation 2.21). The sum of the e^-p and e^+p yields is a particularly useful quantity for examination of the behavior of the different form factor models, since any effects from TPE or lepton charge-odd radiative corrections that are present in the data but not the simulation are canceled in this sum, providing a means of determining the absolute cross section in the absence of such effects. As expected, the models agree at low Q^2 where existing data constrains the models well, but considerable deviations are apparent as Q^2 increases. Since the luminosity normalization is shared between the models, which effectively removes uncertainty contributions from the absolute normalization when comparing the relative values of the ratios in different models, the large deviations between the form factor models at higher Q^2 indicate that the OLYMPUS data can provide constraints on future form factor models. The possibility of these additional physics results will be considered in future OLYMPUS publications.

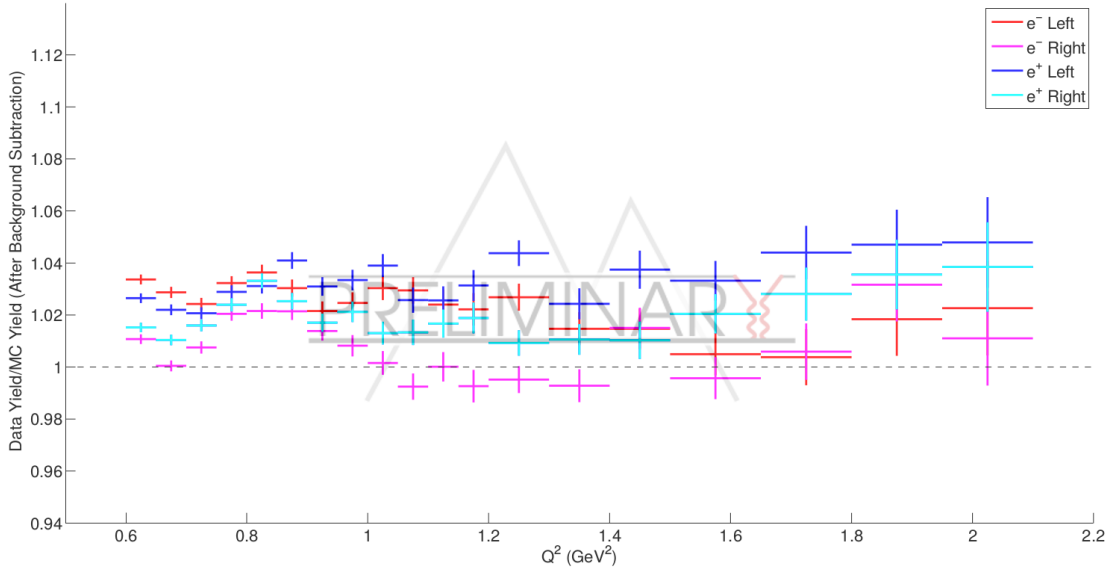


Figure 6-15: The ratio of data yields over simulation yields (background-subtracted) by lepton species and detector side with the Kelly form factor model [77]. Given that uncertainties in the determination of the elastic proton form factors are of the order of at least several percent, especially at the high end of the Q^2 range, the overall agreement between the data and simulation yields is strong. Note that these results are normalized to the slow control luminosity, and are thus subject to a shared systematic uncertainty in the absolute value of all points of several percent.

6.4 Systematic Uncertainties

While the final analyses of the systematic uncertainties associated with the OLYM-PUS $R_{2\gamma}$ result were still underway at the time of writing, this section provides a preliminary assessment of the systematic uncertainties associated with the results presented in Chapter 7, with a particular focus on identifying the remaining dominant uncertainties for consideration in the later stages of the analysis. Note that the systematic uncertainties from the MIE luminosity determination (Section 5.3.2) and the 12° system $e^\pm p$ measurement, used either as a luminosity determination or as an additional kinematic point (Section 5.2.8), are independent from the effects discussed here. In particular, any uncertainty from the luminosity determination applies as a constant shift shared by all points in the determination of $R_{2\gamma}$, rather than as a point-to-point uncertainty.

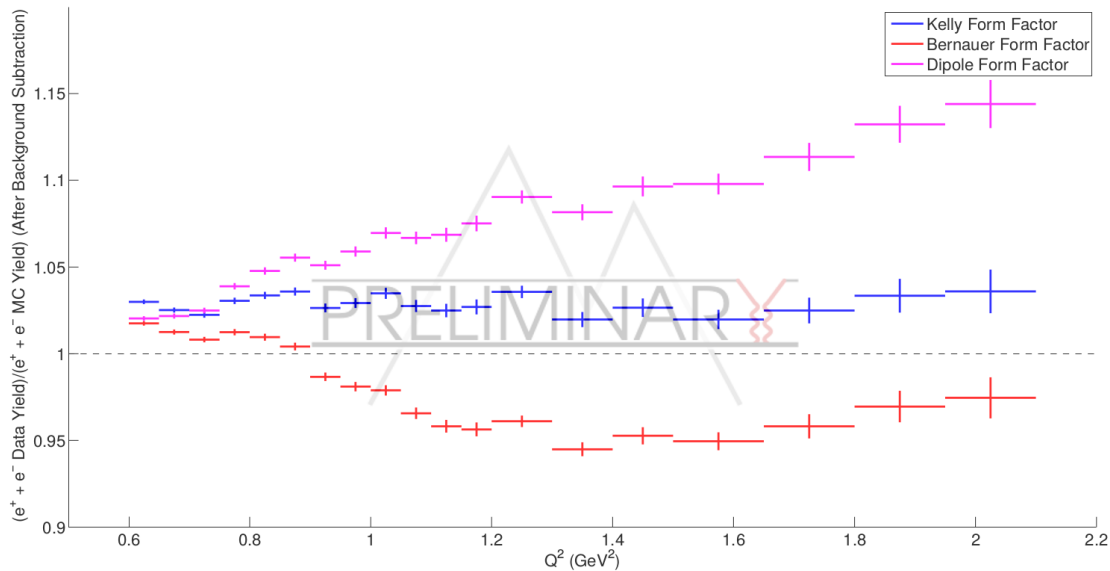


Figure 6-16: Ratio of the summed elastic e^-p and e^+p yields of each species in data and simulation for several form factor models [37,77]. In the summed yield of e^-p and e^+p , effects from TPE and $\mathcal{O}(\alpha^3)$ radiative corrections from lepton vertices cancel. Given the power of the OLYMPUS data to discriminate between models, there exists the potential in the OLYMPUS data to inform future models of the proton elastic form factors. Note that these results are normalized to the slow control luminosity, and are thus subject to a shared systematic uncertainty in the absolute value of all points of several percent.

The estimates presented here should be considered preliminary, and a final analysis (including additional detail) will accompany the published OLYMPUS results.

6.4.1 Detector Acceptance and Efficiency

The complexities of the wire chamber acceptance, efficiency, and its interaction with the magnetic field (both in terms of particle trajectories and the time-to-distance calibration) make a simulation-based approach to estimating the systematic uncertainties associated with such effects infeasible. Due to issues with the drift chamber efficiency, uncertainties in the geometric survey of the detector, and the difficulty of the drift chamber time-to-distance parametrization, these sources of systematic uncertainty are the dominant contributions to the overall uncertainty, and thus it is critical to properly assess them. The redundancy of the left and right detector

systems in OLYMPUS provides a means of estimating the systematic uncertainties from these effects based on examination of the data.

Ideally, the elastic event yields separated by the lepton going left or right in the detector would be identical, or at least any deviations between the left and right yields would be completely accounted for in simulation. Any unexplained left/right deviations provide a first-order estimate of systematic uncertainties due to detector acceptance, efficiency, and magnetic field. Figure 6-17 shows the lepton-left/right ratio of background-subtracted yields for e^-p and e^+p events in data and simulation, and Figure 6-18 shows the ratio of the $R_{2\gamma}$ results for the separate lepton-left and lepton-right samples. While the simulation captures some of the structure in the ratio of left/right yields in data, the structure is not fully accounted for by the inefficiencies implemented in simulation. In particular, the “peak-valley” structure between $Q^2 = 1.1 \text{ GeV}^2$ and $Q^2 = 1.6 \text{ GeV}^2$ is known to be related to the highly inefficient region of the left drift chamber (see Figure 6-1), which reduces the tracking resolution significantly and affects event selection. Most likely, the applied resolutions in the simulation did not degrade the hit quality sufficiently in simulation to precisely match the conditions of data tracking, leading to less difference in the left/right comparison in simulation than data.

Deviations between the data and simulation in Figure 6-17 provide indications of the systematic uncertainty on a possible absolute cross section extraction, while deviations from unity in Figure 6-18 provide an indication of how such uncertainties affect the e^-p and e^+p yields differently and thus provide an estimate of the uncertainty of the $R_{2\gamma}$ result. While the lepton-left and lepton-right data sample are statistically independent, there remain deviations in the value of $R_{2\gamma}$ of $\sim 1\%$ that cannot be attributed to statistical variation between the samples, and thus this is taken as an estimate of the systematic uncertainty due to detector acceptance and efficiency effects (which are additionally heavily convolved with the effects of the magnetic field uncertainty). At this stage, this is the dominant systematic uncertainty for the $R_{2\gamma}$ result, and work is ongoing to reduce it if possible.

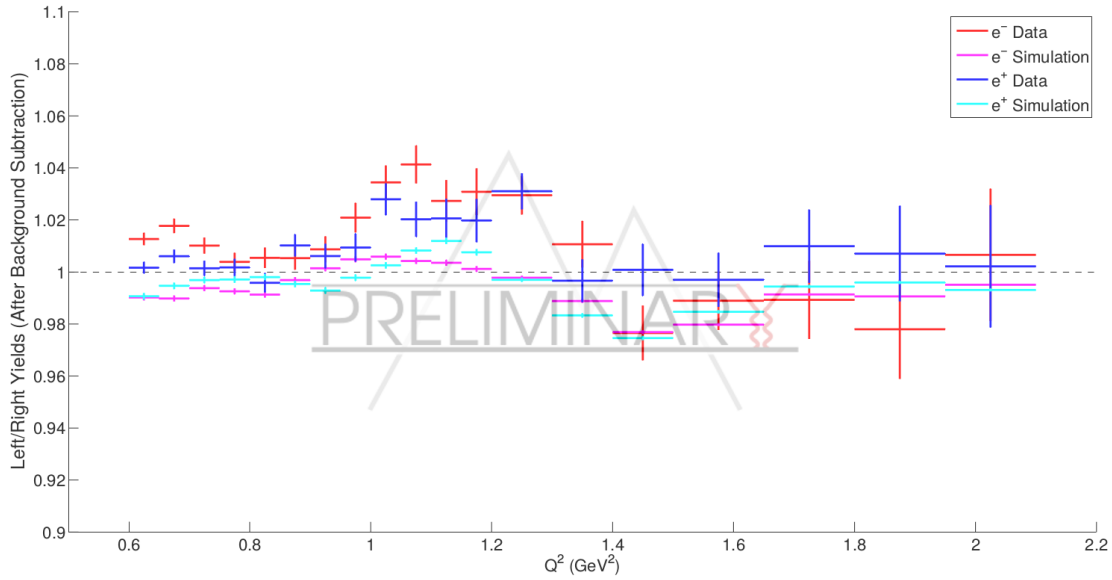


Figure 6-17: Ratio of the lepton left/right background-subtracted elastic $e^\pm p$ yields in data and simulation, separated by lepton species. Structures in this ratio that differ between data and simulation are indicative of effects such as differences in acceptance, detector efficiency, and magnetic field between the left and right sectors that are not fully accounted for in the simulation. These effects contribute to the total systematic uncertainty estimate. The dominant “peak-valley” structure between $Q^2 = 1.1 \text{ GeV}^2$ and $Q^2 = 1.6 \text{ GeV}^2$ is known to be related to the highly inefficient region of the left drift chamber (see Figure 6-1), which reduces the tracking resolution significantly and affects event selection.

6.4.2 Elastic and Fiducial Cuts

To control uncertainties due to the choices of the elastic and fiducial event cuts used in the $R_{2\gamma}$ analysis, these cuts were varied and the results recomputed to examine their effect on the value of $R_{2\gamma}$. Additionally, a potentially stronger analysis of the effects of choices in the $e^\pm p$ event selection is provided by the comparison of the independent analyses of the OLYMPUS data [53, 54] discussed in Section 7.3. It remains useful, however, to consider the effects of the cut choices within a single analysis.

Each of the eight fiducial, pair selection, and elastic cuts applied in the analysis (listed in Section 6.2) was varied individually by $\pm 10\%$ in range, and the resulting change in the value of $R_{2\gamma}$ between these variations was computed bin-by-bin. The quadrature sum of the variations between the values of $R_{2\gamma}$ at $\pm 10\%$ cut ranges for

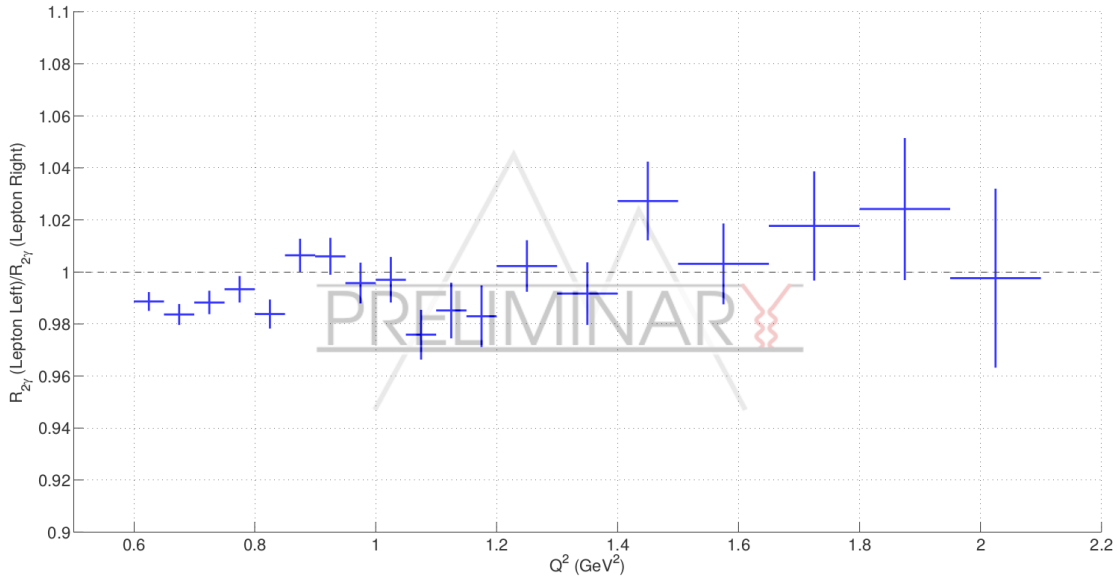


Figure 6-18: Ratio of the $R_{2\gamma}$ results for events in which the lepton was detected in the left and right sectors of the detector. The error bars are statistical, and it should be noted that the lepton-left and lepton-right datasets are statistically independent. Deviations from unity of this ratio that cannot be attributed to statistics provide a means of estimating systematic uncertainties due to effects such as acceptance, magnetic field, and detector efficiency.

the eight cuts is shown in Figure 6-19. For most Q^2 bins, the sum of the variations is less than 0.2%, with the notable exception of the bin at $Q^2 = 1.725$ GeV². To an extent, this lack of effect is expected due to the strategy used for this analysis, which placed loose cuts and allowed the exclusively reconstructed kinematics to determine event selection rather than placing tight elastic cuts that would be more sensitive to detector resolutions. The cause of the larger uncertainty in the $Q^2 = 1.725$ GeV² bin is under investigation, but is dominated by the uncertainty associated with the fiducial cut on the reconstructed z vertex of event pairs.

Additionally, effects from the choices made in particle identification (i.e., the cuts made in the measured vs. expected ToF meantime discussed in Section 6.2.1) were also examined by a similar procedure of varying cut boundaries. In most ToF bars, the separation between leptons and protons was extremely clear and thus variations in the cut had essentially no effect. In the regions where pair particle identification is

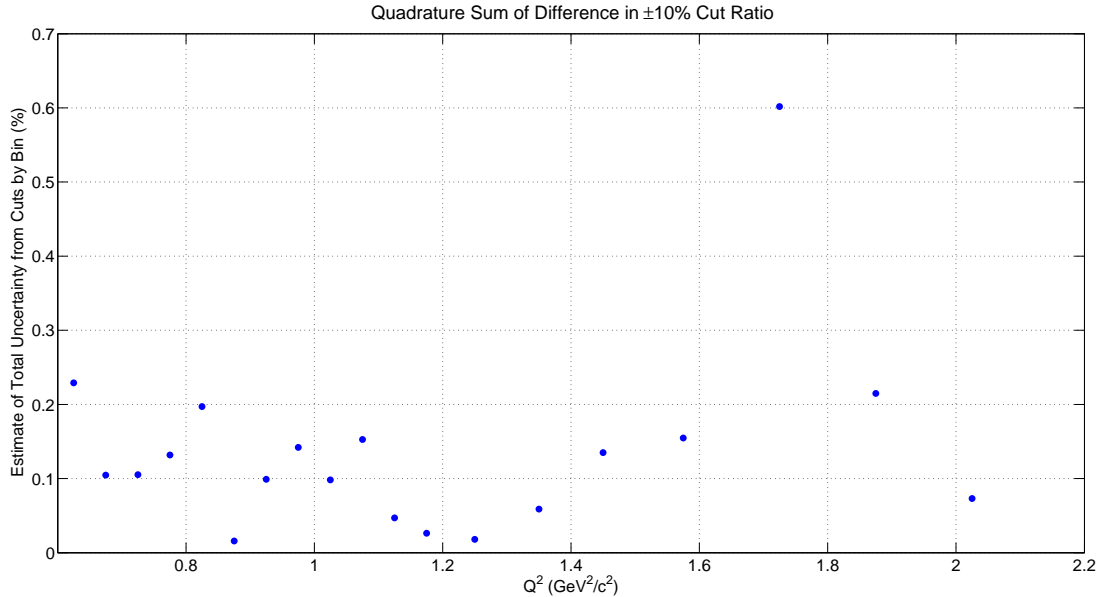


Figure 6-19: Estimate of the total systematic uncertainty due to event selection cuts, computed as the quadrature sum of the variations in $R_{2\gamma}$ caused by varying the boundaries of each of the cuts listed in Sections 6.2.2 and 6.2.4 by $\pm 10\%$. For most Q^2 bins, this uncertainty is on the order of 0.2% or smaller, with the exception of the bin at $Q^2 = 1.725$ GeV 2 .

most ambiguous (the ToF bars in the central region of each detector side), differences between the independent analyses (Section 7.3), which each treated particle identification in a different manner, are likely a more robust measure of the systematic uncertainties due to such analysis choices.

6.4.3 Background Subtraction

Due to the qualitative nature of the various choices made in choosing a background subtraction model (the kinematic quantities on which subtraction is performed, the models used for the elastic peak and background in those quantities, etc.), the final assessment of the systematic uncertainty due to background subtraction will involve a comparison of the independent $R_{2\gamma}$ analyses using the OLYMPUS data, each of which applied different approaches to this problem. It is useful, however, to examine the uncertainties inherent to the background subtraction method used in the analysis presented in this work (Section 6.2.3).

As shown in Figures 6-11 and 6-12, an uncertainty in the background subtraction arises from the uncertainty in the fit of the background model to the data. This uncertainty increases for data as a function of Q^2 as the statistics of the data decrease, but remains relatively constant and comparably small for simulation. In the highest Q^2 bins used for the analysis, the 95% confidence interval for the background fit to the absolute e^-p and e^+p yields in data reaches approximately 2%. Much of this variation is statistical, however, and thus captured somewhat in the final statistical uncertainties associated with those bins. An additional cross check on the background subtraction was conducted by varying the range in the coplanarity histogram away from the peak to which the background model was fit between outside of 3σ to outside of 5σ of the peak. These alterations to the procedure did not affect the background fraction more than the confidence intervals associated with the background fit. Thus, conservatively, a systematic uncertainty of $\sim 0.5\%$ may be ascribed to the background subtraction in the highest Q^2 bins, with much smaller contributions at lower Q^2 .

6.4.4 Radiative Corrections

While a concerted effort was made to properly account for radiative corrections in the analysis of the OLYMPUS data via the full-simulation scheme described in Section 4.3.2, the choice of radiative corrections prescription that is used affects the final $R_{2\gamma}$ result due to the different approximations and assumptions made by different models. The OLYMPUS radiative generator was designed to permit the OLYMPUS results to be presented using a variety of different radiative corrections schemes so as to facilitate comparison with other data. This uncertainty may be eliminated by matching radiative corrections schemes when comparing different experiment results or experimental data to theoretical or phenomenological models, but it is worthwhile to assess the overall effect of different models on the $R_{2\gamma}$ results.

Figures 6-20 and 6-21 present the ratios of the $R_{2\gamma}$ results that arise from making key choices in the application of radiative corrections. The former shows the ratio of the result when the Maximon and Tjon radiative corrections scheme [100] is applied using exponentiated and non-exponentiated methods, while the latter shows the ratio

of the results using the Maximon and Tjon scheme and the Mo and Tsai scheme [99] (the two most commonly applied radiative $e^\pm p$ prescriptions). Each of these ratios shows deviation from unity that increases with Q^2 , reaching 0.5%-1.0% at the upper end of the OLYMPUS acceptance. This illustrates the importance of matching radiative corrections schemes when comparing datasets and predictions and the importance of understanding the exact methods used to apply radiative corrections in different datasets.

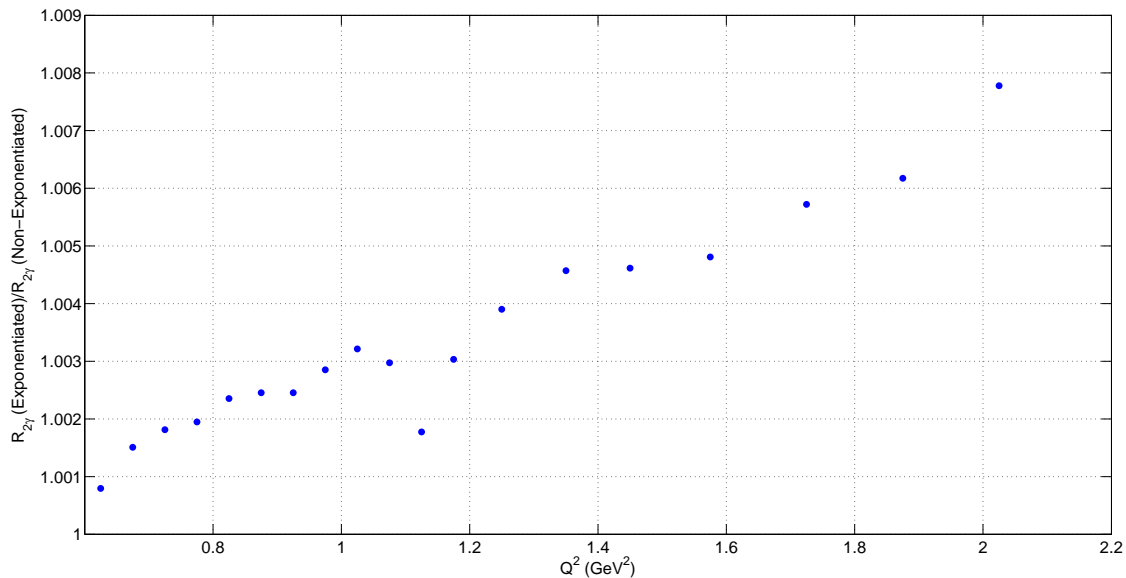


Figure 6-20: Ratio of the $R_{2\gamma}$ results for simulation using exponentiated and non-exponentiated radiative corrections under the prescription of Maximon and Tjon [100]. The statistical uncertainties for each data point are suppressed since they are completely correlated in each radiative corrections model.

6.4.5 Form Factors

While the choice of proton elastic form factor model significantly affects the extracted absolute e^-p and e^+p cross sections (Section 6.3), it is expected in an analysis of $\sigma_{e^+p}/\sigma_{e^-p}$ that effects from the form factor model used should be extremely small in the absence of any errors in the analysis that introduce a bias in the way the kinematics (in particular the value of Q^2) for e^-p and e^+p events are computed. In

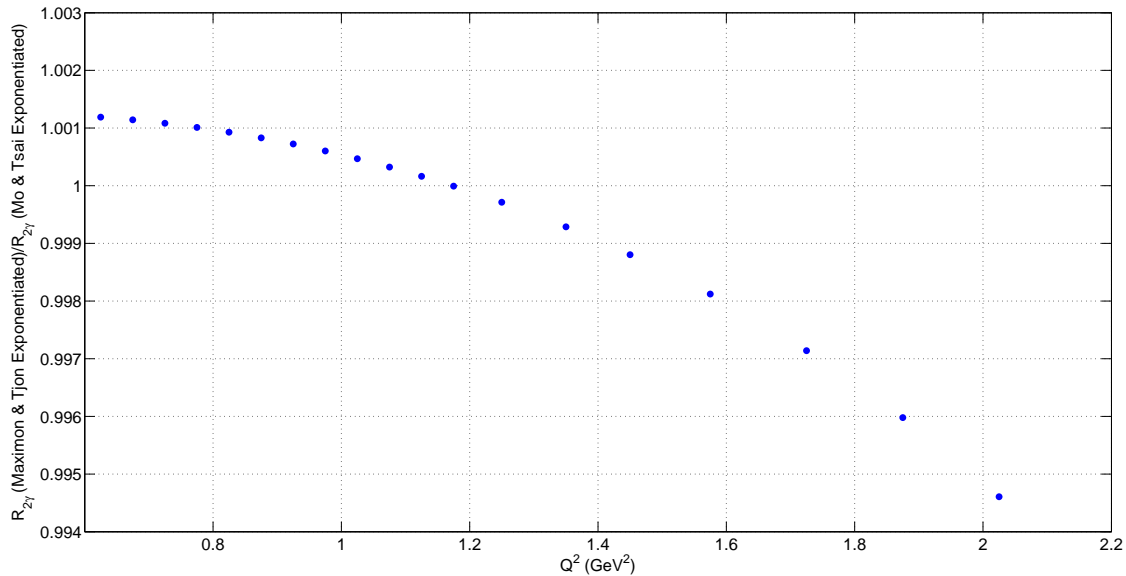


Figure 6-21: Ratio of the $R_{2\gamma}$ results for simulation using the Maximon/Tjon [100] and Mo/Tsai [99] radiative corrections prescriptions. For each simulation, the radiative corrections were applied with exponentiation. The statistical uncertainties for each data point are suppressed since they are completely correlated in each radiative corrections model.

Figure 6-22 presents the ratio of the $R_{2\gamma}$ results computed using the Kelly [77] and Bernauer [37] form factor models. Across the full acceptance, the deviation between the two is much less than 0.01%, indicating that this is a minimal effect in the $R_{2\gamma}$ result and providing a sanity check on the basic calculations of the reconstructed kinematics. For reference, a similar ratio between the $R_{2\gamma}$ results using these form factors, the dipole form factor, or even treating the proton as a point particle gives extremely similar results, providing confidence in the implementation of the form factors in the radiative event generator.

6.4.6 Discussion of Current Total Systematic Uncertainty Estimate

Due to the dominant effects of the detector acceptance and efficiency that contribute to the current systematic uncertainty estimate for this analysis, analogous effects that were shown to be small in the 12° systematic uncertainty analysis (Section 5.2.8), such

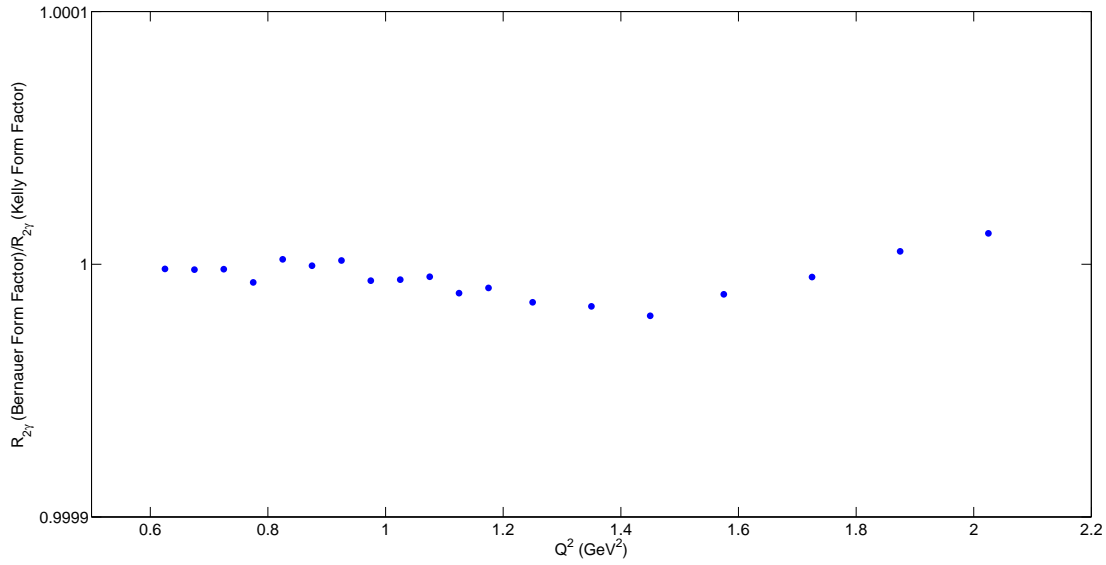


Figure 6-22: Ratio of the $R_{2\gamma}$ results for simulations conducted with the Kelly [77] and Bernauer [37] form factor models. As expected, the total effect from the choice of form factor model is extremely small (much less than 0.01% across the full acceptance). The statistical uncertainties for each data point are suppressed since they are completely correlated in each form factor model.

as beam energy and position, are not considered here, but will be considered as part of the final OLYMPUS results. References [53] and [54] include discussion of additional systematic effects such as those from the ToF detector and track reconstruction efficiencies, but these effects were found to be small relative to the aforementioned dominant effects. For the preliminary results shown in Chapter 7, a conservative 1.5% bin-to-bin total systematic uncertainty is quoted for the $R_{2\gamma}$ results in light of the fact that final analysis of the $R_{2\gamma}$ results and the systematic uncertainties was ongoing at the time of writing. This, however, is likely a considerable overestimate in most bins (especially at low Q^2) and thus should only be considered in the preliminary context of these results. Systematic uncertainties due to the luminosity normalization and for the independent bin constructed using the results from the 12° system are separate from this estimate and are discussed in detail in Sections 5.3.2 and 5.2.8, respectively.

Chapter 7

Results and Discussion

With the methodology of the analysis in place, and in combination with the relative luminosity analyses presented in Chapter 5, the OLYMPUS result for $R_{2\gamma}$ (Equation 1.1) may be constructed. This chapter presents the results of the analysis described in Chapter 6, the result for the value of $\sigma_{e^+p}/\sigma_{e^-p}$ as measured in the 12° system using the MIE luminosity normalization, as well as a preliminary comparison of the different $R_{2\gamma}$ analyses conducted using the OLYMPUS data. As mentioned in Section 6.3, further physics results from the OLYMPUS data pertaining to the absolute elastic $e^\pm p$ cross section and proton form factors may be part of future publications. While such analyses are not part of this work, it is expected that subsequent publications will include results of this nature.

The following results represent $\sim 3.1 \text{ fb}^{-1}$ of data, approximately evenly split between the two leptons species. This corresponded to a total yield (after background subtraction) of approximately $4 \cdot 10^6$ accepted elastic $e^\pm p$ events for each lepton species. The simulation dataset, generated according to the principles described in Section 4.3, included approximately $2 \cdot 10^9$ radiative elastic events, which ensured that the statistical uncertainty of the simulated dataset was negligible in comparison to both the statistical and systematic uncertainties on the data in all regions of the OLYMPUS acceptance. The strong statistical power of the OLYMPUS dataset allows examination of the ratio in continuous fashion across the entire OLYMPUS acceptance.

The results that follow should be considered preliminary and subject to further

investigations of the systematic uncertainties in the analysis. It is expected, however, that these results will accurately represent the effective trends in $R_{2\gamma}$ that will be presented in subsequent OLYMPUS publications, as indicated by the constraints on the systematic uncertainties discussed in Section 6.4 and the consistency of the independent analyses of the OLYMPUS data presented in Section 7.3.

7.1 Note on the Choice of the Luminosity Normalization

As discussed in Section 5.4, the 12° (Table 5.5) and MIE (Equation 5.21) species-relative luminosity measurements were found to be extremely consistent, both as a function of run number (matching the systematic variations relative to slow control, indicated by the lack of time-varying structure in Figure 5-49) and in value (since the two determinations are well within the estimated uncertainties of each other). Since the result for $R_{2\gamma}$ requires only a relative luminosity measurement, rather than an absolute integrated luminosity for each species, the result of the MIE method was chosen as the species-relative luminosity normalization for the results shown, which permits the use of the 12° system result as an additional kinematic point for the measurement of $R_{2\gamma}$. Since the 12° elastic $e^\pm p$ measurement exhibits systematic uncertainties that are largely independent from the reconstruction of elastic events in the main spectrometer, this point provides a valuable cross check on the measurement $R_{2\gamma}$ in the rest of the acceptance as well as a precise and valuable check on the expectation that TPE effects go to zero at high- ϵ . The value of $R_{2\gamma}$ at $\theta \approx 12^\circ$ is discussed in Section 7.2.1.

For possible future analyses of the elastic proton form factors and $e^\pm p$ cross section, it will likely be necessary to use the measurement of the absolute luminosities for each species from the 12° system, since the MIE absolute luminosity analysis is subject to large uncertainties due to event selection cuts. The strong consistency in the relative measurement between the two methods, as well as the agreement between the 12°

absolute estimate and the simulation at forward angles (Section 6.3), provides a high level of confidence in the absolute estimate for future analyses of the OLYMPUS data.

7.2 $R_{2\gamma}$ Results as a Function of ϵ and Q^2

Figures 7-1, 7-2, 7-3, and 7-4 present the results for $R_{2\gamma}$ as found by the analysis described in Chapter 6 as a function of Q^2 and ϵ in two different binnings for each. In each figure, the point at $\theta = 12^\circ$ ($Q^2 = 0.165 \text{ GeV}^2$, $\epsilon = 0.98$) is shown with its full systematic plus statistical uncertainty estimate (Section 7.2.1) while the error bars on the other points are statistical only. As discussed in Section 6.4, the total systematic uncertainty for each point for these results may be considered on the order of 1.5%, although for many bins this is likely an overestimate. The magnitude of the total uncertainty from the MIE luminosity determination, which would apply as a common shift to all data points simultaneously, is represented by the gray box above the horizontal axis of each figure. Additionally, each figure presents the theoretical [37, 46, 47] and phenomenological [39–45] models initially presented with the OLYMPUS projections in Figure 1-2. The results and models were computed using the Maximon and Tjon prescription for radiative corrections [100] and the methodology described in Section 4.3.2. Tables 7.1 and 7.2 list the values presented by the plots in each binning, as well as the average Q^2 and ϵ for each bin.

As previously noted, these results are preliminary and are subject to further analysis, particularly relating to the final estimate of the systematic uncertainty in each bin. As discussed in Section 7.3, it is highly likely that the final OLYMPUS results will strongly resemble the results presented here, but at the time of writing the finalization of the OLYMPUS results for publication was still underway.

7.2.1 The $\sigma_{e+p}/\sigma_{e-p}$ Ratio at $\epsilon \approx 0.98$ ($\theta \approx 12^\circ$)

While the 12° measurement of $\sigma_{e+p}/\sigma_{e-p}$ may be taken as a normalization point for the relative luminosity of electron and positron data collected by the experiment or used in conjunction with the MIE measurement to provide a combined high-precision

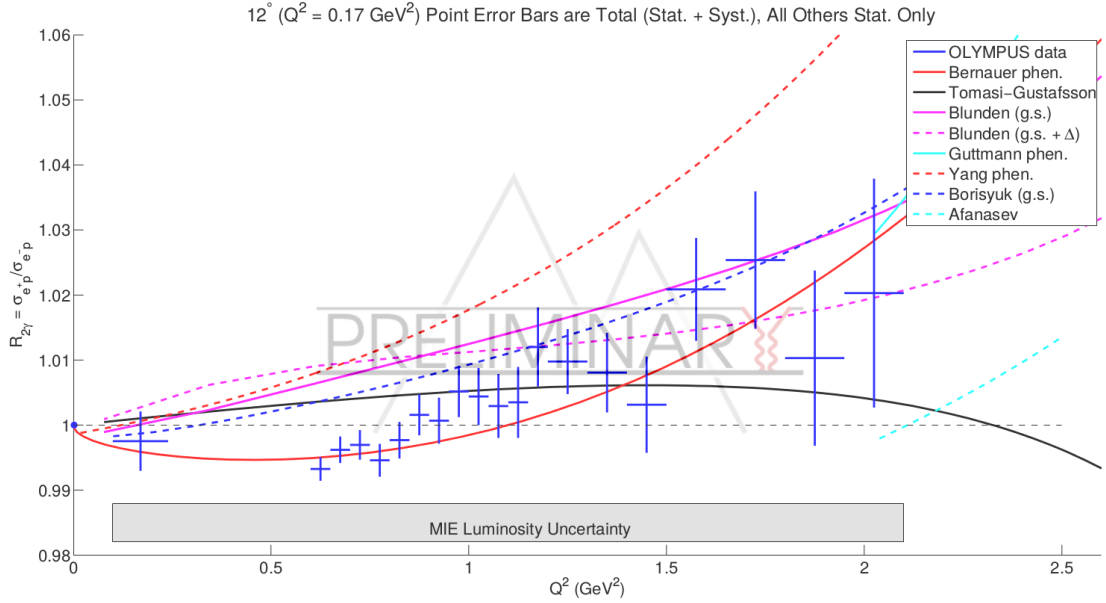


Figure 7-1: Preliminary results for $R_{2\gamma}$ from the analysis presented in Chapter 6, binned finely as a function of Q^2 . The error bars on the points represent the statistical uncertainty of the analysis, with the exception of the point at $Q^2 = 0.165 \text{ GeV}^2$ where the error bar represents the total statistical plus systematic uncertainty. The gray box represents the total (statistical plus systematic) uncertainty from the MIE luminosity analysis, which applies as a constant normalization shift to all data points. The data points in this plot are summarized in Table 7.1. (Phenomenological models: [37,46,47], theoretical models: [39–45])

estimate, it may also be taken as an additional measurement of $R_{2\gamma}$ at $\epsilon \approx 0.98$, $Q^2 \approx 0.165 \text{ GeV}^2$ if the MIE is used as an independent measure of the relative luminosity. This is especially valuable due to the fact that the MIE measurement, while depending in part on elastic $e^\pm p$ scattering, was at a much more forward angle ($\epsilon \approx 0.99975$, $Q^2 \approx 0.002 \text{ GeV}^2$) where the expectation of $R_{2\gamma} = 1$ is extremely strong (physics considerations demand that $R_{2\gamma} = 1$ at $\epsilon = 1$). Taking this approach and utilizing the results of Sections 5.2.9 and 5.3.2, the result is:

$$R_{2\gamma} (\epsilon = 0.98, Q^2 = 0.165 \text{ GeV}^2) = 0.9975 \pm 0.0010 \text{ (stat.)} \pm 0.0053 \text{ (syst.)}, \quad (7.1)$$

where the uncertainties are the result of adding the uncertainties of the individual measurements in quadrature, since the uncertainties of the two measurements are

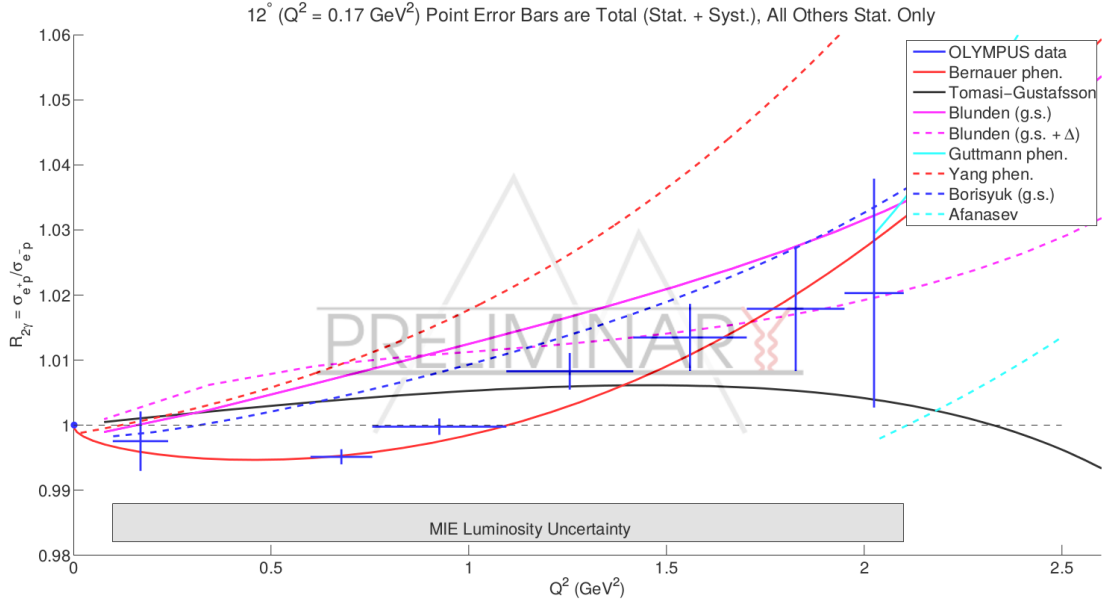


Figure 7-2: Preliminary results for $R_{2\gamma}$ from the analysis presented in Chapter 6, binned coarsely as a function of Q^2 , approximately matching the bins represented by the data points in the projections of Figure 1-2. The error bars on the points represent the statistical uncertainty of the analysis, with the exception of the point at $Q^2 = 0.165 \text{ GeV}^2$ where the error bar represents the total statistical plus systematic uncertainty. The gray box represents the total (statistical plus systematic) uncertainty from the MIE luminosity analysis, which applies as a constant normalization shift to all data points. The data points in this plot are summarized in Table 7.2. (Phenomenological models: [37, 46, 47], theoretical models: [39–45])

essentially completely independent. The measurement is quite valuable for several reasons:

1. it provides a consistency check on the overall scale of $R_{2\gamma}$ as measured in the main spectrometer by providing a measurement from an independent system with largely independent systematic uncertainties,
2. it constrains the behavior of $R_{2\gamma}$ at high ϵ ,
3. it provides some discriminating power between different models for $R_{2\gamma}$ in the high- ϵ region, and
4. it offers insight into the offset that should be applied to the luminosity normalization points used for the VEPP-3 $R_{2\gamma}$ results so as to allow direct comparison

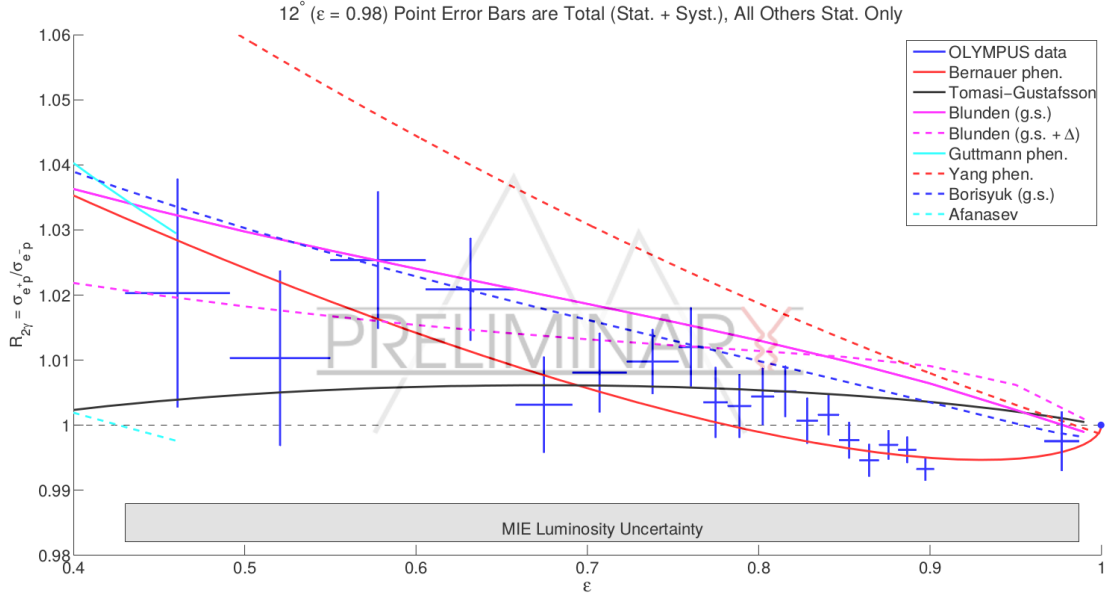


Figure 7-3: Preliminary results for $R_{2\gamma}$ from the analysis presented in Chapter 6, binned finely as a function of ϵ . The error bars on the points represent the statistical uncertainty of the analysis, with the exception of the point at $\epsilon = 0.98$ where the error bar represents the total statistical plus systematic uncertainty. The gray box represents the total (statistical plus systematic) uncertainty from the MIE luminosity analysis, which applies as a constant normalization shift to all data points. The data points in this plot are summarized in Table 7.1. (Phenomenological models: [37,46,47], theoretical models: [39–45])

of those data to models and other experiments.

This measurement constitutes a new benchmark for $\sigma_{e^+p}/\sigma_{e^-p}$ in the forward scattering ($\theta \approx 10^\circ$) region, providing a previously unachieved level of total uncertainty of $\sim 0.54\%$.

7.3 Comparison of Independent Analyses

At the time of writing, three independent $R_{2\gamma}$ analyses of the OLYMPUS data were available: the two analyses described in References [53] and [54] and the analysis described in this work. Each analysis made use of the same sets of tracked and simulated data, but applied different approaches to the analysis. Differences in the analyses included the approaches to particle identification, application of cuts in dif-

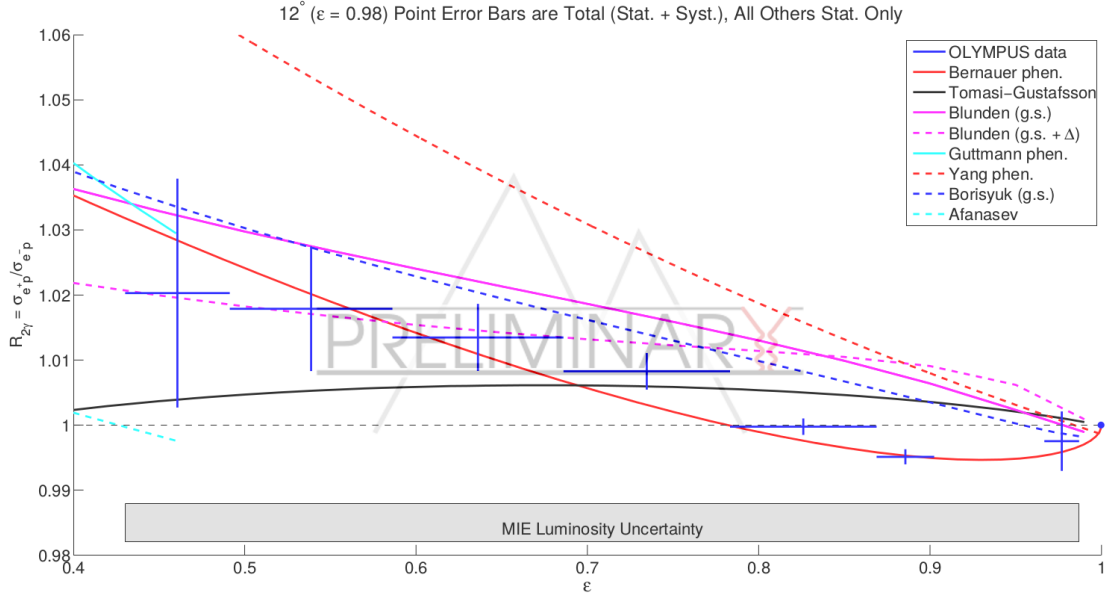


Figure 7-4: Preliminary results for $R_{2\gamma}$ from the analysis presented in Chapter 6, binned coarsely as a function of ϵ , approximately matching the bins represented by the data points in the projections of Figure 1-2. The error bars on the points represent the statistical uncertainty of the analysis, with the exception of the point at $\epsilon = 0.98$ where the error bar represents the total statistical plus systematic uncertainty. The gray box represents the total (statistical plus systematic) uncertainty from the MIE luminosity analysis, which applies as a constant normalization shift to all data points. The data points in this plot are summarized in Table 7.2. (Phenomenological models: [37, 46, 47], theoretical models: [39–45])

ferent kinematic variables, varying stringency in shared kinematic variable cuts, different background subtraction methods and models, as well as different orderings of analysis components.

Figures 7-5 and 7-6 show the results for $R_{2\gamma}$ from the three analyses plotted together as a function of Q^2 in the same binning schemes as Figures 7-1 and 7-2 respectively. The three analyses agree extremely well in terms of the general trend as a function of Q^2 , in that it rises monotonically from a few tenths of a percent below unity at $Q^2 = 0.6 \text{ GeV}^2$ to 2-3% above one at the upper end of the Q^2 acceptance. The point-to-point variations are typically on the order of a few tenths of a percent, which is consistent with the systematic uncertainty associated with choices of kinematic cuts and background subtraction models discussed in Section 6.4. Certain deviations

$\langle Q^2 \rangle$ (GeV ²)	$\langle \epsilon \rangle$	$R_{2\gamma}$	Stat. Uncertainty	Syst. Uncertainty
0.165	0.978	0.9975	± 0.0003	± 0.0046
0.624	0.898	0.9932	± 0.0018	$\sim \pm 0.0150$
0.674	0.887	0.9962	± 0.0020	$\sim \pm 0.0150$
0.724	0.876	0.9970	± 0.0023	$\sim \pm 0.0150$
0.774	0.865	0.9946	± 0.0025	$\sim \pm 0.0150$
0.824	0.853	0.9977	± 0.0028	$\sim \pm 0.0150$
0.874	0.841	1.0016	± 0.0032	$\sim \pm 0.0150$
0.924	0.829	1.0007	± 0.0036	$\sim \pm 0.0150$
0.974	0.816	1.0052	± 0.0040	$\sim \pm 0.0150$
1.024	0.803	1.0044	± 0.0044	$\sim \pm 0.0150$
1.074	0.789	1.0029	± 0.0049	$\sim \pm 0.0150$
1.124	0.775	1.0035	± 0.0055	$\sim \pm 0.0150$
1.174	0.761	1.0120	± 0.0061	$\sim \pm 0.0150$
1.246	0.739	1.0098	± 0.0050	$\sim \pm 0.0150$
1.347	0.708	1.0081	± 0.0062	$\sim \pm 0.0150$
1.447	0.676	1.0031	± 0.0074	$\sim \pm 0.0150$
1.568	0.635	1.0209	± 0.0079	$\sim \pm 0.0150$
1.718	0.581	1.0254	± 0.0106	$\sim \pm 0.0150$
1.868	0.524	1.0103	± 0.0135	$\sim \pm 0.0150$
2.038	0.456	1.0203	± 0.0177	$\sim \pm 0.0150$

Table 7.1: Values of the preliminary $R_{2\gamma}$ results for the finer binning presented in Figures 7-1 and 7-3, including the mean Q^2 and ϵ of all events in each bin.

$\langle Q^2 \rangle$ (GeV ²)	$\langle \epsilon \rangle$	$R_{2\gamma}$	Stat. Uncertainty	Syst. Uncertainty
0.165	0.978	0.9975	± 0.0003	± 0.0046
0.666	0.889	0.9951	± 0.0012	$\sim \pm 0.0150$
0.879	0.840	0.9997	± 0.0013	$\sim \pm 0.0150$
1.220	0.747	1.0083	± 0.0028	$\sim \pm 0.0150$
1.534	0.647	1.0135	± 0.0052	$\sim \pm 0.0150$
1.809	0.547	1.0179	± 0.0097	$\sim \pm 0.0150$
2.039	0.456	1.0203	± 0.0177	$\sim \pm 0.0150$
2.238	0.372	0.9813	± 0.0184	$\sim \pm 0.0150$

Table 7.2: Values of the preliminary $R_{2\gamma}$ results for the wider binning presented in Figures 7-2 and 7-4, including the mean Q^2 and ϵ of all events in each bin.

between the analyses that are larger (such as the difference between the Henderson analysis and the other two in the $Q^2 = 1.725$ GeV² bin) are likely associated with localized increases in systematic uncertainties arising from analysis choices, such as

those shown for the analysis of this work in Figure 6-19. At the time of writing, several additional analyses were underway to provide further cross-checks of the final results prior to publication, but in general the analyses show strong consistency and provide a reasonable level of confidence in the general features of the OLYMPUS $R_{2\gamma}$ result.

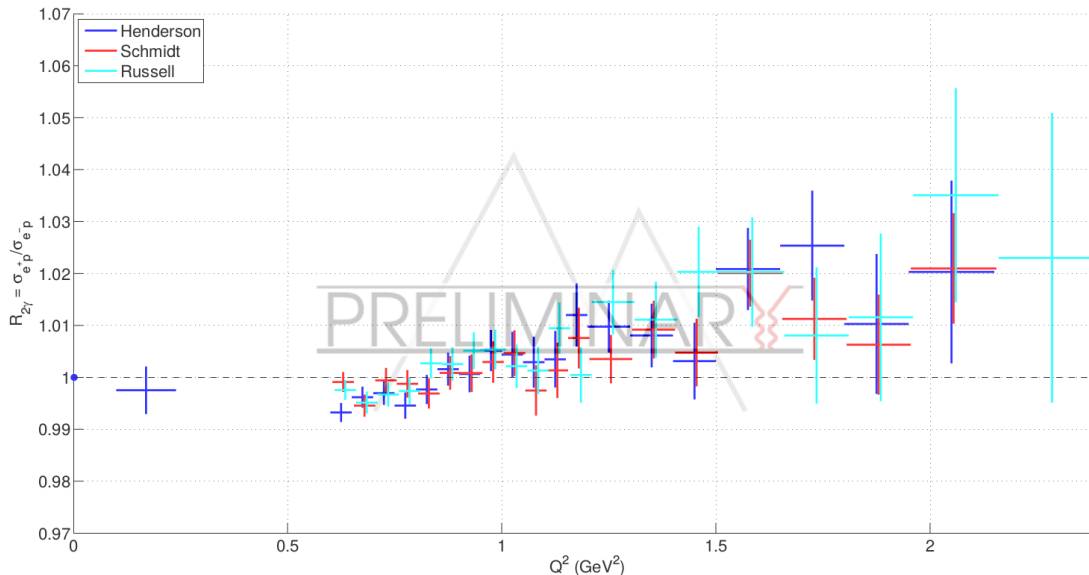


Figure 7-5: Results for $R_{2\gamma}$ as a function of Q^2 in the binning presented in Figure 7-1 as found by three different analyses of the OLYMPUS dataset: Schmidt [53], Russell [54], and Henderson (this work). Each analysis used the same data and simulation but different approaches to particle identification, elastic event selection, background subtraction, etc. In general, the statistical uncertainties shown for the separate analyses are highly, but not entirely, correlated due to differences in the total number of events accepted by each analysis.

7.4 Implications for Two-Photon Exchange and the Proton Form Factors

The results of the three TPE experiments (OLYMPUS, VEPP-3 [115], and CLAS [113, 114]) consistently indicate the presence of a contribution from TPE to elastic $e^\pm p$ scattering, as each shows a generally increasing trend in the value of $\sigma_{e^+p}/\sigma_{e^-p}$

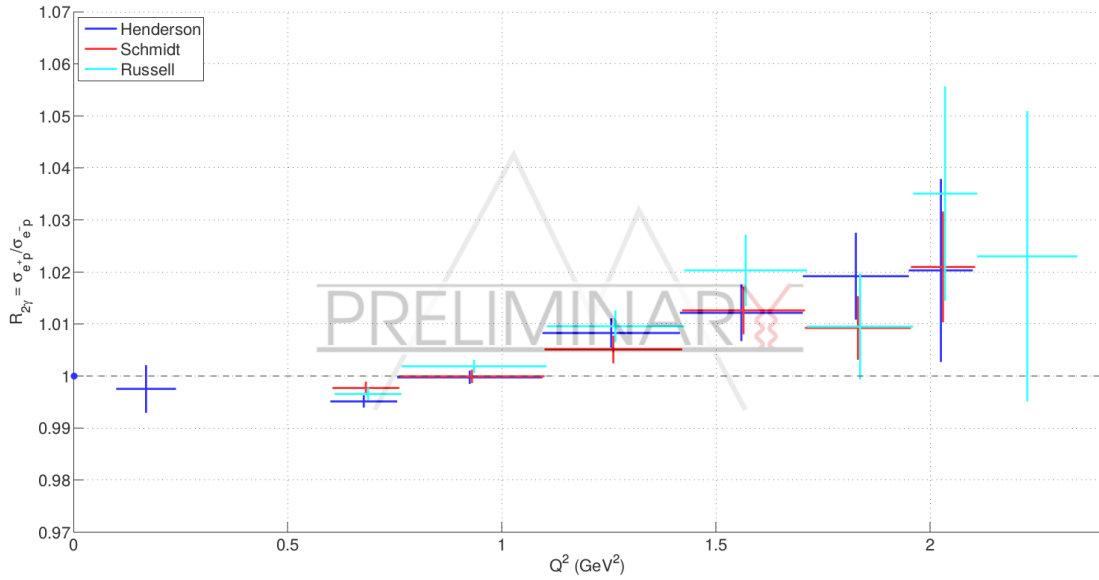


Figure 7-6: Results for $R_{2\gamma}$ as a function of Q^2 in the binning presented in Figure 7-2 as found by three different analyses of the OLYMPUS dataset: Schmidt [53], Russell [54], and Henderson (this work). Each analysis used the same data and simulation but different approaches to particle identification, elastic event selection, background subtraction, etc. In general, the statistical uncertainties shown for the separate analyses are highly, but not entirely, correlated due to differences in the total number of events accepted by each analysis.

with increasing Q^2 /decreasing ϵ . While the experiments differ in kinematic coverage, each provides results that are consistent with an effect of $\lesssim 3\%$ at $\epsilon \approx 0.4$. The general magnitude of this effect is consistent with a number of the theoretical and phenomenological models (as shown in the OLYMPUS results figures), while models predicting larger effects (such as the Yang phenomenological model [46]) are well excluded. The addition of the high-statistics OLYMPUS data begins to place stronger constraints on the more similar models, as it provides the first indications of the shape of the evolution of $R_{2\gamma}$ as a function of Q^2 or ϵ . In particular, the OLYMPUS data strongly suggests that $R_{2\gamma}$ indeed passes below unity at $\epsilon \gtrsim 0.85$ and $Q^2 \lesssim 0.6$ GeV 2 as initially suggested by the CLAS results (see Figure 2-10).

While the OLYMPUS data appear to agree well with the Bernauer phenomenological model [37], which would suggest that the form factor discrepancy may be explained by TPE contributions to elastic $e^\pm p$ scattering, the assumptions under-

lying the model as well as the relative consistency of the combined experimental data with the general trends and magnitudes of other models remain a question that must be examined carefully by the hadronic physics community prior to drawing any definitive conclusions. Since most theoretical calculations do not predict $R_{2\gamma} < 1$ at high ϵ , as indicated by the experimental data, this behavior in particular will need to be considered as models and calculations for the proton form factors are assessed. As noted, however, the three experiments provide a clear indication of the presence of TPE in $e^\pm p$ scattering, and the strength of the OLYMPUS data should provide strong guidance in discriminating between proton form factor and TPE models going forward.

7.5 Outlook

OLYMPUS has measured the $\sigma_{e^+p}/\sigma_{e^-p}$ ratio to high statistical precision over the kinematic range ($0.4 \leq \epsilon \leq 0.9$), ($0.6 \leq Q^2 \leq 2.2$) GeV^2/c^2 , with systematic uncertainties on the order of 1-2%. The OLYMPUS data indicates that $\sigma_{e^+p}/\sigma_{e^-p}$ is below unity at high- ϵ and then rises monotonically by several percent across the range of the data. The systematic uncertainties are currently dominated by knowledge of the drift chamber acceptance and efficiency, and will likely be reduced as further studies are completed prior to the publication of the final $R_{2\gamma}$ results. Additionally, the OLYMPUS 12° telescope tracking system, in combination with the multi-interaction event luminosity determination, has provided an extremely precise measurement (0.56% total uncertainty) of $R_{2\gamma}$ at high ϵ /small θ . This result provides a valuable normalization point for the VEPP-3 TPE experiment [115], providing guidance for the absolute scale of their luminosity normalization point at similar kinematics.

While the three TPE experiments indicate that there is a significant contribution from TPE to elastic $e^\pm p$ scattering, whether the effect is large enough to fully account for the $\mu_p G_E/G_M$ ratio discrepancy will likely be a topic of considerable debate in the hadronic physics community. In particular, the validity of different models in the kinematic ranges relevant to the experimental data will need to be carefully consid-

ered before drawing definitive conclusions. While the measurement of a very large TPE effect ($\sim 6\%$ at $\epsilon = 0.4$) would have likely provided a complete and convincing resolution of the discrepancy, there may be value in an additional measurement of $R_{2\gamma}$ at higher Q^2 (where the form factor ratio discrepancy is more significant) to provide final confirmation of the trends suggested by the TPE experiments below $Q^2 = 2 \text{ GeV}^2$. Such an experiment, however, would be extremely challenging due to the reduced elastic cross section at higher Q^2 in combination with increased cross sections for background processes (which differ between e^-p and e^+p scattering).

Future OLYMPUS publications will include the $R_{2\gamma}$ result (after final analyses of the systematic uncertainties are conducted) and likely also limited results on the absolute cross section and proton elastic form factors, as discussed in Section 6.3. The consistency between the analyses presented in Reference [53], Reference [54], and this work suggest that the final result from OLYMPUS will strongly resemble the preliminary results shown, but further analyses will be conducted to provide greater confidence in the OLYMPUS results. The OLYMPUS results provide the most statistically significant measurement of $R_{2\gamma}$ over a wide kinematic range, including extending measurements to higher Q^2 values where the form factor discrepancy is more significant. The data will be valuable in distinguishing between different phenomenological and theoretical TPE models, providing insight into the structure of the proton and the possible causes of the form factor discrepancy.

Appendix A

The OLYMPUS 3D Event Display

As a tool for the development of the OLYMPUS analysis, a three-dimensional event display was created for the OLYMPUS analysis framework that permitted the visualization of the detector geometry, the results of hit and track reconstruction, and the results of simulated events. The program functions as a standalone visualization tool to allow adaptation for other purposes, but is useful when integrated with an analysis framework (such as the one developed by J.C. Bernauer for OLYMPUS) to permit the simultaneous analysis of the events being visualized. The event display was extremely useful in diagnosing issues both with data reconstruction and simulation by allowing direct inspection of events, especially those events for which a particular procedure was not functioning.

The event display utilizes elements from the ROOT Event Visualization Environment originally developed for the ALICE experiment [52, 203] and OpenGL to produce the detector visualization [204]. The detector geometry is imported via the GDML format discussed in Section 4.1.1 [154], and thus the display is capable of visualizing any geometry in that format. The display provides functionality to control which elements of the detector are displayed, how and which elements of the data and reconstruction are displayed, completely control the camera view of the detector and to switch between orthographic and perspective viewing modes, and to save images of the display. The display also provides information relevant to the events displayed and inherits functionality from the OLYMPUS analysis framework that allows di-

rect access to specific events in a file and viewing of analysis histograms as they are filled by the events being displayed. Figure A-1 shows an example of the interface, displaying the detector and a reconstructed elastic e^-p event.

The source code for the OLYMPUS Event Display (written in C++ using ROOT libraries) is available from the author for academic purposes, and is easily adaptable for other particle physics experiments. Notably, Geant4 includes the functionality to export geometries written in the Geant4 geometry framework to GDML, providing immediate compatibility with the OLYMPUS event display [155].

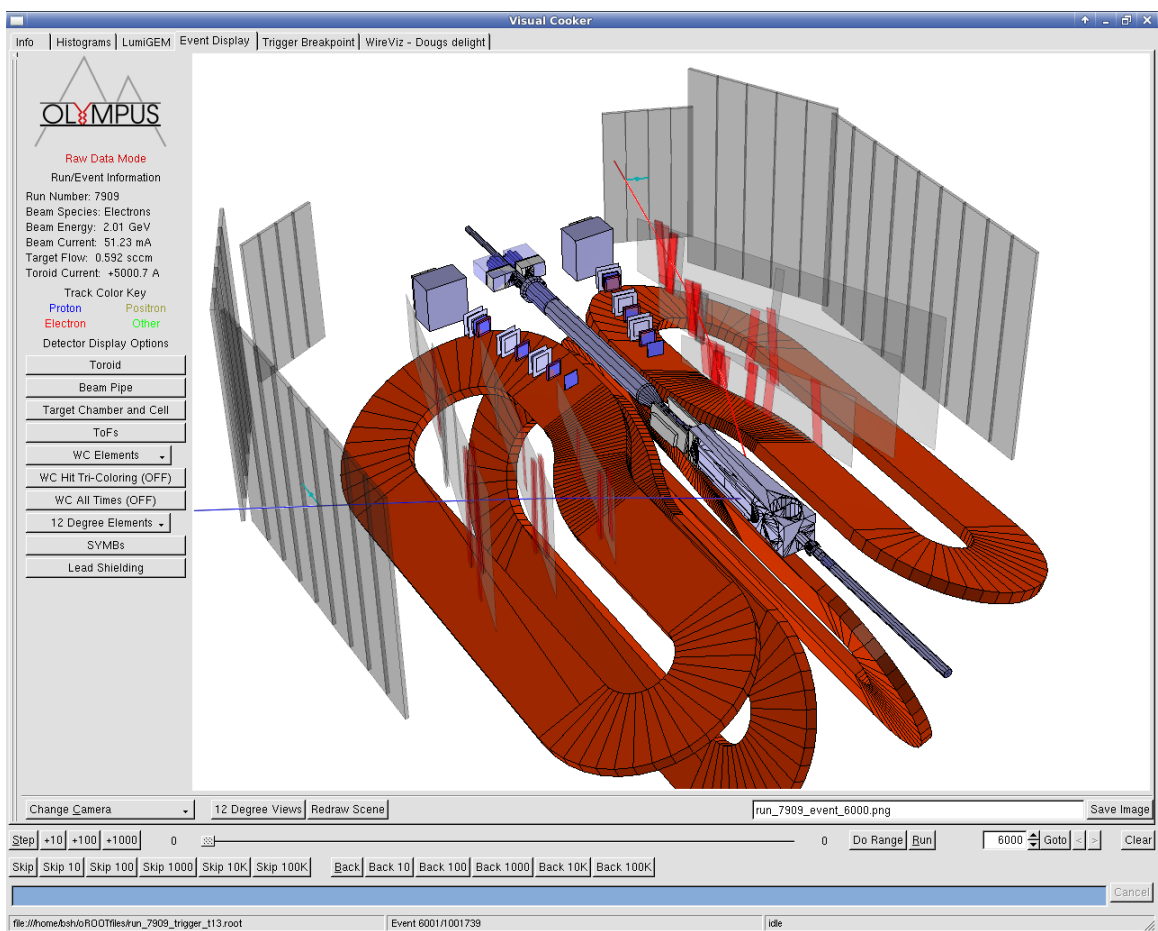


Figure A-1: The user interface of the OLYMPUS 3D event display, running in conjunction with the OLYMPUS analysis framework for reconstruction of events from data. The main display area can be used to visualize the geometry of the detector, hits in the various detector elements, and the results of track reconstruction. The controls surrounding it provide options for changing visualization options, stepping through events, and the ability to save the display window as an image.

Appendix B

Histograms of Data Events by the Quantities used for the Elastic Event Selection

This appendix provides 2D histograms of events after initial pair selection for each of the kinematic cut parameters used in the elastic pair selection described in Section 6.2.2 and the reconstructed lepton angle θ_{e^\pm} . Two histograms are presented for each parameter: one corresponding to elastic e^-p event selection and the other to e^+p selection. Each histogram has been normalized by the Rosenbluth cross section (using dipole form factors for simplicity) as a function of θ_{e^\pm} to make the scale of the counts across the entire histogram more uniform and thus make the resolution of the reconstructed parameters and shape of the background at back angles visible at all θ_{e^\pm} . In general, the corresponding simulation histograms were effectively identical up to the removal of the background and slightly better resolutions in some parameters.

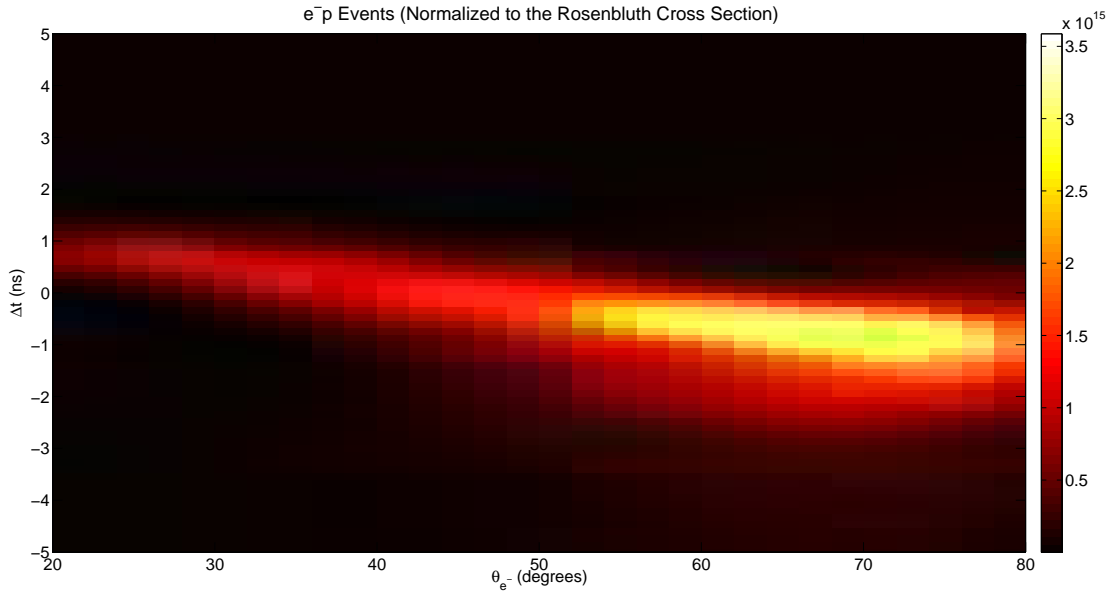


Figure B-1: Histogram of the Δt cut parameter (uncorrected for vertex position) for the e^-p initial pair selection (before background subtraction) as a function of the electron scattering angle, normalized to the Rosenbluth cross section.

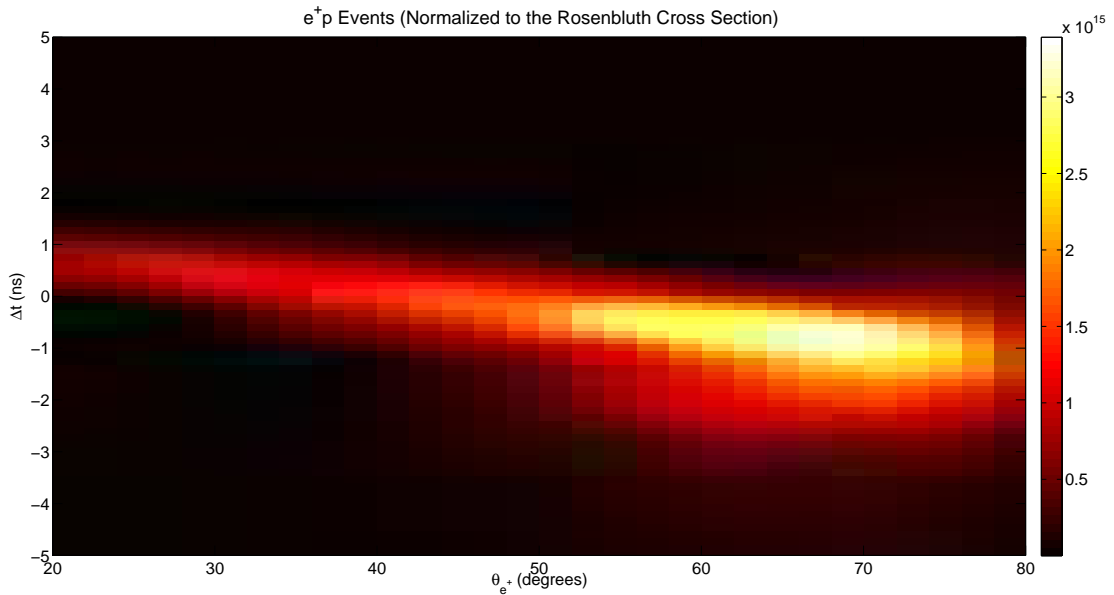


Figure B-2: Histogram of the Δt cut parameter (uncorrected for vertex position) for the e^+p initial pair selection (before background subtraction) as a function of the positron scattering angle, normalized to the Rosenbluth cross section.

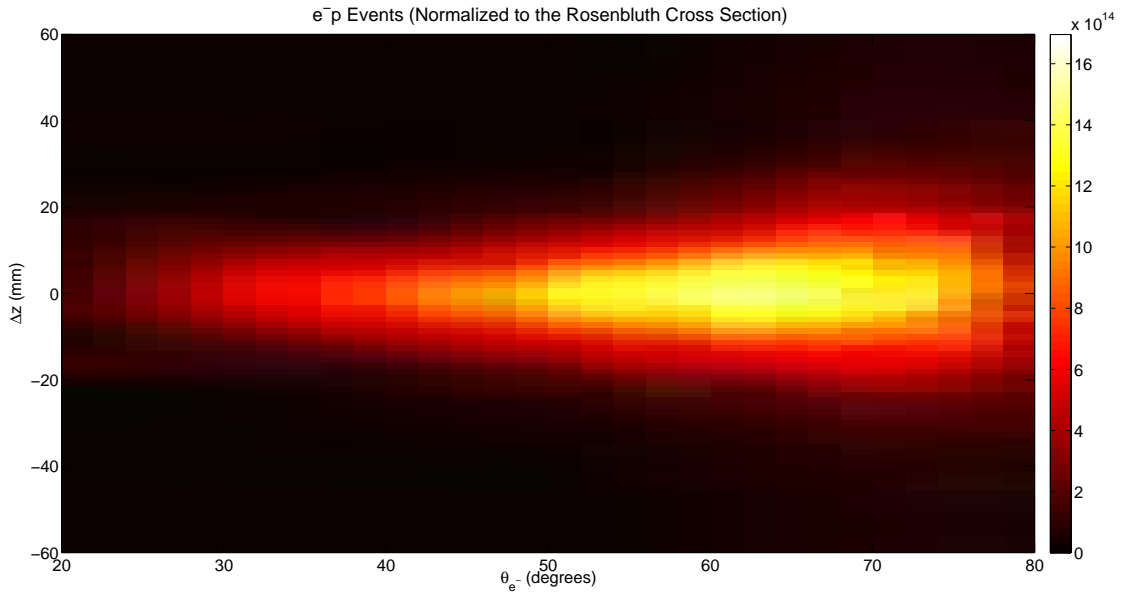


Figure B-3: Histogram of the Δz cut parameter for the e^-p initial pair selection (before background subtraction) as a function of the electron scattering angle, normalized to the Rosenbluth cross section.

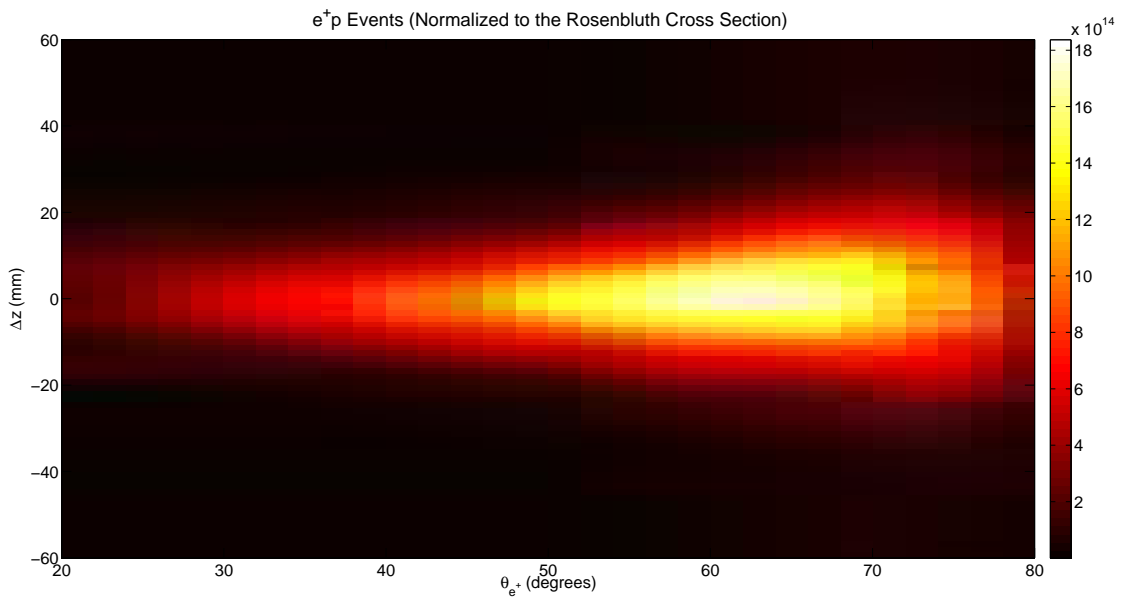


Figure B-4: Histogram of the Δz cut parameter for the e^+p initial pair selection (before background subtraction) as a function of the positron scattering angle, normalized to the Rosenbluth cross section.

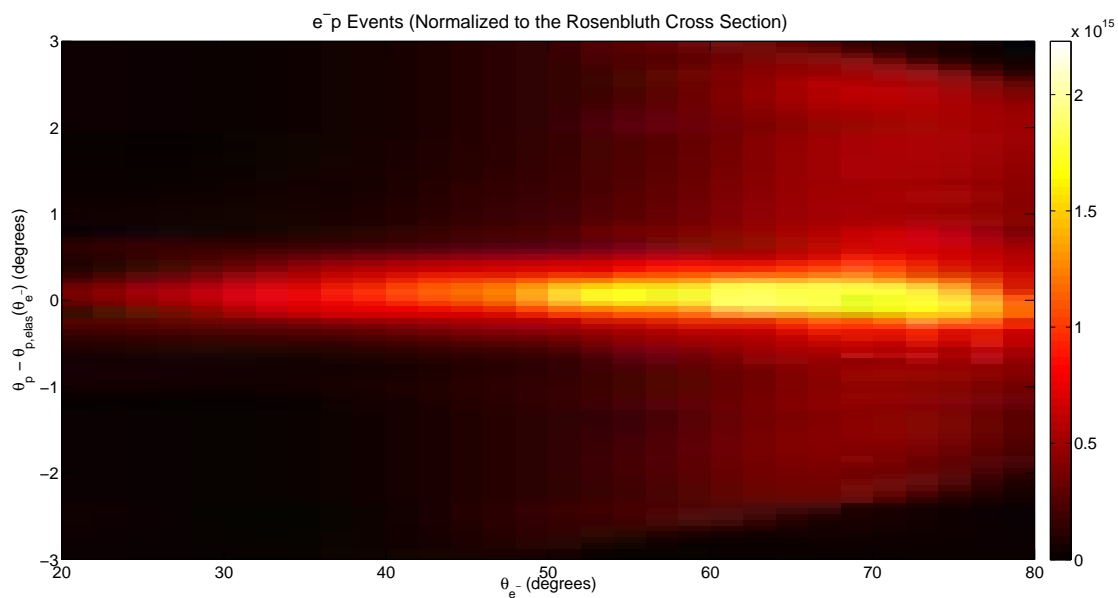


Figure B-5: Histogram of the elastic angle correlation cut parameter for the e^-p initial pair selection (before background subtraction) as a function of the electron scattering angle, normalized to the Rosenbluth cross section.

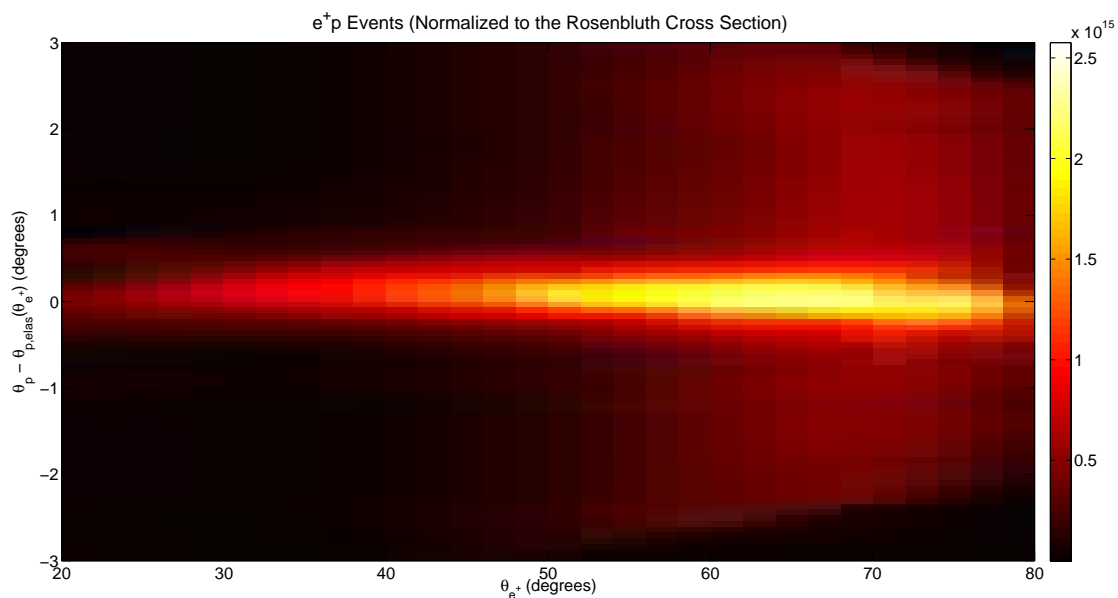


Figure B-6: Histogram of the elastic angle correlation cut parameter for the e^+p initial pair selection (before background subtraction) as a function of the positron scattering angle, normalized to the Rosenbluth cross section.

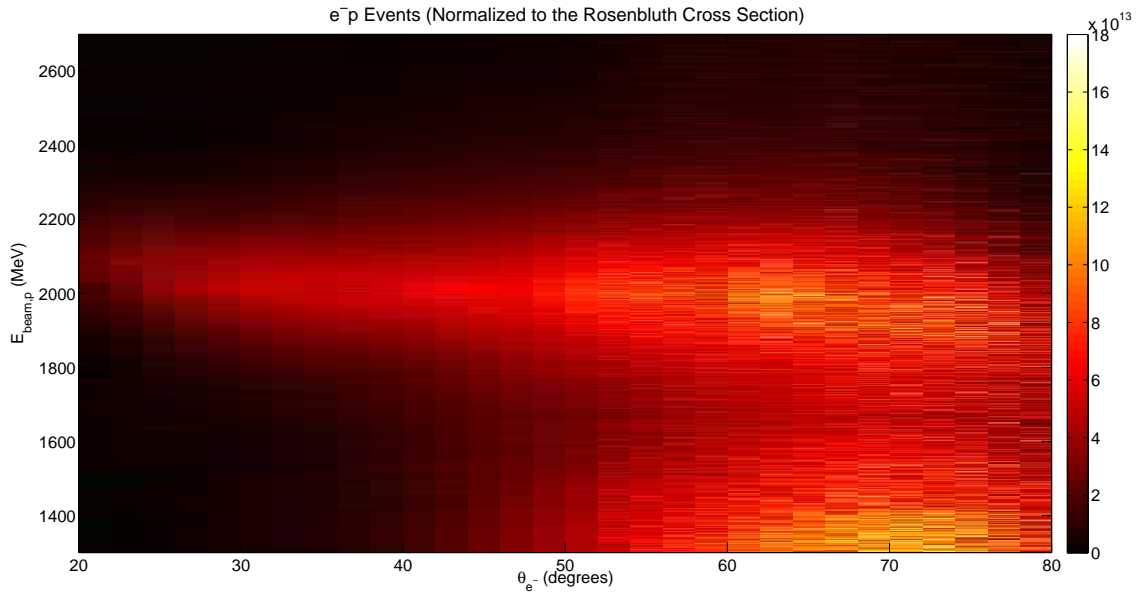


Figure B-7: Histogram of the $E_{\text{beam},p}$ cut parameter for the e^-p initial pair selection (before background subtraction) as a function of the electron scattering angle, normalized to the Rosenbluth cross section.

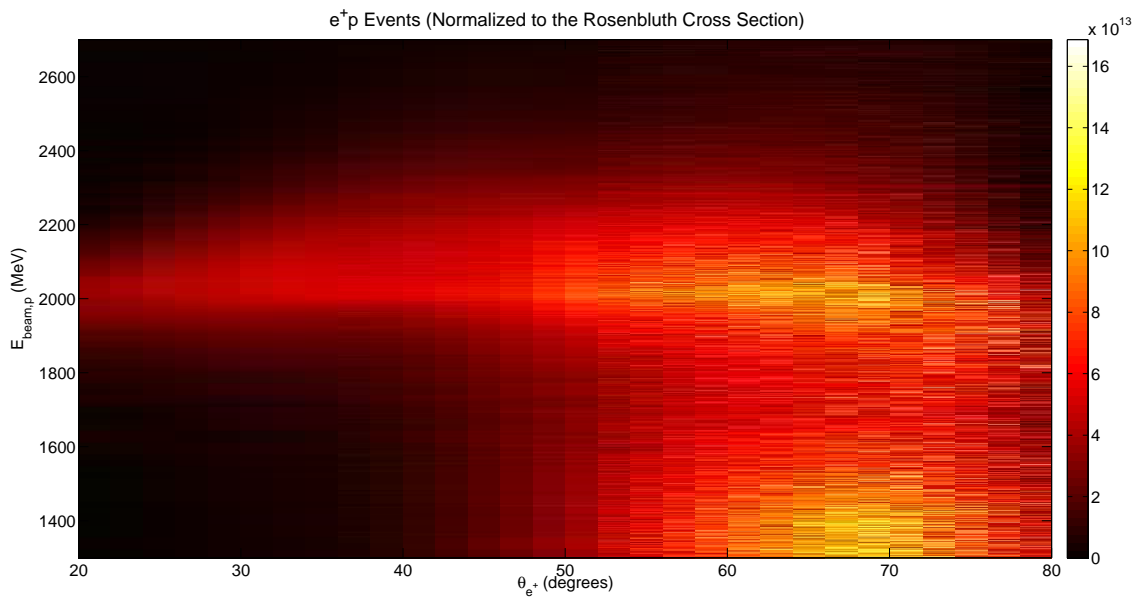


Figure B-8: Histogram of the $E_{\text{beam},p}$ cut parameter for the e^+p initial pair selection (before background subtraction) as a function of the positron scattering angle, normalized to the Rosenbluth cross section.

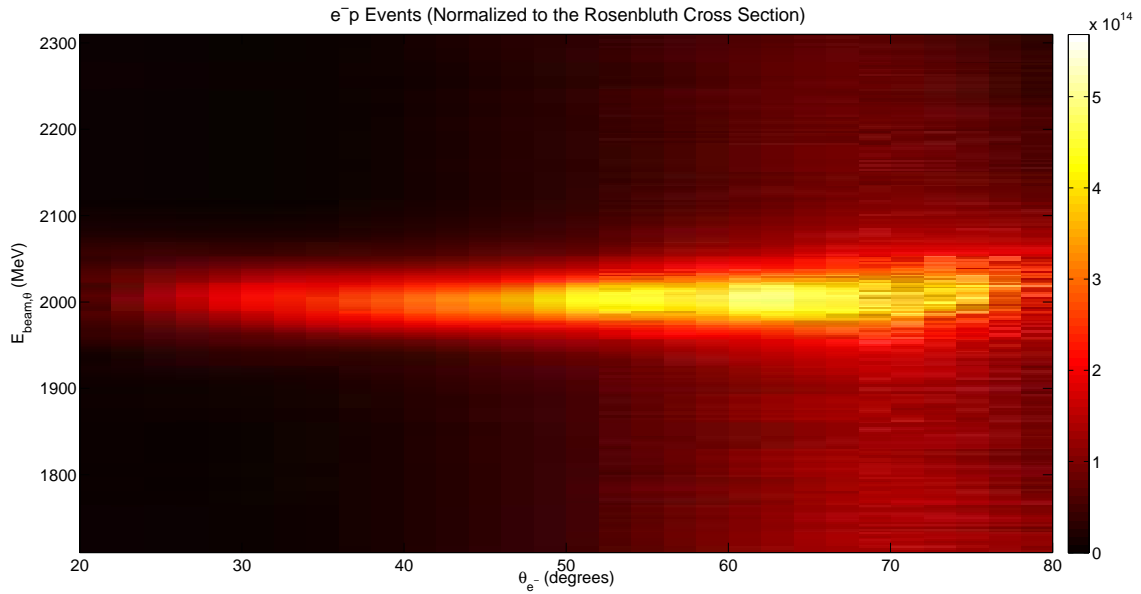


Figure B-9: Histogram of the $E_{\text{beam},\theta}$ cut parameter for the e^-p initial pair selection (before background subtraction) as a function of the electron scattering angle, normalized to the Rosenbluth cross section.

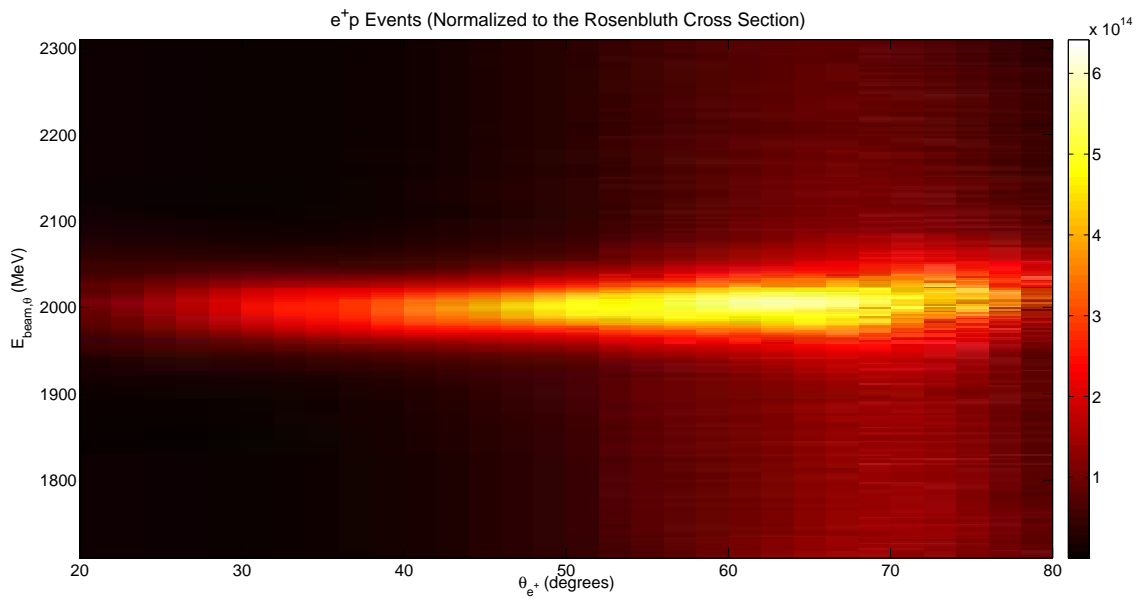


Figure B-10: Histogram of the $E_{\text{beam},\theta}$ cut parameter for the e^+p initial pair selection (before background subtraction) as a function of the positron scattering angle, normalized to the Rosenbluth cross section.

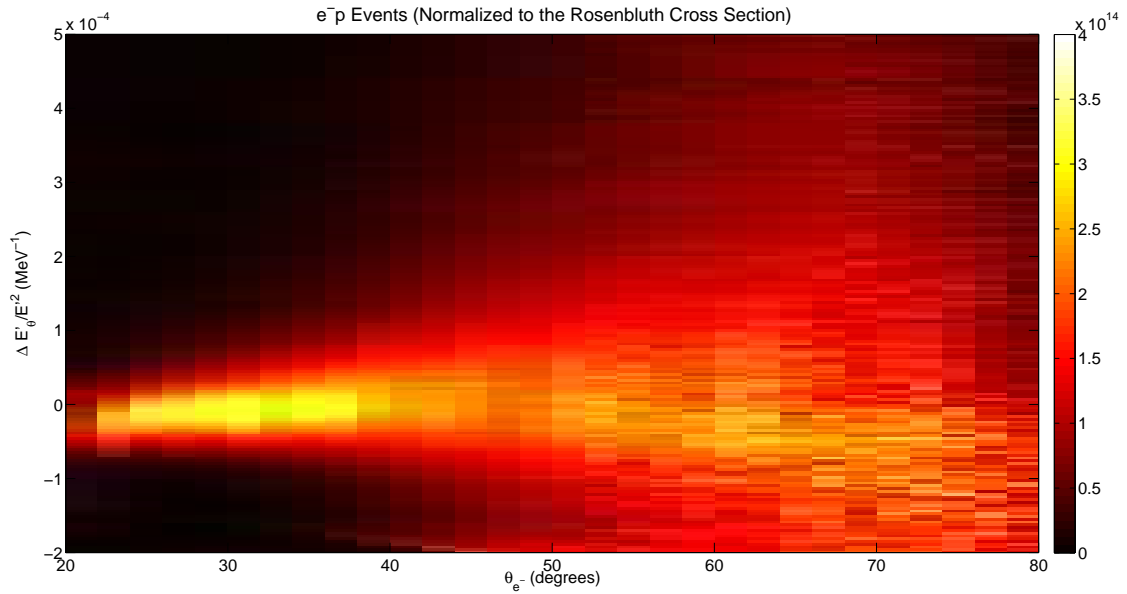


Figure B-11: Histogram of the $\Delta E'_\theta/E'^2$ cut parameter for the e^-p initial pair selection (before background subtraction) as a function of the electron scattering angle, normalized to the Rosenbluth cross section.

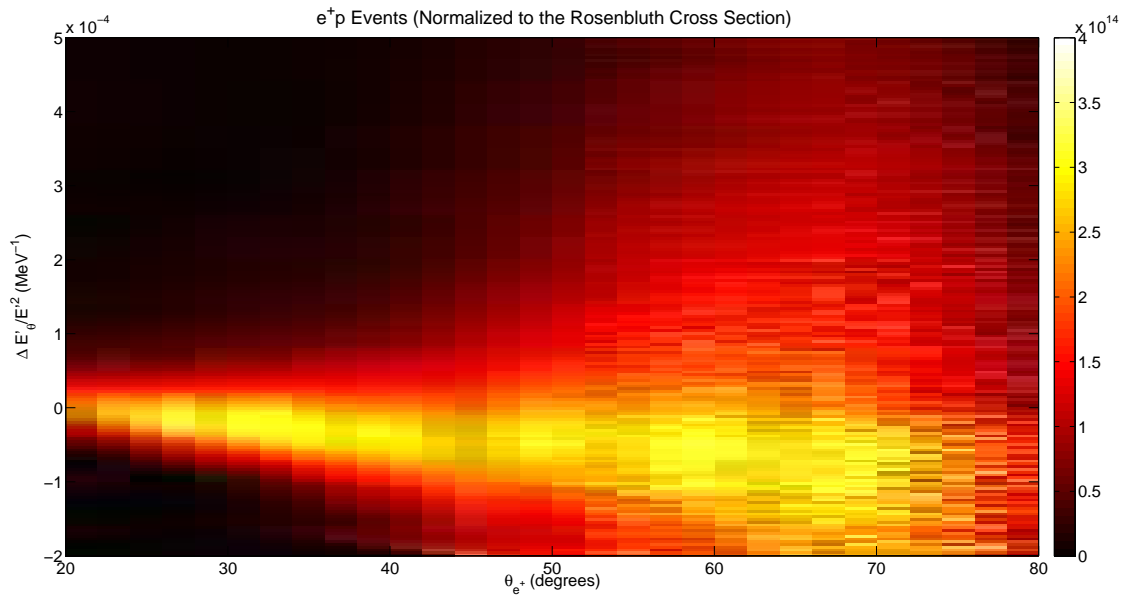


Figure B-12: Histogram of the $\Delta E'_\theta/E'^2$ cut parameter for the e^+p initial pair selection (before background subtraction) as a function of the positron scattering angle, normalized to the Rosenbluth cross section.

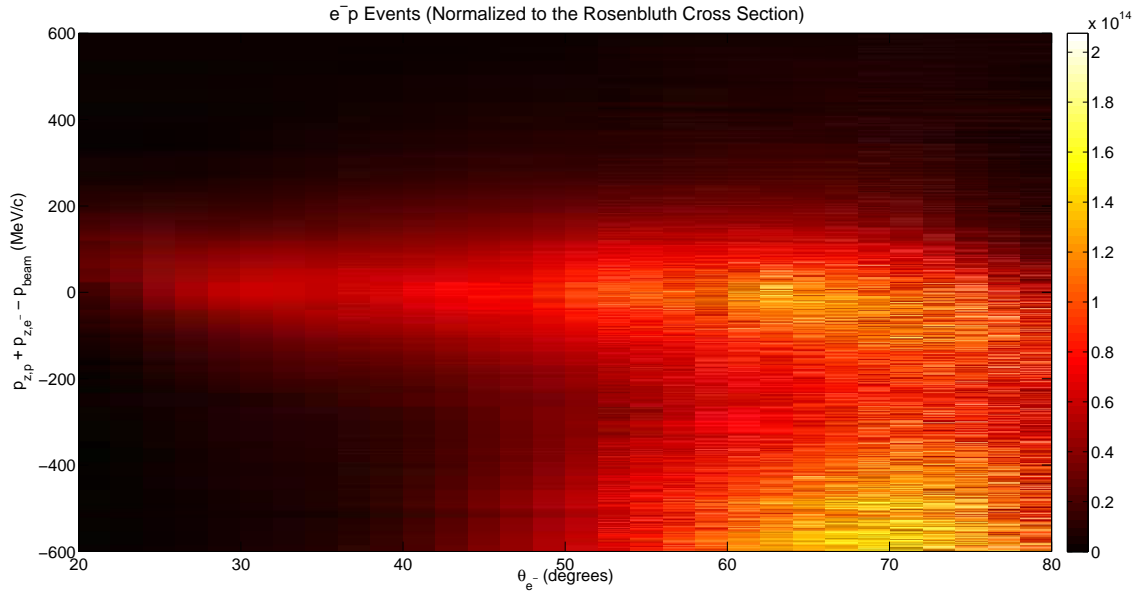


Figure B-13: Histogram of the p_z balance cut parameter for the e^-p initial pair selection (before background subtraction) as a function of the electron scattering angle, normalized to the Rosenbluth cross section.

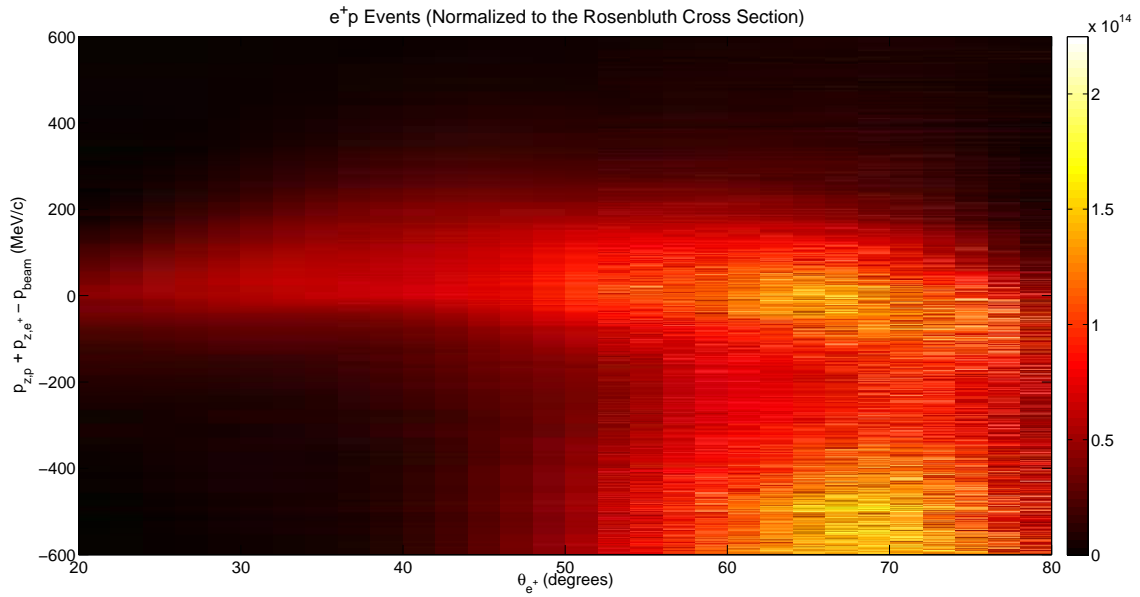


Figure B-14: Histogram of the p_z balance cut parameter for the e^+p initial pair selection (before background subtraction) as a function of the positron scattering angle, normalized to the Rosenbluth cross section.

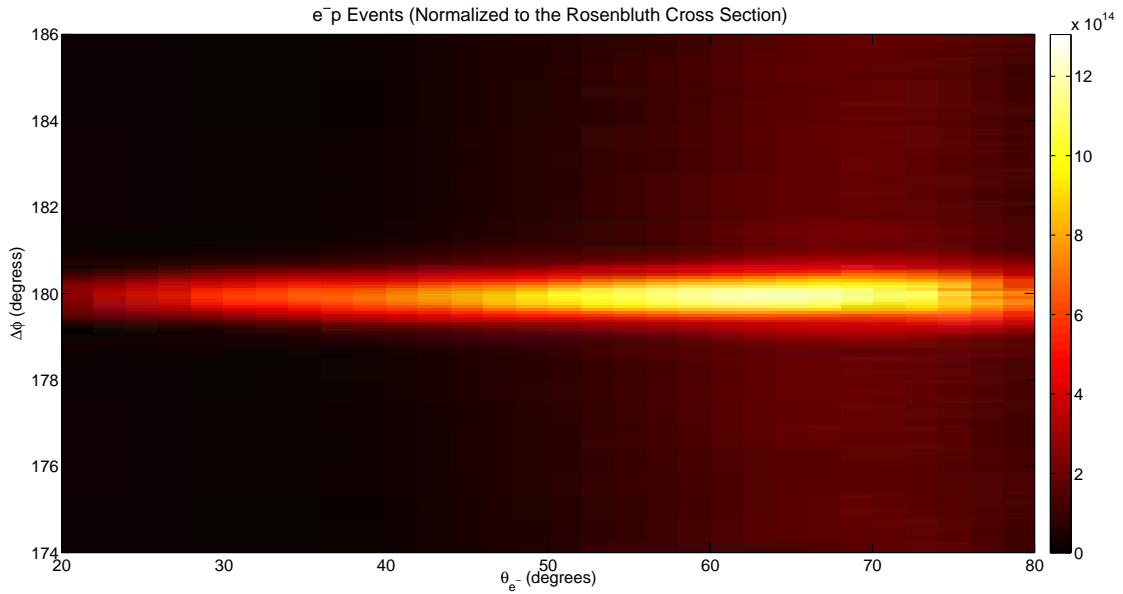


Figure B-15: Histogram of the $\Delta\phi$ cut parameter for the e^-p initial pair selection (before background subtraction) as a function of the electron scattering angle, normalized to the Rosenbluth cross section.

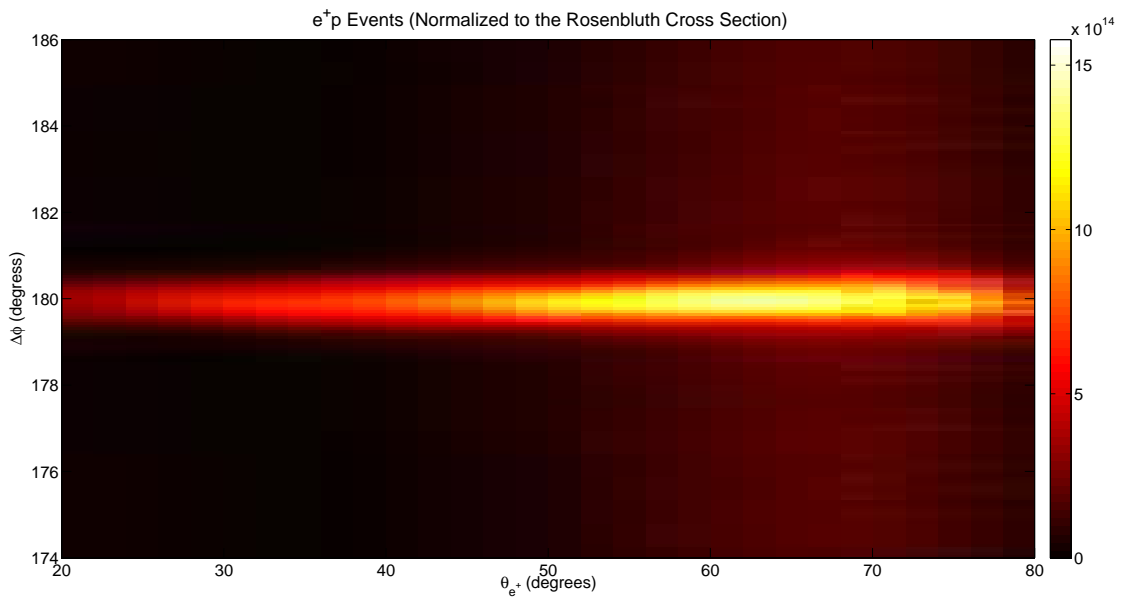


Figure B-16: Histogram of the $\Delta\phi$ cut parameter for the e^+p initial pair selection (before background subtraction) as a function of the positron scattering angle, normalized to the Rosenbluth cross section.

Bibliography

- [1] E. Rutherford, “Collision of α particles with light atoms. IV. An anomalous effect in nitrogen,” *Philosophical Magazine*, vol. 90, no. sup1, pp. 31–37, 1919 (2010).
- [2] E. Rutherford, “Bakerian Lecture. Nuclear Constitution of Atoms,” *Proceedings of the Royal Society of London A: Mathematical, Physical and Engineering Sciences*, vol. 97, no. 686, pp. 374–400, 1920.
- [3] J. Chadwick, “Possible existence of a neutron,” *Nature*, vol. 129, no. 3252, p. 312, 1932.
- [4] J. Chadwick, “Bakerian Lecture. The Neutron,” *Proceedings of the Royal Society of London A: Mathematical, Physical and Engineering Sciences*, vol. 142, no. 846, pp. 1–25, 1933.
- [5] Frisch, R. and Stern, O., “Über die magnetische Ablenkung von Wasserstoffmoleklen und das magnetische Moment des Protons. I,” *Z. Phys.*, vol. 85, pp. 4–16, 1933.
- [6] Frisch, R. and Stern, O., “Über die magnetische Ablenkung von Wasserstoffmoleklen und das magnetische Moment des Protons. II,” *Z. Phys.*, vol. 85, pp. 17–24, 1933.
- [7] R. Hofstadter and R. W. McAllister, “Electron scattering from the proton,” *Phys. Rev.*, vol. 98, pp. 217–218, Apr 1955.
- [8] R. W. McAllister and R. Hofstadter, “Elastic Scattering of 188-MeV Electrons from the Proton and the Alpha Particle,” *Phys. Rev.*, vol. 102, pp. 851–856, May 1956.
- [9] R. Hofstadter, “Electron scattering and nuclear structure,” *Rev. Mod. Phys.*, vol. 28, pp. 214–254, Jul 1956.
- [10] M. Gell-Mann, “A schematic model of baryons and mesons,” *Physics Letters*, vol. 8, no. 3, pp. 214 – 215, 1964.
- [11] G. Zweig, “An SU_3 model for strong interaction symmetry and its breaking; Version 2,” p. 80 p, Feb 1964.

- [12] E. D. Bloom *et al.*, “High-Energy Inelastic $e - p$ Scattering at 6° and 10° ,” *Phys. Rev. Lett.*, vol. 23, pp. 930–934, Oct 1969.
- [13] M. Breidenbach *et al.*, “Observed behavior of highly inelastic electron-proton scattering,” *Phys. Rev. Lett.*, vol. 23, pp. 935–939, Oct 1969.
- [14] P. Skands, *Introduction to QCD*, ch. 8, pp. 341–420.
- [15] K. A. Olive *et al.*, “Review of Particle Physics,” *Chin. Phys.*, vol. C38, p. 090001, 2014.
- [16] D. H. Perkins, “Proton decay experiments,” *Ann. Rev. Nucl. Sci.*, vol. 34, pp. 1–52, 1984.
- [17] G. Senjanović, “Proton decay and grand unification,” *AIP Conference Proceedings*, vol. 1200, no. 1, 2010.
- [18] R. L. Jaffe, “Where does the proton really get its spin?,” *Physics Today*, pp. 24–30, September 1995.
- [19] H. Kolster *et al.*, *The BLAST Polarized H/D Target*, ch. 5, pp. 37–41.
- [20] C. E. Carlson, “The proton radius puzzle,” *Progress in Particle and Nuclear Physics*, vol. 82, pp. 59 – 77, 2015.
- [21] C. Perdrisat, V. Punjabi, and M. Vanderhaeghen, “Nucleon electromagnetic form factors,” *Progress in Particle and Nuclear Physics*, vol. 59, no. 2, pp. 694 – 764, 2007.
- [22] J. Arrington, “Implications of the discrepancy between proton form factor measurements,” *Phys. Rev. C*, vol. 69, p. 022201, Feb 2004.
- [23] M. N. Rosenbluth, “High energy elastic scattering of electrons on protons,” *Phys. Rev.*, vol. 79, pp. 615–619, Aug 1950.
- [24] J. Litt *et al.*, “Measurement of the ratio of the proton form factors, G_E/G_M , at high momentum transfers and the question of scaling,” *Physics Letters B*, vol. 31, no. 1, pp. 40 – 44, 1970.
- [25] W. Bartel *et al.*, “Measurement of proton and neutron electromagnetic form factors at squared four-momentum transfers up to $3 (\text{GeV}/c)^2$,” *Nuclear Physics B*, vol. 58, no. 2, pp. 429 – 475, 1973.
- [26] L. Andivahis *et al.*, “Measurements of the electric and magnetic form factors of the proton from $Q^2 = 1.75$ to $8.83 (\text{GeV}/c)^2$,” *Phys. Rev.*, vol. D 50, pp. 5491–5517, 1994.
- [27] R. C. Walker *et al.*, “Measurements of the proton elastic form factors for $1 \leq Q^2 \leq 3 (\text{GeV}/c)^2$ at SLAC,” *Phys. Rev.*, vol. D 49, pp. 5671–5689, June 1994.

- [28] C. B. Crawford *et al.*, “Measurement of the proton’s electric to magnetic form factor ratio from $^1\vec{h}(\vec{e}, e'p)$,” *Phys. Rev. Lett.*, vol. 98, p. 052301, Jan 2007.
- [29] V. Punjabi *et al.*, “Proton elastic form factor ratios to $Q^2 = 3.5 \text{ GeV}^2$ by polarization transfer,” *Phys. Rev.*, vol. C 71, p. 055202, 2005.
- [30] M. K. Jones *et al.*, “Proton G_E/G_M from beam-target asymmetry,” *Phys. Rev. C*, vol. 74, p. 035201, Sep 2006.
- [31] A. J. R. Puckett *et al.*, “Recoil polarization measurements of the proton electromagnetic form factor ratio to $Q^2 = 8.5 \text{ geV}^2$,” *Phys. Rev. Lett.*, vol. 104, p. 242301, Jun 2010.
- [32] A. J. R. Puckett *et al.*, “Final analysis of proton form factor ratio data at $Q^2 = 4.0, 4.8, \text{ and } 5.6 \text{ geV}^2$,” *Phys. Rev. C*, vol. 85, p. 045203, Apr 2012.
- [33] M. Paolone *et al.*, “Polarization transfer in the $^4\text{He}(\vec{e}, e' \vec{p})^3\text{H}$ reaction at $Q^2 = 0.8 \text{ and } 1.3 \text{ (GeV/c)}^2$,” *Phys. Rev. Lett.*, vol. 105, p. 072001, Aug 2010.
- [34] J. Arrington, “How well do we know the electromagnetic form factors of the proton?,” *Phys. Rev. C*, vol. 68, p. 034325, Sep 2003.
- [35] M. E. Christy *et al.*, “Measurements of electron-proton elastic cross sections for $0.4 < Q^2 < 5.5 \text{ (GeV/c)}^2$,” *Phys. Rev.*, vol. C 70, p. 015206, 2004.
- [36] I. A. Qattan *et al.*, “Precision Rosenbluth measurement of the proton elastic form factors,” *Phys. Rev. Lett.*, vol. 94, p. 142301, 2005.
- [37] J. C. Bernauer *et al.*, “Electric and magnetic form factors of the proton,” *Phys. Rev. C*, vol. 90, p. 015206, Jul 2014.
- [38] R. Milner, D. Hasell, M. Kohl, U. Schneekloth, *et al.*, “The OLYMPUS Experiment,” *Nucl. Instrum. Meth.*, vol. A 741, no. 0, pp. 1–17, 2014.
- [39] P. G. Blunden, W. Melnitchouk, and J. A. Tjon, “Two photon exchange and elastic electron proton scattering,” *Phys. Rev. Lett.*, vol. 91, p. 142304, 2003.
- [40] Y. C. Chen *et al.*, “Partonic calculation of the two-photon exchange contribution to elastic electron-proton scattering at large momentum transfer,” *Phys. Rev. Lett.*, vol. 93, p. 122301, Sep 2004.
- [41] A. V. Afanasev *et al.*, “Two-photon exchange contribution to elastic electron-nucleon scattering at large momentum transfer,” *Phys. Rev.*, vol. D72, p. 013008, Jul 2005.
- [42] P. G. Blunden, W. Melnitchouk, and J. A. Tjon, “Two-photon exchange in elastic electron-nucleon scattering,” *Phys. Rev.*, vol. C72, p. 034612, Sep 2005.

- [43] S. Kondratyuk, P. G. Blunden, W. Melnitchouk, and J. A. Tjon, “ Δ resonance contribution to two-photon exchange in electron-proton scattering,” *Phys. Rev. Lett.*, vol. 95, p. 172503, Oct 2005.
- [44] D. Borisyuk and A. Kobushkin, “Box diagram in the elastic electron-proton scattering,” *Phys. Rev.*, vol. C74, p. 065203, 2006.
- [45] E. Tomasi-Gustafsson *et al.*, “Compilation and analysis of charge asymmetry measurements from electron and positron scattering on nucleon and nuclei,” *Phys. Atom. Nucl.*, vol. 76, pp. 937–946, 2013.
- [46] Y.-C. Chen, C.-W. Kao, and S.-N. Yang, “Is there model-independent evidence of the two-photon-exchange effect in the electron-proton elastic scattering cross-section?,” *Phys. Lett.*, vol. B652, pp. 269–274, 2007.
- [47] J. Guttmann *et al.*, “Determination of two-photon exchange amplitudes from elastic electron-proton scattering data,” *The European Physical Journal A-Hadrons and Nuclei*, vol. 47, pp. 1–5, 2011. 10.1140/epja/i2011-11077-4.
- [48] D. Yount and J. Pine, “Scattering of high-energy positrons from protons,” *Phys. Rev.*, vol. 128, pp. 1842–1849, Nov 1962.
- [49] A. Browman, F. Liu, and C. Schaerf, “Positron-proton scattering,” *Phys. Rev.*, vol. 139, pp. B1079–B1085, 1965.
- [50] B. Bouquet *et al.*, “Backward scattering of positrons and electrons on protons,” *Physics Letters B*, vol. 26, no. 3, pp. 178 – 180, 1968.
- [51] J. Mar *et al.*, “A comparison of electron-proton and positron-proton elastic scattering at four-momenta transfers up to $5.0 \text{ (GeV}/c)^2$,” *Phys. Rev. Lett.*, vol. 21, pp. 482–484, 1968.
- [52] R. Brun and F. Rademakers, “ROOT - An Object Oriented Data Analysis Framework, Proceedings AIHENP’96 Workshop, Lausanne, Sep. 1996,” *Nucl. Inst. & Meth. in Phys. Res.*, vol. A 389, pp. 81–86, 1997.
- [53] A. Schmidt, *Measuring the lepton sign asymmetry in elastic electron-proton scattering with OLYMPUS*. PhD thesis, Massachusetts Institute of Technology, Cambridge, Massachusetts, 2016.
- [54] R. Russell, *A Measurement of the Two-Photon Exchange Effect in Elastic Electron-Proton Scattering with OLYMPUS*. PhD thesis, Massachusetts Institute of Technology, Cambridge, Massachusetts, 2016.
- [55] C. O’Connor, *The Contribution of Two Photon Exchange in Elastic Lepton-Proton Scattering*. PhD thesis, Massachusetts Institute of Technology, Cambridge, Massachusetts, 2017.

- [56] D. Griffiths, *Introduction to Elementary Particles*. Weinheim, Germany: Wiley-VCH, 2 ed., 2008.
- [57] C. Grupen and B. Shwartz, *Particle Detectors*. Cambridge, United Kingdom: Cambridge University Press, 2 ed., 2008.
- [58] M. E. Peskin and D. V. Schroeder, *An Introduction to Quantum Field Theory*. Boulder, Colorado: Westview Press, 1995.
- [59] S. Aoki *et al.*, “Light hadron spectrum and quark masses from quenched lattice QCD,” *Phys. Rev. D*, vol. 67, p. 034503, Feb 2003.
- [60] C. T. H. Davies *et al.*, “High-precision lattice qcd confronts experiment,” *Phys. Rev. Lett.*, vol. 92, p. 022001, Jan 2004.
- [61] S. Dürr *et al.*, “Ab initio determination of light hadron masses,” *Science*, vol. 322, no. 5905, pp. 1224–1227, 2008.
- [62] M. E. Rose, “The charge distribution in nuclei and the scattering of high energy electrons,” *Phys. Rev.*, vol. 73, pp. 279–284, Feb 1948.
- [63] J. Arrington, C. D. Roberts, and J. M. Zanotti, “Nucleon electromagnetic form factors,” *Journal of Physics G: Nuclear and Particle Physics*, vol. 34, no. 7, p. S23, 2007.
- [64] J. Arrington, P. Blunden, and W. Melnitchouk, “Review of two-photon exchange in electron scattering,” *Prog. Part. Nucl. Phys.*, vol. 66, pp. 782–833, 2011.
- [65] C. E. Carlson and M. Vanderhaeghen, “Two-Photon Physics in Hadronic Processes,” *Ann. Rev. Nucl. Part. Sci.*, vol. 57, pp. 171–204, 2007.
- [66] R. Pohl *et al.*, “The size of the proton,” *Nature*, vol. 466, pp. 213–216, Jul 2010.
- [67] P. J. Mohr, B. N. Taylor, and D. B. Newell, “CODATA recommended values of the fundamental physical constants: 2006,” *Rev. Mod. Phys.*, vol. 80, pp. 633–730, Jun 2008.
- [68] M. Niering *et al.*, “Measurement of the hydrogen 1S-2S transition frequency by phase coherent comparison with a microwave cesium fountain clock,” *Phys. Rev. Lett.*, vol. 84, pp. 5496–5499, Jun 2000.
- [69] I. Sick, “On the rms-radius of the proton,” *Physics Letters B*, vol. 576, no. 12, pp. 62 – 67, 2003.
- [70] M. Born, “Quantenmechanik der stoßvorgänge,” *Zeitschrift für Physik*, vol. 38, no. 11, pp. 803–827, 1926.
- [71] S. Boffi, C. Giusti, F. D. Pacati, and M. Radici, *Electromagnetic Response of Atomic Nuclei*. New York: Oxford University Press, 1996.

- [72] N. F. Mott, “The scattering of fast electrons by atomic nuclei,” *Proceedings of the Royal Society of London A: Mathematical, Physical and Engineering Sciences*, vol. 124, no. 794, pp. 425–442, 1929.
- [73] N. F. Mott, “The scattering of electrons by atoms,” *Proceedings of the Royal Society of London A: Mathematical, Physical and Engineering Sciences*, vol. 127, no. 806, pp. 658–665, 1930.
- [74] L. L. Foldy, “The electromagnetic properties of Dirac particles,” *Phys. Rev.*, vol. 87, pp. 688–693, Sep 1952.
- [75] L. N. Hand, D. G. Miller, and R. Wilson, “Electric and magnetic form factors of the nucleon,” *Rev. Mod. Phys.*, vol. 35, pp. 335–349, Apr 1963.
- [76] R. G. Sachs, “High-energy behavior of nucleon electromagnetic form factors,” *Phys. Rev.*, vol. 126, pp. 2256–2260, Jun 1962.
- [77] J. J. Kelly, “Nucleon charge and magnetization densities from Sachs form factors,” *Phys. Rev. C*, vol. 66, p. 065203, Dec 2002.
- [78] T. Janssens *et al.*, “Proton form factors from elastic electron-proton scattering,” *Phys. Rev.*, vol. 142, pp. 922–931, 1966.
- [79] D. H. Coward *et al.*, “Electron-proton elastic scattering at high momentum transfers,” *Phys. Rev. Lett.*, vol. 20, pp. 292–295, Feb 1968.
- [80] L. E. Price *et al.*, “Backward-angle electron-proton elastic scattering and proton electromagnetic form factors,” *Phys. Rev. D*, vol. 4, pp. 45–53, Jul 1971.
- [81] C. Berger *et al.*, “Electromagnetic form factors of the proton at squared four-momentum transfers between 10 and 50 fm²,” *Physics Letters B*, vol. 35, no. 1, pp. 87 – 89, 1971.
- [82] K. M. Hanson and other, “Large-angle quasielastic electron-deuteron scattering,” *Phys. Rev. D*, vol. 8, pp. 753–778, Aug 1973.
- [83] F. Borkowski *et al.*, “Electromagnetic Form-Factors of the Proton at Low Four-Momentum Transfer,” *Nucl. Phys.*, vol. B 93, p. 461, 1975.
- [84] A. F. Sill *et al.*, “Measurements of elastic electron-proton scattering at large momentum transfer,” *Phys. Rev. D*, vol. 48, pp. 29–55, Jul 1993.
- [85] O. Gayou *et al.*, “Measurements of the elastic electromagnetic form-factor ratio $\mu_p G_{E_p}/G_{M_p}$ via polarization transfer,” *Phys. Rev.*, vol. C 64, p. 038202, 2001.
- [86] O. Gayou *et al.*, “Measurement of G_{E_p}/G_{M_p} in $\vec{e}p \rightarrow e\vec{p}$ to $Q^2 = 5.6 \text{ GeV}^2$,” *Phys. Rev. Lett.*, vol. 88, p. 092301, Mar 2002.

- [87] G. MacLachlan *et al.*, “The ratio of proton electromagnetic form factors via recoil polarimetry at $Q^2 = 1.13 \text{ (GeV/c)}^2$,” *Nucl. Phys.*, vol. A764, pp. 261–273, 2006.
- [88] M. K. Jones *et al.*, “ G_{E_p}/G_{M_p} Ratio by Polarization Transfer in $\vec{e}p \rightarrow e\vec{p}$,” *Phys. Rev. Lett.*, vol. 84, pp. 1398–1402, Feb 2000.
- [89] G. Ron *et al.*, “Measurements of the proton elastic-form-factor ratio $\mu_p G_E^p/G_M^p$ at low momentum transfer,” *Phys. Rev. Lett.*, vol. 99, p. 202002, Nov 2007.
- [90] X. Zhan *et al.*, “High-precision measurement of the proton elastic form factor ratio at low Q^2 ,” *Physics Letters B*, vol. 705, no. 12, pp. 59 – 64, 2011.
- [91] G. Ron *et al.*, “Low- Q^2 measurements of the proton form factor ratio $\mu_p G_E/G_M$,” *Phys. Rev. C*, vol. 84, p. 055204, Nov 2011.
- [92] R. C. Fernow, *Introduction to Experimental Particle Physics*. Cambridge, United Kingdom: Cambridge University Press, 1986.
- [93] A. I. Akhiezer and R. M. P., “Polarization phenomena in electron scattering by protons in the high energy region,” *Sov. Phys. Dokl.*, vol. 13, p. 572, Dec 1968.
- [94] A. I. Akhiezer and R. M. P., “Polarization effects in the scattering of leptons by hadrons,” *Sov. J. Part. Nucl.*, vol. 4, p. 277, 1974.
- [95] R. G. Arnold, C. E. Carlson, and F. Gross, “Polarization transfer in elastic electron scattering from nucleons and deuterons,” *Phys. Rev. C*, vol. 23, pp. 363–374, Jan 1981.
- [96] N. Dombey, “Scattering of polarized leptons at high energy,” *Rev. Mod. Phys.*, vol. 41, pp. 236–246, Jan 1969.
- [97] G. Simon *et al.*, “Absolute electron-proton cross sections at low momentum transfer measured with a high pressure gas target system,” *Nuclear Physics A*, vol. 333, no. 3, pp. 381 – 391, 1980.
- [98] Y.-S. Tsai, “Radiative corrections to electron-proton scattering,” *Phys. Rev.*, vol. 122, pp. 1898–1907, Jun 1961.
- [99] L. W. Mo and Y. S. Tsai, “Radiative corrections to elastic and inelastic ep and up scattering,” *Rev. Mod. Phys.*, vol. 41, pp. 205–235, Jan 1969.
- [100] L. C. Maximon and J. A. Tjon, “Radiative corrections to electron-proton scattering,” *Phys. Rev. C*, vol. 62, p. 054320, Oct 2000.
- [101] W. A. McKinley and H. Feshbach, “The Coulomb scattering of relativistic electrons by nuclei,” *Phys. Rev.*, vol. 74, pp. 1759–1763, Dec 1948.
- [102] R. R. Lewis, “Potential scattering of high-energy electrons in second Born approximation,” *Phys. Rev.*, vol. 102, pp. 537–543, Apr 1956.

- [103] S. D. Drell and M. A. Ruderman, “Proton polarizability correction to electron-proton scattering,” *Phys. Rev.*, vol. 106, pp. 561–563, May 1957.
- [104] S. D. Drell and S. Fubini, “Higher electromagnetic corrections to electron-proton scattering,” *Phys. Rev.*, vol. 113, pp. 741–744, Jan 1959.
- [105] J. A. Campbell, “Algebraic computation of radiative corrections for electron-proton scattering,” *Nuclear Physics B*, vol. 1, no. 5, pp. 283 – 300, 1967.
- [106] J. A. Campbell, “Accuracy of radiative corrections to electromagnetic scattering from protons,” *Phys. Rev.*, vol. 180, pp. 1541–1546, Apr 1969.
- [107] G. K. Greenhut, “Two-photon exchange in electron-proton scattering,” *Phys. Rev.*, vol. 184, pp. 1860–1867, Aug 1969.
- [108] P. A. M. Guichon and M. Vanderhaeghen, “How to reconcile the Rosenbluth and the polarization transfer method in the measurement of the proton form-factors,” *Phys. Rev. Lett.*, vol. 91, p. 142303, 2003.
- [109] M. Rekaló and E. Tomasi-Gustafsson, “Polarization phenomena in en elastic scattering, for axial parametrization of two-photon exchange,” *Nuclear Physics A*, vol. 742, no. 3, pp. 322 – 334, 2004.
- [110] R. Anderson *et al.*, “Scattering of positrons and electrons from protons,” *Phys.Rev.Lett.*, vol. 17, pp. 407–409, 1966.
- [111] G. Cassiday *et al.*, “Comparison of elastic positron-proton and electron-proton scattering cross sections,” *Phys. Rev. Lett.*, vol. 19, pp. 1191–1192, Nov 1967.
- [112] W. Bartel *et al.*, “Scattering of positrons and electrons from protons,” *Physics Letters B*, vol. 25, no. 3, pp. 242 – 245, 1967.
- [113] D. Adikaram *et al.*, “Towards a resolution of the proton form factor problem: New electron and positron scattering data,” *Phys. Rev. Lett.*, vol. 114, p. 062003, Feb 2015.
- [114] D. Rimal *et al.*, “Measurement of two-photon exchange effect by comparing elastic $e^\pm p$ cross sections.” Pre-print: arXiv:1603.00315, 2016.
- [115] I. A. Rachek *et al.*, “Measurement of the two-photon exchange contribution to the elastic $e^\pm p$ scattering cross sections at the VEPP-3 storage ring,” *Phys. Rev. Lett.*, vol. 114, p. 062005, Feb 2015.
- [116] R. Alarcon and the BLAST Collaboration, “BLAST: A new tool for intermediate energy nuclear physics,” *Nuclear Physics A*, vol. 663664, no. 0, pp. 1111c–1114c, 2000.
- [117] D. Hasell, T. Akdogan, R. Alarcon, W. Bertozzi, E. Booth, *et al.*, “The BLAST experiment,” *Nucl. Instrum. Meth.*, vol. A 603, pp. 247–262, 2009.

- [118] DESY Accelerator Division (M-Division), “DORIS.” http://doris.desy.de/index_eng.html, 2015.
- [119] G. A. Voss, “Report on DORIS,” *IEEE Trans. Nucl. Sci.*, vol. NS-22, no. 3, pp. 1363–1365, 1975.
- [120] “Technical Design Report for the OLYMPUS Experiment,” tech. rep., The OLYMPUS Collaboration, 2010.
- [121] W. Hillert, “The Bonn Electron Stretcher Accelerator ELSA: Past and future,” *The European Physical Journal A - Hadrons and Nuclei*, vol. 28, no. 1, pp. 139–148, 2006.
- [122] H. Albrecht *et al.*, “Observation of $B^0 - \overline{B}^0$ mixing,” *Physics Letters B*, vol. 192, no. 1, pp. 245 – 252, 1987.
- [123] “DORIS.” http://www.desy.de/research/facilities__projects/doris/index_eng.html, 2016.
- [124] J. Bernauer *et al.*, “The OLYMPUS internal hydrogen target,” *Nucl. Instrum. Meth.*, vol. A 755, no. 0, pp. 20–27, 2014.
- [125] U. Schneekloth. Personal communication.
- [126] D. Cheever *et al.*, “A highly polarized hydrogen/deuterium internal gas target embedded in a toroidal magnetic spectrometer,” *Nucl. Instrum. Meth.*, vol. A556, pp. 410–420, 2006.
- [127] A. Airapetian *et al.*, “The HERMES polarized hydrogen and deuterium gas target in the HERA electron storage ring,” *Nucl. Instrum. Meth.*, vol. A540, pp. 68–101, 2005.
- [128] J. Bernauer *et al.*, “Measurement and tricubic interpolation of the magnetic field for the OLYMPUS experiment,” *Nucl. Instrum. Meth.*, vol. A 823, pp. 9 – 14, 2016.
- [129] K. A. Dow *et al.*, “Magnetic field measurements of the BLAST spectrometer,” *Nucl. Instrum. Meth.*, vol. A 599, no. 23, pp. 146 – 151, 2009.
- [130] Bicron, “Organic scintillation materials,” 2015.
- [131] W. Blum, W. Riegler, and L. Rolandi, *Particle Detection with Drift Chambers*. Berlin, Germany: Springer-Verlag, 2 ed., 2008.
- [132] B. Foster, “Whisker growth in test cells,” Proceedings of the Workshop on Radiation Damage to Wire Chambers, Berkeley, CA, 1986.
- [133] Kohl, Michael, “The Muon Scattering Experiment (MUSE) at PSI and the proton radius puzzle,” *EPJ Web of Conferences*, vol. 81, p. 02008, 2014.

- [134] J. Balewski *et al.*, “The DarkLight Experiment: A Precision Search for New Physics at Low Energies,” 2014.
- [135] J. Diefenbach. Personal communication.
- [136] F. Sauli, “The gas electron multiplier (GEM): Operating principles and applications,” *Nucl. Instrum. Meth.*, vol. A 805, pp. 2 – 24, 2016.
- [137] M. Kohl. Personal communication.
- [138] M. French *et al.*, “Design and results from the APV25, a deep sub-micron CMOS front-end chip for the CMS tracker,” *Nucl. Instrum. Meth.*, vol. A466, pp. 359–365, 2001.
- [139] P. Musico *et al.*, “Hybrid silicon mustrip and GEM tracker for JLab Hall-A high luminosity experiments,” *IEEE Nucl. Sci. Symp. Conf. Rec.*, vol. 2011, pp. 1306–1308, 2011.
- [140] N. Bondar *et al.*, “Third Generation Coordinate ReadOut System – CROS-3,” *PNPI High Energy Physics Division Main Scientific Activities 2002-2006*, p. 334, 2007.
- [141] R. Veenhof, “GARFIELD, recent developments,” *Nucl. Instrum. Meth.*, vol. A419, pp. 726–730, 1998.
- [142] A. Andreev *et al.*, “Multiwire proportional chambers in the HERMES experiment,” *Nucl. Instrum. Meth.*, vol. A 465, pp. 482–497, May 2001.
- [143] Møller, C. *Ann. Phys.*, vol. 14, p. 531, 1932.
- [144] Bhabha, H.J. *Proc. Roy. Soc. (London)*, vol. A 154, p. 195, 1935.
- [145] R. P. Benito *et al.*, “Design and performance of a lead fluoride detector as a luminosity monitor,” *Nucl. Instrum. Meth.*, vol. A 826, pp. 6 – 14, 2016.
- [146] S. Köbis *et al.*, “Proceedings of the Fifth International Conference on Advanced Technology and Particle Physics: The analog trigger processor for the new parity violation experiment at MAMI,” *Nuclear Physics B - Proceedings Supplements*, vol. 61, no. 3, pp. 625 – 629, 1998.
- [147] R. Kothe, *Aufbau und Betrieb einer schnellen Kalorimerelektronik für ein Experiment zur Messung der Paritätsverletzung in der elastischen Elektronenstreuung*. PhD thesis, Johannes Gutenberg-Universität, Mainz, Germany, 2008.
- [148] S. Baunack *et al.*, “Realtime calibration of the A4 electromagnetic lead fluoride calorimeter,” *Nucl. Instrum. Meth.*, vol. A640, pp. 58–68, 2011.
- [149] D. Anderson *et al.*, “Lead fluoride: An ultra-compact cherenkov radiator for em calorimetry,” *Nucl. Instrum. Meth.*, vol. A 290, no. 2, pp. 385 – 389, 1990.

- [150] S. A. Lewis, “Overview of the Experimental Physics and Industrial Control System: EPICS,” tech. rep., Lawrence Berkeley National Laboratory.
- [151] C. Schmidt, *Development of a new data acquisition system for the CB-ELSA experiment*. PhD thesis, Universität Bonn, Bonn, Germany, 2004.
- [152] J. Zoll, “Zebra Reference Manual book FZ,” tech. rep., CERN Program Library.
- [153] “MEA2 - Vermessung.” http://geo.desy.de/index_ger.html. Accessed: 2016-07-14.
- [154] R. Chytracsek *et al.*, “Geometry description markup language for physics simulation and analysis applications,” *IEEE Transactions on Nuclear Science*, vol. 53, pp. 2892–2896, Oct 2006.
- [155] S. Agostinelli *et al.*, “GEANT4: A Simulation toolkit,” *Nucl. Instrum. Meth.*, vol. A 506, pp. 250–303, 2003.
- [156] J. Bernauer. Personal communication.
- [157] U. Schneekloth *et al.*, “Calibration of OLYMPUS/DORIS beam position monitors,” Proceedings of IBIC2014, Monterey, CA, 2014.
- [158] F. Lekien and J. Marsden, “Tricubic interpolation in three dimensions,” *International Journal for Numerical Methods in Engineering*, vol. 63, no. 3, pp. 455–471, 2005.
- [159] C. B. Crawford, *Precision Measurement of the Proton Electric to Magnetic Form Factor Ratio with BLAST*. PhD thesis, Massachusetts Institute of Technology, Cambridge, Massachusetts, 2005.
- [160] S. Biagi, “Monte Carlo simulation of electron drift and diffusion in counting gases under the influence of electric and magnetic fields,” *Nucl. Instrum. Meth.*, vol. A 421, no. 12, pp. 234 – 240, 1999.
- [161] M. Dell’orso and L. Ristori, “A highly parallel algorithm for track finding,” *Nucl. Instrum. Meth.*, vol. A 287, no. 3, pp. 436 – 438, 1990.
- [162] C. O’Connor. Personal communication.
- [163] M. Ohlsson, C. Peterson, and A. L. Yuille, “Track finding with deformable templates the elastic arms approach,” *Computer Physics Communications*, vol. 71, no. 1, pp. 77 – 98, 1992.
- [164] M. Ohlsson, “Extensions and explorations of the elastic arms algorithm,” *Computer Physics Communications*, vol. 77, no. 1, pp. 19 – 32, 1993.
- [165] N. Meister and D. R. Yennie, “Radiative corrections to high-energy scattering processes,” *Phys. Rev.*, vol. 130, pp. 1210–1229, May 1963.

- [166] R. Ent *et al.*, “Radiative corrections for $(e, e'p)$ reactions at GeV energies,” *Phys. Rev. C*, vol. 64, p. 054610, Oct 2001.
- [167] A. V. Gramolin *et al.*, “A new event generator for the elastic scattering of charged leptons on protons,” *Journal of Physics G: Nuclear and Particle Physics*, vol. 41, no. 11, p. 115001, 2014.
- [168] C. S. Epstein and R. G. Milner, “QED Radiative Corrections to Low-Energy Møller and Bhabha Scattering.” Pre-print: arXiv:1602.07609, 2016.
- [169] D. Yennie *et al.*, “The infrared divergence phenomena and high-energy processes,” *Annals of Physics*, vol. 13, no. 3, pp. 379 – 452, 1961.
- [170] F. Ignatov, “Vacuum polarization.” <http://cmd.inp.nsk.su/~ignatov/vp1/>. Accessed: 2016-05-23.
- [171] F. Ignatov, “Calculation of the vacuum polarization,” The 4th Meeting of the Working Group on Rad. Corrections and MC Generators for Low Energies, IHEP, Beijing, 2008.
- [172] A. Bettini, *Introduction to Elementary Particle Physics*. Cambridge, United Kingdom: Cambridge University Press, 2008.
- [173] J. C. Maxwell, “Illustrations of the dynamical theory of gases.—Part I. On the Motions and Collisions of Perfection Elastic Spheres,” *Phil. Mag.*, vol. 19, pp. 19–32, 1860.
- [174] J. C. Maxwell, “Illustrations of the dynamical theory of gases.—Part II. On the process of diffusion of two or more kinds of moving particles among one another,” *Phil. Mag.*, vol. 20, pp. 21–37, 1860.
- [175] A. Roth, *Vacuum Technology*. Amsterdam: North-Holland Publishing Company, 2 ed., 1982.
- [176] M. Knudsen, “Thermischer Molekulardruck der Gase in Röhren,” *Ann. Physik.*, vol. 33, p. 1435, 1910.
- [177] W. Steckelmacher, “Knudsen flow 75 years on: the current state of the art for flow of rarefied gases in tubes and systems,” *Reports on Progress in Physics*, vol. 49, no. 10, p. 1083, 1986.
- [178] W. Sutherland, “The viscosity of gases and molecular force,” *Phil. Mag.*, vol. 36, pp. 507–531, 1893.
- [179] R. Weast, ed., *CRC Handbook of Chemistry and Physics*. Boca Raton, Florida: CRC Press, 62 ed., 1981.
- [180] M. Knudsen, ed., *The kinetic theory of gases: some modern aspects*. Methuen’s monographs on physical subjects, London: Methuen, 1952.

- [181] W. Steckelmacher, “Molecular flow conductance of long tubes with uniform elliptical cross-section and the effect of different cross-sectional shapes,” *Journal of Physics D: Applied Physics*, vol. 11, no. 4, p. 473, 1978.
- [182] COMSOL, inc., “COMSOL Multiphysics Software.” <https://www.comsol.com/products>.
- [183] F. Pan *et al.*, “The 18th international vacuum congress (ivc-18): The positional and angular distribution of molecules flowing through cylindrical tube in free molecular flow,” *Physics Procedia*, vol. 32, pp. 513 – 524, 2012.
- [184] K. Ackerstaff *et al.*, “The HERMES Spectrometer,” *Nucl. Instrum. Meth.*, vol. A 417, no. 23, pp. 230 – 265, 1998.
- [185] Y. Takeuchi *et al.*, “Signal shape and charge sharing between electrodes of GEM in dimethyl ether,” *Journal of Instrumentation*, vol. 7, no. 03, p. C03042, 2012.
- [186] S. H. Han *et al.*, “Charge-sharing and electron-transfer characteristics of a gas electron multiplier (GEM),” *Journal of the Korean Physical Society*, vol. 40, no. 5, pp. 820–825, 2002.
- [187] P. Arce, “GEANT4E: Error propagation for track reconstruction inside the GEANT4 framework,” CHEP 2006, Mumbai, February 13–17, 2006.
- [188] P. E. Gill and W. Murray, “Algorithms for the Solution of the Nonlinear Least-Squares Problem,” *SIAM J. Numer. Anal.*, vol. 15, pp. 977–992, 1997.
- [189] J. J. Moré, “The MINPACK Project,” in *Sources and Development of Mathematical Software* (W. J. Cowell, ed.), pp. 88–111, Upper Saddle River, NJ: Prentice-Hall, 1984.
- [190] F. Devernay, “C/C++ Minpack,” 2014.
- [191] R. Russell. Personal communication.
- [192] J. Bernauer. Personal communication.
- [193] F. Brinker. Personal communication.
- [194] H. Albrecht *et al.*, “Physics with ARGUS,” *Phys. Rept.*, vol. 276, pp. 223–405, 1996.
- [195] J. Bernauer. Personal communication.
- [196] S. Actis *et al.*, “Quest for precision in hadronic cross sections at low energy: Monte carlo tools vs. experimental data,” *The European Physical Journal C*, vol. 66, no. 3, pp. 585–686, 2010.
- [197] J. J. Kelly, “Simple parametrization of nucleon form factors,” *Phys. Rev. C*, vol. 70, p. 068202, Dec 2004.

- [198] D. Rimal, *Proton Form Factor Puzzle and the CEBAF Large Acceptance Spectrometer (CLAS) Two-Photon Exchange Experiment*. PhD thesis, Florida International University, Miami, Florida, 2014.
- [199] T. Benisch *et al.*, “The luminosity monitor of the HERMES experiment at DESY,” *Nucl. Instrum. Meth.*, vol. A 471, no. 3, pp. 314 – 324, 2001.
- [200] A. Schmidt and J. C. Bernauer, “The comparator saturation hypothesis,” tech. rep., The OLYMPUS Collaboration, 2016.
- [201] R. Russell. Personal communication.
- [202] L. N. Hand, “Experimental investigation of pion electroproduction,” *Phys. Rev.*, vol. 129, pp. 1834–1846, Feb 1963.
- [203] M. Tadel, “Raw-data Display and Visual Reconstruction Validation in ALICE,” Proceedings of CHEP 07, Victoria, Canada, 2007.
- [204] D. Shreiner, *OpenGL Programming Guide: The Official Guide to Learning OpenGL, Versions 3.0 and 3.1*. Addison-Wesley Professional, 7th ed., 2009.